Faculty of Engineering and Science

Design and Performance Analysis of the Energy Extractor for the Solar Chimney Power Plant

Pavitri Apparavoo

0000-0002-0117-4550

This thesis is presented for the Degree of
Master of Philosophy (Mechanical Engineering)
of
Curtin University

January 2022

Declaration

To the best of my knowledge and belief, this thesis contains no material previously published by any other person except where due acknowledgement has been made.

This thesis contains no material which has been accepted for the award of any other degree or diploma in any university.

Signature: Pavitri Apparavoo

Date: 31/01/2022

Dedication

I would like to dedicate this thesis to my parents

Mr Apparavoo Subramanyam

&

Mrs Mahaletchumy Appalanaidu

Thank you for always believing in me

Acknowledgement

My sincere gratitude to the Curtin Malaysia Graduate School (CMGS), Faculty of Engineering and Science (FOES) and Curtin University Malaysia for the Tuition Fee Waiver awarded for this project and the resources provided, without which this work may not have been possible. My unalloyed gratitude to my supervisor, Dr Sukanta Roy, for believing in me and supporting me with constructive feedback and fruitful advice that has made me a better researcher today. A word of thanks also goes out to my thesis committee, A/Prof Agus Saptoro and Dr Yam Ke San, who were willing to help me out in difficult times through helpful suggestions and technical aid. Thank you to Mr Shiekh, the Petrel Lab Officier, who was always prompt to help me with my software issues, and Ms Florence for not only aiding in administrative matters but also for the constant motivation. My sincere thanks to my internal assessors, A/Prof Moola Mohan Reddy and A/Prof Wee Siaw Khur, who have provided sound feedback to strengthen this work.

My deepest gratitude to my father and mother, who always supported me in my undertakings and provided me with words of encouragement when I was in difficult situations. My heartfelt thanks to both my brothers, who always reminded me of good sibling times and never stopped cheering me up. I would also like to thank my sister-in-law and aunty for their moral support. My heartfelt thanks to my friends who were there for me and supported me emotionally when I was feeling down during my Master's Degree. My sincere thanks to Dr Rethnaraj Rambabu for all the guidance, motivation and support given, which has helped me abundantly in completing my thesis. Thank you to Nur Syahirah, Sarah Danial, Sofiah, Kirrthana, Sanchita, Rachita, Ain Fawzi, Dr Rakesh, Arul, Shankar, Karthick, Rishi, Anbarasan, Dr Harrindran, Mr Prasad and his wife Ms Thanisa, Aunty Maria and lakeside cleaning aunties, Uncle Ganesan, Aunty Radha, Pavitrashini, Ms Shubashini Krishnan and Neshan for all the emotional and moral support given throughout my work. Thank you to all the authors of engineering youtube channels, journals, conference papers and books for the insightful information given, which has formed the framework for this work.

Last but most importantly, thank you, God, for always showing me light when in the darkness, giving me the strength to undergo many challenges and always making me feel loved and cared for.

Abstract

Modern civilisations rely heavily on non-renewable energy resources such as gas and petroleum for power generation, where these resources are employed in various sectors, be it global economic domination or social development. The after-effects that impact the environment and social well-being are inevitable with elevated usage of perishable energy resources. Hence, the usage of renewable energy is dynamically encouraged and explored to sustain the current global advancement with minimal or no adverse effect on the ecosystem. This work proposed the application of a Vertical Axis Wind Turbine (VAWT), namely, the Savonius Style Wind Turbine (SSWT) in the Solar Chimney Power Plant (SCPP), which is a form of a renewable energy system that utilises solar radiation for its operation. Previous literature on power extraction improvement in the SCPP showed that there had been limited exploration of the turbine component of the system. Moreover, the performance of the SSWT in the collector region of the SCPP has not been analysed. Thus, this research explored the effectiveness of the SSWT under two different axes of operations in the SCPP (i.e., Horizontal Installation (H_{Ins}) and Vertical Installation (V_{Ins})). The SSWT was validated using experimental and numerical values obtained from previous studies by Roy and Saha (2015), and Roy and Ducoin (2016). The SCPP model was validated against the experimental results reported from the Manzanares plant in Spain. ANSYS Fluent was used for the numerical analysis, where the Sliding Mesh approach was utilised for the SSWT, while the radiation model was adopted for the SCPP. The optimal operation of the SCPP was suggested through the operational axis of the Savonius turbine, which was defined based on the fluid flow velocity, pressure and power output of the system. The fluid flow velocity in the collector region was enhanced by 72.84% with 1° chimney divergence and 114.21% with 2° chimney divergence compared to the conventional chimney design. The analysis of the best performing configuration showed that the H_{Ins} performed better than the V_{Ins} with a conventional chimney design and a 1° chimney divergence design by 2.78% and 3.92%, respectively. However, the inverse was encountered with 2° chimney divergence, where the V_{Ins} 2° outperformed the H_{Ins} 2° by 58.97%. The performance comparison of the SSWT between different chimney divergence suggested that with 1° chimney divergence, the V_{Ins} 1° and H_{Ins} 1° improved by 41.67% and 43.24% compared to V_{Ins} 0° and H_{Ins} 0°, respectively. The power augmentation of V_{Ins} 1° and H_{Ins} 1° enhanced by 634.46% and 640.94% compared to V_{Ins} 0° and H_{Ins} 0°. With 2° chimney divergence, the performance of the V_{Ins} 2° was increased by 8.33%, but the H_{Ins} 2° was reduced by 56.76% compared to V_{Ins} 0° and H_{Ins} 0°. Nevertheless, the power production of V_{Ins} 2° and H_{Ins} 2° increased by 970.48% and 327.44% against the V_{Ins} 0° and H_{Ins} 0° due to higher fluid flow velocity resulting from the 2° chimney divergence. The greater fluid flow velocity caused by the 1° and 2° chimney divergence resulted in a substantial boost in power. The performance of the SSWT enhanced by 22.22% compared to V_{Ins} 0° under the influence of the guide vane and shield at 45° (GVS 45°). In the presence of a deflector, the performance of the SSWT with Def 150° improved by 6.67% against V_{Ins} 0°. The numerical analysis provided positive results in improving the turbine component's efficiency with the application of the SSWT under various configurations in the SCPP.

Table of Contents

List of Tables

List of Figures

List of Abbreviations

Abbreviations	Definitions
VAWT	Vertical Axis Wind Turbine
ANSYS	ANSYS Fluent 2019 R3
CFD	Computational Fluid Dynamics
SSWT	Savonius Style Wind Turbine
SCPP	Solar Chimney Power Plant
HAWT	Horizontal Axis Wind Turbine
SUPP	Solar Updraft Power Plant System
SUT	Solar Updraft Tower
CAD	Computer-Aided Design
URANS	Unsteady Reynolds Averaged Navier Stokes
GIT	Grid Independence Test
TSR	Tip Speed Ratio
H_{Ins}	Horizontal Installation
V_{Ins}	Vertical Installation
TSR	Tip Speed Ratio
V_{Ins} 0°	Vertical Installation in 0° Chimney Divergence
V_{Ins} 1°	Vertical Installation in 1° Chimney Divergence
V_{Ins} 2°	Vertical Installation in 2° Chimney Divergence
H_{Ins} 0°	Horizontal Installation in 0° Chimney Divergence
H_{Ins} 1°	Horizontal Installation in 1° Chimney Divergence
H_{Ins} 2°	Horizontal Installation in 2° Chimney Divergence
GV	Guide Vane
GVS	Guide Vane and Shield
GVS 0°	Guide Vane and Shield at 0° Guide Vane Angle
GVS 22.5°	Guide Vane and Shield at 22.5° Guide Vane Angle
GVS 45°	Guide Vane and Shield at 45° Guide Vane Angle
Def	Deflector
Def 140°	Deflector at 140° Angle
Def 145°	Deflector at 145° Angle
Def 150°	Deflector at 150° Angle

List of Nomenclature

Nomenclature	Parameter
C_p	Coefficient of Performance/ Performance Coefficient
C_m	Coefficient of Moment/Moment Coefficient
θ	Angle of Guide Vane/Deflector
$\emptyset$	Azimuth Angle

CHAPTER 1
INTRODUCTION

1.0 Introduction

1.0.1 Solar Chimney Power Plants

The solar chimney power plant, SCPP, is currently one of the potential solar energy conversion systems for commercial electrical power generation. The SCPP converts the solar energy indirectly to electrical energy using the collector as a heat exchanger, the chimney as a pressure tube to exhaust the generated buoyant air from the collector and the turbine to extract the energy in the buoyant air while the mechanical energy generated from the rotation of the turbine is extracted to electricity using a generator. The solar chimney has been identified to be of long service should the efficiency be improved (Zhou, Yuan and Bernardes 2013; Bernardes and Zhou 2013). Schlaich (1995) and Schlaich et al. (2005) stated that the chimney component of the SCPP, when constructed to standard specification with reinforced concrete in areas having dry climatic conditions, will have an unlimited lifetime. The SCPP is made up of three components, namely, the collector, the chimney and the turbine. The collector currently has about 20% to 30% efficiency, the turbine efficiency has been proven to be above 66% efficiency for a shrouded wind turbine, while the chimney efficiency has mainly been a function of the chimney height and ambient temperature (Al-Kayiem and Aja 2016). Currently, the major issues associated with the SCPP are based on the chimney component and the collector. The chimney efficiency for a 1000 m height cylindrical tube has been found to be in the range of 3%. Consequently, the total efficiency of the SCPP will be affected considering that the efficiency of the SCPP is a product of the efficiencies of the collector, chimney and turbine efficiencies. Figure 1.1 illustrates the main components of the SCPP and operation manner of the working fluid, where point 1 is the solar-air-collector inlet, point 2 is the solar-air-collector outlet, point 3 is the turbine region and point 4 is the chimney region.

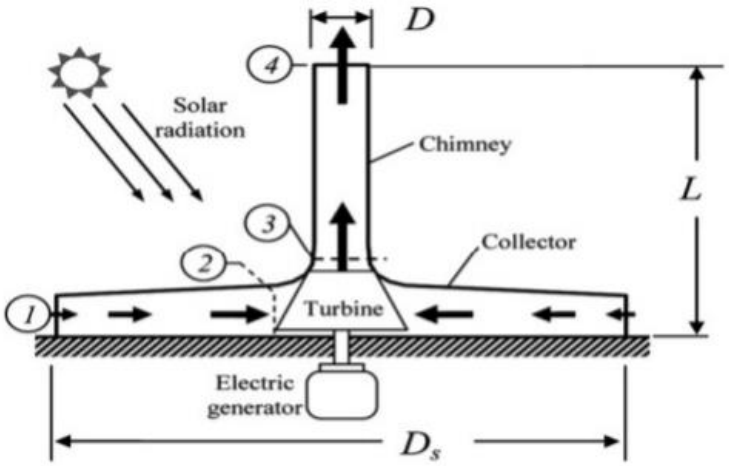

Figure 1.1: Components and operating illustration of a Solar Chimney Power Plant (Beneke, Fourie and Huan 2016)

1.0.2 Wind turbines

Wind turbines are typically used to convert kinetic energy into mechanical energy for power generation. Predominantly, wind turbines can be categorized based on their axis of rotation, namely, the horizontal axis wind turbine (HAWT) and the vertical axis wind turbine (VAWT). The vertical axis wind turbines are also known as the drag type wind turbines. This is due to the drag principle used to generate torque unto the rotating shaft (Yunus 2010). Figure 1.2 shows the types of vertical axis wind turbines.

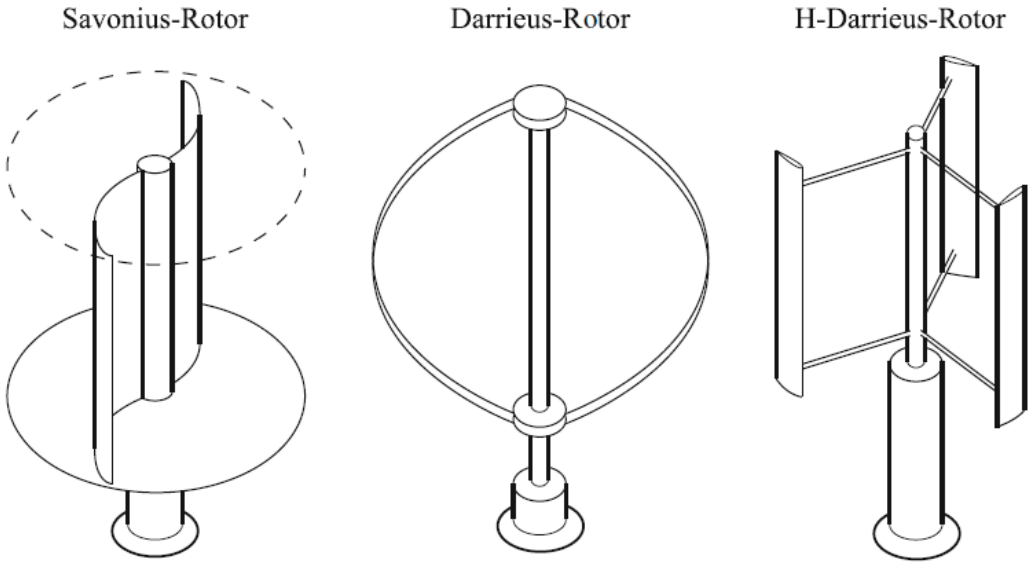

Figure 1.2: Types of vertical axis wind turbine (Schaffarczyk 2020)

One of the biggest benefits of the VAWT is the ability to function without a specific wind angle (Schaffarczyk 2020). The Savonius wind turbine is a type of vertical axis

wind turbine that works based on the drag principle. This wind turbine is able to perform well in low wind velocities due to its low starting torque capabilities and its general independence towards wind direction (Wenehenubun, Saputra and Sutanto 2015).

1.1 Problem Statement

Conventionally, SCPPs are designed such that the ground acts as the absorber/heat exchanger, thus requiring a large area of flat land with no alternative usage for the operation of the system (Schlaich et al. 2005; Zhou and Xu 2014). The SCPP undergoes a serial energy conversion process leading to losses at the different processes as well as contributing to the low plant efficiency, which the SCPP is suffering as a setback (Al-Kayiem et al. 2019b). The energy from the sun is dependent on location, season and time of the day, thus leads to fluctuation of the power generated by the plant at various times of the day across the year (Al-Kayeim, Aurybi and Gilani 2019). The turbine component being the only moving part in the SCPP, has received minimal focus on performance enhancement (Guo et al. 2019). Most literature exhibits the SCPP's performance based on the air velocity, temperature and optimum power generation without including the turbine region (Hooi and Thangavelu 2018; Patel, Prasad and Ahmed 2014; Zhou et al. 2008; Ming et al. 2008). Moreover, the performance enhancement studies that were performed experimentally and numerically with the turbine region employing a real wind turbine are comparatively minute (Guo et al. 2015; Gannon and von Backstro¨ m 2003; Tingzhen et al. 2008; Gholamalizadeh and Chung 2017a, 2017b; Ayadi, Driss, et al. 2018a; Ayadi, Driss, et al. 2018b; Fluri 2008; Ayadi, Nasraoui, et al. 2018). Although a commendable number of improvement studies have been conducted on the chimney region, very few investigate the effects of a diverging chimney on the performance of the SCPP (Hu, Leung and Chan 2017; Hassan, Ali and Waqas 2018). The addition of guiding vanes to improve fluid attack on turbine blades has claimed improved performance in the turbine component, although the benefit is confined to its constrained parameters and model type. (Negrou et al. 2018; Denantes and Bilgen 2006; Fluri 2008).

1.2 Objectives

Following the challenges associated with SCPP as in Section 1.1, the objective of this study is to investigate the performance of the SSWT and chimney components in improving the overall power generated by the system. The above main objective will be achieved by accomplishing the sub-objectives listed below.

1. To numerically model and investigate the performance of the SSWT in the SCPP.
2. To numerically study the effect of the conventional and divergent chimney on the performance of the SSWT.
3. To numerically study the effect of guide vanes introduction on the performance of the SSWT in the SCPP.

1.3 Significance of Study

Several significant factors can be addressed through this research. This section discusses the economic, social and environmental importance of the proposed study.

Firstly, the proposed new design of the turbine and chimney region improves the performance of the SCPP. The design consisting of guide vanes and a diverging chimney is predicted to command greater power output than models without either one of the properties. With this outcome, the constraints of the turbine and the chimney section on its low efficiency can be lessened. While the conventional operational methods of the Manzanares plant produced an efficiency not exceeding 0.05%, the current SCPPs from previous literature states that the plant efficiency is around 2% compared to the Manzanares plant (Schlaich et al. 2005). The prediction of more significant power augmentation through the efficiency enhancement of the turbine and chimney components through this work can lighten the economic constriction of the SCPP.

Secondly, the suggested layout of the SCPP is able to contribute to the society living around the area of construction. The proposed design of the SCPP is able to generate energy through natural means at a low maintenance cost. This will be highly beneficial for the surrounding population as it can compensate a certain percentage of daily electricity consumption throughout the day, thereby indirectly reducing the daily living costs of residential areas near the SCPP. Furthermore, since many turbine installations

for power extraction are recommended in this work, the conclusion of this study supports simpler maintenance of the turbine component without halting the overall power generation.

Thirdly, the energy produced from the proposed SCPP design is a form of green energy based on its natural operating means that positively affects the environment. The power generated from the SCPP can compensate certain, if not all, of the electrical energy produced through coal-fired power plants. Increased usage of the proposed SCPP design decreases the dependency on fossil fuels as an energy source for power generation, thereby reducing the adverse effects of non-renewable energy on the environment, such as the emission of greenhouse gases.

1.3.1 Scientific Merits

The driving force of the wind turbine is attained from the airpower generated in the SCPP system. The power in the air is dependent on the buoyant air velocity. The design of the solar chimney has always been such that the air in the collector will be sufficient for low solar radiation for the plant to operate. The plant is restricted by the inlet height of the collector and the associated inclined angle, which determines the air volume in the system. The maximum power available to be harnessed by the turbine in open flow operation from the wind flow stream is formed upon taking the velocity of the wake region, V_w into consideration as shown in Equation 1.1. The wake velocity acts as a disturbance in fluid flow at the turbine region, where if minimised, higher power can be yield from the upstream buoyant air velocity. This can be achieved by introducing guide vanes at the energy extractor, which promotes the optimum angle of air attack on the turbine blades for maximum power yield. In addition, Equation 1.1 depicts that the power extraction by the rotor is also dependant on the pressure differential, Δp_d between the inlet and the exit of the chimney, in which the turbine is positioned. Thus, decreasing the diffuser exit pressure well below the atmospheric pressure promotes greater power augmentation. To do this, increasing the divergence angle of the chimney to a certain limit is expected to achieve lower backpressure at the rear of the turbine.

$$P_{extracted\ by\ rotor} = Q\left[\frac{1}{2}\rho V_u^2 - \frac{1}{2}\rho V_w^2\right] - Q\Delta p_d \qquad 1.1$$

1.4 Scope of Work

In this proposed research, several numerical studies were conducted to evaluate the SCPP's performance-enhancing properties. Firstly, the performance of a proposed Vertical Axis Wind Turbine (VAWT) in the SCPP was analysed by incorporating the data obtained from the validated SCPP. The operation of the proposed VAWT was studied under two different configurations.

Secondly, the performance of a diverging chimney on the SCPP was investigated. The difference between the angle of divergence of the chimney was studied for its best ability to generate power. The influence of two different chimney divergent angles on the performance of the VAWT was explored. The optimum configurations of these parameters on the power generation based on the air velocity of the wake region, pressure, and power production were determined.

Thirdly, the impact of adding guiding vanes in the turbine area was studied. The performance of the guide vanes on power augmentation was examined under various parametric parameters, such as the angle of the guide vanes and their location with regard to the rotors. The guide vanes with the best dimensional arrangement for an optimum air attack on the turbine blades were analysed.

The numerical studies planned for this work was performed using the Computational Fluid Dynamics Software (CFD), ANSYS Fluent, as it is versatile in predicting numerous performance effects of a model by manipulating the parametric dimensions in a short span of time at a minimal cost. The numerical models were developed based on the dimensions of the Manzanares plant constructed in Spain and the previous experimental and numerical studies conducted on the proposed turbine.

1.5 Summary of Chapter 1

This chapter discussed the general out-view of a Solar Chimney Power Plant (SCPP) where it was introduced as a renewable form of power production, the problem statement revolving around the SCPP, which conversed the current lacking in the system, the main objective of this study, which is to understand the performance of the proposed VAWT on power generation in the SCPP, the significance and scientific advantages of conducting this research and the scope of work undertaken in this investigation, to ensure its feasibility within the speculated time-frame and the budget of the project.

CHAPTER 2
LITERATURE REVIEW

2.0 Introduction

This section presents the studies conducted by researchers in the past on SCPP and their developments. The section discusses the fundamental principles of SCPP, the effects of various components on the plant operation, the impact of ambient and other conditions on plant operations and performance. It also reports the different hybrid models developed and their model contributions. The enhancement studies conducted on the turbine region has also been covered in this section.

2.1 Background

The concept of buoyancy-driven flow employed in SCPP could be traced to the procedure employed by Leonardo da Vinci (1452-1519), who used a buoyancy driven windmill to spin meat in a roasting spit for even heating (Francke et al. 2013). This same concept was later employed by a Spanish Colonel, Isidoro Cabanyes in describing the first fundamentals of SCPP in 1903 in his work titled “Proyecto de motor solar (solar engine project)” (Bernardes 2011). Another important milestone in the history of SCPP is the proposal by Professor Bernard Dubos in 1926 to the French Academy of Science to consider solar energy power as an alternative energy for the future by constructing an SCPP at the tall mountains in North Africa and export the energy to Europe. The proposal of constructing a large scale SCPP was considered expensive at the time, as other energy sources were comparatively cheaper (Al-Kayiem and Aja 2016). Several other works were published as patents between 1926 and 1978 before Professor Schlaich presented the SCPP technology again in a congress which birthed the first operational SCPP that was constructed between 1980 and 1982 and was employed for 50 kW daily energy generation till its decommissioning in 1989 (Pasumarthi and Sherif 1998). Figure 2.1 illustrates the collector, turbine and chimney region in the first pilot plant in Manzanares, Spain.

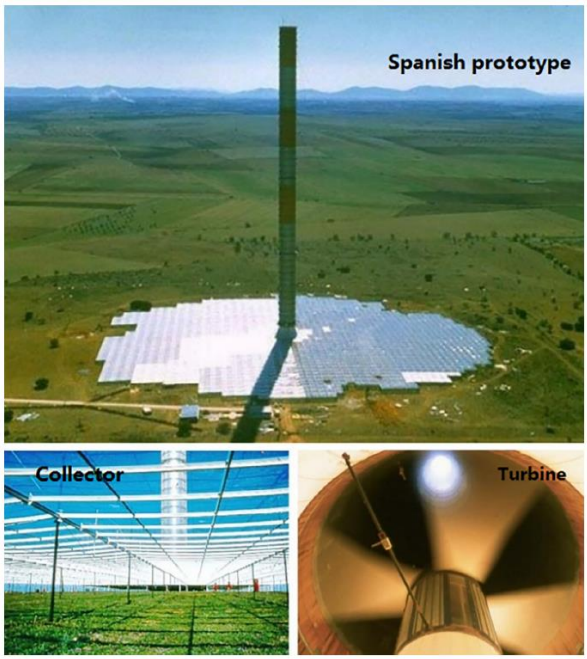

Figure 2.1 Pioneer SCPP prototype at Manzanares, Spain (Guo et al. 2019)

The development of the first operational SCPP by Schlaich (Haaf et al. 1983) supported by results of the experiments (Lautenschlager, Haaf and Schlaich 1985; Haaf 1984b) brought clarity to the concept. The SCPP has been a focal point to most researchers involved in low temperature solar thermal power plants for electricity generation. A proof of the concept was not enough for the commercialization of the plant as many countries were focused on the cost of energy generated from the plant, the initial investment cost, the payback period and the plant efficiency. These points mentioned are all the functions of the plant's efficiency when considering the investment and return over time. Researches in the solar chimney power plant have indicated that the two major areas of concern to the success of the plant are the open-solar-air collector and the chimney components of the plant. The solar air collector operates with an efficiency of about 20% to 30%, while the chimney has an efficiency of about 3% for a 1000 m high chimney and less than 1% efficiency for a 300 m high chimney (Schlaich 1995). This can be shown using the chimney efficiency, η_{ch} in Equation 2.1 which is a function of the gravitational acceleration g, chimney height H_c, specific heat capacity of air c_p and the ambient temperature at ground level T_0.

$$\eta_{ch} = \frac{g \cdot H_c}{c_p \cdot T_0} \qquad 2.1$$

2.2 Principle of Operation of SCPP

The fundamental principles of operation of SCPP have been described in different research, which includes the collector operating principles, chimney and turbo-generator principles. In line with the three operating components of the SCPP, the subsections below describe their operations by components.

2.2.1 Operating Principles of Open-Solar-Air Collector

The fundamental principles of the open-solar-air collector can be described with the energy conversion processes that occur at the collector. The open-solar-air collector comprises of an absorber (which materials may be made of ground, concrete, metal plate and others), a transparent cover held over the absorber using structures and the operating fluid (air). The flow and energy interaction in the solar collector are described using the fundamental laws of thermodynamics. The flow and the energy equations incorporated in the collector analysis include continuity, momentum and energy. The continuity of flow in a solar collector with both ends open could be described as a flow through a pipe, as shown in Equation 2.2. Similarly, the momentum generated by buoyant fluid in the flow direction can be explained using Equation 2.3 in laminar-steady state fluid flow (Pretorius 2004; Pretorius and Kröger 2006; Hedderwick 2000).

$$\frac{\partial}{\partial r}\left(\rho_{air} v_{col-exit} r_{coll} h_{g\_c}\right) = 0 \qquad 2.2$$

$$\rho_{air} v_{coll-exit} h_{g\_c} \frac{\partial v_{coll-exit}}{\partial r} = h_{g\_c} \frac{\partial p_{sys\_air}}{\partial r} - \tau_{sys\_air} \qquad 2.3$$

In the above equations, ρ_{air} represents the average air density with respect to the hydrodynamic diameter of the flow channel of the collector described in radius form, r_{coll} is the hydrodynamic radius of the collector, $v_{coll-exit}$ is the collector exit air velocity, h_{g_c} is the distance between the ground and the cover where the air flows, τ_{sys_air} is the shear stress present in the buoyant air in the open-solar-air collector due to the drag present from the braces that provide support to the cover of the collector and the friction loss caused due to the air flow and the collector wall, and p_{sys_air} is

the difference in pressure between ambient air and the air inside the collector (Al-Kayiem and Aja 2016).

The energy interactions in the collector can be associated to the energy source, the energy conversion and transfer processes, and the materials that carry the energy in and out of the system. The source of energy to the solar collector when there is no supplementary energy source is mainly the sun. The collector gains energy from the sun by converting the solar radiation into thermal energy at the absorber or ground S_g and the cover S_c. The total energy gained by the collector is transferred in the form of radiation, convection and conduction at different sections of the collector system. To analyse this interaction or energy transfer, energy balance at different collector components could be applied. The energy balance includes energy balance at the cover, ground and flow channel.

2.2.1.1 Energy balance at ground level

At the ground, the energy gained is transferred in the form of radiation between the ground and the cover q_{g_c-rad}, convection between the ground and the working fluid (air), $q_{g\_air-conv}$, and conduction between the ground surface and the earth-core $q_{g\_core-cond}$ as expressed in Equation 2.4.

$$S_g = q_{g\_c-rad} + q_{g\_air-conv} + q_{g\_core-cond} \qquad 2.4$$

Where $q_{g\_core-cond} = -k_g \frac{\partial T_g}{\partial z}\Big|_{z=0}$,

k_g represents the thermal conductivity of the ground with respect to depth of the core, ∂T_g represents the change in temperature between the ground surface and the core, and ∂z represents the change in depth from the ground surface towards the core.

2.2.1.2 Energy balance at the cover level

At the cover, the interaction of the energy in the solar collector includes energy gain from the ground re-radiated heat transfer and the absorbed energy from the sun, and in some cases, mostly in the morning, the cover gains energy from the buoyant air. This energy gained by the cover can be transferred to the ambient in the form of radiation

to the sky, $q_{c\_sky-rad}$, convective thermal loss to the ambient by wind effect $q_{c\_wind-conv}$, and may have some transfer of heat from the cover to the working fluid when the cover temperature exceeds the temperature of the working fluid, $q_{c\_air-conv}$. Thus, there are two cases in which convective heat transfers are considered. In the case when the temperature of the air is higher than the temperature of the cover, the cover gains heat from the air by convection and also gain heat from the ground by re-radiation heat transfer as shown in Equation 2.5 and Equation 2.6. On the other hand, when the cover temperature exceeds the temperature of the air, the cover transfers heat to the working fluid as depicted in Equation 2.7 and Equation 2.8 (Al-Kayiem and Aja 2016).

$$S_c + q_{g\_c-rad} + q_{c\_air-conv} = q_{c\_wind-conv} + q_{c\_sky-rad} \quad 2.5$$

$$S_c A_c + h_{g_c-rad} A_g (T_g - T_c) + h_{\text{air\_c-conv}} A_{cov} (T_{air} - T_c) = h_{\text{c\_wind-conv}} A_c (T_c - T_{wind}) + h_{c\_sky-rad} A_c (T_c - T_{sky}) \quad 2.6$$

$$S_c + q_{g-rad} = q_{c-wind} + q_{c-rad} + q_{air-conv} \quad 2.7$$

$$S_c A_c + h_{g_c-rad} A_g (T_g - T_c) = h_{\text{air\_c-conv}} A_{cov} (T_{air} - T_c) + h_{\text{c\_wind-conv}} A_c (T_c - T_{wind}) + h_{c\_sky-rad} A_c (T_c - T_{sky}) \quad 2.8$$

Equation 2.9 presents the heat transfer coefficient through radiation from the cover to the sky, where σ is the Stefan-Boltzmann constant, ε_c is the transparent cover emittance, T_c is the temperature of the transparent cover, T_s is the temperature of the sky and T_a is the ambient temperature. The temperature of the sky can be calculated using Equation 2.10. The convective heat transfer coefficient between the air in the system and the transparent cover can be determined using Equation 2.11, where the $k_{t,\,\text{air}\_c}$ is the thermal conductivity between the air in the system and the transparent cover and $H_{\text{g\_c}}$ is the height between the ground and the collector cover.

$$h_{c\_sky-rad} = \frac{\sigma \varepsilon_c (T_c^2 + T_s^2)(T_c + T_s)(T_c - T_s)}{(T_c - T_a)} \quad 2.9$$

$$T_s = 0.0552 T_a^{1.5} \qquad 2.10$$

$$h_{air\_c\text{-}conv} = Nu_{air\text{-}c} \left(\frac{k_{t,\ air\_c}}{H_{g\_c}} \right) \qquad 2.11$$

The thermal conductivity of the thin air film near the cover region is presented in Equation 2.12, where T_{t,air_c} is the average temperature between the air in the system and the collector cover, which can be calculated using Equation 2.13.

$$k_{t,\ air\_c} = 0.0257 \left(\frac{T_{t,\ air\_c}}{293} \right)^{0.86} \qquad 2.12$$

$$T_{ave,air\_c} = \frac{T_{air} + T_c}{2} \qquad 2.13$$

The Nusselt number (Raithby and Hollands 1998) for the air near the cover region is presented by Equation 2.14, where the positive exponent represents the positive values resulting from the terms in the square brackets. Equation 2.15 presents the Rayleigh number for the air near the cover region, where the kinematic viscosity and thermal diffusivity are considered in Equation 2.16.

$$Nu_{air\_c} = 1 + 1.44 \left[1 - \frac{1708 \sin(1.8\beta)^{1.6}}{Ra_{air-c} \cos(\beta)} \right] \left[1 - \frac{1708}{Ra_{air-c} \cos(\beta)} \right]^{+} + \left[\left(\frac{Ra_{\text{air}\ -c} \cos(\beta)}{5830} \right)^{\frac{1}{3}} - 1 \right]^{+} \qquad 2.14$$

$$Ra_{\text{air}\ \_c} = \frac{g\ \beta'_{t,\ \text{air}\ -c}\ (T_{\text{air}}\ - T_c)\ H^3_{g\_c}}{v_{t,air\_c}\ \alpha_{t,air\_c}} \qquad 2.15$$

$$Ra_{\text{air}\ \_c} = \frac{cp_{t,air\_c}\ \rho^2_{t,air\_c}\ g\ \beta'_{t,air\_c} (T_{air} - T_c) H^3_{\text{g}\_c}}{\mu_{t,air\_c}\ k_{t,air\_c}} \qquad 2.16$$

where, $v = \frac{\mu}{\rho}$

$$\alpha = \frac{k}{c_p \rho}$$

and $v\alpha = \frac{\mu k}{c_p \rho^2}$

Equation 2.17 presents the volumetric expansion coefficient of the thin air film near the cover region.

$$\beta'_{t,air\_c} = \frac{1}{T_{t,air\_c}} \quad 2.17$$

The dynamic viscosity, specific heat capacity and air density of the thin air film near the collector cover can be calculated using Equation 2.18, Equation 2.19 and Equation 2.20 (John and Duffie 2013).

$$\mu_{air\_c} = 1.81 \times 10^{-5} \left(\frac{T_{t,air\_c}}{293}\right)^{0.735} \quad 2.18$$

$$c_{p_{air\_c}} = 1006 \left(\frac{T_{t,air\_c}}{293}\right)^{0.0155} \quad 2.19$$

$$\rho_{air\_c} = \frac{97500}{287.045 T_{t,\ air\_c}} \quad 2.20$$

2.2.1.3 Energy balance in the flow

At the air flow channel of the collector, the energy gained by the air is either from the ground or from a combination of the ground and the cover by convection. The energy gained by the air is used to excite the internal energy of the air particles, which creates the driving force described as useful energy, q_u. When the temperature of the cover is lower than the temperature of the working fluid, the working fluid loses heat to the cover thus, the useful energy is as shown in Equation 2.21. Similarly, when the cover temperature gains heat such that its temperature is higher than that of the air, the air gains heat such that the useful energy equation could be represented as shown in Equation 2.22.

$$q_u = q_{g-conv} - q_{air-conv} \quad 2.21$$

$$q_u = q_{g-conv} + q_{air-conv} \quad 2.22$$

The useful energy in the buoyant air can be analysed in the form of a driving force where the useful energy which is a function of the specific heat capacity of air c_p and change in temperature can be explained in Equation 2.23, where the mass flow rate $\dot{m}$ is described in Equation 2.24 with the collector air density ρ_{coll}, collector air velocity v_c and collector area A_c as its function.

$$q_u = \dot{m} c_p \Delta T \qquad 2.23$$

$$\dot{m} = \rho_{coll} v_c A_c \qquad 2.24$$

2.2.2 Operating Principles of the Chimney Component of the SCPP

The following fundamental principles describing the operation of the chimney component of the SCPP is the differential pressure between the fluid volume in the chimney and the ambient air. The pressure variation is associated with the temperature difference leading to a drop in working fluid density which is the basis for the buoyancy effect experienced in the chimney (Al-Kayiem and Aja 2016). The pressure difference generated in the chimney is as shown in Equation 2.25 was presented by Schlaich (1995).

$$\Delta p_{tot} = \int_0^{H_{ch}} (\rho_{amb-air} - \rho_{air-in})\, dh \qquad 2.25$$

The working fluid in the chimney area undergoes certain thermodynamic processes which are expressed in terms of the continuity, momentum and air flow energy balance equations as expressed in Equation 2.26, Equation 2.27 and Equation 2.28.

$$\frac{\partial}{\partial h}(2\pi \rho_{air-ch} v_{air-ch} r_{ch} h_{ch}) = \frac{\partial}{\partial h}\left(\rho_{air-ch} \dot{V}_{air-ch}\right) = 0 \qquad 2.26$$

$$\rho_{air-ch} \dot{V}_{air-ch} \frac{\partial \dot{V}_{air-ch}}{\partial h} = -\frac{\partial p_{air-ch}}{\partial h} - \frac{2\tau_{air-ch}}{r_{ch}} - g\rho_{air-ch} \qquad 2.27$$

$$Cp_{air-ch}T_{air-ch}\frac{\partial}{\partial h}\left(\rho_{air-ch}\dot{V}_{air-ch}\right) + \rho_{air-ch}\dot{V}_{air-ch}\frac{\partial}{\partial h}\left(Cp_{air-ch}T_{air-ch}\right) + \frac{\partial}{\partial h}\rho_{air-ch}g\dot{V}_{air-ch} = 0 \quad 2.28$$

Where, ρ_{air-ch} represents the air density at any given height along the chimney, r_{ch} represents the radius of the chimney, v_{air-ch} represents air velocity along the height of the chimney, h_{ch} represents the height of the air at any point of the chimney end to end, τ_{air-ch} represents the shear stress experienced by the buoyant air flowing upwards towards the chimney end, $\dot{V}_{air-ch}$ represents the volumetric flowrate of the chimney air, Cp_{air-ch} represents the specific heat capacity of the working fluid in the chimney at a defined height and T_{air-ch} represents the temperature of the working fluid at a defined height in the chimney (Al-Kayiem and Aja 2016).

2.2.3 Operating Principles of the Wind Turbine Component

The operating principles of the wind turbine are based on the flow energy available (kinetic energy in the buoyant air) to the turbine, which could be converted to mechanical and electrical energy using the turbine and generator.

2.2.3.1 Maximum Power

The total power of buoyant air readily available for conversion into electrical power is the kinetic energy resulting from the buoyancy in the air. The total power in the air at open space can be expressed as shown in Equation 2.29 (El-Wakil 1985).

$$P_{tot} = \frac{1}{2g_c}\rho A V_i^3 \quad 2.29$$

Where P_{tot} represents the total buoyant air power, ρ represents the average density of the air, g_c is the power conversion factor (1 kg/Ns^2), A represents the wind turbine surface area exposed to the incoming wind velocity and V_i represents the incoming velocity of the air to the wind turbine blade.

The total power generated in the buoyant air can be converted into mechanical energy by the wind turbine, but the energy extracted will depend on the turbine efficiency and the surrounding effect impact on the airflow as well as the turbine operation. For all the wind energy to be converted into mechanical energy at 100% efficiency, the exiting

air velocity after the turbine needs to be $V_e = 0$. Similarly, the dispersion of the airflow stream should be zero, which is impracticable considering that wind cannot accumulate at the turbine exit (El-Wakil 1985). Thus, the optimum velocity of the exiting air, $V_{e,opt}$ was defined by El-Wakil (1985) as shown in Equation 2.30 for non-bounded wind turbine exposed to air flow.

$$V_{e,opt} = \frac{1}{3} V_i \qquad 2.30$$

The maximum power that the turbine can harness in open flow operation from the wind flow stream is formed upon taking the optimum velocity of the exiting air $V_{e,opt}$ into consideration as shown in Equation 2.31. The maximum turbine efficiency is simply the ratio of the maximum power harnessed from the wind to the total energy of the wind, which is expressed in Equation 2.32. The wind turbine efficiency shows that the wind turbine is able to harness around 60% only of the total power generated by the wind (El-Wakil 1985).

$$P_{max} = \frac{8}{27 g_c} \rho A V_i^3 \qquad 2.31$$

$$\eta_{max} = \frac{P_{max}}{P_{tot}} = \frac{8}{27 g_c} \times 2 g_c = \frac{16}{27} = 0.5926 \qquad 2.32$$

However, the wind turbine used in a solar chimney power plant is a shroud type wind turbine since the chimney region acts as a duct in which the wind turbine operates. The pressure balance equation for a ducted wind turbine with a cylindrical control volume expressed by Siavash et al. (2020) is described in Equations 2.33, 2.34 and 2.35.

$$p_u + \frac{1}{2} \rho V_u^2 = p_r^+ + \frac{1}{2} \rho V_r^2 \qquad 2.33$$

$$p_r^- + \frac{1}{2} \rho V_r^2 = p_e + \frac{1}{2} \rho V_e^2 + \Delta p_d \qquad 2.34$$

$$p_e + \frac{1}{2} \rho V_e^2 = p_u + \frac{1}{2} \rho V_w^2 \qquad 2.35$$

Where, p_r^+ represents the static pressure in front of the rotor plane, p_r^- signifies the static pressure behind the rotor plane and Δp_d embodies the pressure drop across the duct (chimney region), p_u is the upstream buoyant air pressure, V_u is upstream buoyant

air velocity leading to the turbine respectively, V_r describes the shrouded wind turbine rotor plane velocity, p_e and V_e represents the duct exit buoyant air pressure and velocity, and V_w is the velocity in far-wake of the shrouded wind turbine.

Equation 2.36 expresses the energy balance equation for a steady-state incompressible flow of the buoyant air in the chimney region of the solar power plant. The power extracted by the rotor of the shrouded wind turbine is shown to be a function of the upstream buoyant air velocity, far-wake air velocity, pressure drop across the turbine and airflow rate Q.

$$P_{extracted\ by\ rotor} = Q\left[\frac{1}{2}\rho V_u^2 - \frac{1}{2}\rho V_w^2\right] - Q\Delta p_d \qquad 2.36$$

The association between the upstream buoyant air velocity and the far-wake air velocity is further described in Equation 2.37 (Tavares Dias do Rio Vaz et al. 2014; Phillips 2003; Siavash et al. 2020).

$$V_w = (1 - 2a)V_u \qquad 2.37$$

Where a, is the axial induction factor represented as shown in Equation 2.38 (Tavares Dias do Rio Vaz et al. 2014).

$$a = \frac{1}{1+\mathrm{K}} \qquad 2.38$$

In the above equation, K is a parameter integrating the function of shroud shape and turbine rotor geometry in the flow velocity, which can be evaluated using Equation 2.39 (Tavares Dias do Rio Vaz et al. 2014).

$$K = \frac{4F\sin^2\emptyset}{\gamma^2\sigma c_N} \qquad 2.39$$

Where F is the Prandtl tip loss factor of the turbine, $\emptyset$ is the flow angle which is vertical for a cylindrical chimney, γ is the velocity speed-up ratio of the maximum axial velocity of flow in a shroud with relation to the upstream velocity, σ is the solidity of the turbine and c_N is coefficient of normal force.

2.2.3.2 Actual power

The real efficiency η can be expressed as the product of the ideal efficiency and η_{max}, which is also the ratio of the actual power to the total power by the wind turbine as shown in Equation 2.40.

$$P = \eta P_{tot} = \eta \frac{\rho}{2g_c} A V_i^3 \qquad 2.40$$

Where η is the real efficiency with values ranging between 30% and 40% for real turbines (El-Wakil 1985).

2.3 Principle of Operation of the Modifed Savonius Wind Turbine

The Savonius wind turbine works based on the drag principle. This novel SSWT incorporates the characteristics of the conventional SSWT with added lift performance due to its modified curved structure (Roy and Ducoin 2016). The performance characteristics of this novel turbine can be studied through the formula discussed in this subsection.

The longitudinal coefficient of drag, C_D and lateral coefficient of lift, C_L experienced by the SSWT is expressed in Equations 2.41 and 2.42.

$$C_D = \frac{F_D}{\frac{1}{2}\rho A V^2} \qquad 2.41$$

$$C_L = \frac{F_L}{\frac{1}{2}\rho A V^2} \qquad 2.42$$

Where, F_D is the drag force, F_L is the lift force, A is the swept area of the turbine (m^2) and V is the free-stream wind speed (m/s).

The total drag force, F_D in the x-direction (N) and the total lift force, F_L in the y-direction (N) are represented in Equations 2.43 and 2.44.

$$F_D = F_{D1} + F_{D2} \qquad 2.43$$

$$F_L = F_{L1} + F_{L2} \qquad 2.44$$

Where F_{D1}, F_{D2}, F_{L1} and F_{L2} are the longitudinal and lateral forces (N) that is acting on both blades, 1 and 2, respectively.

The resulting force from the lift and drag is represented as resultant force coefficient, C_{res}, presented in Equation 2.45.

$$C_{res} = \sqrt{{C^2}_D + {C^2}_L} \quad 2.45$$

The performance of the turbine is characterized by the instantaneous moment coefficients (C_M) and power coefficient (C_P) presented in Equations 2.46 and 2.47.

$$C_M = \frac{M}{\frac{1}{2}\rho ARV^2} \quad 2.46$$

$$C_P = \frac{P_{turbine}}{P_{available}} = \frac{P}{\frac{1}{2}\rho AV^2} = \frac{M}{\frac{1}{2}\rho ARV^2}\frac{\omega_s R}{V} = C_M\lambda \quad 2.47$$

M is the total moment generated from the advancing and returning blades of the turbine, P is the generated power by the turbine (W), ω_s is the turbine rotation speed (rad/s), and R is the rotational radius of the turbine (m). λ is the tip speed ratio which is represented in Equation 2.48.

$$\lambda = \frac{\omega_s R}{V} \quad 2.48$$

2.3.1 Turbine Settings for Sliding Mesh in CFD

The time step setting and number of time steps for the transient analysis of the turbine is an important aspect to generate accurate results (Satrio et al. 2018). The time step size (TSS) and the number of time steps (NTS) found in the solution interface of ANSYS Fluent can be set in accordance with Equations 2.49 and 2.50.

$$NTS = N\frac{360}{\theta} \quad 2.49$$

$$TSS = \frac{N}{(\omega\ x\ 0.15915)\ x\ number\ of\ time\ step} \quad 2.50$$

N is the number of rotations, θ is the time step rotation degree or angle in increment, ω is the rotational speed of the turbine (rad/s) and 0.15915 is a conversion constant from rad/s to rot/s unit (Satrio et al. 2018).

2.4 Geometrical Impact on The Performance of the SCPP

The three main components that make up the operating system of SCPP include the open-solar-air collector, solar chimney and turbine-generator. Many studies have

shown that the collector area and the chimney height and radius strongly affect the performance of the SCPP (Das and Chandramohan 2019; Zou and He 2015; Guo et al. 2019; Muhammed and Atrooshi 2019). The geometry of the collector cover and the chimney shape also has an impact on the system's performance. Even for a rooftop solar chimney design, researchers have claimed that the increase in collector area and chimney height increases the air velocity, thus increasing system performance (Al-Kayiem, Sreejaya and Gilani 2014). However, very few researchers have found the optimum geometry dimension needed for solar plants of different sizes. Cottam et al. (2019) inferred in their studies that the optimum performance of a solar plant relates to the collector radius, chimney height and chimney radius. They also stated that the relationship of the chimney's performance to the collector radius, chimney diameter, and chimney height had an impact not only on electricity generation, but also on cost efficiency for developing smaller scale plants with a solar collector radius of up to 3000m compared to larger plants. Most studies showed that taller chimneys provide better system performance, however, the studies failed to include the economic aspects of it (Guo et al. 2019).

Cuce, Sen, and Cuce (2020) analysed the influence of the chimney's height on the performance of the SCPP. The analysis was performed by developing a 3D axisymmetric model using ANSYS Fluent, where the DO radiation model with solar ray tracing was incorporated. The influence of the five different heights of the chimney ranging from 100 m to 500 m was studied based on the maximum air velocity, mass flow rate, collector temperature rise, dynamic pressure variation at the turbine area, the efficiency of the whole system and the power output of the system. The analysis reported that the mass flow rate that was obtained from the maximum velocity had an exponential growth on H. Conversely, the collector temperature-rise decreased with increasing H. At the height of 500m, the overall efficiency was reported to be 0.67%. With a height of 200m and 500m of the chimney, the system was able to produce 55kW and 134kW, respectively. The power output (P) was proven to increase linearly with the increment in H.

2.4.1 The Impact of Collector Glazing on the Performance of the SCPP

Nasraoui, Driss, and Kchaou (2020) conducted an investigation on the system performance of SCPP with the aim of enhancing solar collector efficiency. They

developed two different models of solar collector covers where one model was with parallel air flow of double glazing, and the other was with counter air flow of double glazing, which the air enters from the top of the glass and circulate through the channel between the upper glass and the auxiliary glass while the air moves to the chimney through the space between the ground and the auxiliary glass. The above two models were modelled along with a conventional SCPP model to compare the performance of the models with the established system. The model with counter air flow showed an increase in the collector efficiency by 25.8% without increasing the solar collector ground surface area, while the parallel flow model showed an improved collector efficiency of 19.4% over the standard single glazing SCPP.

2.4.2 The Impact of Collector Cover Inclination on the Performance of the SCPP

Other studies have also tried to investigate the system's performance with different collector cover tilt angles. Das and Chandramohan (2019) suggested that when the collector cover inclination increased, the air velocity was also increased. However, with an inclination angle of more than 20°, a decline in power output by 71.1% was observed. The same paper also reported that the power output improved by 83.4% when the diameter of the absorber plate was increased from 3.5 m to 12 m, but also resulted in a decrease in temperature gradient by 94.2% from the chimney base to the outlet (Das and Chandramohan 2019). Das and Chandramohan (2019) stated that the increase of chimney's height from 3m to 8m significantly raised the air velocity by 44% and subsequently reported a 93% increase in the plant power output.

2.4.3 The Impact of Internal Guide Wall and Chimney Divergence on the Performance of the SCPP

Hu et al. (2016) investigated the effect of guide walls on the performance of the SCPP and showed that the use of guide walls significantly increased the power output of SCPP. The guide wall was designed in the form of a frustum, where the top diameter is constant while the base diameter varies as well as the height of the frustum guide wall. The results showed that variation in the base diameter of guide walls had minimal impact on the power output, unlike the height of the guide walls. The study also investigated the effect of guide walls on diverging chimney designs and reported that the diverging chimney with guide walls had higher output power compared to the cylindrical chimneys that used the guide walls, with a range of power improvement of

880% for no guide wall and 690% for the system with 12 m guide wall at the chimney location, where the chimney heights were fixed at 195 m.

Cuce et al. (2021) studied the impact of divergent and convergent chimney geometry on the performance of the solar chimney power plant. The work covered area ratio (AR) 0.5 to 10, which covered both divergent and convergent chimney designs. The performance of the chimney designs was evaluated based on the temperature, velocity and pressure distribution in the system, the temperature of air rise in the collector, turbine area mass flow rare, turbine area dynamic pressure difference, overall plant minimum static pressure, efficiency of the system and the power generated. The mass flow rate was suggested to increase by 45.18% when the AR was increased to an optimum value of 4 from AR=1. The efficiency of the system was claimed to be enhanced by 0.83%, with an AR of 4.1 compared to AR 1. The authors suggested that the electrical power of the improved design in its optimal AR value state could increase by 210.31% compared to the conventional Manzanares design.

2.4.4 Effect of Thermal Storage on the Performance of the SCPP

In an experiment conducted using sloped solar updraft power plants with a focus on increasing the power generation of the plant using thermal storage, Kalash, Naimeh, and Ajib (2013) showed that energy gained in the hours of sunshine was released during the cloudy hours of the day as well as night time. It was also shown that after solar noon, the energy held in the soil gradually reduced as solar energy decreased. The stored energy was transferred to the working fluid and served for an average of 3 hours upon sunset. It was observed that the improvement in the power output was significant after solar noon and showed a daily power output improvement as a result of the after-sunset power generation.

A study to compare the performance of SCPP operation with and without thermal storage was also conducted by Amudam and Chandramohan (2019). The analysis on both the models was carried out numerically at different timings, which are 10.00 am, 12.00 pm, 1.00 pm, 2.00 pm and 4.00 pm, with model 2 extended until 8.00 pm. The study showed that the heat energy stored in the thermal storage was released to the air in the collector, resulting in a working system up till 8 pm. The maximum overall efficiency was reported to be 1.01% and 0.918% at 4 pm for the model, with and without TES respectively, due to the lower input heat and higher power generation at

that time. The study also showed that after 4 pm, the global solar radiation was low, resulting in no buoyancy-driven flow for energy generation from the model without TES since the ambient air now lacked thermal energy to cause a drive in the working fluid of the system. On the other hand, it was observed that the use of TES showed continuous energy generation, which declined through sunset to night-time. The overall efficiency of the plant for the system with TES at 7 pm and 8 pm was about 1%, where the output power was 0.808W and 0.404W, respectively.

2.4.5 Limitations of Geometrical Impact on the Performance of the SCPP

Many previous works have studied the effects of the chimney height and the collector region (i.e., inclination, double glazing, area). The impact of heat storage to improve the plant's power generation has also been widely studied. However, the implementation of guide walls and divergent chimneys, which augments high power output is rarely investigated.

2.5 Environmental Effects on the Performance of the SCPP

Ming et al. (2012) studied the influence of ambient crosswinds (ACW) on the power generation of an SCPP, considering the wind sweep across the plant's collector and the chimney outlet. The results of the study reported that a strong ACW, with a velocity above 10 m/s across the chimney outlet at solar radiations over $0\ W/m^2$ increased the mass flow rate, concurrently increasing the output power. Whereas a weak ACW, less than 10 m/s, deteriorated the flow in the chimney since the low wind speed acted as a cover at the chimney outlet, causing a low power production. Based on Bernoulli's principle, higher ACW velocity over the chimney causes a negative pressure area which promotes a suction effect through the SUPPS's chimney outlet.

A similar study by Shen et al. (2014) also reported the benefits of a strong ACW on the power generation even at low solar radiations, indicating that there is less pressure across the chimney exit when the wind velocity across the chimney is high. In support of the negative effect of low velocity ACW, Pretorius and Kröger (2009) reported in their work that the presence of ACW significantly reduced the power generation in the SCPP by approximately 10% annually as compared to the same plant that does not face such wind surroundings. Guo et al. (2019) investigated the effect of ACW on the performance of SCPP with respect to the collector component and reported that the

ACW increases thermal loss at the collector, thereby leading to a reduction in collector efficiency compared to a situation where there is no wind effect.

Jafarifar, Behzadi, and Yaghini (2019) studied the efficiency of the SUTs in strong wind flow regions with low solar radiation. The focused study area was the Orkney Islands in Scotland. The analysis was performed using ANSYS Fluent, where the effects from a 3D axisymmetric model were applied to a 2D model for further investigation of the performance of the SUT with and without suction due to ambient wind. The effect of the airflow due to the turbine has been neglected. 14 m/s of velocity was obtained at the axis of the 2D Manzanares model (23 m above the ground), while a maximum air velocity of 15.7 m/s was developed at the outlet of the Manzanares model. The outcome of the study showed that the internal air velocity and the efficiency of the plant improved by 15% and 50% respectively, with the presence of strong and steady ambient crosswinds. The erection of the plant in the Orkney region is suggested to improve the efficiency of the plant by more than 70% compared to the conventional Manzanares plant. The paper reported that the installation of an enclosed wind turbine in the SUT with a specified power capacity can be an alternative plan to the installation of conventional wind turbines at high altitudes in open air.

2.5.1 Limitations

The research regarding the favourable impacts of ambient wind on the performance of the SCPP was geography dependant. As reported, only a strong wind flow above 10 m/s was able to improve the plant's performance, whereas anything below that would deteriorate the plant’s power generating capacity.

2.6 Influence of Turbulence Models on Solar Chimney Power Plant

An investigation of the effects of turbulence models on airflow characteristics inside an SCPP was performed by Ayadi, Bouabidi, et al. (2018). Airflow attributes such as airflow velocity, static and dynamic pressure, temperature and turbulent kinetic energy and dissipation rate were analysed. The most favourable turbulence model was identified based on experimental data. The experimental data was extracted from an SCPP with dimensions 2000 mm and 200 mm for the chimney height and diameter, 3000 mm for the collector diameter, 60 mm for the collector roof height and 4 mm for

the chimney thickness. The same dimensions were employed in the five different turbulence model numerical simulations, which were the standard k-ε model, RNG k-ε model, Realizable k-ε, transition-k–kl–ω model and the transition-SST model. The outcome suggested that for air temperature along the collector radius, the k-ε models portrayed better agreement with the experimental data obtained, compared to the transition-k–kl–ω model and the transition-SST model. The numerical analysis conducted on temperature, airflow velocity, static and dynamic pressure, turbulent kinetic energy, and turbulent dissipation rate implied that the different turbulence models had varying effects on these parameters. Out of the five different models, the k-ε model showed satisfactory results with the experimental data.

2.6.1 Limitations

Many different geometrical configurations were taken into account for the study, such as chimney height, collector area and collector roof height. However, neither of the models examined included the turbine component. As a result, the impact of utilising the proposed turbulence model with a structure that includes the turbine component remains unknown.

2.7 Hybrid Solar Chimney Power Plants

Hybrid solar chimney power plants are SCPP systems combined with a secondary system (e.g. waste heat energy, water condensing system, coal-fired plants, heat exchangers) with the sole aim of increasing power production or recovering energy from other alternative energy sources. With regards to the enhancement of power output and sustainability of power generation in SCPP, Cao et al. (2014) studied the integration of a geothermal energy source with the SCPP. They developed and examined the operation of three different models and compared their performances under various operating conditions. The operating conditions investigated by the study included full solar mode (FSM), full geothermal mode (FGM) and hybrid geothermal-solar mode (GSM). The results suggested that with the use of the GSM, power was able to be generated continuously. Also, the paper reported that the impact of the GSM on power generation was greater during winter, which was 8.8% higher than the daily generated power by the FSM due to the lower ambient temperature during winter days. However, the authors claimed that during summer, the daily power generation of the

GSM was still higher than the FSM by 5.8%, but not as high as that of winter due to the higher ambient temperature during summer. As a whole, the annual power generation by the GSM was claimed to be 26.3% higher than the FSM. The paper suggested that the GSM was able to improve the power generation by 2.0, 2.3, 2.7 and 3.0 times more, at higher temperatures of geothermal water at 50°C, 60°C, 70°C and 80°C respectively, at the same mass flow rate of 300 kg/s.

Another novel method of investigation to increase the SCPP performance was the introduction of reflectors to the conventional SCPP designed by Hussain and Al-Sulaiman (2018). The integrated reflectors and SCPP used the reflectors to channel the diffuse and reflected rays from the sun to the absorber of the solar collector to enhance the energy gain by the absorber and heat transfer from the absorber to the adjacent air in the greenhouse. This, in turn, increased the temperature of the air higher than the resulting air temperature obtained in conventional SCPP without an external heat source. The paper reported that with the use of the reflectors, only 10% of the solar radiation energy was lost due to transmission and absorption by the mirrors and the deck, while the remaining 90% were made available to the SCPP collector absorber. As a result, this hybrid system was able to increase the mass flow rate of air at the chimney base by 134%, the chimney inlet velocity by 135% and the floor temperature by 9.89%. The efficiency of the hybrid system also showed an increment of 22.61% when compared to a conventional model of the same size. The power generated by the hybrid system also increased by 133% over the output of the conventional model.

Shariatzadeh et al. (2015) investigated the hybrid SCPP with cogeneration solid oxide electrolysis (fuel cell). In this study, additional electricity was produced by high-temperature electrolysis, which produces hydrogen. This hydrogen was then stored in tanks, which was later converted to electricity by solid oxide fuel cells (SOFC) based on demand or necessity.

Zou and He (2015) conducted a study on waste heat recovery using Hybrid Cooling Tower Solar Chimney (HCTSC). In this study, the waste heat was modelled to be transferred to the HCTSC through heat exchangers with a flat arrangement. This meant that the inlet of the collector and the frontal area of the heat exchanger was equivalent. The HCTSC model, excluding the radiator part, was validated using test data from the Spanish prototype. The authors claimed that the HCTSC was able to outperform a

conventional solar chimney power plant with similar geometric dimensions by 20 times. Nevertheless, this large power output correlated with a higher heat dissipation capacity which had the possibility to impair the coupled thermal power plant. To overcome this problem, the authors suggested increasing the area of the heat exchanger to the HCTSC.

In another study, Li et al. (2017) investigated the operation of SCPP combined with waste heat from a coal-fired power plant. A fitting equation was developed by the authors based on the collector radii and the solar radiation intensity on the hybrid system since it showed a positive influence on the optimal turbine pressure drop. The study suggested that for this hybrid system, a large solar collector was not recommended for low solar intensity areas since the increase in collector radii only slightly affected the power output. This system's optimization method, which was integrated with a 660W supercritical coal-fired power unit, was claimed to be better by Li et al. (2017) than two previously proposed optimization methods made by Zou, Guan, and Gurgenci (2014) and Zandian and Ashjaee (2013). For a range of solar collector radii between 100m and 600m, the average power generated by the optimisation method suggested by this study was 2.5% (0.14GWh) higher than the Zou scheme and 11.06% (0.38 GWh) higher than the Zandian scheme.

A research study was conducted in the region of China by Zuo et al. (2018) to investigate the effects of structural parameters on a wind supercharged solar chimney power plant combined with seawater desalination. The results suggested that the 3-blade turbine generated low shaft power. The authors claimed that the optimum number for turbine blades was 4 or 5 for optimum power output and cost-effectiveness. Other than that, the paper suggested that the turbine blade angle at 17° provided the highest mass flow rate with minimal velocity loss and highest turbine shaft power. Next, the paper claimed that the mass flow rate increased with the increase in relative radial clearance. Therefore, the maximum relative radial clearance suggested by Zuo et al. (2018) was 2%. Above this value, a sharp decline in turbine shaft power was noticed. The installation of guide vanes was reported to have increased the turbine efficiency by 139%. Furthermore, the authors claimed that in relation to flow field optimisation, the installation of guide vanes can improve the mass flow rate of air and the turbine shaft power due to the redirection of air towards the turbine. The study on the H-type vertical wind wheel blade by Zuo et al. (2018) further suggested that the

shaft power was at its peak with an installation angle of 3°. The authors also claimed that the helix type wind pressure ventilator was capable of improving the self-starting performance and promoting more stability to the turbine region.

In another study, Zuo, Liu, et al. (2020) investigated the influence of waste heat in an SCPP combined freshwater generation in the absence and presence of a wind supercharged device. In both the investigated models, the gas heating channel was introduced. The outcome of the study suggested a performance increase with greater chimney height and flue gas temperature. The increase in solar intensity and flue gas mass flow rate demonstrated an increased power augmentation, however, it reduced freshwater production. The analysis also suggested that the model with the wind supercharging device performed better than the model without the device.

In the subsequent investigation, Zuo, Dai, et al. (2020) performed a 3-dimensional numerical analysis of the wind supercharging SCPP combined with gas waste heat and seawater desalination using ANSYS Fluent. The performance of the newly proposed SCPP model was analysed by the variation of the turbine rotational speed, nozzle length, chimney outlet radius and chimney mixing section length. The outcome of the study suggested that the presence of the flue gas in the plant enhanced the fluid flow speed in the chimney area. Next, with an increase in the rotational speed of the turbine, the rate of desalination decreased, however, the power augmentation by the turbine shaft increased with the peak at 200 rpm. The increase in chimney outlet area indicated that the freshwater output and the power production increased to a peak and decreased subsequently. The same trend was implied for the increase in the nozzle length and the chimney mixing section length. The analysis demonstrated better plant performance through the 200 rpm turbine rotational speed, 6m nozzle length, 9m chimney outlet radius, and 60m chimney mixing section length.

Vakilabadi et al. (2019) investigated the energy and exergy in a hybrid solar-fossil fuel power plant. Based on the energy and exergy analysis, the component claimed to have the highest energy loss was the condenser, while the component with the highest exergy destruction was the collector. The total energy loss by the condenser was reported to be 47% of the total energy loss. On the other hand, 68.32% out of the total exergy loss was reported to be due to the collector and the boiler. The authors claimed that the hybrid plant experienced maximum energy efficiency of 23% at 12 am. On the

other hand, the plant experienced a minimum exergy efficiency of 32.7% during the day due to solar high solar radiation available. The maximum exergy efficiency of 44.94% was then reported to be seen when there was no solar radiation at night. However, when turbine inlet pressure was about 95 bar, the hybrid system was claimed to have had a maximum exergy efficiency of 26%. In general, the increase in heat transfer from the fluid in the study showed a linear increase in the output power of the hybrid system.

To increase the efficiency enhancement of a solar chimney power plant, Fathi et al. (2018) studied the recovery of waste heat from a nuclear power plant. The outcome of the study showed that a regular 1000MW nuclear power plant with a theoretical thermal efficiency of 35.3% when integrated with the SCPP had an enhanced efficiency of 42% as compared to the efficiency of a stand-alone SCPP. Using the Manzanares design for the SCPP, it was demonstrated by the authors that the combined design was able to enhance electricity output in the SCPP turbine at a range of 0% to 300% from summer through winter. Furthermore, the study suggested that the proposed design was able to increase the generated power by the Manzanares type SCPP at an average of 150% yearly. The authors also claimed that the novel design was an added advantage in arid environments as there is no dependency on the water in its cooling system.

In another study done on waste heat recovery, Aurybi et al. (2018) studied the usage of an external heat source in the SCPP for uninterrupted power generation mathematically. The proposed system passed the flue gas in the collector through metal channels which dissipated heat to the air in the collector, in addition to the existing solar radiation. The effect of the external heat source was reported to be seen at a low solar intensity and started decreasing upon reaching 400 W/m^2 of solar intensity. Due to this, the authors claimed that thermal channels were effective during the night, cloudy days, and were even capable of generating power early in the morning when the solar radiation is low (100 W/m^2 to 300 W/m^2). The temperature of the collector air was reported to have sharply increased with the presence of the external heat source at the solar radiation range of 800 W/m^2 to 1000 W/m^2. However, a downward trend was noticed by the authors after the solar radiation value exceeded 1000 W/m^2. This was suggested to be due to the increase in thermal loss from the

outer surface of the canopy to the ambient. Thus, at a solar intensity value of $1000W/m^2$ and thermal channels temperature at 100°C, the collector air temperature was reported to be increased by 5.88%. Also, the authors claimed that the usage of thermal channels increased the output power by 23.1% compared to the conventional solar chimney power plant.

Similarly, Al-Kayiem et al. (2019a) further performed a numerical analysis on a hybrid system using waste heat recovery. The system worked based on heat transfer from the thermal channels to the air in the collector, in addition to the heat obtained from the absorber, resulting in a high air temperature upon reaching the chimney inlet. The proposed system was evaluated under three different cases, which are, with TECs integration (case 1), without TECs integration (case 2) and with added external heat source (case 3). Comparing the results between cases 1 and 2, the velocity fluctuation caused by the ambient wind was claimed to have improved by 12% with the insertion of channels. With reference to air velocity, the average maximum air velocity percentage and the air velocity at the chimney base in 24 hours were enhanced in case 2 by 5.9% and 6.87%, respectively.

In terms of thermal enhancement, the average air temperature enhancement over a span of 24 hours data was claimed to be 6.3%. This was suggested to be due to the larger absorbing area with the addition of TECs, which provided additional heat and kinetic energy for power generation (Al-Kayiem et al. 2019a). From case 1 and case 2, the performance of the collector was claimed to have an average percentage of enhancement up to 7.0%. In case 3, the TECs were injected with flue gas with a mass flow rate of 0.0015 kg/s, which was equivalent to 1.25 m/s, and temperature at 116 ℃. Estimated electric power generated was claimed to be improved by an average of 23.0% in the presence of flue gas usage at different solar irradiation values ranging from 100 W/m^2 to 1000 W/m^2. With the injection of the flue gas, the air velocity, especially at night, was reported to be doubled to 100%. Furthermore, on average, the collector efficiency at night was said to have improved by 32.5%. Overall, the collector efficiency was claimed to have improved by 12%, while the air mass flow rate was reported to have improved by 64%.

2.7.1 Limitations

Although there is undeniable power output enhancement through hybrids, the studied hybrid systems were restricted to specific energy recovery sources at certain parameters. Hence, there is limited liberty in system applications in certain locations. Moreover, systems that recover heat for power production would require large areas for the plant's construction, which may not be favourable in constricted industrial areas or countries/regions with minimal land. Furthermore, very few integration studies have been performed in the presence of the turbine component.

2.8 Turbine Performance Enhancement of Solar Chimney Power Plant

The study conducted by Guo et al. (2015) incorporated a radiation model, solar load model and real turbine into a 3D numerical analysis. To study the power regulating strategy option for solar chimney turbines, a variety of turbine performances with rotational speed was examined. A four-blade pressure-staged turbine with the use of Multiple Reference Frame (MRF) was adopted for the real turbine analysis, while a fan model considering the pressure drop effects was also adopted for comparison against the real turbine in the simulation. The airflow modelling in the SCPP was performed using the standard k- ε model. The solar radiation intensities were fixed at 400, 600, 800 and 1000 W/m^2 to observe the effects of solar radiation on the turbine performance. The maximum value of turbine efficiency is approximately 70% at various rotational speeds and solar radiations. The maximum power output and the turbine optimum rotational speed was suggested to not coincide with any solar radiation intensities. For solar radiation intensity of 800 W/m^2, the rotational speed of approximately 130 rpm was achieved at maximum turbine efficiency. However, the optimal performance of the system power output was obtained at 150rpm of the turbine rotational speed for the same solar intensity of $800W/m^2$. It was reported that the usage of the fan model provided a decent approach to investigate the turbine pressure drop and updraft velocity in the SCPP without consideration of the turbine efficiency, with a maximum relative error of not more than 3%. To predict system power output, an acceptable prediction of the turbine efficiency was needed when using the fan model for simulation. The study proposed that a real turbine was still a better option to be incorporated into the numerical simulation to achieve higher accuracy of power output and aerodynamic performance of the turbine.

Guo et al. (2016) explored the parameters that impacted the optimal turbine pressure drop ratio, which included ambient parameters, solar radiation, surrounding temperature and collector shape. The study was performed analytically to obtain the optimum expression for turbine pressure drop, and numerically to simulate the influence of different factors on the optimum pressure drop. Component m in the pressure difference expression was found to be an influencing factor of the optimal turbine pressure drop. When the solar radiation was increased from 200 to $800 W/m^2$, a decline of 17% was observed in component *m*, which suggested that the pressure difference increased with solar radiation. A 20K increase in ambient temperature suggested an average increase by 4.3% in component *m*, which portrayed that the turbine pressure difference declined with increasing ambient temperature. The investigation also suggested that a circular collector design exhibits better performance than a square collector design of the same area under increasing pressure drop of the turbine. The study suggested that the optimal value of the turbine pressure drop for the Spanish prototype ranges from 0.90 to 0.94 under typical meteorological conditions.

Hanna et al. (2016) numerically constructed an experimental SCPP system in Aswan, Egypt at 23˚58'N and 32˚47'E to evaluate the performance of the turbine and the aspects of the power generated by the system in the hottest site where Aswan is located. CFX, ANSYS 16.1 was used for the simulation of the flow through the turbine and the overall system. The standard k- ε turbulence model was used for the flow modelling analysis. The turbine used in the CFD simulation was a 6-blade turbine, where the geometry of the flow passage and the turbine constructed was in accordance with the dimensions of the experimental set-up. The power output achieved by the system ranged from 1.2W to 4.4W. The outcome of the research portrayed that the pressure drop across the turbine affected the turbine rotational speed minimally beyond 1650rpm, which was identified as the optimum point, with average turbine efficiency of 57%. The CFD simulation of the set-up proved to be valid and predicted the performance of the system with a relative error of 8.4% for the overall efficiency. The power available for the turbine was simulated to be 7.3% greater than the results obtained experimentally. The numerical CFD model that was created demonstrated good compliance with the experimental results.

Kasaeian et al. (2017) performed a 3D CFD simulation of the Manzanares plant with consideration to the turbine blades. The turbulence model used for simulation was the k- ε model, while to simulate the air flow in the turbine region, the Multiple Reference Frame (MRF) method was used. The CFD simulation was verified using the experimental data obtained from the Manzanares prototype. The study ran 12 different CFD simulations using turbine rotational speed of 40, 80 and 100 rpm, a number of turbine blades of 3, 4 and 5, collector diameter of 122, 244 and 366m, and chimney height of 100, 200 and 300m. The outcome of the CFD simulations was analysed through the outlet air velocity, air mass flow rate, torque and power. It was shown that increment of the rotational speed caused a decrease in the mass flow rate of air, but saw an increment in torque and power developed by the turbine at a constant number of blades. Next, with the increase of the blade number, the mass flow rate of air was seen to have decreased, while the torque and power were increased when angular velocity was at a constant. The mass flow rate of air and power output boosted with an increasing chimney height and collector diameter. The study proposed that using a constant 5-blade turbine, the outlet velocity decreased by 21% while the torque increased by 76%, with an increase in angular velocity of the turbine by 150%. The power generated by the turbine was increased 333% with a 150% increase in the rotational speed of the turbine. 200% increase in chimney height with a rotational speed of 80 rpm increased the outlet velocity, mass flow rate of air, power and torque by 84%, 84%, 114% and 94%, respectively. When the collector diameter was increased from 122m to 366m, that is, by 200% at an angular velocity of 80 rpm, a subsequent increase in outlet velocity, the mass flow rate of air, torque and generated power by 15%, 16%, 19% and 19% were recorded. At an average of 80rpm angular velocity, outlet velocity 9.5, 13.7 and 17.5 m/s were noticed for chimney heights 100, 200 and 300m accordingly. The 5-blade turbine was suggested to be able to harness the highest power at 91kW.

A 3D numerical analysis of the Manzanares prototype with an actual turbine was conducted by Gholamalizadeh and Chung (2017a) to investigate the fluid flow and the heat transfer attribute of the plant. ANSYS 15.0 was employed where the turbulent model utilised for the numerical analysis was the RNG k-ε turbulence closure. The Multiple Reference Frame (MRF) was used to analyse the relationship between the airflow and the turbine. A 4-bladed turbine with the FX W-151-A blade profile was

employed at the bottom of the chimney. Also, a reverse fan model was studied to investigate its feasibility in simulating the effects of the turbine accurately. The temperature, velocity and distribution of pressure within the system were analysed. The simulation outcome of the SCPP coupled with the real turbine proved good agreement with the experimental data obtained from the Manzanares plant, with relative errors of 1.8% for pressure drop across the turbine, 2.3% for inlet velocity of the chimney, and 1.7% collector temperature increment. The turbine efficiency of the model was reported to be 68.4%, with optimal performance at the rotational speed of 140rpm and an ideal power of 52.8kW. In the case of the reverse fan model, the pressure jump value was 43.7% lesser than the real turbine. The pressure, temperature and velocity distributions of the reverse fan model were portrayed to be uniform as opposed to the actual turbine model, which was non-uniform. It was suggested that the real turbine model was a much more appropriate option when considering the system performance of the SCPP compared to the reverse fan model.

In a different investigation conducted by Gholamalizadeh and Chung (2017b), the accuracy of prediction using different blade profile modelling, namely FXW-151-A and CLARK Y obtained from three different studies by Gholamalizadeh and Chung (2017a), Guo et al. (2015) and Tingzhen et al. (2008) were analysed. The FXW-151-A blade profile was also used to analyse the effects of different rotational speeds of the turbine on the mass flow rate of air, pressure drop, turbine efficiency and power generation. The 3D simulation integrated the 4 bladed shrouded pressure-staged wind turbine with the FX W-151-A blade profile to simulate the Manzanares prototype. The numerical analysis used the k-ε turbulence model to simulate the flow in the system, while the Multiple Reference Frame was used for the chimney-turbine relationship. Figure 2.2 illustrates the modelled SCPP with its boundary conditions. The outcome of the simulation was validated with the Manzanares data where relative errors 1.8%, 2.3% and 1.7% were obtained for pressure drop, chimney inlet velocity and temperature increase in the collector, respectively. The three different models were comparatively studied at solar radiation intensity of 800 W/m^2. The mass flow rate in Tingzhen et al. (2008)'s model (3 bladed turbine) was much greater than that of Gholamalizadeh and Chung (2017a) and Guo et al. (2015) (4 bladed turbine). It was suggested that a higher number of turbine blades decreased the mass flow rate of air. The pressure drop in the Gholamalizadeh and Chung (2017a)'s model increased with

rotational speed, which portrayed good agreement with Tingzhen et al. (2008)'s model. However, it was suggested that Tingzhen et al. (2008)'s model and Guo et al. (2015)'s model overestimated the pressure drop due to the blade profile CLARK Y. The relationship between the turbine efficiency and varying rotational speeds of FXW-151-A and CLARK Y were similar, where the peak values were 120 rpm and 130 rpm, respectively, while the efficiency of the turbines were 73% and 70% accordingly. The power generation with increasing rotational speed showed a similar trend to the turbine efficiency with optimum rotational speeds at 140rpm and 150rpm for Gholamalizadeh and Chung (2017a)'s and Guo et al. (2015)'s models, while Tingzhen et al. (2008)'s model portrayed an underestimating power generation. It was suggested that the 4 bladed FXW-151-A was slightly better in terms of mass flow rate of air, pressure drop, turbine efficiency and power output compared to the blade profile CLARK Y.

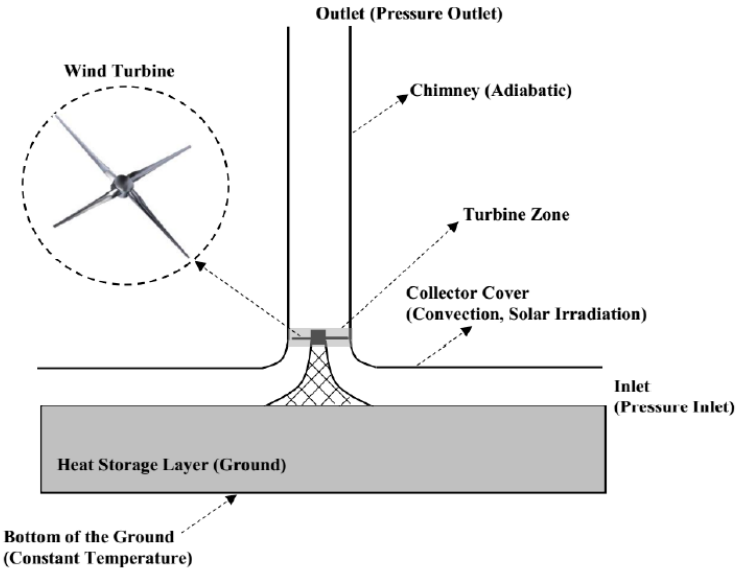

Figure 2.2 Illustration of SCPP with Specified Boundary Conditions

Ayadi, Driss, et al. (2018a) studied the effects of various turbine diameters on the power output of the solar chimney power plant. In this study, four different turbine diameters were adopted to identify the effects on a solar chimney power plant coupled with a turbine. For each turbine diameter, the air temperature, distribution of the magnitude velocity and pressure were considered. The dimensions used in the investigation were collector diameter 2750mm, collector roof height 50mm, chimney height, 3000mm and turbine diameter 90, 120, 140 and 150mm. The numerical analysis was performed using the ANSYS Fluent 17.0, where the simulation between

the turbine and the chimney was conducted using the Multiple Reference Frame (MRF) model. The results of the numerical analysis were in good agreement with the experimental data obtained. The study suggested that the increase in turbine diameter improved the air circulation at the bottom of the chimney. The analysis with regards to the air velocity suggested that an increase in the blade radius of the turbine increased the air velocity in the surrounding zones of the blades. Based on the numerical results of the study, the magnitude of air velocity was observed to be dependent on the turbine diameter. On the contrary, the numerical results suggested that the distribution of the temperature in the SCPP reduced while the static pressure increased with an increasing turbine diameter. The outcome of the investigation proposed that the increase in turbine diameter with variation equal to 60mm could result in an increase in power output by 155%. The turbine diameter increment was indicated to be a critical parameter in power enhancement.

In a subsequent study, Ayadi, Driss, et al. (2018b) investigated the impact of the number of turbine blades on the airflow and thermal performance of a small SCPP. The air temperature, distribution of magnitude velocity, static pressure and turbulent kinetic energy and viscosity were analysed for 4 different turbine blade structures with 4, 6, 8 and 10 blades. The dimensions of the studied prototype were collector diameter 2750mm, collector roof 50mm, chimney height 3000m, chimney diameter 160mm and turbine diameter 150mm. The blade pitch was 40, while the length and width of the blade were equivalent to 37mm and 30mm, respectively. The numerical analysis was conducted via ANSYS Fluent 17.0, where the Multiple Reference Frame (MRF) was adopted to simulate the turbine-chimney relationship. The magnitude velocity suggested that the turbine with an increasing number of blades reduced the rotational speed of the turbine due to the increased drag of the turbine shaft. The air temperature was indicated to decrease with the increase in turbine blade numbers. The turbine with 10 blades was observed to have the highest static pressure amongst the 4 turbine blade configurations. The maximum turbulent kinetic energy and turbulent viscosity in the investigation were obtained from the 8 blades turbine with a value of 1.58 m^2/s^2 and 1.58 kg/ms, respectively. The 10-bladed turbine achieved the highest power generation since the power generated increased with the number of blades.

Negrou et al. (2018) developed a model using the inverse design methodology on the wind turbine to anticipate the characteristics of the operation of the SCPP. The model was constructed with inlet guide vanes for pre-gyration of the airflow to determine the flow distribution on the inverse method of the turbine. The inlet guide vanes facilitated the flow to the duct of the rotor which reduced the turbine exit kinetic energy at the diffuser. The static energy at the diffuser outlet was boosted by 21% with the introduction of the inlet guide vanes in the SCPP. The model was coupled with geothermal energy for constant system operation with the continuous hot water flow through tubes in the collector space. The coupled design with the inverse method turbine model suggested a maximum power output of 5MW and 77% turbine efficiency with 140m^3/h of hot water flow.

Liu, Tian, and Nie (2018) proposed a novel method to optimize the turbine component in the SCPP by designing the blade of a wind turbine based on the collector exit Reynolds number and the wind power utilisation theory. The numerical analysis was conducted using Profili and Xfoil, where the class-shape-transformation (CST) parameterization method was employed. The NACA4418 airfoil portraying the highest lift-drag ratio with an optimum angle of attack equivalent to 7°, lift coefficient 1.126 and drag coefficient 0.009 was selected. The airfoil's best chord length and setting angle were identified using the blade element theory for maximum aerodynamic performance. The modelling of the blade was performed first on AutoCAD and imported to Solidworks based on the optimised data obtained from Profili and Xfoil. The modelled blade was suggested to be used for further performance analysis of the SCPP.

Rabehi et al. (2018) investigated the performance of the Spanish prototype of the SCPP numerically by adopting the fan model for the turbine component. The temperature, velocity and pressure on collector efficiency and power output were analysed based on the pressure difference of the turbine and the solar radiation under load and no-load conditions. The 3D simulation of the SCPP was conducted using ANSYS Fluent, where the standard k-ε turbulence model was employed. The verification of the numerical model developed using the experimental data obtained from the Spanish prototype reported a 30.02% error due to the usage of the fan model, which did not account for the structural parameters of a real turbine. During the turbine load

condition, the temperature and static pressure were suggested to have increased, while the air velocity decreased compared to the off-load condition. The study suggested that the varying solar intensities affected the airflow and heat transfer attributes within the system. In the case of solar radiation, for a constant value of $800W/m^2$, the average air velocity declined by 17%, while the average temperature increased by 4.25K during turbine operation. The pressure difference of the turbine had minimal effect on the collector performance but has an appreciable impact on the generated power. The power loss was suggested to be lesser at higher pressure drop values.

Balijepalli, Chandramohan, and Kirankumar (2020) investigated a small scale SCPP for powering household devices. The experimentation was run for 10 days, while the results presented were based on one day's data. The highest velocity obtained from above and below the turbine were 4.7 m/s and 5.5 m/s, respectively. On the other hand, the average velocity attained above and below the turbine component was 53.62% and 45.82% lower than the highest velocity. The actual power output obtained at 0.82 W was 40.15% lower than the theoretical power generated. The estimated chimney and total plant efficiencies were estimated to be 0.0187% and 0.0128%, respectively.

Zuo et al. (2021) studied the usability of the axial flow hydraulic turbine and axial flow pump impeller with the optimal turbine pressure drop under the influence of solar radiation in 3D. The study adopts the RNG k-epsilon method to simulate the turbulent flow. The authors incorporated the turbine from Tingzhen et al. (2008)'s study for validation since it closely matched the Manzanares load condition. The turbine rotational speed was variated to study the effect on the performance. The turbine was suggested to improve the peak power output by 30.46% due to the maximum pressure drop and pressure drop ratio being 178.63Pa and 0.95, respectively. The optimal turbine pressure drop increased from 0.90 to 0.92 with solar radiation. Also, at higher solar radiation, the turbine rotational speed range was proposed to be larger.

2.8.1 Limitations

Turbine studies have been performed based on many parameters such as the turbine design, number of blades, rotational speed, solar intensity and location of the plant. Studies have been carried out on different SCPP scales that incorporate an actual

turbine. However, there is a lack of clarity on the power augmentation in the collector region of the plant.

2.9 Influence of Time Step Size and Number of Time Step in CFD Turbine Analysis

Satrio et al. (2018) studied the impact of the time step setting on the results of the CFD simulation performed on a vertical axis tidal current turbine. Two main parameters that were needed for a stable result were investigated. These parameters were the time step size, which represented one turbine rotation at a calculated degree, and the number of time steps, which ensured the steadiness of the outcome. The 2D analysis adopted the Sliding Mesh technique in ANSYS Fluent in order to solve the URANs equation. The solver inculcated the second-order scheme and the SIMPLE algorithm for the transport equations. Upon validation, the number of time step sizes were tested at different increment angles. The best outcome was analysed with a varying number of rotations. The outcome of the study suggested that results improved with a more specific time step size. However, the downfall was the increase in computational time. Time step size 5 degree to 1 degree was proposed for a more desirable outcome. The steadiness of the results was obtained at a minimum of 6 turbine rotations.

2.9.1 Limitations

The accuracy of the results obtained from turbine studies was suggested to be more accurate with a precisely defined time step size. However, it was also discussed that a highly specific time step size would increase the computational time, resulting in a higher cost. Furthermore, the minimum turbine rotation needed to achieve stability of the results was based on a specific free stream velocity input. Thus, the number of turbine rotations required for result stability at a high free stream velocity or Reynolds number is unknown and still relies on the output data analysis.

2.10 Application of Savonius Turbine in Confined Areas

Chen et al. (2013) investigated the usage of a vertical axis water turbine for power supply to devices that maintain water quality in a pipeline. The vertical axis water turbine was designed for a 100mm pipeline with an average water velocity of 1.5 m/s

and a head loss of 5m. The novel design was analysed by the performance of the turbine and the resultant water flow characteristics in the pipeline using Fluent and Gambit. The results obtained from the simulation were used in fabricating prototypes and testing the actual power output. Although the difference between the simulation and experimental results was large, the authors suggested that the simulation studies could provide a good guide for the rotor design. The outcome of the study suggested that the rotor with a hollow body in the presence of an eye-shaped slanted block that acted as a guide vane was the highest power generating turbine at 88.2W, compared to other designs of the vertical axis rotors. The authors proposed that the generated study was a good information guide for power generation in enclosed conditions.

2.10.1 Limitations

The power output of the Savonius turbine in confined areas was applaudable. However, the investigation was conducted with constant fluid characteristics, leaving the performance of the Savonius at different free stream velocities and fluid densities uncertain.

2.11 Comparison Study Between a Novel and Conventional Savonius Style Wind Turbine

Roy and Ducoin (2016) investigated the instantaneous longitudinal drag and lateral lift forces acting on a novel two-bladed Savonius-style wind turbine in a transient manner. The 2D analysis was performed in StarCCM+ by incorporating the SST k-omega turbulence model at a Reynolds number of $1.23\,x\,10^5$. The Gauss-Seidel iterative method was incorporated in the solvent, where the URANS equations were discretized to the second-order under the SIMPLE algorithm. The numerical model was validated against previous experimental data before proceeding with the analysis. The performance of the new SSWT (Savonius style wind turbine) was compared to the conventional SSWT, where it was shown that the moment arms and drag force magnitude were similar for both turbines. However, a significant improvement was noticed with regards to the lift contribution to the power generation. This was suggested to be due to the increase in curvature of the blade that promoted flow retention at higher angles of attack at the initial stage of the turbine rotation. This, in turn, increased the depressure and benefited the lift force. The authors also suggested

that though there were minor effects on the average drag, there was a considerable increase in the lift due to the delay in stalling. Authors further promoted the usage of the new SSWT for off-grid electricity generation, extraction of energy in exhaust systems and ventilation in buildings.

2.12 Summary of Literature Review

This section denotes the key findings from previous research with relevance to this research.

1. The introduction of guide vanes at the turbine region improves air attack on shrouded turbine blades, therefore improving turbine efficiency and power generation.

2. A divergent chimney improves the performance of the chimney component and enhances the power generation in the system.

3. Numerical performance analysis of the SCPP using a real turbine model is a better option than a fan model due to the availability of structural parameters in the real turbine.

4. The usage of SSWT is applicable in confined areas.

5. The SSWT performs well under low velocity, has a low starting torque, and is encouraged for energy extraction in exhaust and ventilation systems.

2.13 Research Gap

Numerous studies have been conducted by researchers over the years in enhancing the SCPP performance and increasing the power yield drawn from its operations. Nevertheless, various areas still lack detailed research for further improvement studies and significant operating developments of the SCPP. Many investigations were conducted with regards to the performance enhancement of the collector and chimney region. In general, the conventional SCPP struggles to achieve a commendable overall plant efficiency. The common scope that is not taken critically into account is the operation enhancement of the turbine efficiency. Amongst the many different turbine

designs adopted in previous studies, the potential of the SSWT in the SCPP has not yet been explored. Furthermore, the influence of a diverging chimney on the fluid flow has not been studied in the presence of the SSWT. In addition, the effect of guide vane parameter variation on the performance of the SSWT in the SCPP has not been addressed. As most studies focus on the turbine's performance in the chimney section, the possibility of power augmentation in the collector region of the SCPP is not clear.

2.14 Novelty

The literature review in the section above emphasising the turbine component suggests that several aspects of performance analysis have not been addressed. The novelties of this work that address the aforementioned research gaps are listed below.

1. The performance of the SSWT under two axes of operations (i.e. horizontal and vertical) in the collector region of the SCPP.
2. The influence of chimney divergence on the SSWT's power production performance.
3. The influence of guiding vanes parameter variations on SSWT operation in the SCPP.

2.15 Summary of Chapter 2

This chapter discussed the previous background studies conducted on the SCPP by various renowned scholars, with attention given to the findings and inadequacy of each study. This chapter also focussed on types of turbine efficiency improvements suggested by researchers for enhanced power generation compared to the conventional SCPP. The common lack of these studies has been identified and discussed as the research gap. The deployment of the Savonius turbine in the collector area, as well as a study into the impact of diverging chimneys and guiding vanes on the performance of the suggested rotor, as proposed in the scope of work, will cover the discussed research gaps from prior literature. The novelty of the proposed investigations addressing the research gaps has been reviewed in the end section of this chapter.

CHAPTER 3
METHODOLOGY

3.0 Introduction

This chapter presents the methods undertaken to validate the SCPP and the SSWT. Next, the approaches taken to conduct the investigations proposed in this work are shown. The domains, governing equations, boundary conditions, ANSYS Fluent set up, and solution schemes adopted for the validations and the analysis to achieve the objectives of this work are presented.

3.1 Model Development

The conventional solar chimney power plant is proven to have a low efficiency of less than 2%, requiring flat land which has little or no competitive usage (Schlaich et al. 2005). The improvements undertaken for the turbine component of the SCPP to improve its overall efficiency is at a minimum Guo et al. (2019). The fundamental challenge to the SCPP system is the fixed inlet gap for airflow into the collector, the low efficiency of the chimney and the poor energy conversion at the turbine. This study proposes to analyse the feasibility of using the SSWT in the SCPP for power generation. The pressure differential caused by varying chimney divergence was investigated for further power enhancement. This study was also designed to enhance the performance of the SSWT in the SCPP by improving the angle of air attack onto turbine blades through the introduction of guide vanes and varying its parameters for the optimum configuration. The methods employed to accomplish these investigations were through numerical means using the ANSYS CFD simulation software. A 2D numerical model was developed to identify the performance of the proposed VAWT in the SCPP under two different operational axes. Next, the suitable diverging angle of the chimney for improved performance of the SCPP was numerically analysed to determine the most effective arrangement for optimum power generation. In addition, the optimum parametric configurations for the introduced guide vanes in the presence of the VAWT was also analysed. The subsections detail the numerical methods that were employed to achieve the aims of this work.

3.2 Numerical Modelling

The numerical model involved modelling the Manzanares plant and the SSWT to the highest possible accuracy. The model was developed and simulated using a computational fluid dynamic software, ANSYS Fluent, considering essential input data such as the ambient temperature, solar radiation, wind velocity, and wind direction, which are important boundary conditions. The models' simulation was validated with experimental results from the Manzanares plant and past experimental and numerical data for the SSWT before modelling the improved prototype. This particular software was chosen due to its availability in the university with a research license, its ability to compute numerical models in a short period of time and its user-friendliness.

The numerical analysis involved five stages of modelling. In the first stage, the proposed SSWT model was developed by adopting the Sliding Mesh method and validated against experimental and numerical data from past studies. In the second stage, a simple model of the solar chimney power plant was developed to the same dimensions as the Manzanares plant and was validated using available experimental data from the Manzanares plant. In the third stage, the turbine model was tested under two different configurations in a smaller domain incorporating the wind velocity and pressure characteristics obtained from the Manzanares plant. The turbine installation site was selected upon identifying the highest average velocity in the collector region (for maximum power output) from the velocity profile obtained in the second stage. In the fourth stage, varying divergent chimney angles were added to the Manzanares model and simulated. The flow characteristics of the divergent models were determined and applied for turbine testing. In the fifth stage, the turbine model domain was incorporated with guide vanes at the turbine section. The guide vanes' parameters were varied and studied for the best configuration allowing optimum power generation. The designed model was investigated based on the air velocity at the wake region of the turbine, pressure and power generation.

3.3 Numerical Modelling Governing Equations

The following subsections present the fluid flow physics and the fundamental governing equations associated with the numerical modelling of the SCPP.

3.3.1 Governing Equations for the Flow

The fluid flow and thermal field in the SCPP are based on control volume analysis, thus analysed based on continuity, momentum and energy in the system (Bird, Stewart and Lightfoot 2007; Demirdžić and Muzaferija 1995; Ferziger and Perić 2002; Perić, Kessler and Scheuerer 1988).

In control volume analysis, the continuity and momentum equations are described in the Navier Stokes equation as continuous integral as expressed in Equation 3.1. The equation is a function of the convective flux term, pressure gradient, viscous flux and buoyancy.

$$\oint_A (\rho \mathbf{v})(\mathbf{v} - \mathbf{v_g}).\, da = -\oint_A p\boldsymbol{I}.\, da + \oint_A \mathbf{T}.\, da + \int_V f_g\, dV \qquad 3.1$$

3.3.2 Continuity Equation

Equation 3.2 expresses the fluid flow discrete continuity equation, where $\dot{m}_f^*$ is the uncorrected mass flow rate for respective faces, which is used to compute the average interior continuum and pressure boundary faces, while $\dot{m}_f{}'$ is the mass flow rate correction factor used for rectification.

$$\sum_f \dot{m}_f = \sum_f (\dot{m}_f^* + \dot{m}_f{}') = 0 \qquad 3.2$$

The uncorrected face of the mass flow rate for interior faces is expressed in Equation 3.3 as a function of face fluid density, ρ_f, average velocity within cell zones, v_0^* and v_1^*, G_f is the grid flux and Υ_f is the Rhie-Chow-Type dissipation. Thus, Equation 3.3 can be represented as shown in Equation 3.4 where v_f is the average face velocity of buoyant fluid while a is the face area vector.

$$\dot{m}_f^* = \rho_f \left[a.\left(\frac{\mathbf{v_0^*} + \mathbf{v_1^*}}{2} \right) - G_f \right] - \Upsilon_f \qquad 3.3$$

$$\dot{m}_f^* = \rho_f (\mathbf{v_f}.\, a - G_f) - \Upsilon_f \qquad 3.4$$

3.3.3 Momentum Equation

The momentum equation shown in Equation 3.5 is formed when Equation 3.1 is applied to cell centred control volume. The momentum equation is also otherwise known as the discretized equation for flow transport which is a function of the viscous flux, where $\boldsymbol{v}$ represents the bulk fluid velocity, $\boldsymbol{v}_g$ represents the grid velocity, a is the face area vector, p is the pressure, $\boldsymbol{I}$ is the identity matrix, $\boldsymbol{T}$ is the viscous stress tensor and f_g is the force on the body due to gravity. Equation 3.6 denotes the stress tensor, $\boldsymbol{T}$, for the viscous flux.

$$\sum_f \left[\boldsymbol{v}\rho(\boldsymbol{v}-\boldsymbol{v}_g)\cdot a\right]_f = -\sum_f (p\boldsymbol{I}\cdot a)_f + \sum_f \boldsymbol{T}\cdot a + \sum_V (f_g \cdot v)_V \qquad 3.5$$

$$\boldsymbol{T} = \mu_{eff}\left[\nabla\boldsymbol{v} + \nabla\boldsymbol{v}^T - \frac{2}{3}(\nabla\cdot\boldsymbol{v})\boldsymbol{I}\right] \qquad 3.6$$

where $\mu_{eff} = \mu + \mu_t$

3.3.4 Governing Equations for Fluid Energy

The energy in the control volume of buoyant driven flow is a function of convection, diffusion, viscosity and buoyancy of fluid, thus Equation 3.7 expresses the energy interaction in the control volume.

$$\oint_A \left[\rho H(\mathbf{v}-\mathbf{v_g}) + \mathbf{v_g}p\right].da = -\oint_A \dot{q}".da + \oint_A \mathbf{T}.\mathbf{v}\,da + \int_V f_g.\mathbf{v}\,dV \qquad 3.7$$

where H is enthalpy and $\dot{q}"$ is heat flux vector.

The interaction between bulk fluid flow can be defined using the heat flux vector as shown in Equation 3.8, which is also known as the Fourier's law of heat conduction where, k_{eff} is the effective thermal conductivity, while T is the temperature.

$$\dot{q}" = -k_{eff}\nabla T \qquad 3.8$$

Equation 3.9 expresses the effective thermal conductivity considering the thermophysical property of the fluid in terms of the thermal conductivity of the fluid, **k**, the effect of turbulence describing the turbulent viscosity, μ_t, the effect of specific heat C_p, and turbulent Prandtl number, σ_t.

$$k_{eff} = \mathbf{k} + \frac{\mu_t C_p}{\sigma_t} \quad 3.9$$

The energy transfer by convection in the control volume is represented as Equation 3.10 for the diffusion term of heat transfer from boundary faces to fluid volume, where h is the convective heat transfer coefficient, T_∞ is the reference temperature and T_{sf} is the face temperature.

$$\dot{q}''.a = h(T_\infty - T_{sf}) \quad 3.10$$

3.3.5 Governing Equations for Incompressible and Constant Density Flows, and Boussinesq Approximation

The buoyancy of the fluid varied by the fluid density differences is a function of the temperature in a buoyancy-driven flow. The terms in the momentum equation in Equation 3.1, which are the convective flux, pressure gradient and viscous flux, remain influenced by the buoyancy of the working fluid. Equation 3.11 expresses the Boussinesq approximation, where β is the coefficient of bulk expansion and T_{ref} is the operating temperature of the buoyant fluid.

$$f_g = \rho g \beta (T_{ref} - T) \quad 3.11$$

3.3.6 Governing Equations for Turbulence

3.3.6.1 RNG k-epsilon model

The RNG k-epsilon model is a more refined version of the standard k-epsilon model. An additional term in its ϵ equation makes the RNG k-epsilon model more accurate for rapidly strained flows and improves the accuracy in swirl flows. This model is adopted in solving the SCPP model.

The solution to the transport equations for the turbulent kinetic energy, k, and the turbulent dissipation rate, ε is found with the utilization of the RNG k-epsilon model as expressed in Equation 3.12 and 3.13 where, G_k is the kinetic energy generation due to velocity gradients, G_b is the kinetic energy generation due to buoyancy, Y_M is the contribution of fluctuating dilatation, and S_k and S_ε are the user-defined terms, C_1,

C_2, $C_{1\varepsilon}$ and $C_{3\varepsilon}$ are turbulent model constants, μ_{eff} is the dynamic viscosity and α_k and α_ϵ are the inverse effective Prandtl number for k and ϵ, respectively.

$$\frac{\partial}{\partial t}(\rho k) + \frac{\partial}{\partial x_i}(\rho k u_i) = \frac{\partial}{\partial x_j}\left[(\alpha_k \mu_{eff})\left(\frac{\partial k}{\partial x_j}\right)\right] + G_k + G_b - \rho\varepsilon - Y_M + S_k \qquad 3.12$$

$$\frac{\partial}{\partial t}(\rho\varepsilon) + \left(\frac{\partial}{\partial x_i}\right)(\rho\varepsilon u_i) = \frac{\partial}{\partial x_j}\left[(\alpha_\epsilon \mu_{eff})\left(\frac{\partial \varepsilon}{\partial x_j}\right)\right] + C_{1\epsilon}\frac{\epsilon}{k}(G_k + C_{3\epsilon}G_b) - C_{2\epsilon}\rho\frac{\epsilon^2}{k} - R_\epsilon + S_\varepsilon \qquad 3.13$$

The model coefficients values $C_{1\epsilon} = 1.42$, $C_{2\epsilon} = 1.68$ are constants that are used in ANSYS Fluent. The inverse effective Prandtl number at large Reynold's number is taken to be $\alpha_k = \alpha_\in \approx 1.393$ (Fluent 2009).

3.3.6.2 Shear Stress Transport (SST) k-omega model

The SST k-omega model developed by Menter (1994) is a more accurate formulation of the k-omega model in the near-wall region with the far-field free stream independence of the k-epsilon model. The model blends both functions together at the near-wall regions while reducing to zero when away from the surface which activates the k-epsilon model. The SST k-omega model is suggested to be more reliable in solving adverse pressure gradient flows and airfoil problems compared to the standard k-omega model (Fluent 2009). The addition of the cross-diffusion term in the omega equation together with the blending function ensures good behaviour at both the near-wall regions and the far-field regions. This model is incorporated to solve the turbine related problems in this study.

The equation of the SST k-omega model, which is similar to the standard k-omega model, is represented in Equations 3.14 and 3.15, where it is used to solve the transport equations for the turbulent kinetic energy, k, and the specific dissipation rate, ω.

$$\frac{\partial}{\partial t}(\rho k) + \frac{\partial}{\partial x_i}(\rho k u_i) = \frac{\partial}{\partial x_j}\left[(\Gamma_k)\left(\frac{\partial k}{\partial x_j}\right)\right] + \tilde{G}_k - Y_k + S_k \qquad 3.14$$

$$\frac{\partial}{\partial t}(\rho\omega) + \left(\frac{\partial}{\partial x_i}\right)(\rho\omega u_i) = \frac{\partial}{\partial x_j}\left[(\Gamma_\omega)\left(\frac{\partial \omega}{\partial x_j}\right)\right] + G_\omega - Y_\omega + D_\omega + S_\omega \qquad 3.15$$

From the equations above, $\tilde{G}_k$ is the kinetic energy generation due to velocity gradients, G_ω is the specific dissipation rate generation, Γ_k and Γ_ω are representations of the effective diffusion of k and omega, Y_k and Y_ω are the representations of the turbulence dissipation of k and omega, D_ω is the representation of the cross-diffusion term, while S_k and S_ε are the user-defined terms (Fluent 2009).

The effective diffusion of k and omega and be calculated using Equations 3.16 and 3.17, where the σ_k and σ_ω are the turbulent Prandlt numbers for k and omega, while the μ_t is the turbulent viscosity.

$$\Gamma_k = \mu + \frac{\mu_t}{\sigma_k} \quad 3.16$$

$$\Gamma_\omega = \mu + \frac{\mu_t}{\sigma_\omega} \quad 3.17$$

3.4 Turbine Validation

This section discusses the type of turbine utilised for power generation in the solar chimney power plant. The model specifications of the turbine, the mesh settings, setup and solution methods of the simulations are discussed in detail.

3.4.1 Geometry Specifications

This subsection presents the turbine geometry that was used in the study. The turbine model that was incorporated in this study was adopted from the work of Roy and Saha (2015) and Roy and Ducoin (2016). This particular turbine geometry type was chosen for its advantage in lift generation at low velocities compared to a conventional Savonius wind turbine, as discussed in the literature studies (Section 2.11). The novel two-bladed Savonius wind turbine blade profile with coordinates is presented in Figure 3.1.

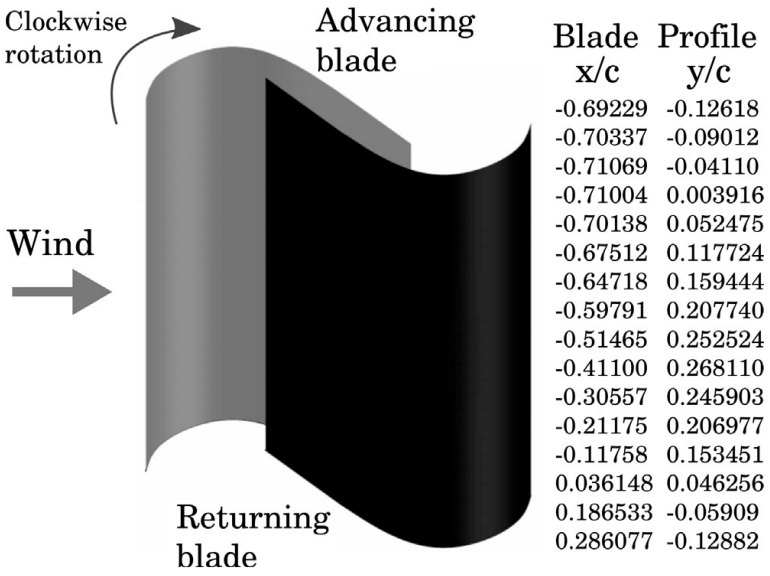

Figure 3.1: The novel Savonius Style Wind Turbine with coordinates (Roy and Ducoin 2016)

The coordinates of the blade profile were inputted into excel, which was then exported to Solidwork through a text file. The blade profile was reconstructed and then scaled to a diameter of 0.21 (D). The turbine was tested in a circular domain with a diameter of 2D. An outer rectangular domain of 14D length and 6D width was constructed in which the circular domain and the turbine were contained. The circular domain was positioned 3D from the left end of the rectangular domain. The whole sketch was converted into a 2D planar surface, as shown in Figure 3.2.

Figure 3.2: 2D Planar Turbine Domain

3.4.2 ANSYS Fluent: Geometry Interface

The 2D planar surface from Solidworks was imported into ANSYS Fluent's "Geometry" interface as a "STEP" file. First, the circular domain and both turbine

blades were subtracted from the rectangular domain, with preservation of the subtracted body. Second, both turbine blades were subtracted from the circular domain, with no preservation of the subtracted body. The model was then generated and transferred to the meshing interface, which will be discussed in the following subsection.

3.4.3 ANSYS Fluent: Mesh Interface

This subsection presents the mesh settings used for the validation of the energy extractor. Table 3.1 displays the detailed mesh settings used for the validation of the proposed SSWT.

Table 3.1: Mesh Settings for the turbine validation

Parameters	Values
Type of mesh	Triangular
Rectangular Domain	0.012 m
Circular Domain (R=0.21m)	0.001 m
Sub-Circular Domain (R=0.12m)	0.0007 m
Circular Domain (Inner/Outer): Number of Division	200
Turbine Blade Long Edge Division	250
Turbine Blade Short Edge Division	4
Inflation	• 1st layer thickness = 3.9113×10^{-5} • 10 layers • Growth rate = 1.14
y+	≤ 1

The mesh type used for this model was the triangular mesh since the domain was more prone to curved geometries. The “Sphere of Influence” method was used for the element sizing for the Circular and Sub Circular Domain. The “inner circular domain” edge was selected by using the hide option for the rectangular domain, while the “outer circular domain” edge was selected by applying the hide option for the circular

domain. This step is vital to enable the “sliding mesh” interface discussed in Subsection 3.4.4. The first layer thickness of the inflation is calculated based on the required “y+” value of less than 1, at fluid air properties at $25°C$. Figure 3.3, Figure 3.4 and Figure 3.5 presents the mesh for the turbine validation, mesh for the circular domain and inflation of the turbine blade, respectively. Each boundary was given a “Named Selection” for the setting of the mesh. These named boundaries were transferred to the following “Setup” interface discussed in Subsection 3.4.4.

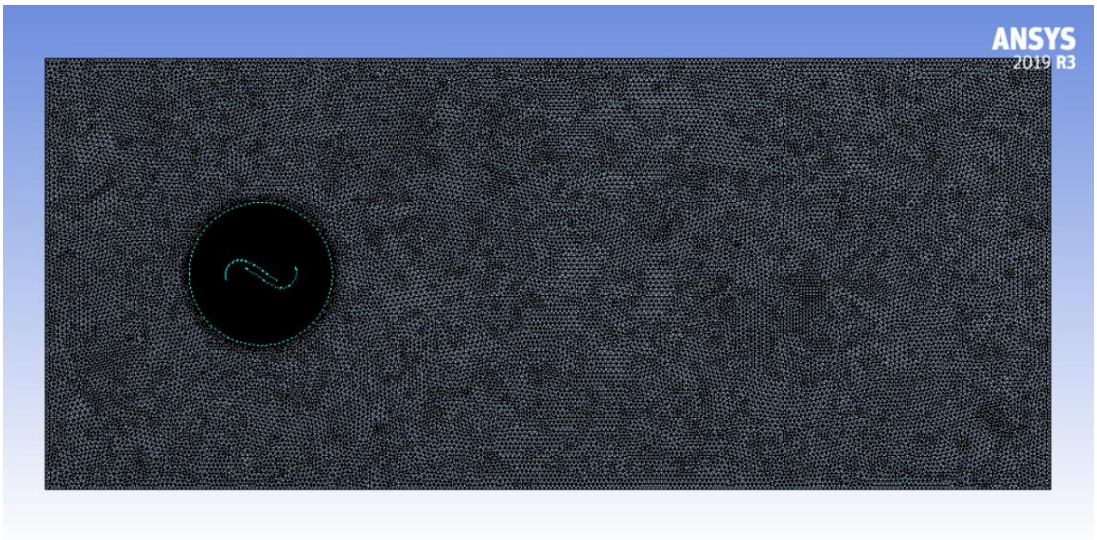

Figure 3.3: Mesh for Turbine Validation

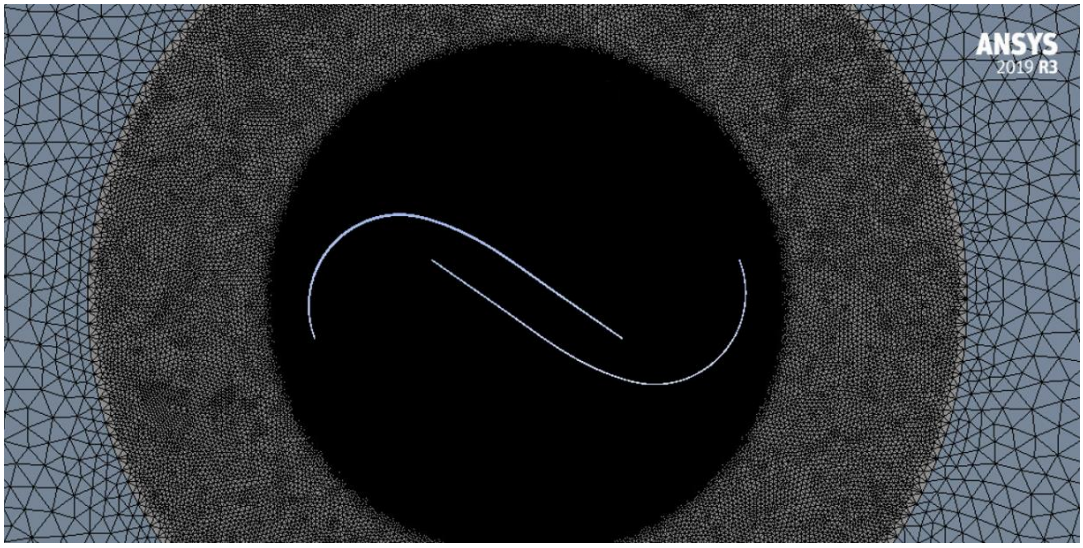

Figure 3.4: Mesh of Circular Domain

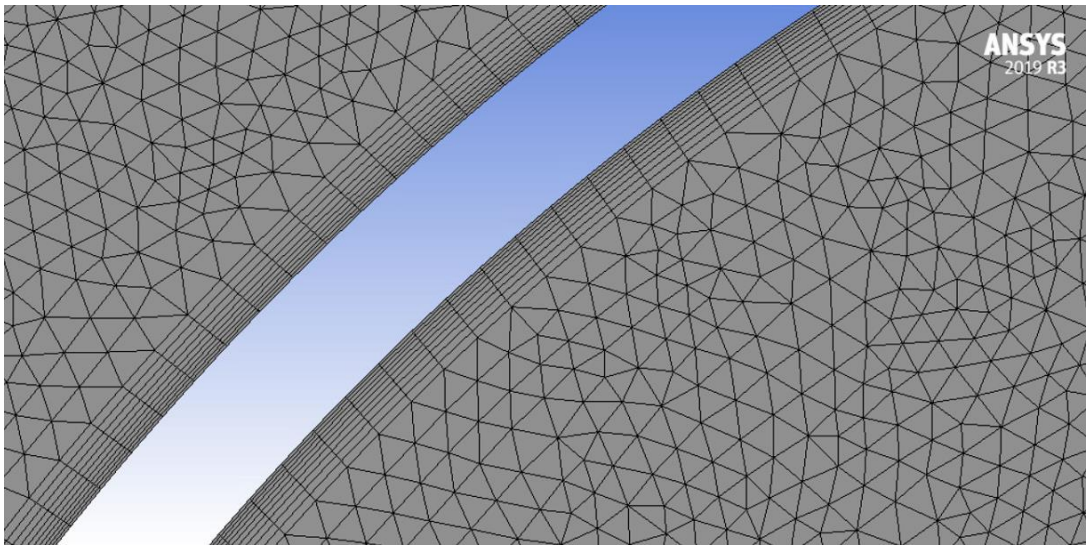

Figure 3.5: Turbine Blade Inflation

3.4.4 ANSYS Fluent: Setup Interface

This subsection presents the setup for the turbine validation. The model chosen to solve the transport equations in the turbine validation is the SST k-ω model since this model is able to predict near-wall fluid flow values accurately. The material properties adopted for the turbine validation is tabulated in Table 3.2.

Table 3.2: Material properties for turbine validation

Properties/Material	Air	Aluminium
Density (kg/m3)	1.1845	2719
Viscosity (kg/m-s)	1.8444e-5	Nil

The cell zone conditions for the rectangular and circular domains were set to be fluid. The rectangular domain was set to be a static fluid mesh, while the circular domain was set to be a rotating fluid mesh. The rotational speed was inputted based on the TSR tested at a constant wind velocity of 7.8 m/s. A mesh interface was created between the outer circular and inner circular domains to connect the mesh cell from the rectangular domain to the circular domain for fluid flow. These two boundaries were set as a moving wall to create a “sliding mesh”. Different turbulence intensity and viscosity ratio values were tested considering the medium turbulence setup of the application, and the final values were selected according to the percentage error against the validation results. The walls are allowed to move relative to the adjacent cell zone.

Table 3.3 displays the boundary conditions of the rectangular domain and circular domain. The turbulence characteristics were selected after a series of parametric studies based on medium-ranged turbulence.

Table 3.3: Boundary Conditions for Turbine Validation

Boundary	**Conditions**
Velocity-Inlet	• Velocity Magnitude = 7.8 m/s • Turbulence intensity = 5% • Turbulent Viscosity Ratio = 10
Pressure-Outlet	• Turbulence intensity = 5% • Turbulent Viscosity Ratio = 10
Outer Circular Domain	• Mesh Interface • Rotational Motion • Move relative to adjacent cell zone
Inner Circular Domain	• Mesh Interface • Rotational Motion • Move relative to adjacent cell zone
Turbine Blades	• Rotational Motion • Move relative to adjacent cell zone

The reference values are set up for the turbine validation to determine the moment coefficient at the turbine blades. The depth for a 2-dimensional analysis is typically set as 1m in the z-direction. The fluid properties selected were based on the temperature at 298 K. These values are tabulated in Table 3.4.

Table 3.4: Reference Values for Turbine Validation

Reference	Values
Area (m2)	0.21
Density (kg/m3)	1.1845
Depth (m)	1
Length (m)	0.105
Temperature (K)	298
Velocity (m/s)	7.8
Viscosity (kg/m-s)	$1.8444\ x\ 10^{-5}$

3.4.5 ANSYS Fluent: Solution Interface

The SIMPLE scheme was chosen for the pressure-velocity coupling. The "Least Square Cell-Based" was used for the Spatial Discretization of the Gradient, while pressure, momentum, turbulence and transient calculation were set to the second order. An ideal value of 10^{-3} was selected for the convergence criterion. 4000-time steps were used with a time step size of 0.0005s for a more accurate result as the smallest mesh size in the whole domain was 0.0005m. The maximum number of iterations per time step was set to 20.

3.5 Solar Chimney Power Plant Validation

This section presents the geometric configurations, the mesh settings, setup and solution used in ANSYS Fluent for the validation of the solar chimney power plant. The results obtained from these configurations were validated using the experimental results obtained from the Manzanares plant in Spain.

3.5.1 Geometry Specifications

The geometry of the solar chimney power plant was constructed with reference to the Manzanares plant dimensions from Haaf et al. (1983), Haaf (1984a) and Cuce, Sen, and Cuce (2020). The dimensions utilized for the model sketch are displayed in Table 3.5.

Table 3.5: Axisymmetric Design Parameters of the Solar Chimney Power Plant

Design Parameters	Dimensions
Chimney Height	197 m
Chimney Diameter	5 m
Collector Radius	122 m
Mean Collector Height	1.85 m

3.5.2 ANSYS Fluent: Geometry Interface

The 2D axisymmetric model was imported into the ANSYS Fluent geometry interface in a "STEP" file. The model was sketched with the x-axis as the axis of rotation to enable the axisymmetric function. Figure 3.6 shows the geometry that was modelled and imported into the ANSYS Fluent geometry interface.

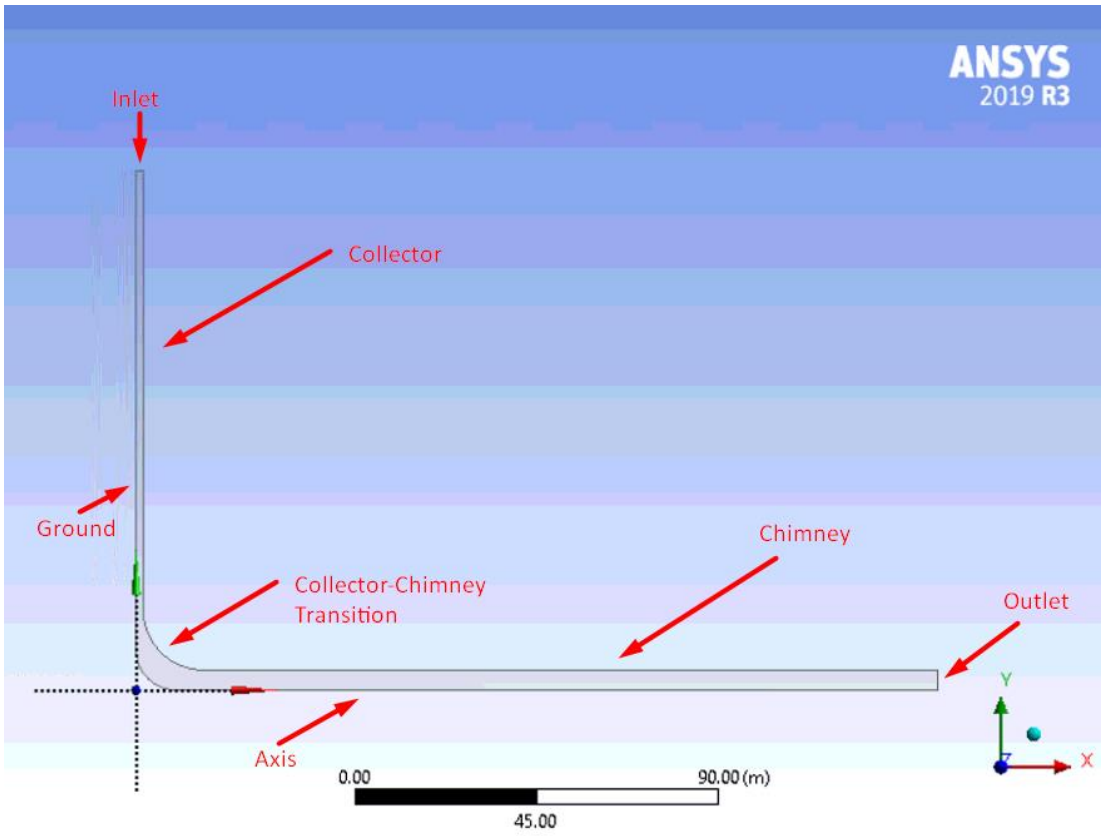

Figure 3.6: SCPP model in the Geometry Interface

3.5.3 ANSYS Fluent: Mesh Interface

This subsection presents the mesh settings used for the SCPP model. The mesh settings used has been tabulated in Table 3.6.

Table 3.6: Design Parameters for the Validation of the SCPP

Design Parameters	Dimensions
Mesh Type	Triangular
Element size	0.08 m
Number of elements	249696

The triangular mesh was adopted for the whole domain as the flow characteristics in the curved areas were vital for the analysis. Figure 3.7 and Figure 3.8 shows the model with the applied mesh.

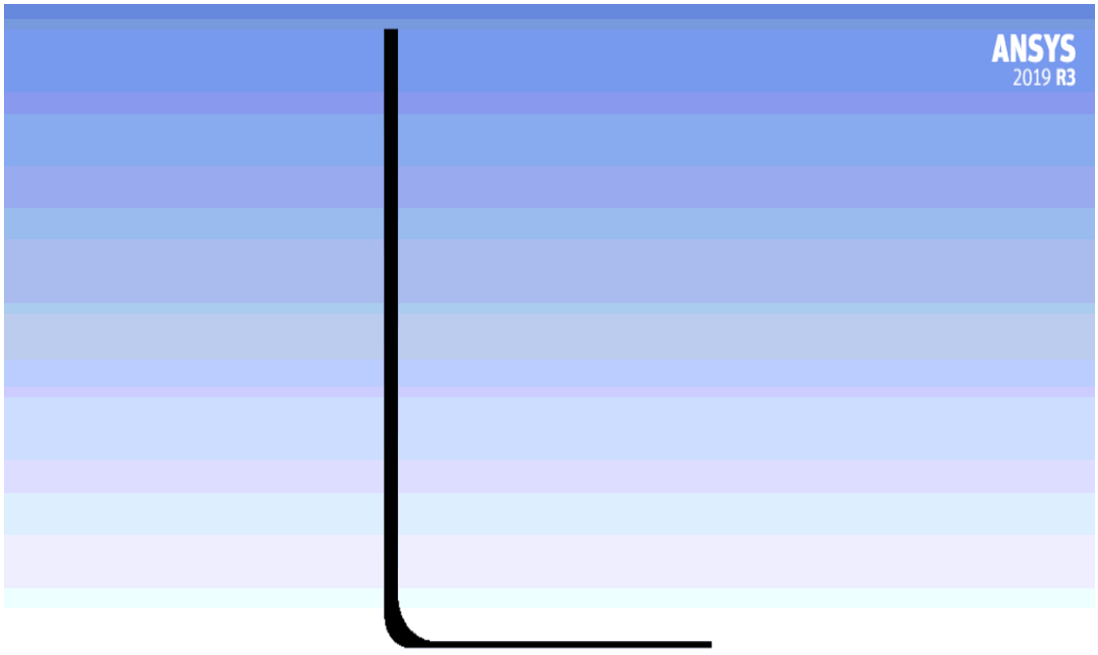

Figure 3.7: Common meshing for the whole SCPP domain

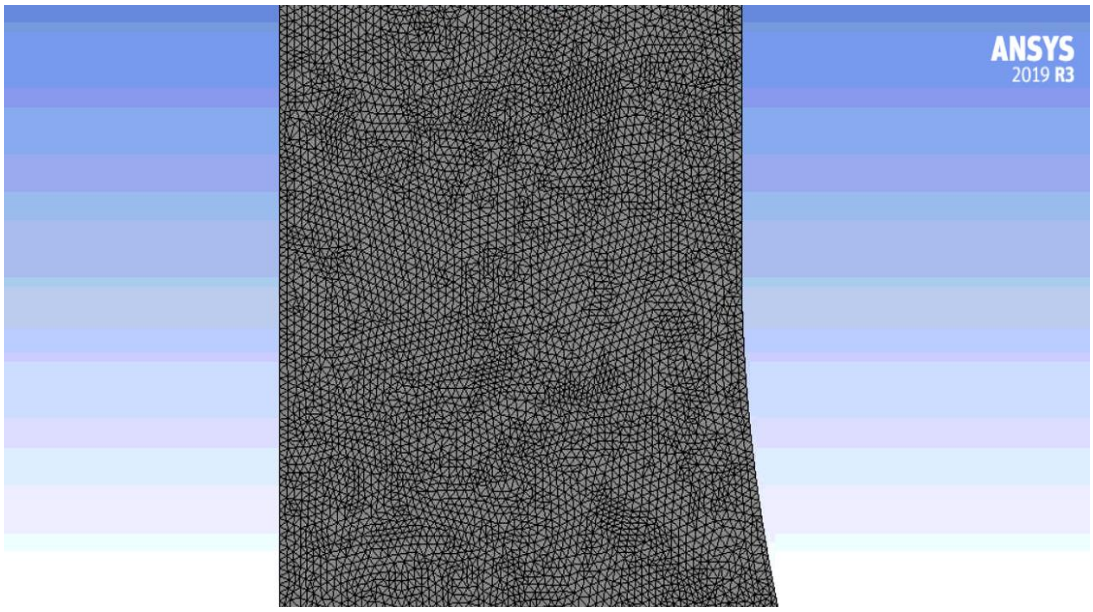

Figure 3.8: Triangular meshing used in the domain

3.5.4 ANSYS Fluent: Setup Interface

This subsection presents the setup and the boundary conditions applied to the SCPP domain for the validation. The pressure-based solver is chosen with a steady-state axisymmetric 2D space. Gravitational acceleration is applied at the x-axis at a value of -9.81 m/s. The energy equation was utilized to activate the thermal settings in Fluent. The RNG k-epsilon model with standard wall functions and full buoyancy effects were used for turbulent flow, while the Discrete Ordinates (DO) model was activated as the radiation model. The material properties adopted for the fluid and solid regions are listed in Table 3.7. The Boussinesq approximation was incorporated for the identification of the air density under the influence of temperature.

Table 3.7: Material properties for the SCPP Validation

Physical properties (unit)	**Air**	**Glass**	**Ground**	**Aluminium**
Density (kg/m3)	1.2046 (boussinesq)	2500	2160	2719
Specific heat capacity, Cp (j/kg-k)	1006.43	750	710	871

Thermal conductivity (W/mK)	0.0259	1.15	1.83	202.4
Viscosity (kg/ms)	1.7894e-5	-	-	-
Absorption Coefficient (1/m)	0.00331	0.03	0.9	0
Thermal Expansion Coefficient (1/k)	0.0034112	-	-	-
Refractive Index	1	1.516	1	1
Thickness (m)	-	0.004	0.5	0.00125

The operating pressure was set to an ambient pressure of 101325 Pa, while the operating temperature under the Boussinesq parameter was set to an ambient temperature of 293.15K. The boundary conditions considered in the CFD modelling is tabulated in Table 3.8. The heat transfer coefficient was calculated using equations obtained from Section 2.2.1. The turbulence length scale value was selected based on the natural convection type flow at the inlet and outlet.

Table 3.8: Boundary Conditions for SCPP Validation

Boundary Conditions	**Categories**	**Values**
Axis	Axis	• Nil

Chimney	Wall	• Momentum
		  ○ Stationary Wall
		  ○ No slip
		• Thermal
		  ○ Heat Flux = 0 W/m2
		  ○ Wall thickness = 0.00125m
		  ○ Material Name = Aluminium
		• Radiation
		  ○ BC Type = Opaque

Collector	Wall	• Momentum
		  ○ Stationary Wall
		  ○ No slip
		• Thermal
		  ○ Convection
		  ▪ Heat Transfer Coefficient = 10 w/m2-k
		  ▪ Free Stream Temperature = 293.15K
		  ▪ Wall thickness = 0.004m
		  ▪ Material Name = Glass
		• Radiation
		  ○ BC Type = Semi-transparent
		  ○ Direct Radiation = 1000 w/m2
		  ○ Beam Direction: X= -1

Ground	Wall	• Momentum
		  ○ Stationary Wall
		  ○ No-slip
		  ○ Sand-Grain Roughness Height (m) = 0.05
		• Thermal
		  ○ Heat Flux = 0 W/m2
		  ○ Wall thickness = 0.5m
		  ○ Material Name = Ground
		• Radiation
		  ○ BC Type = Opaque

Inlet	Pressure-inlet	• Momentum
		  ○ Gauge Total Pressure (Pa) = 0
		  ○ Turbulent Intensity = 5%
		  ○ Turbulent Length Scale (m) = 0.01
		• Thermal
		  ○ Total Temperature = 293.15K

Interior-Fluid area	Interior	• Nil

Outlet	Pressure-outlet	• Momentum
		  ○ Gauge Total Pressure (Pa) = 0
		  ○ Backflow Turbulent Intensity = 5%
		  ○ Backflow Turbulent Length Scale (m) = 0.01
		• Thermal
		  ○ Backflow Total Temperature = 293.15K

3.5.5 ANSYS Fluent: Solution Interface

This subsection presents "Solution Methods" used to validate the SCPP. The "SIMPLE" Scheme under the Pressure-Velocity Coupling was chosen to identify the interaction between pressure and velocity. Under "Spatial Discretization", the "Green-Gauss Cell-Based" is adopted for the gradient while the "PRESTO!" technique was used for the interpolation of pressure. The governing equations, momentum, turbulent model and energy equation, were discretized by the second-order upwind, while the Discrete Ordinates (DO) radiation model was discretized by the first-order upwind method. The solar calculator was used to incorporate the specific latitude and longitude of the Manzanares, Spain plant in the radiation model for the distinct calculation of the solar beam direction. Figure 3.9 displays the programmed solar radiation characteristics for the SCPP validation. An ideal value of 10^{-6} was selected for the convergence criterion.

```
/define/models/radiation/solar-calculator
Latitude (deg) [39]
Longitude (deg) [-3.37]
Timezone (+-GMT) [2]
North (X-direction) [1]
North (Y-direction) [0]
East (X-direction) [0]
East (Y-direction) [1]
Day [21]
Month [6]
Hour [13]
Minute [0]
Choose method ('no' for Fair Weather Conditions and 'yes' for Theoretical Maximum) [no]
Sunshine Factor [1]

Fair Weather Conditions:
  Sun Direction Vector:  X: -0.237349, Y: 0.295768, Z: -0.925304
  Sunshine Fraction: 1
  Direct Normal Solar Irradiation (at Earth's surface) [W/m^2]: 871.789
  Diffuse Solar Irradiation - vertical surface: [W/m^2]: 88.869
  Diffuse Solar Irradiation - horizontal surface [W/m^2]: 116.82
  Ground Reflected Solar Irradiation - vertical surface [W/m^2]: 92.3489
```

Figure 3.9: Programmed Latitude and Longitude of the SCPP

3.6 Energy Extractor Performance in SCPP for Diameter 0.25m

This section presents the methods used to analyze the performance of a 0.25m diameter Savonius wind turbine in the SCPP. Through the validation of the SCPP, a potential location, 9m from the centre of the plant, was identified for the turbine installation in the collector region. The geometrical dimensions, mesh, boundary conditions and

solving methods for the determination of the performance of the energy extractor in the SCPP are discussed in the following subsections.

3.6.1 Geometrical Dimensions

This subsection presents the computational domain used for the energy extractor analysis that was adopted from the turbine validation and subsequently modified to suit the current study. The diameter of the turbine was set to 0.25m. The length of the domain was set to 14D, while the width of the domain was set to match the height of the collector. The concept of the domain was created to simulate the collector region and potential turbine installation area at a minimal computational time. Figure 3.10 shows the domain used for the analysis. Figure 3.11 and Figure 3.12 shows an illustration of the Vertical Installation (V_{Ins}) and the Horizontal Installation (H_{Ins}) studied.

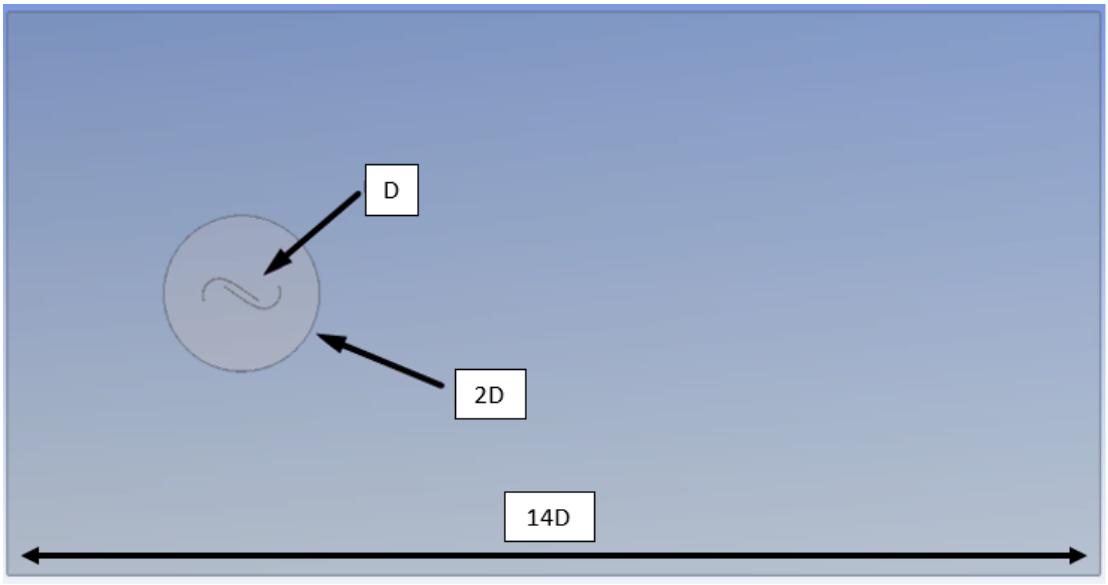

Figure 3.10: Computational Domain for the Energy Extractor Performance Analysis in the SCPP

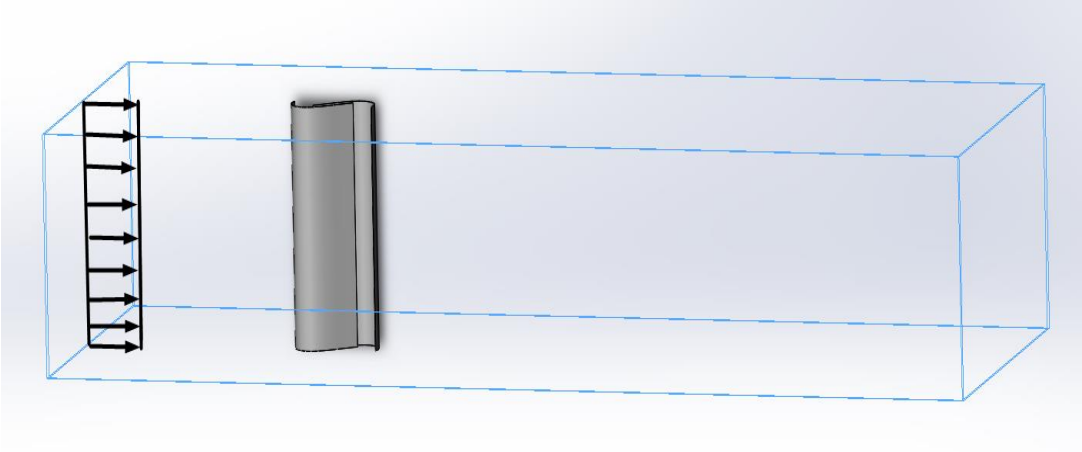

Figure 3.11: Vertical Installation

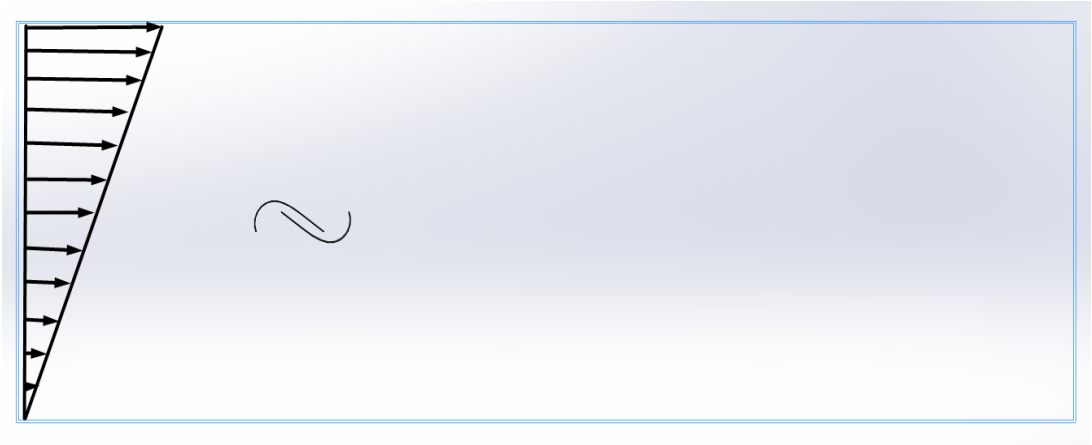

Figure 3.12: Horizontal Installation

3.6.2 Meshing, Setup and Solution Methods

The mesh settings that were incorporated in this analysis were adopted from the turbine validation. For the ANSYS Fluent Setup, the transient model in a 2D planar space was chosen. The SST k-omega turbulence model was considered. The fluid properties were based on the ambient temperature of 293.15K. The fluid in the circular domain cell zone region was set to motion with rotational velocity based on TSR 0.6, 0.8, 1.0 and 1.2. The boundary conditions for the domain in this analysis were adopted from the turbine validation and altered accordingly for the fluid flow characteristics and turbine performance study. These values have been tabulated in Table 3.9.

Table 3.9: Boundary Conditions for the Energy Extractor Performance in SCPP Analysis

Boundary Conditions	**Values**
Velocity-Inlet	• Velocity Magnitude = 7.88 m/s • Turbulence intensity = 5% • Turbulent Viscosity Ratio = 10
Pressure-Outlet	• Turbulence intensity = 5% • Turbulent Viscosity Ratio = 10
Outer Circular Domain	• Mesh Interface • Rotational Motion • Move relative to adjacent cell zone
Inner Circular Domain	• Mesh Interface • Rotational Motion • Move relative to adjacent cell zone
Turbine Blades	• Rotational Motion • Move relative to adjacent cell zone

The reference values for the determination of the coefficient of moment from the turbine blades were conditioned based on the inlet velocity and fluid air properties at the temperature of 293.15K. The solution method chosen to solve the pressure-velocity interaction is the “SIMPLE” scheme. The “Least Square Cell-Based” method is considered for the gradient computation, while the governing equations, pressure and transient formulation were discretized at the second order. The time step size of 0.0005s was chosen for a more accurate result based on the smallest cell size, while the number of time steps was set for a 2 seconds rotation analysis according to TSR 0.6, 0.8, 1.0 and 1.2.

3.7 Energy Extractor Performance at Chimney Divergence 1° and 2°

This section discusses the methods used to investigate the performance of the SSWT under the influence of 1° and 2° diverging chimneys. The dimensions of both the models were set to be the dimensions presented in Table 3.5, with the exception of the chimney divergence that is calculated from the chimney inlet. Figure 3.13 and Figure 3.14 presents the SCPP at 1° and 2° diverging chimneys, respectively. The models were developed in Solidworks and imported into the ANSYS Fluent Geometry interface. The Meshing, Setup and Solution settings applied for these two models were adopted from the SCPP Validation in Section 3.5. The velocity and pressure data obtained 9m from the chimney inlet of both 1° and 2° diverging chimney models were incorporated into the computational domain as explained in Section 3.6.2 for the energy extractor performance investigation.

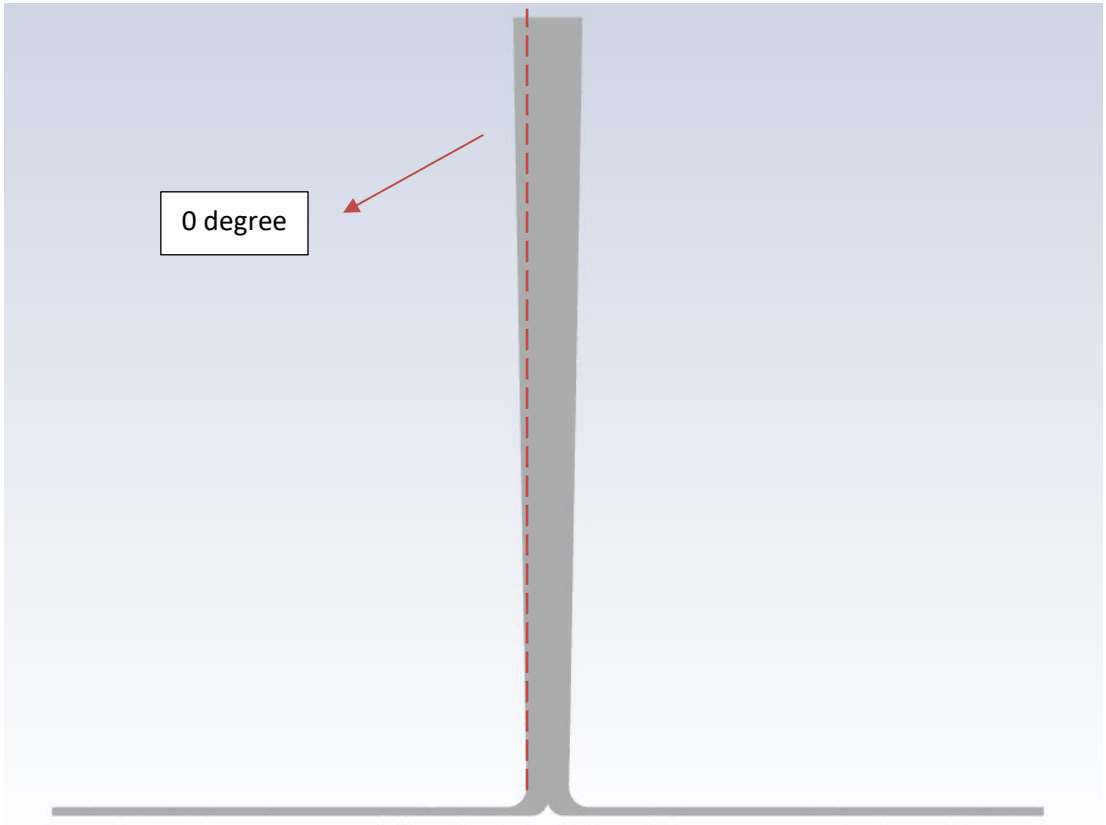

Figure 3.13: Solar Chimney Power Plant at 1° Chimney Divergence

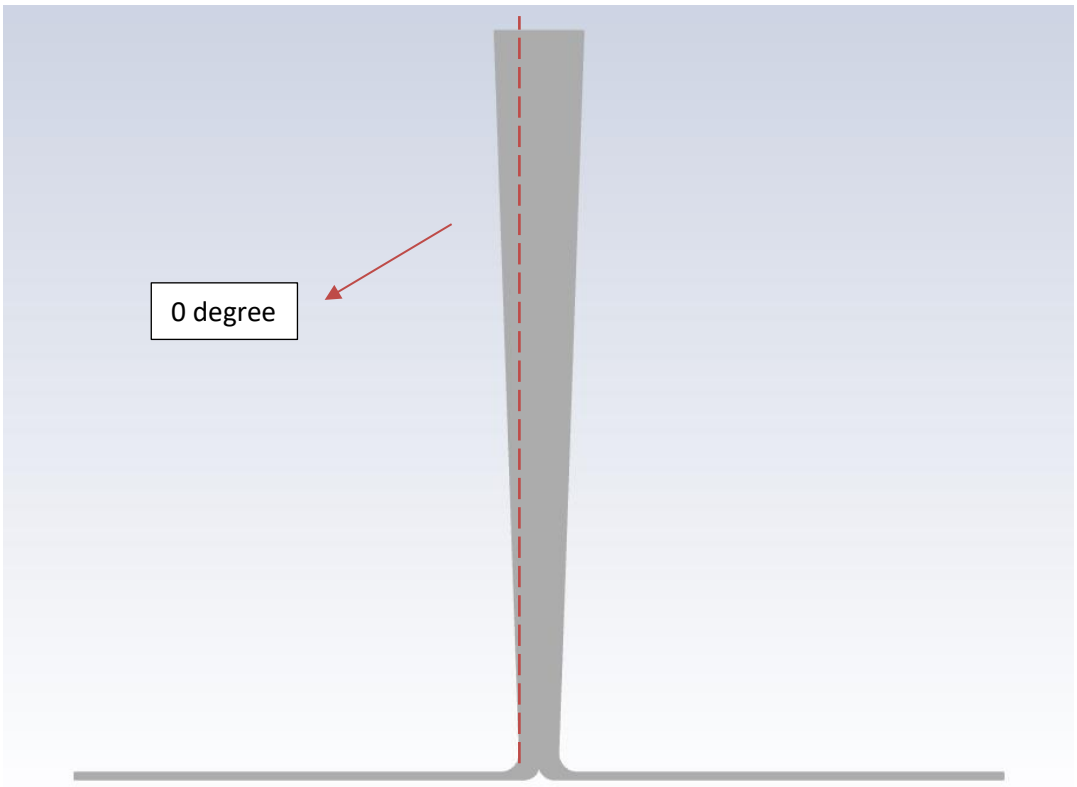

Figure 3.14: Solar Chimney Power Plant at 2° Chimney Divergence

3.8 Influence of the Guide Vanes on the Performance of the Energy Extractor

This section discusses the methods used to study the performance of the SSWT under the influence of guide vanes. The performance of the SSWT was determined based on the position of the guide vane, which works either as a guide vane or a deflector, and the angle of the guide vane with regards to the SSWT.

Table 3.10: Values of Parameters Used to Study the Performance of the Guide Vanes

Position	Function	Angle °
Relative to Advancing Blade	Guide Vane with Shield	0
		22.5
		45
Relative to Returning Blade	Deflector	140
		145
		150

Table 3.10 presents the angles used for the guide vane and the deflector for the performance study. Figure 3.15, Figure 3.16 and Figure 3.17 illustrate the guide vane with shield at was examined at angles 0°, 22.5° and 45°, while Figure 3.18, Figure 3.19 and Figure 3.20 show the deflectors investigated at angles 140°, 145° and 150°, respectively. The meshing, setup, and solution methods adopted for this analysis follows the settings mentioned in Section 3.6, where the velocity and pressure data input is that of the 0° chimney, while the rotational speed of the SSWT is that of TSR 0.8.

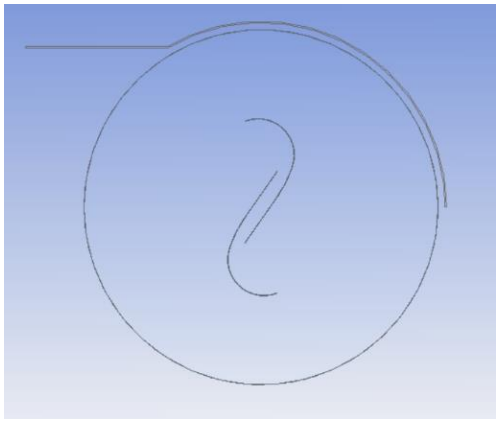

Figure 3.15: 0° Guide Vane with Shield (GVS 0°)

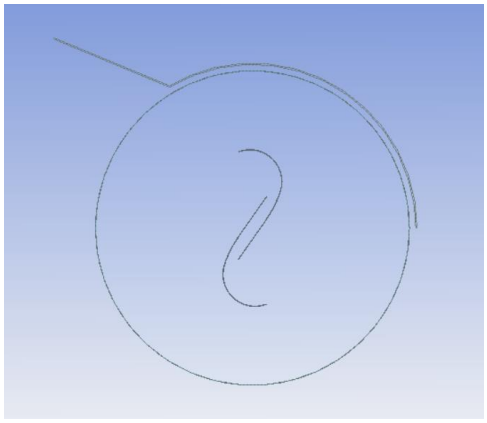

Figure 3.16: 22.5 ° Guide Vane with Shield (GVS 22.5°)

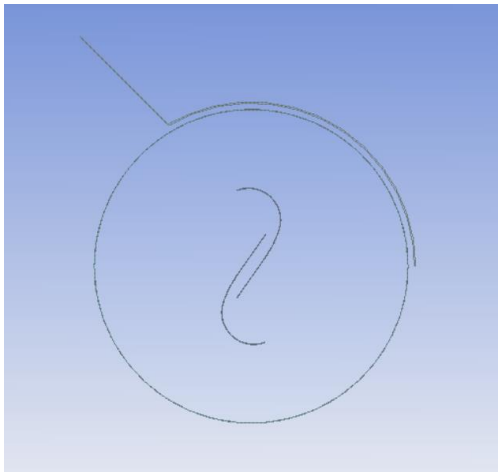

Figure 3.17: 45° Guide Vane with Shield (GVS 45°)

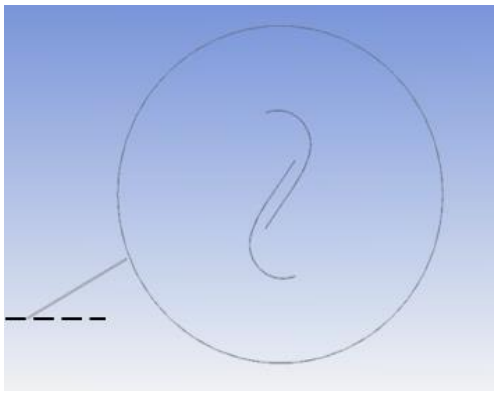

Figure 3.18: 150° Deflector (Def 150°)

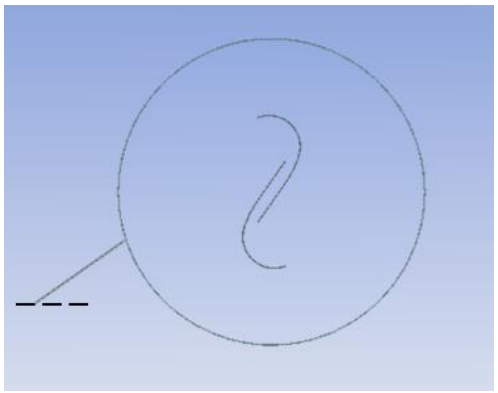

Figure 3.19: 145° Deflector (Def 145°)

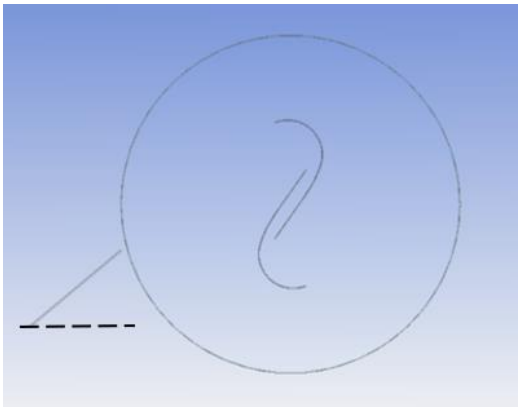

Figure 3.20: 140° Deflector (Def 140°)

3.9 Summary of Chapter 3

In this chapter, the governing equations of the SCPP with respect to the solar air collector, chimney, and turbine components that revolve around the system's physics was presented for further understanding. Aside from discussing the numerical stages involved in this analysis, the numerical methods incorporated for the SCPP validation and the proposed SSWT validation were also presented, where the performance of the SSWT at TSR 0.2, 0.4, 0.6, 0.8, 1.0 and 1.2 was validated, respectively. The approaches used to investigate the performance of the SSWT at chimney divergence 0°, 1° and 2° and under the influence of guide vanes were also discussed. The performance of the SSWT was evaluated at TSR 0.6, 0.8, 1.0 and 1.2 for the varying chimney angles and TSR 0.8 for the guide vanes.

CHAPTER 4
RESULTS AND DISCUSSION

4.0 Introduction

This chapter presents the results and potential reasons for the outcome of the analysis conducted. The turbine validation for TSR 0.2, 0.4, 0.6, 0.8, 1.0 and 1.2 are presented and discussed. The results from the validated SCPP model in steady-state are portrayed and discussed. Following these two validations, the performance analysis of the SSWT in the collector region at chimney divergence 0°, 1° and 2° are presented and discussed. Finally, the performance SSWT under the influence of guide vanes is evaluated with potential reasoning.

4.1 Turbine Validation Results and Discussion

This section presents the results obtained from the turbine validation for TSR 0.2, 0.4, 0.6, 0.8, 1.0 and 1.2. The quality of the mesh is ensured through the orthogonal quality and the skewness of the elements. A Grid Independence Test (GIT) was performed to determine the optimal grid structure with the smallest grid number with little difference in the simulation results. Figure 4.1 portrays the Grid Independence Test conducted for the turbine. The value of the coefficient of moment was observed to be consistent at $C_M \approx 0.39$. This value was consistent even at a greater number of elements. To reduce the computational time and cost, the grid size with the number of elements 437, 322 with $C_M = 0.39$ was chosen for further analysis.

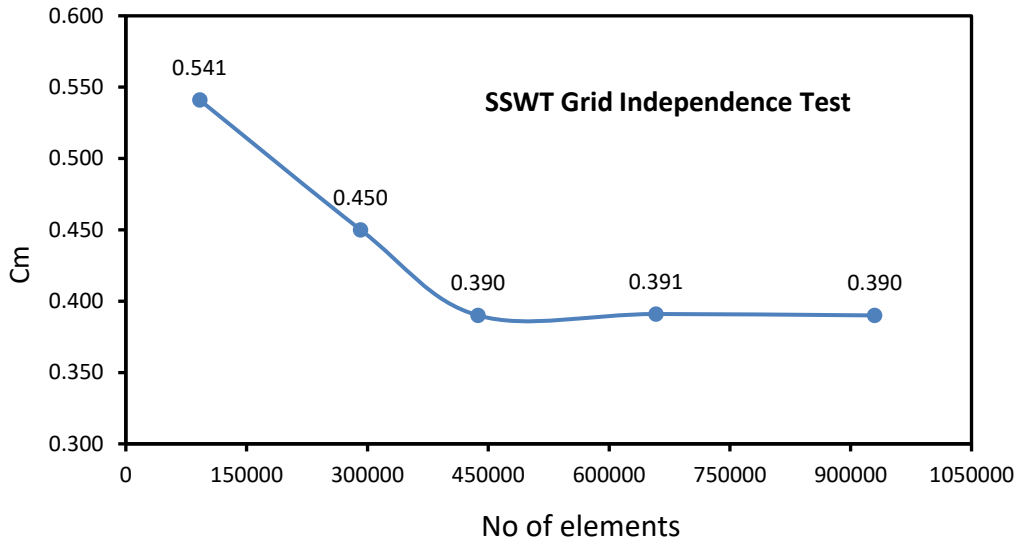

Figure 4.1: Turbine Validation Grid Independence Test

The average y+ value throughout the analysis was maintained at a value lesser than 1 for a low Reynolds-number resolution and for an accurate prediction of the wall friction and boundary layer detachment at the blade surface (Roy and Ducoin 2016). Figure 4.2 shows the average y+ value of the simulations.

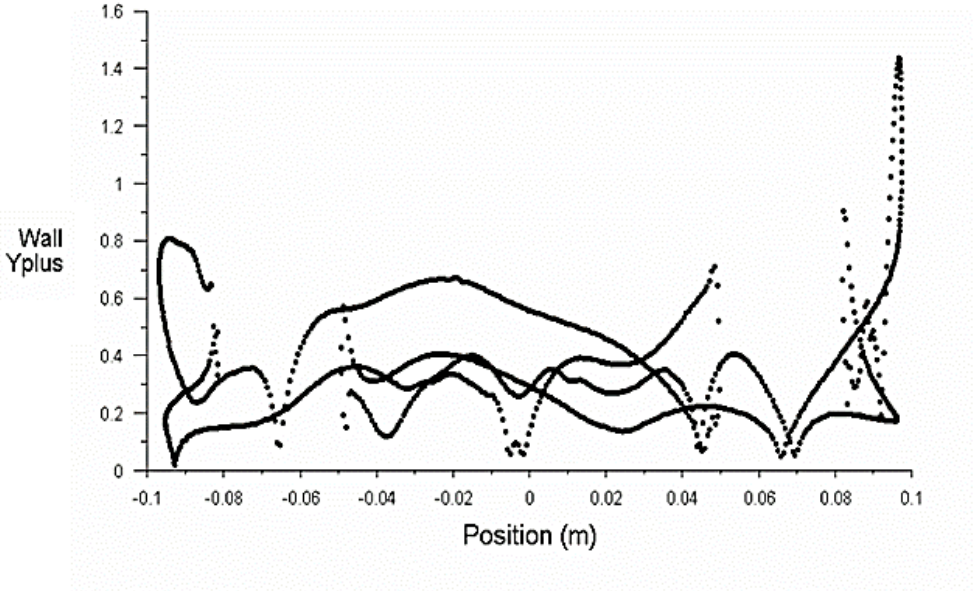

Figure 4.2: Average y+ value for turbine blades

The transient Unsteady Reynolds-Averaged Navier-Stokes (URANS) equation was performed at Reynolds number equivalent to 1.05×10^5. The turbine blades at each TSR were operated for a minimum of 12 rotations to ensure stability before analysing the flow parameters around the blades and the resultant coefficient of moment. The simulation results obtained for the validation were calculated based on the last four rotations of each simulation. The acquired results from the simulations at varying TSRs are validated against experimental data of Roy and Saha (2015) and simulation data of Roy and Ducoin (2016). Figure 4.3 shows the moment coefficient from each TSR validated against the previous experimental and numerical studies.

The outcome of the present turbine validation agrees with the results from previous literature (Roy and Saha 2015; Roy and Ducoin 2016). The cumulative percentage difference between the present validation and prior work was 4.85% and 16.82% against Roy and Saha and Roy and Ducoin respectively, indicating that the current validation model may be utilized for the present work. The trend presented is acceptable since external environmental conditions and different measuring

procedures in the experimental studies are expected to influence the outcome. The variations in the environmental temperature conditions in the experimental study may have affected the fluid's properties when the turbines were tested experimentally, thus causing some difference in the results as plotted in Figure 4.3.

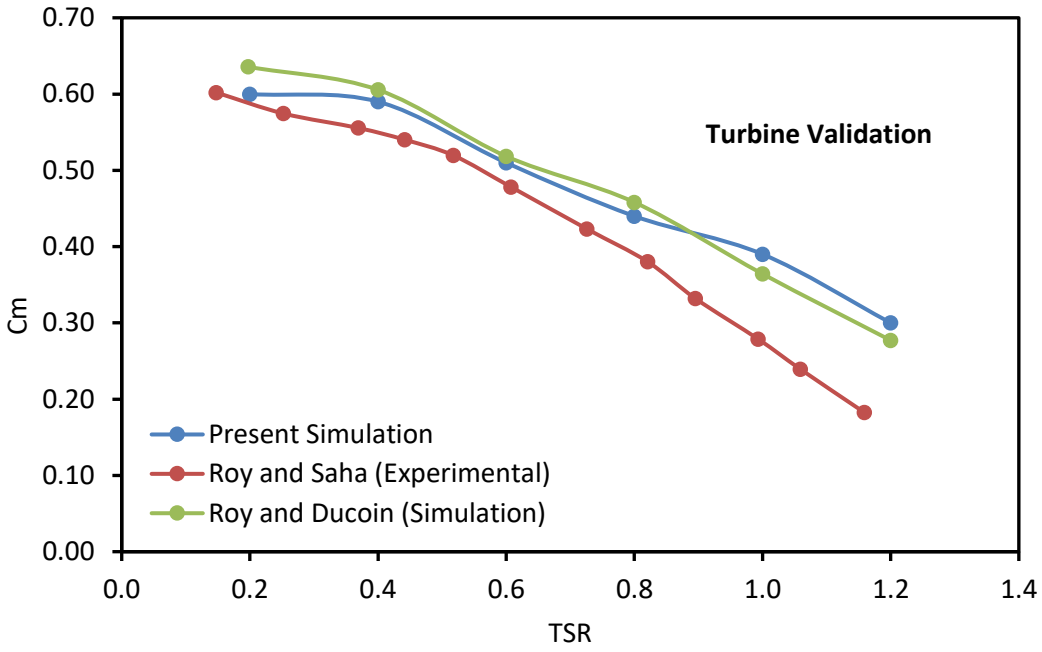

Figure 4.3: Turbine Validation Against Previous Studies

4.2 SCPP Validation Results and Discussion

This section presents and discusses the results obtained from the steady-state SCPP simulation. The full SCPP model was modelled in an axisymmetric manner about the x-axis considering its structure to reduce the computational time significantly. Geometries with different dimensions from a few studies were tested, and the dimensions and simulation approaches similar to Hu et al. (2016); Haaf et al. (1983) and Cuce, Sen, and Cuce (2020) were chosen.

Figure 4.4 shows the Grid Independence Test performed on the SCPP to acquire the optimal grid number required to reach minimal difference in the simulation results. The convergence velocity is attained at 13.2 m/s with 249696 number of elements in the GIT. This velocity value remained constant at a greater number of elements. Therefore, the mesh setting with element number 249696 was incorporated for following SCPP investigations to reduce the computational time and cost.

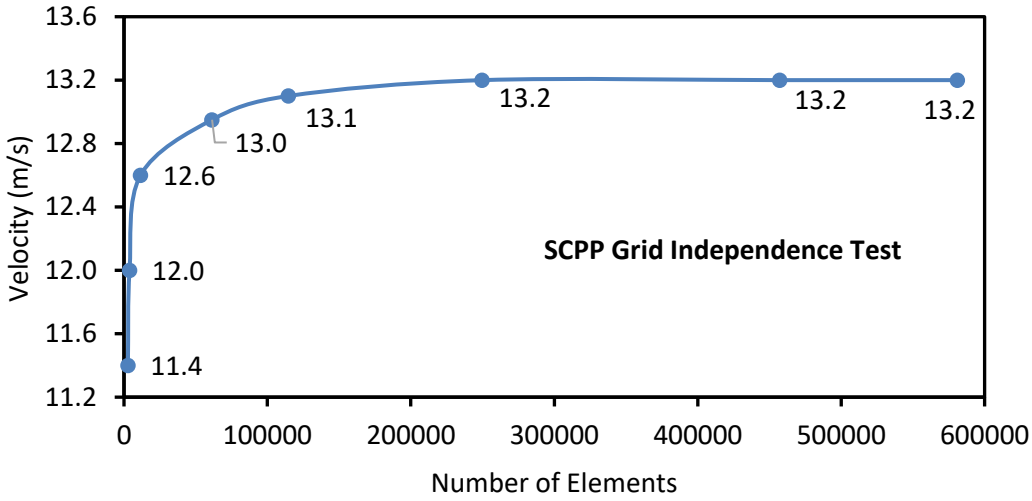

Figure 4.4: SCPP Validation Grid Independence Test

Table 4.1 summarizes the velocity and temperature rise values obtained from the SCPP. The velocity value at the chimney entrance of the simulated model was 13.2 m/s with a 12.0% error, while the temperature rise obtained was Δ 22°C with a 10% error against the Manzanares plant, respectively.

Table 4.1: Validation of the SCPP Simulation Model against the Manzanares Plant

Parameter	**Haaf (1983)**	**Present Simulation**	**Error %**
Chimney velocity (m/s)	15	13.2	12
Temperature rise (℃)	20	22.0	10

The velocity and temperature rise values were attained from the velocity and temperature contour respectively in which the contour were obtained from the numerical analysis as displayed in Figure 4.5 and Figure 4.6 presented in Section 4.2.1. The contributing factors for the difference in the validation results against the experimental results may be due to the changes in the environment. The 2-dimensional analysis, which does not include the effects from the circular collector, may have also given rise to the difference in the chimney velocity and the temperature difference. Aside from that, Haaf et al. (1983) discussed that “side winds” present during the experimental Manzanares investigation promoted convective losses from the plant to

the environment, while the atmospheric "temperature stratification", which varied with weather conditions, affected the pressure conditions at the chimney outlet, causing either an agreeable or disagreeable circumstances to the operating pressure itself.

Furthermore, due to the location of the Manzanares plant, the dust content present in the air did not only affect the amount of global radiation received by the plant but also resulted in lesser radiation absorbed by the air in the collector and the ground due to the dust settled on the collector sheet (Haaf et al. 1983). These external circumstances were not taken into account in the 2D SCPP, thus possibly contributing to the error in the upwind velocity and temperature rise that is achieved in this numerical analysis.

4.2.1 Velocity-Temperature Profiles for SCPP

This subsection presents the results from the validation of the SCPP. Figure 4.5 and Figure 4.6 show the velocity and temperature profile of the SCPP with mesh element size 0.08m. Figure 4.5 shows the potential area for the turbine installation in the collector- 9m from the plant's centre. Figure 4.6 shows the temperature rise in the collector sector with a minimal difference with the experimental values obtained from the Manzanares plant at solar intensity of 1000 W/m^2.

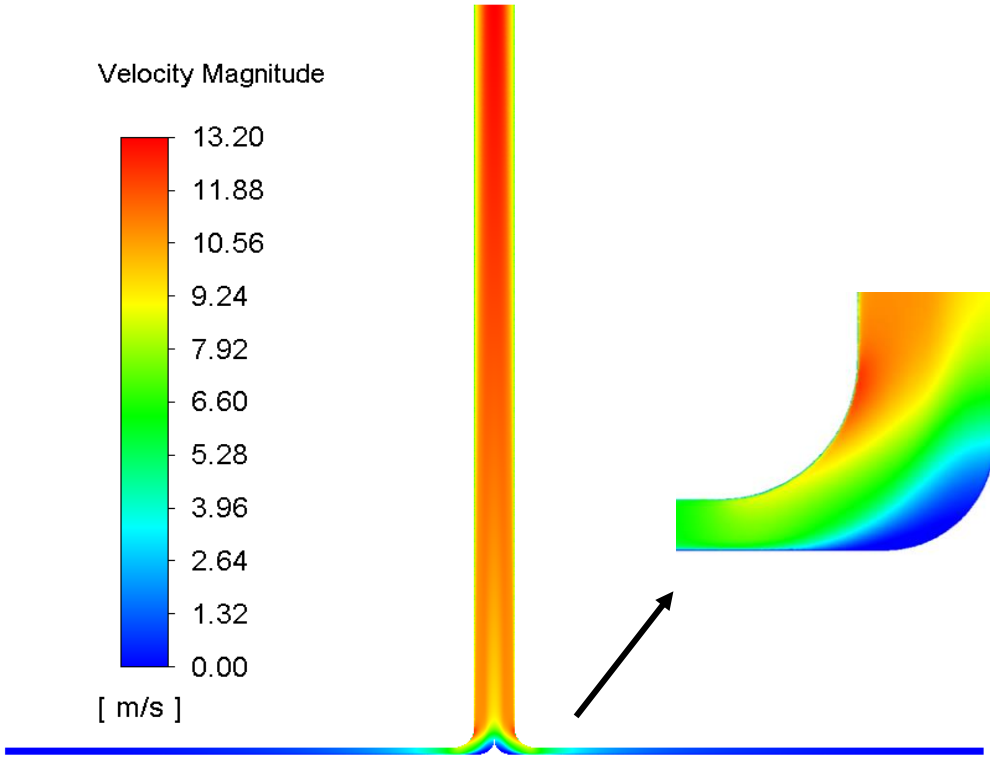

Figure 4.5: Velocity Profile for the SCPP

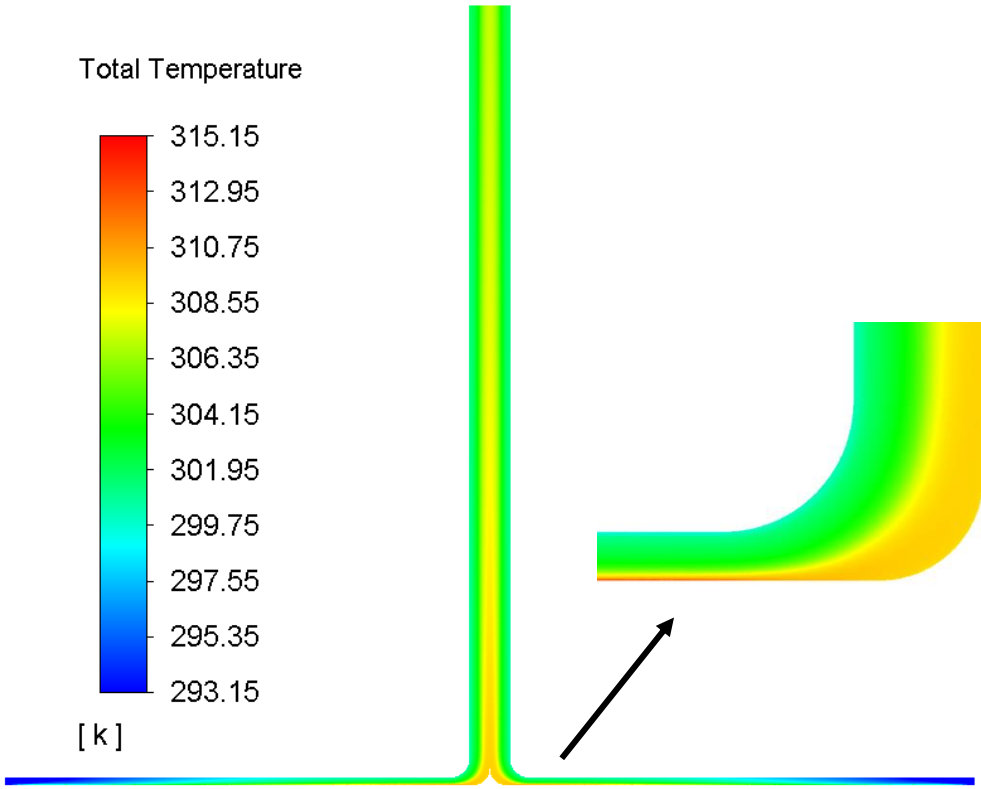

Figure 4.6: Temperature Profile for the SCPP

4.3 The Influence of Chimney Divergence on the Fluid Flow Properties

This subsection presents and discusses the effects of the chimney divergence at 1° and 2° on the fluid flow properties at $T = 293.15\ K$. The fluid flow properties, such as the velocity, temperature and pressure, were compared to the conventional chimney with 0° divergence. The velocity, temperature and pressure values 9m from the chimney based were identified. These values were incorporated into the SSWT performance analysis at three chimney divergence conditions of 0°, 1° and 2°.

4.3.1 Velocity Profiles of SCPP at 0°, 1° and 2° Chimney Divergence

Figure 4.7, Figure 4.8 and Figure 4.9 present the velocity profiles of the SCPP with 0°, 1° and 2° chimney divergence. The average velocity obtained 9m from the plant's centre increases with chimney divergence. At 1° chimney divergence, the velocity at the site of interest is enhanced by 72.84% compared to the cylindrical chimney with 0° divergence. At 2° chimney divergence, the average velocity increases by 23.40% compared to the 1° model and 114.21% compared to the 0° cylindrical chimney model.

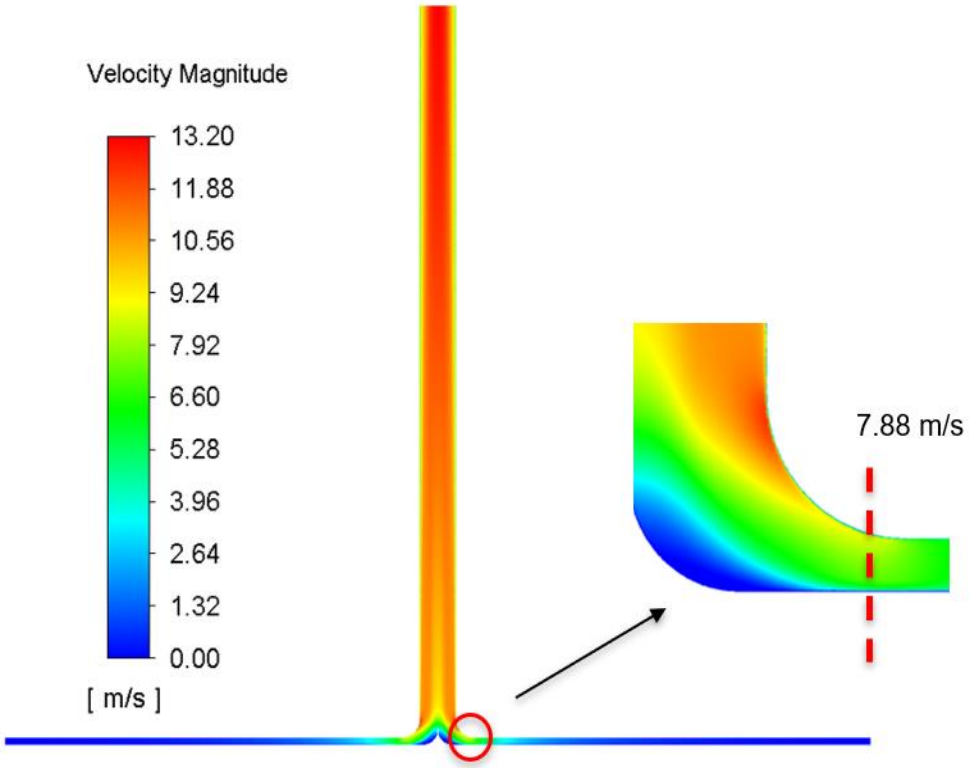

Figure 4.7: Velocity Profile of SCPP at 0° Chimney Divergence

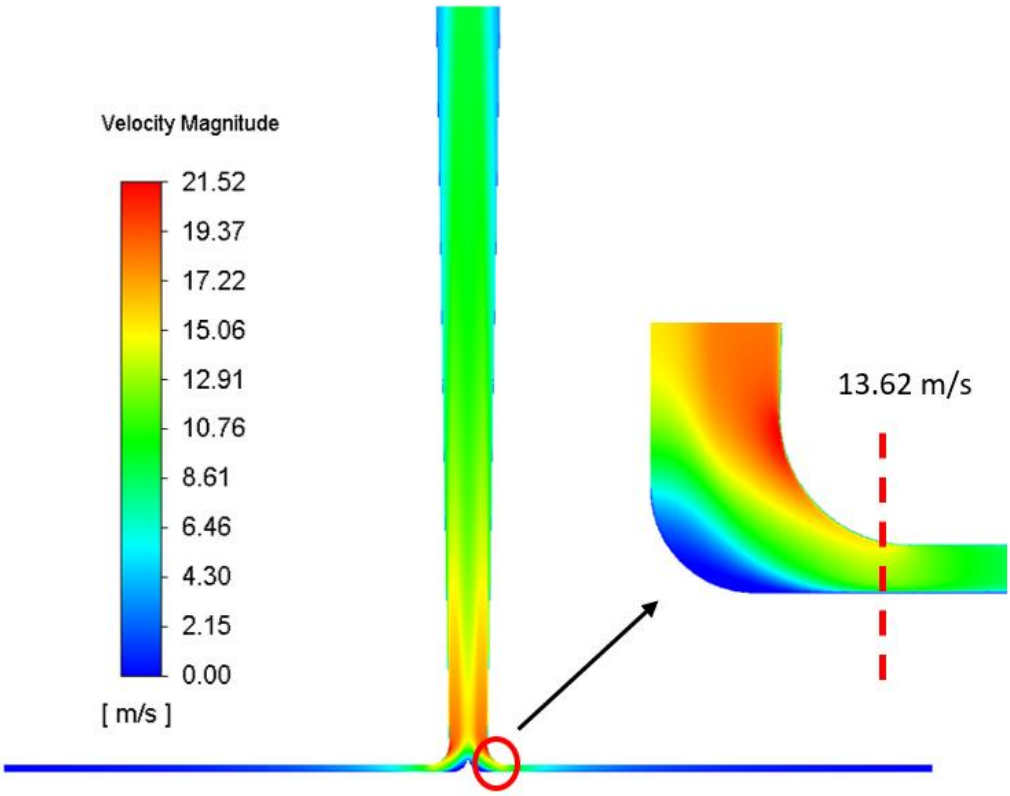

Figure 4.8: Velocity Profile of the SCPP at 1° Chimney Divergence

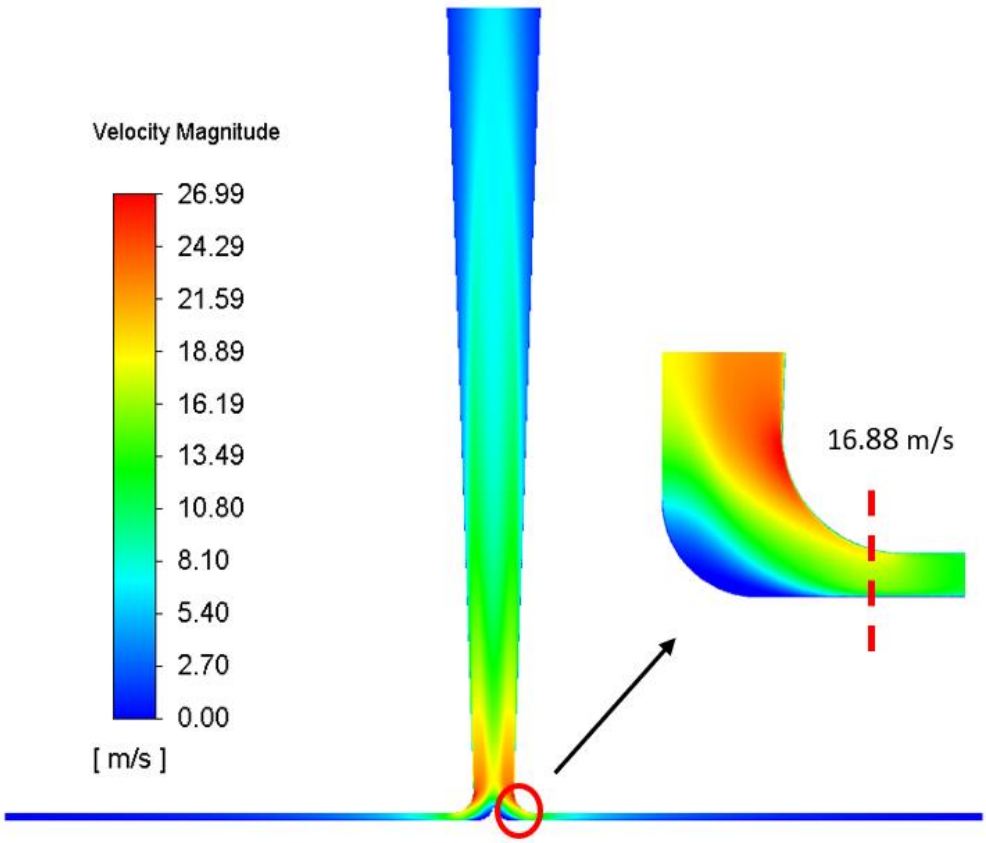

Figure 4.9: Velocity Profile of the SCPP at 2° Chimney Divergence

4.3.2 Temperature Profiles of SCPP at 0°, 1° and 2° Chimney Divergence

Figure 4.10, Figure 4.11 and Figure 4.12 present the temperature profiles of the SCPP with 0°, 1° and 2° chimney divergence. The temperature rise decreases with increasing chimney divergence. At 1° divergence, the temperature rise is 21.95% lesser than the cylindrical 0° chimney. At 2° divergence, the temperature rise is 2.69% lesser than the 1° chimney divergence model and 24% lesser than the cylindrical 0° chimney divergence model.

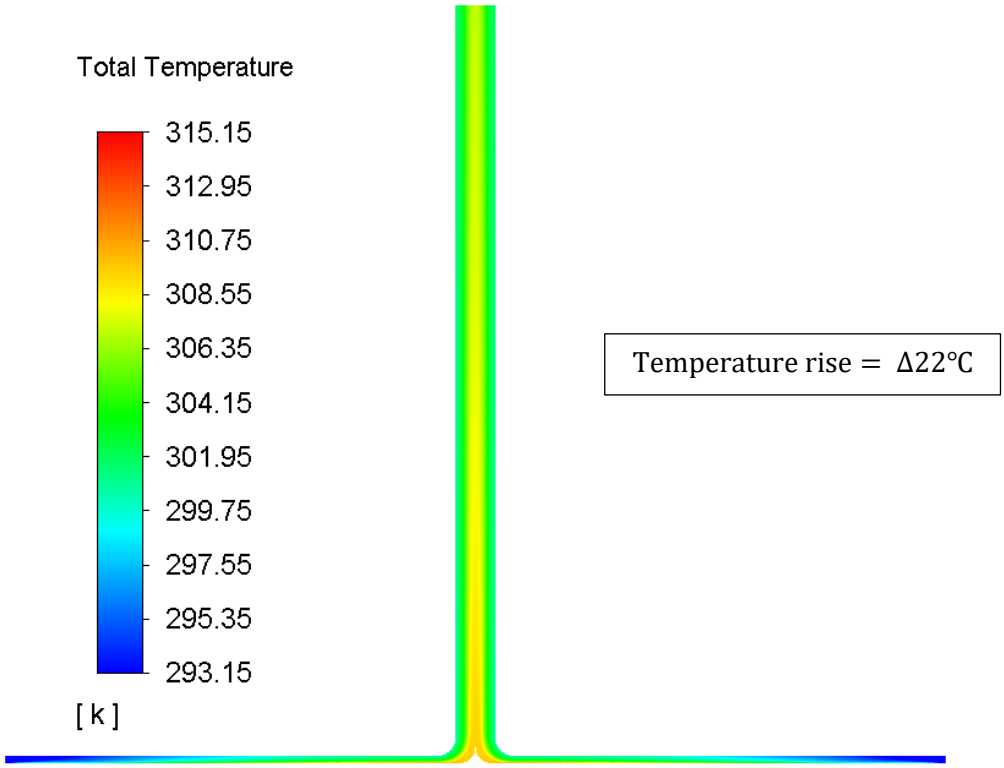

Figure 4.10: Temperature Profile of SCPP at 0° Chimney Divergence

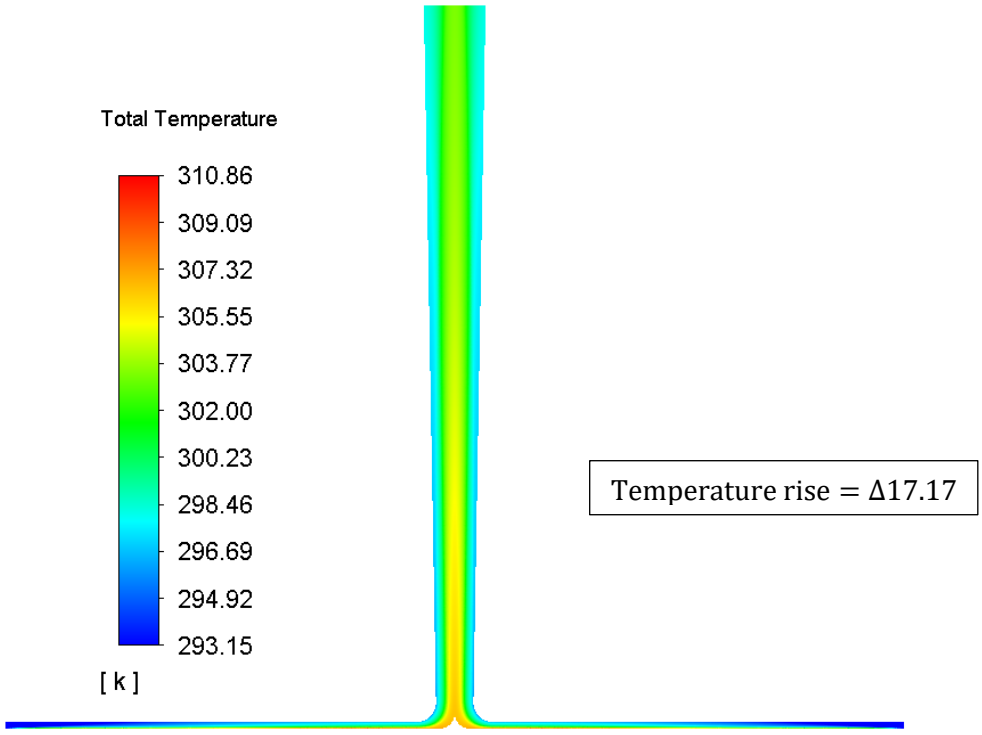

Figure 4.11: Temperature Profile of SCPP at 1° Chimney Divergence

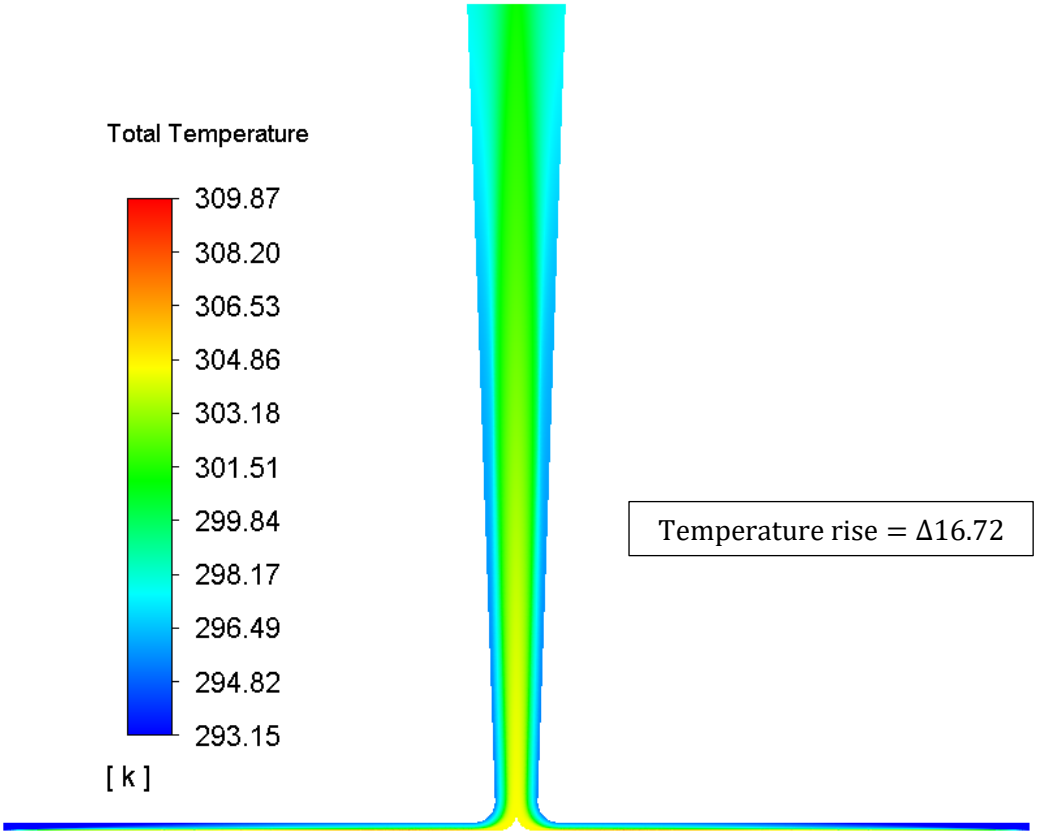

Figure 4.12: Temperature Profile of the SCPP at 2° Chimney Divergence

4.3.3 Pressure Profiles of SCPP at 0°, 1° and 2° Chimney Divergence

Figure 4.13, Figure 4.14 and Figure 4.15 present the static pressure profiles of the SCPP with 0°, 1° and 2° chimney divergence. The static pressure range is observed to increase with greater chimney divergence. At 1° chimney divergence, the pressure $(P_{b0} - P_{a0}) < (P_{b1} - P_{a1})$, while at 2° chimney divergence, $(P_{b2} - P_{a2}) > (P_{b1} - P_{a1}) > (P_{b0} - P_{a0})$. From observation, the larger chimney divergence decreases the pressure in the chimney region.

Sections 4.3.1, 4.3.2 and 4.3.3 demonstrate that increasing chimney divergence leads to velocity increase, temperature difference decrease, and static pressure range increase. The area of the chimney outlet is larger in diverging chimneys compared to the cylindrical chimney (0° divergent chimney). Figure 4.7, Figure 4.8 and Figure 4.9 show the flow area's effect on the mass flow rate, where a higher velocity region is observed at the chimney inlet for chimneys with larger divergent angles than the cylindrical constant-area chimney. The increase in the chimney exit area increases the

mass flow rate in the system, resulting in a greater velocity region at the chimney entrance that maintains a conserved mass flow rate.

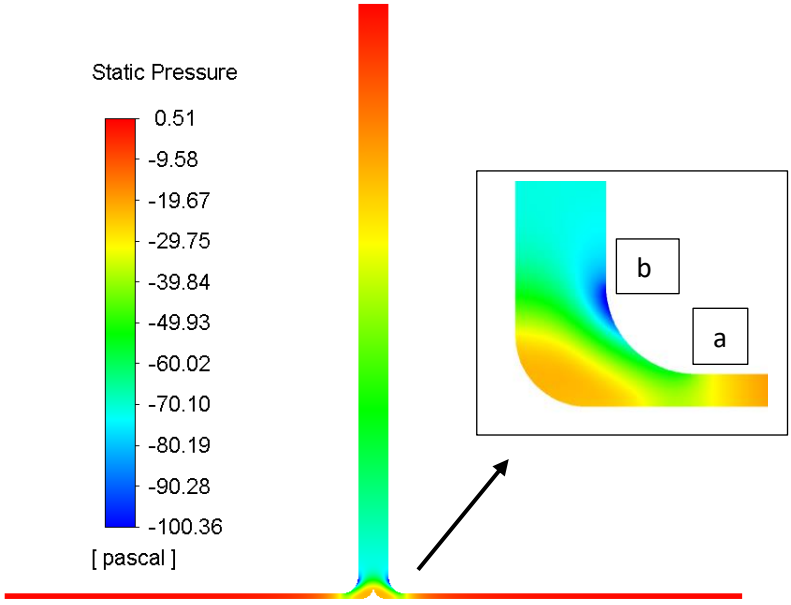

Figure 4.13: Pressure Profile of SCPP at 0° Chimney Divergence

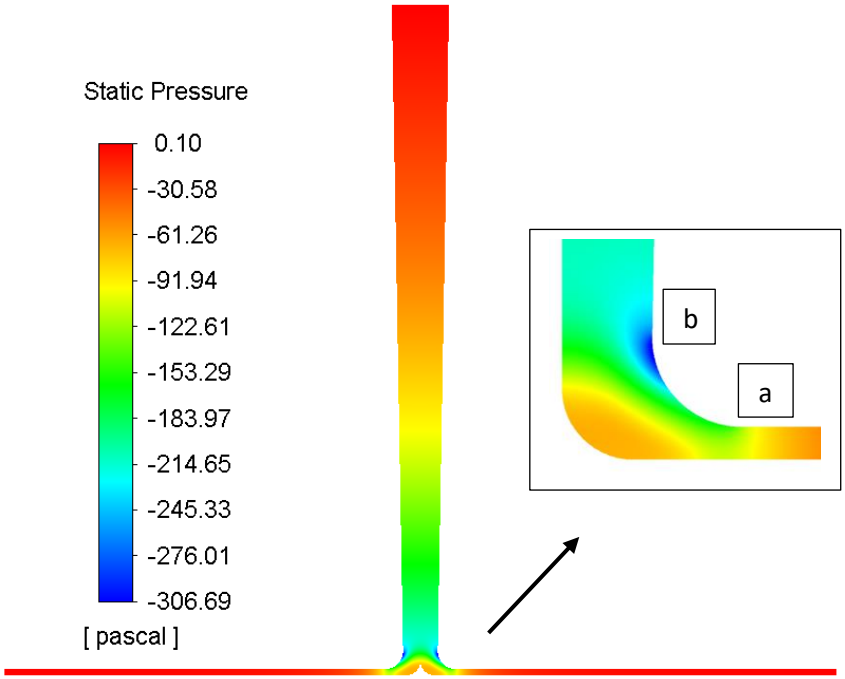

Figure 4.14: Pressure Profile of SCPP at 1° Chimney Divergence

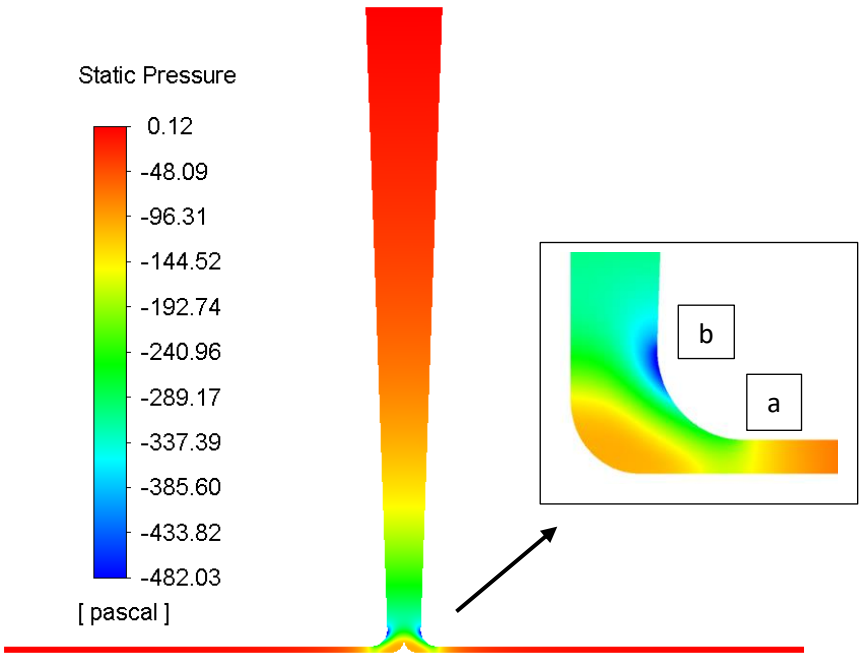

Figure 4.15: Pressure Profile of the SCPP at 2° Chimney Divergence

Next, from Figure 4.10, Figure 4.11 and Figure 4.12, the temperature rise values are observed to decrease with an increasing chimney exit area. According to the principle of conservation of energy, a higher mass flow rate would result in a lower temperature rise for an equal amount of energy input. According to the law of conservation of mass, the fluid flow requires less acceleration to move from the chimney entrance to the diverging chimney outlet compared to the standard cylindrical chimney with 0° divergence. This results in a lower pressure gradient across the diverging chimney. Thus, this occurrence is more prominently seen in the 2° diverging chimney compared to the 1° diverging chimney and subsequently, the cylindrical chimney with 0° divergence as shown in Figure 4.13, Figure 4.14 and Figure 4.15.

Gannon and von Backstro¨ m (2003) inferred that the appropriate expansion of the chimney outlet reduces the kinetic energy loss, where the dynamic pressure converts into static pressure for greater power augmentation. However, the increase in divergence beyond 3 degrees is suggested to decline the power output, which may result from boundary layers separation at the chimney walls (Hu, Leung and Chen 2017). The outcome presented in this section agrees with the study performed by Koonsrisuk and Chitsomboon (2013) and Zuo, Dai, et al. (2020), which inferred that diverging chimney increases static pressure, mass flow rate and power augmentation. The velocity and pressure data obtained from all three chimney models were extracted and applied to the test domain of the following sections to identify the performance of

the SSWT in a conventional cylindrical chimney compared to that under the influence of diverging chimneys.

4.4 0° Divergence - Performance Analysis of the Turbine under Vertical Installation and Horizontal Installation

This section presents the results obtained from the analysis of the SSWT at TSR 0.6, 0.8, 1.0 and 1.2 under the influence of the 0° chimney divergence for the V_{Ins} and H_{Ins}, respectively. The moment coefficient, performance coefficient, and power output of the turbine are demonstrated and discussed. The instantaneous moment coefficient and performance coefficient for one complete turbine rotation for both configurations are compared and studied at TSR 0.8, respectively. The difference between the turbine configurations is analysed through the velocity and pressure profiles at TSR 0.8.

4.4.1 C_m, C_p and Power Output for V_{Ins} and H_{Ins} at 0° Divergence

Figure 4.16 presents the moment coefficient of the V_{Ins} and H_{Ins} at TSR 0.6, 0.8, 1.0 and 1.2 for a 0° chimney divergence SCPP model. The values of the coefficient of moment decrease with increasing TSR for both configurations. The highest coefficient of moment is noticed at TSR 0.6 with a value of 0.53 under the H_{Ins}, while the lowest coefficient of moment is noticed at TSR 1.2 with a value of 0.24 under the V_{Ins}. The H_{Ins} shows a slightly higher moment coefficient compared to the V_{Ins}. The distributed free stream velocity flow in the V_{Ins} causes an equal amount of force exerted on both the advancing and returning blade. As a result, higher negative torque is produced by the returning blade compared to the H_{Ins}.

The generation of high negative torque is a known problem in the operation of the Savonius that reduces the overall torque produced by the rotor. However, the non-distributed free stream velocity flow in the H_{Ins}, results in a higher velocity flow attack on the advancing blade, while having a relatively low velocity impact on the returning blade. Consequently, the negative torque created by the returning blade is lesser than that of the advancing blade, resulting in a higher total produced torque compared to the V_{Ins}. Therefore, the different impacts on the advancing and returning blade in both configurations may have caused the H_{Ins} to exert a higher moment than the V_{Ins} at all TSR values.

Figure 4.17 presents the performance coefficient of the V_{Ins} and H_{Ins} at TSR values 0.6, 0.8, 1.0 and 1.2 for the 0° chimney divergence. The performance of the H_{Ins} is observed to be better than the V_{Ins}. The highest performance coefficient value is observed at TSR 0.8 under the H_{Ins} with a value of 0.37, which is 2.78% higher than the V_{Ins}. In contrast, the lowest performance coefficient is obtained at TSR 1.2 under the V_{Ins} with a value of 0.29, which is 3.45% lower than H_{Ins}. The higher performance of the H_{Ins} compared to the V_{Ins} is an influence of the torque generation in both configurations.

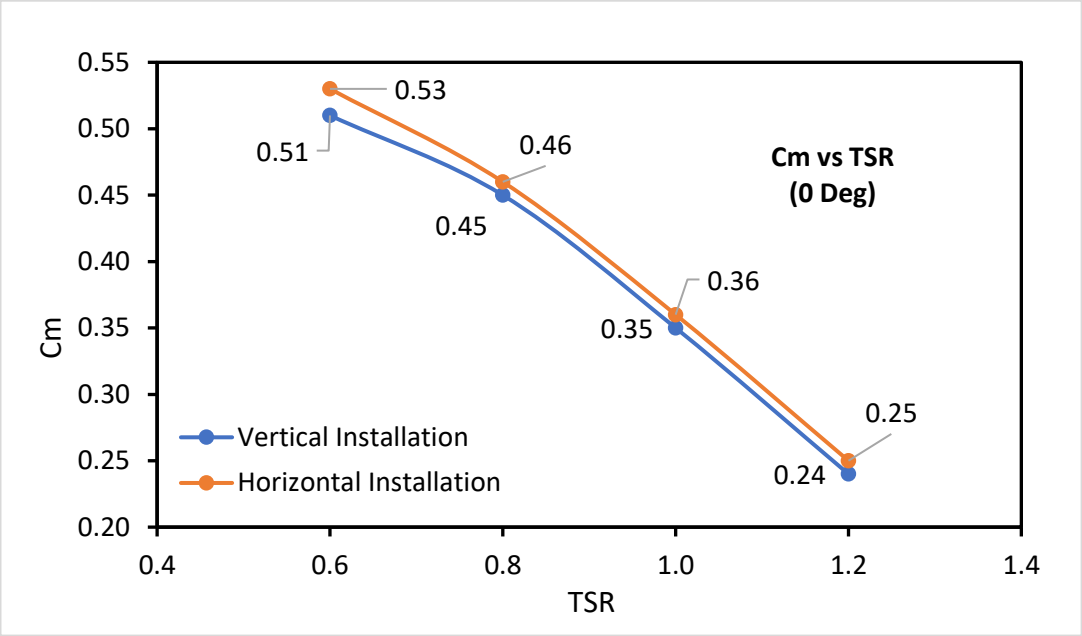

Figure 4.16: Coefficient of Moment for the Vertical and Horizontal Installation at 0° Chimney Divergence

In both configurations, the performance increases from TSR 0.6, peaks at TSR 0.8 and reduces thereafter till TSR 1.2. Thus, the optimal performance for both configurations is observed under TSR 0.8. The finding in this study is consistent with previous studies, in which the optimal coefficient of power was experimentally proven to be in the range of TSR 0.75 to TSR 0.82 (Hassanzadeh, Mohammadnejad and Mostafavi 2021; Roy and Saha 2015; Roy 2014; Chan, Bai and He 2018; Fujisawa and Gotoh 1994).

The tip speed ratio (TSR) of a wind turbine is the ratio between the incoming free stream velocity and the speed of the tip of the turbine blade. Therefore, the greater the speed of the turbine, the higher the tip speed ratio. At TSR 0.8, the free stream velocity

dominates the rotational speed of the turbine blades. During this occurrence, the drag contribution is significantly higher than TSR 0.2-0.6 and TSR 1.0-1.2. Since the Savonius turbine works based on the drag principle, it experiences the optimum performance at TSR 0.8.

Moreover, for the chosen Savonius blade design, the lift contributing factor has been modified and enhanced, thus improving its performance compared to a conventional Savonius turbine design (Roy and Ducoin 2016). Above TSR 1.0, the drag force acting on the blade reduces since the incoming free stream velocity is now equivalent to or higher than the rotational speed of the turbine blade. The rotational speed, in turn, dominates the free stream velocity at TSR 1.2, causing a poorer drag formation on the rear side of the advancing blade. For these reasons, the VAWT has a better starting ability compared to the HAWT (Alom and Saha 2019).

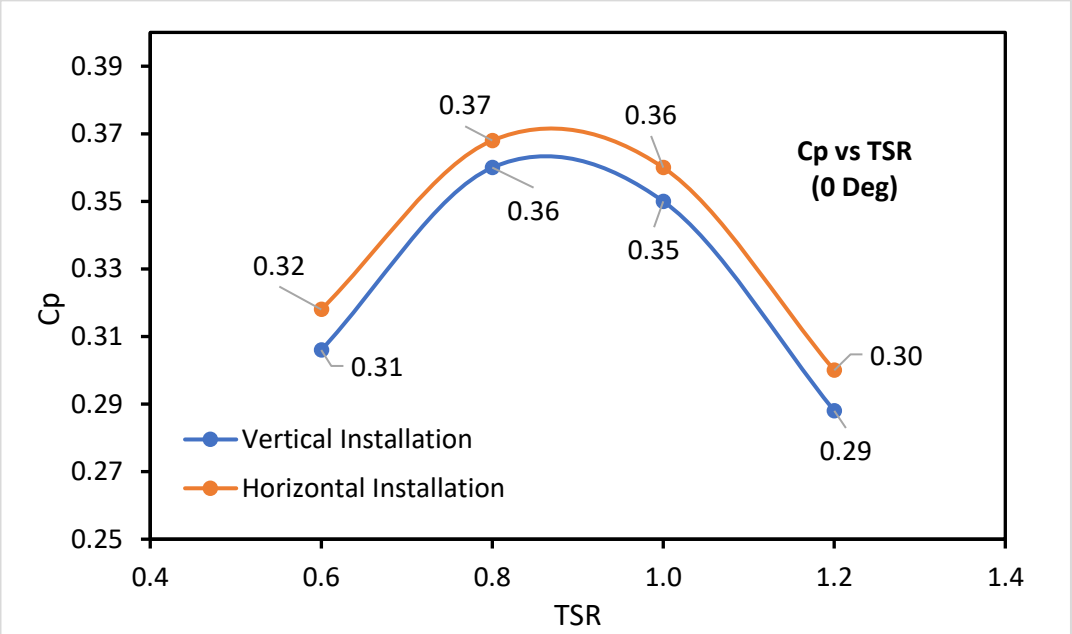

Figure 4.17: Coefficient of Performance for the Vertical and Horizontal Installation at 0° Chimney Divergence

Figure 4.18 presents the power generated for the V_{Ins} and H_{Ins} at TSR 0.6, 0.8, 1.0 and 1.2 in the cylindrical 0° divergent chimney. The outcome shows that the H_{Ins}'s power generation is slightly higher than the V_{Ins} for all TSR values. The H_{Ins} produces the highest power at a value of 27.11 W, 2.22% greater than V_{Ins} at TSR 0.8. In comparison, the V_{Ins} generated the lowest power with a value of 21.22 W at TSR 1.2, 4.15% lower than H_{Ins}.

Based on the discussion on the moment coefficient and the performance coefficient above, the H_{Ins} may have experienced increased torque and performance due to the non-distributed flow present in the configuration. The total torque available from the V_{Ins} and H_{Ins} influences the power generated by the turbine. Consequently, a higher generated power may have been demonstrated by the H_{Ins} than the V_{Ins}.

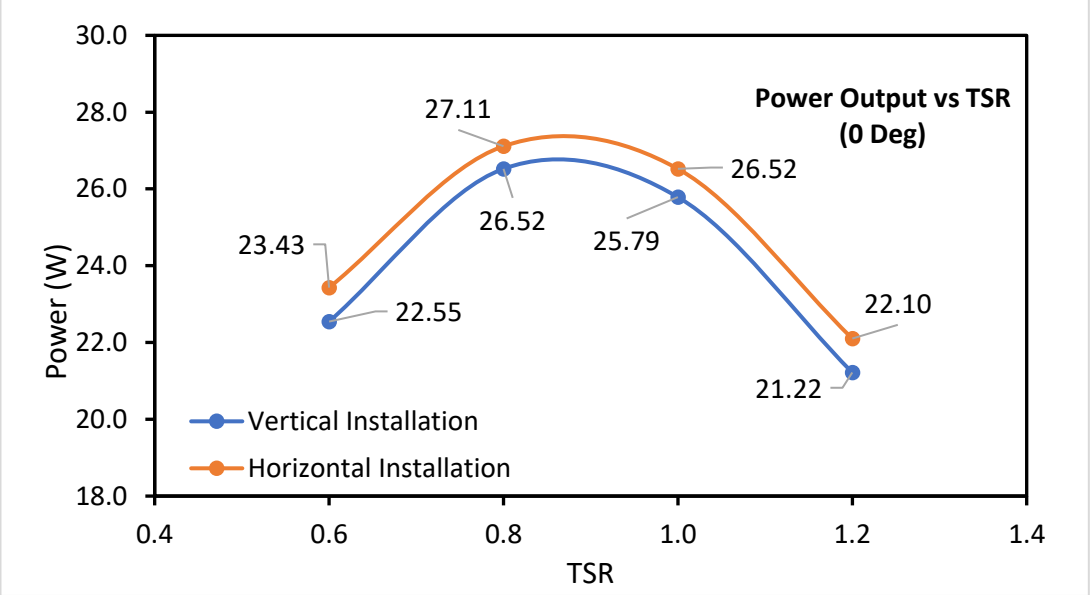

Figure 4.18: Power Output for the Vertical and Horizontal Installation at 0° Chimney Divergence

4.4.2 Instantaneous C_m and C_p for V_{Ins} and H_{Ins} at 0° Chimney Divergence

Figure 4.19 presents the instantaneous moment coefficient of the V_{Ins} and H_{Ins} at 0° chimney divergence. The H_{Ins} shows a higher amplitude from 20 degrees to 80 degrees and 200 degrees to 240 degrees which suggests a higher moment generation at these azimuth angles compared to the V_{Ins}. The blade design is suggested to have a higher lift contribution at these angles, thus working as a lift device. Beyond these angles, the blade acts as a drag device. Thus, the higher velocity attacking the advancing blade in the H_{Ins} may have influenced a higher lift generation compared to the advancing blade in the V_{Ins}.

Figure 4.20 presents the instantaneous performance coefficient of the V_{Ins} and H_{Ins} at 0° chimney divergence. The H_{Ins} shows a higher performance with a larger amplitude compared to the V_{Ins} at 20 degrees to 80 degrees and 200 degrees to 240 degrees. As reflected in Figure 4.19, a higher torque generation was suggested at these azimuth

angles due to the lift contribution resulting from the blade's aerodynamic design. Consequently, the higher performance experienced by the H_{Ins} may have been the influence of the higher torque generation at these mentioned azimuth angles.

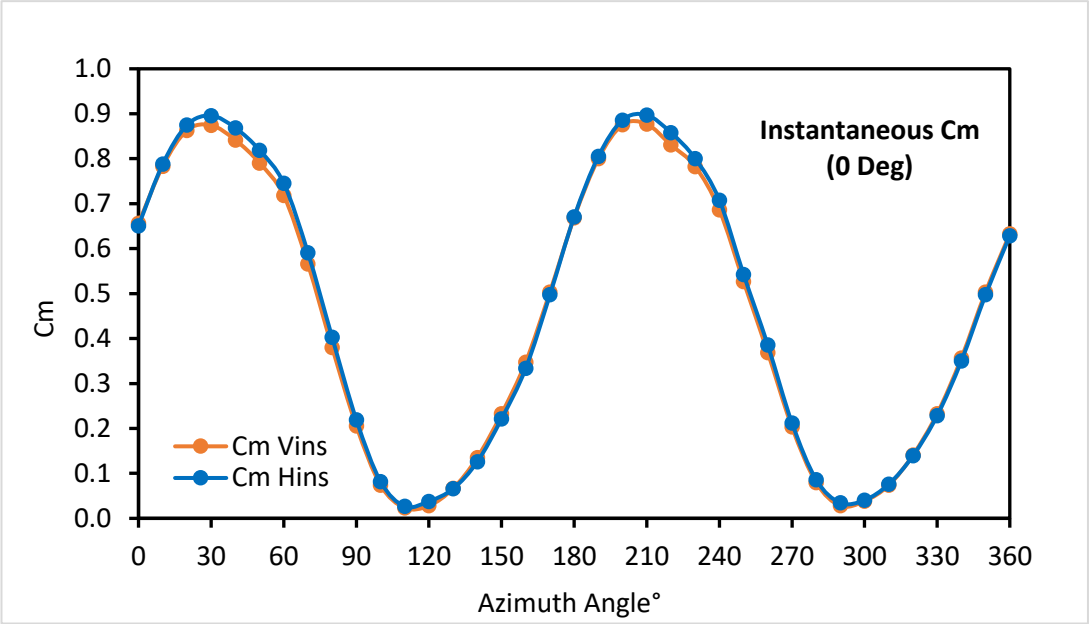

Figure 4.19: Instantaneous C_m at 0° Chimney Divergence

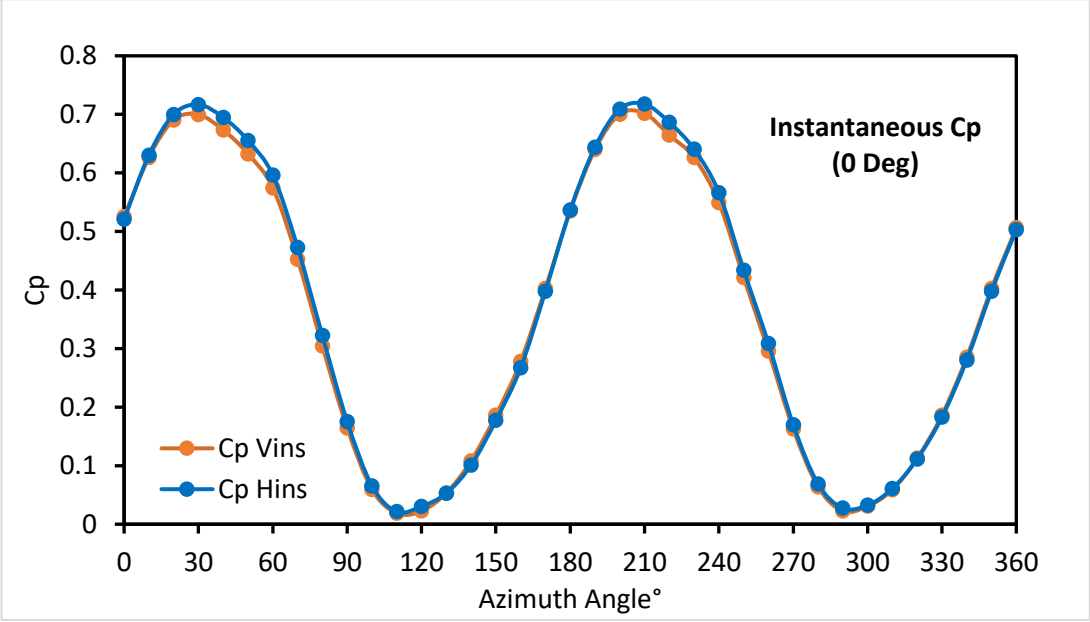

Figure 4.20: Instantaneous C_p at 0° Chimney Divergence

4.4.3 Velocity-Pressure Profiles at TSR 0.8 for Azimuth Angle, $\emptyset = 0°$

Figure 4.21 presents the velocity and pressure profiles for the V_{Ins} and H_{Ins} at an azimuth angle of 0°. In both configurations, a higher velocity region can be observed

at the convex of the advancing blade. This is due to a Coanda flow like effect. Coanda flow is the tendency of a fluid jet to remain attached to a convex surface due to a low-pressure region that results in a suction-like effect.

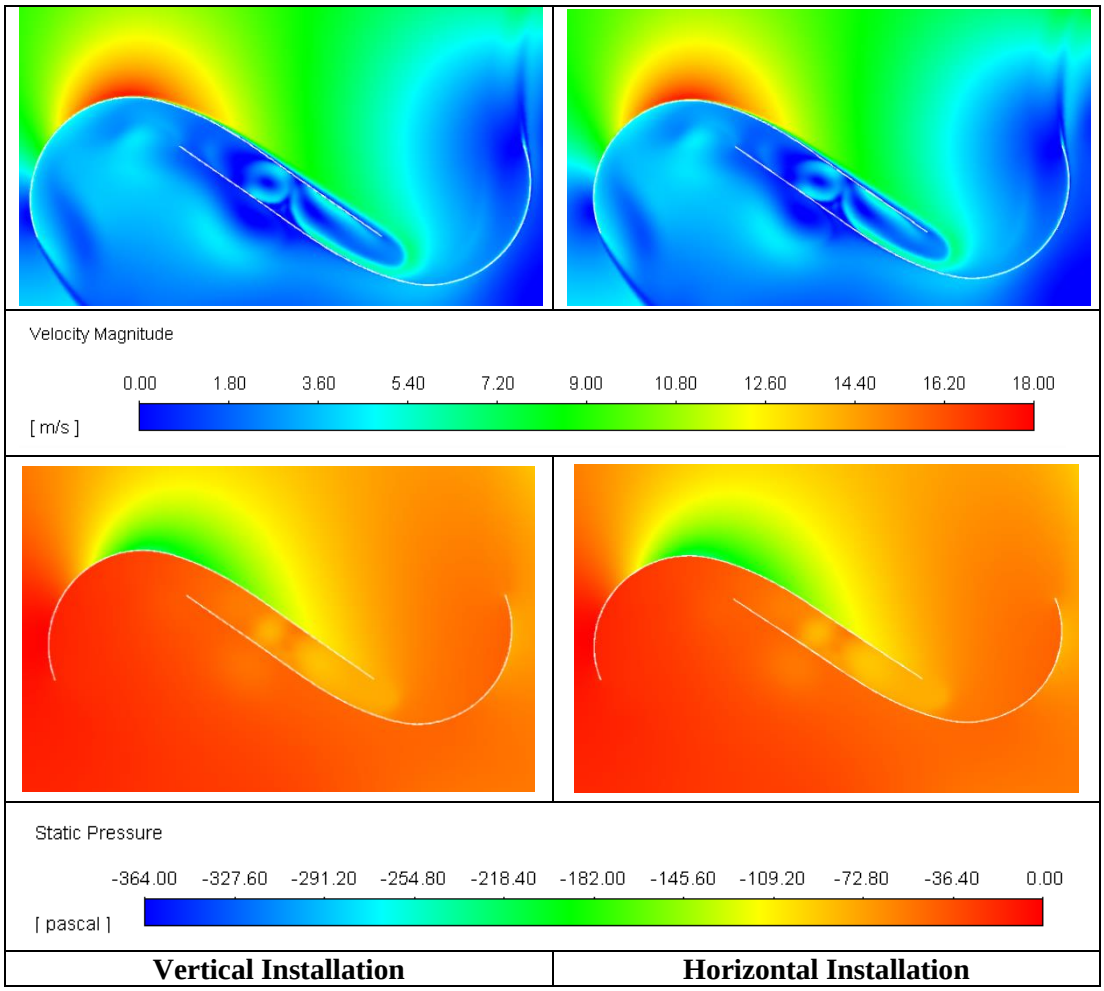

Figure 4.21: 0° Divergence-Velocity and Pressure Profiles for the Vertical and Horizontal Installation at $\emptyset = 0°$

In the pressure profiles, a lower pressure region formation can be observed at the rear side of the advancing blade in both configurations. Both the pressure profiles of the V_{Ins} and H_{Ins} have similar lift regions on the rear side of the advancing blade. The high-pressure difference between the concave and convex sides of the advancing blade causes a positive torque generation which contributes to the rotation of the turbine rotor. The similar velocity and pressure effects on both the configurations may have contributed to a similar torque production for the H_{Ins} and the V_{Ins}.

4.4.4 Velocity-Pressure Profiles at TSR 0.8 for Azimuth Angle, $\emptyset = 45°$

Figure 4.22 presents the velocity and pressure profile for the V_{Ins} and H_{Ins} at an azimuth angle of 45°. In the velocity profile, a higher lift generation is observed at the rear side of the advancing blade in the H_{Ins} compared to the V_{Ins}. In the pressure profile, a more prominent low-pressure wake region is observed at the rear side of the advancing blade in the H_{Ins} than the V_{Ins}. Furthermore, a slightly greater difference between the convex and concave sides at the mid-section is observed, leading to a higher drag generation in the H_{Ins} than the V_{Ins}. The higher lift and drag generation and the greater pressure difference between the convex and concave sides of the advancing blade may have contributed to a larger generated torque in the H_{Ins} than V_{Ins}.

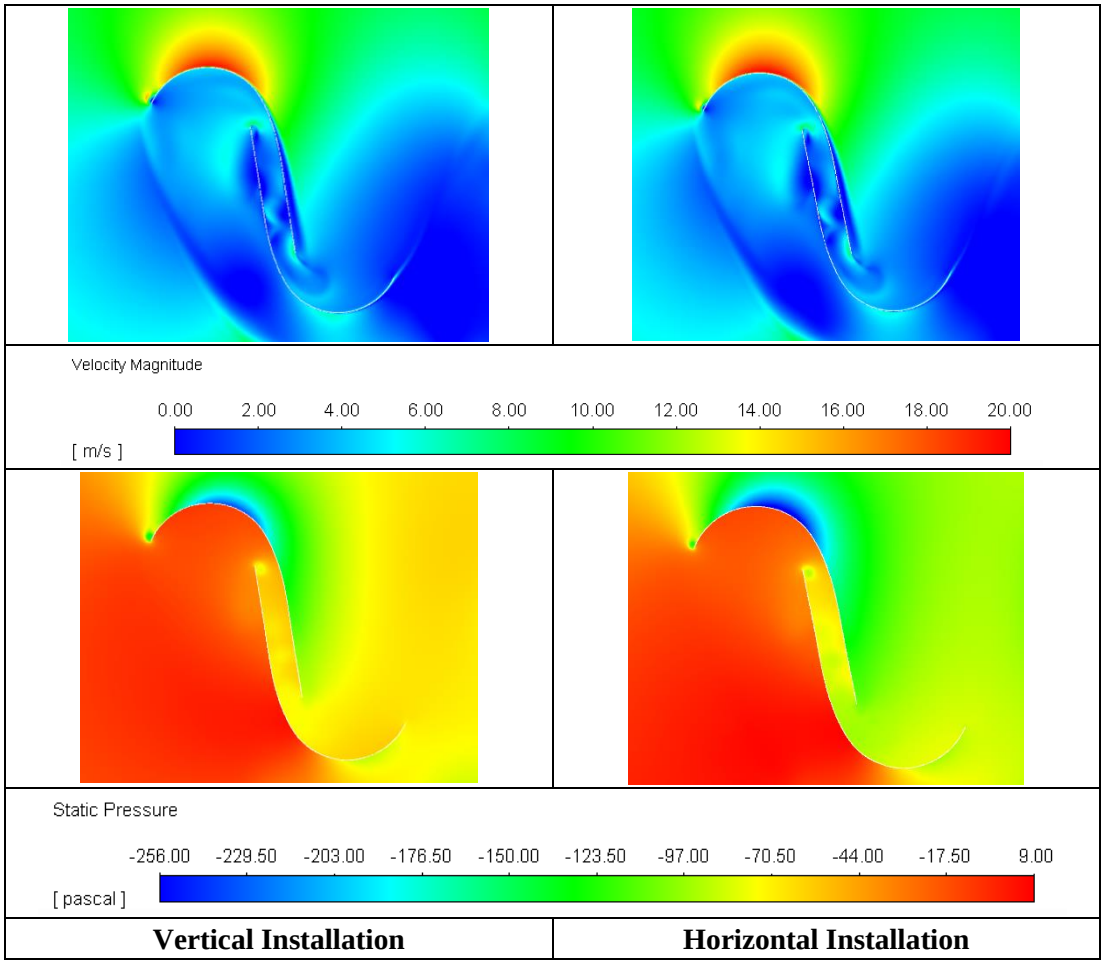

Figure 4.22: 0° Divergence-Velocity and Pressure Profiles for the Vertical and Horizontal Installation at $\emptyset = 45°$

4.4.5 Velocity-Pressure Profiles at TSR 0.8 for Azimuth Angle, $\emptyset = 90°$

Figure 4.23 presents the velocity and pressure profiles of the V_{Ins} and H_{Ins} at an azimuth angle of 90°. In the velocity profiles, the H_{Ins} is seen to produce similar tip vortices at the tip of the advancing blade, contributing to a similar lift generation as the V_{Ins}. In the pressure profile, a similar low-pressure wake region can be observed to be forming at the tip of the advancing blade in both the H_{Ins} and V_{Ins}. On both configurations, a similar difference in pressure is noticed at the front and rear of the advancing blade resulting in a similar lift formation. Thus, the similar lift generated by the low-pressure wake region on the tip of the advancing blade in the H_{Ins} and V_{Ins} may have contributed to similar torque production.

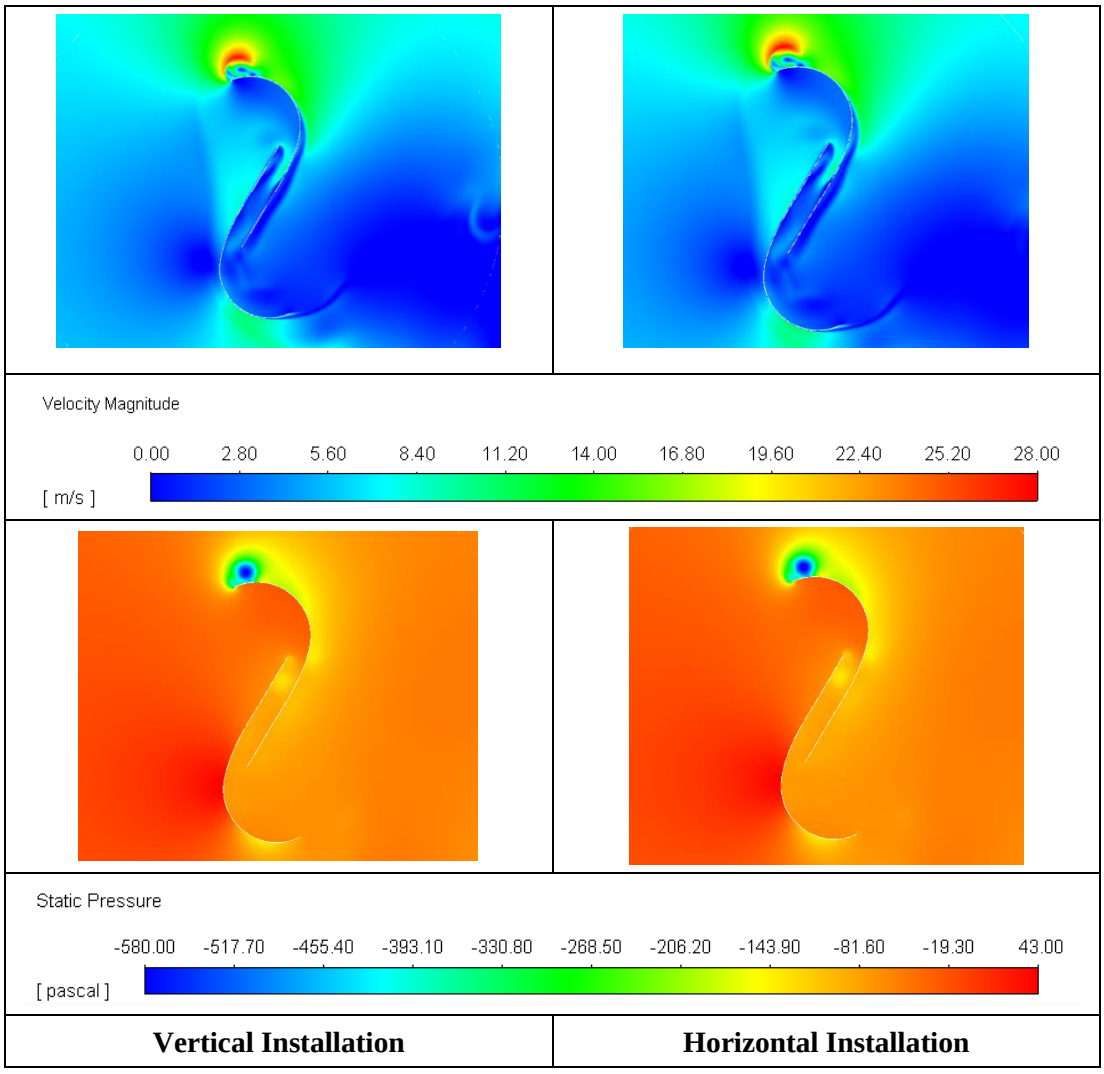

Figure 4.23: 0° Divergence-Velocity and Pressure Profiles for the Vertical and Horizontal Installation at $\emptyset = 90°$

4.4.6 Velocity-Pressure Profiles at TSR 0.8 for Azimuth Angle, $\emptyset = 135°$

Figure 4.24 presents the velocity and pressure profiles of the V_{Ins} and H_{Ins} at an azimuth angle of 135°. In the velocity profile, a slightly higher lift generation can be observed from the high-velocity formation on the tip region of the advancing blade of the H_{Ins} than the V_{Ins}. This effect is evidently seen in the pressure profile comparison, where the H_{Ins} has a lower pressure wake region formation at the tip region of the advancing blade than the V_{Ins}. Nevertheless, a slightly higher pressure difference between the concave and convex of the advancing blade creating drag is noticed in the V_{Ins} than the H_{Ins}. The higher pressure difference in the V_{Ins} may have improved the configuration's torque generation, hence, resulting in a similar overall torque production in the H_{Ins} and V_{Ins}.

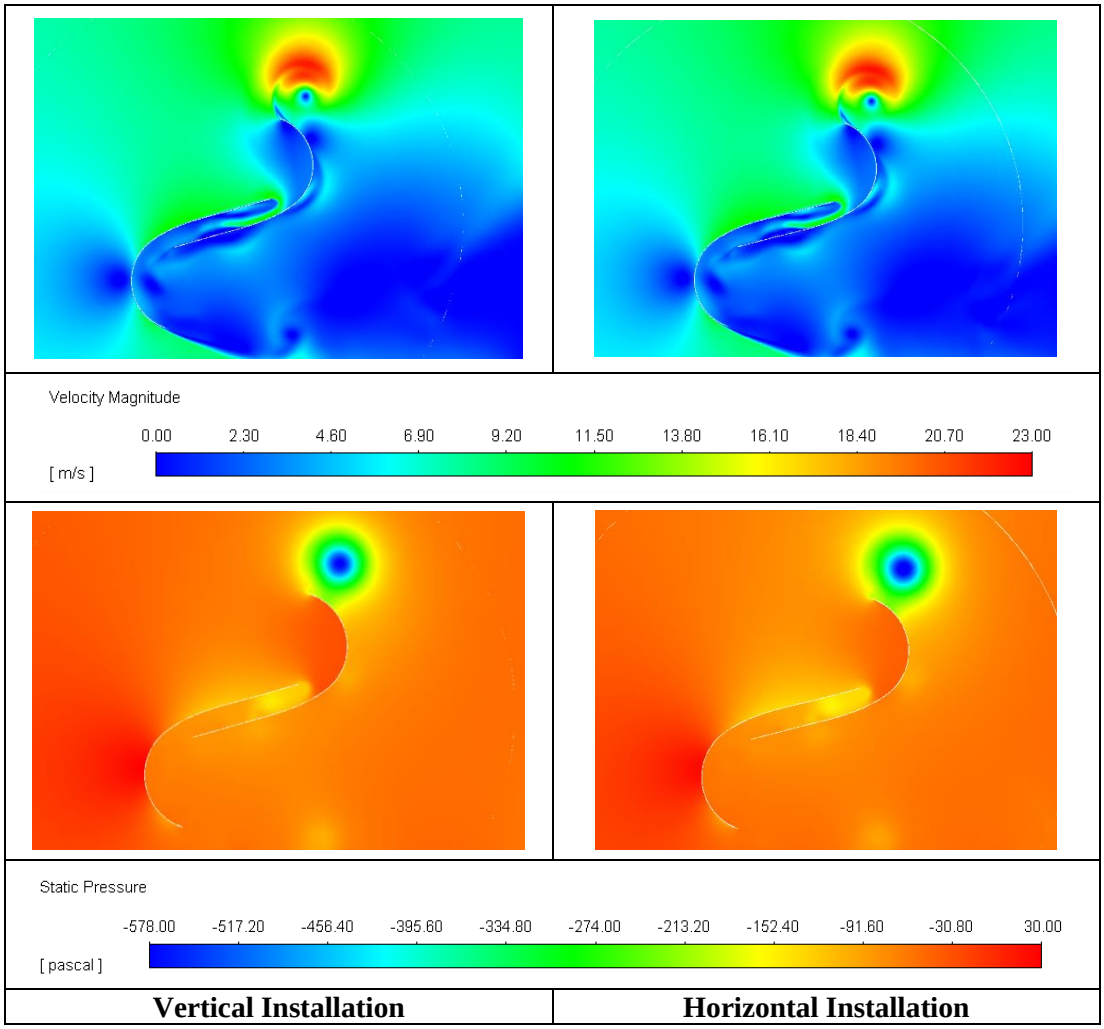

Figure 4.24: 0° Divergence-Velocity and Pressure Profiles for the Vertical and Horizontal Installation at $\emptyset = 135°$

4.5 1° Divergence - Performance Analysis of the Turbine under Vertical Installation and Horizontal Installation

This section presents the results obtained from the analysis of the SSWT at TSR 0.6, 0.8, 1.0 and 1.2 under the influence of the 1° chimney divergence for the V_{Ins} and H_{Ins}, respectively. The moment coefficient, performance coefficient, and power output of the turbine are presented and discussed. The instantaneous moment coefficient and performance coefficient for one complete turbine rotation for both configurations are compared and studied at TSR 0.8, respectively. The difference between the turbine configurations is analysed through the velocity and pressure profiles at TSR 0.8.

4.5.1 C_m, C_p and Power Output for V_{Ins} and H_{Ins} at 1° Divergence

Figure 4.25 presents the moment coefficient for the V_{Ins} and H_{Ins} at 1° chimney divergence. The trend of both the configurations is seen to be decreasing from TSR 0.6 to TSR 1.2. At TSR 0.6, both the V_{Ins} and H_{Ins} share the same magnitude of moment coefficient at 0.69. As the tip speed ratio moves to TSR 0.8, it is observed that the H_{Ins} has a higher moment coefficient magnitude than the V_{Ins} by 3.13%. At TSR 1.0, the H_{Ins} supersedes the moment coefficient of the V_{Ins} by 100%. At TSR 1.2, the moment coefficient of the V_{Ins} is 50% lower than the H_{Ins}.

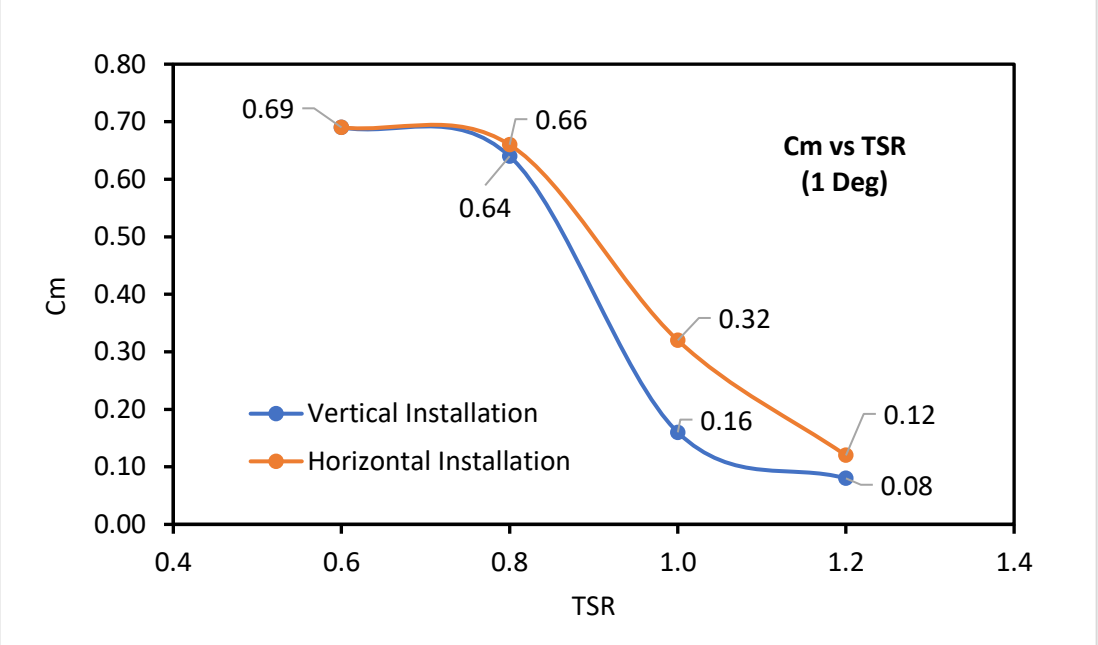

Figure 4.25: Coefficient of Moment for the Vertical and Horizontal Installation at 1° Chimney Divergence

At a lower TSR of 0.6, the force from the fluid flow exerted on the turbine blade is low, which may have influenced a similar magnitude of moment coefficient in both H_{Ins} and V_{Ins}. As the TSR value is gradually increased to TSR 0.8, the higher force of air attack from the non-distributed flow of the H_{Ins} may have aided the configuration to produce higher torque than the V_{Ins}. Similar behaviour may have occurred at TSR 1.0 and TSR 1.2, where the generated torque of the H_{Ins} is higher than the V_{Ins}.

However, at TSR 1.0, the incoming fluid velocity is equivalent to the rotational rate of the turbine, which means that the drag experienced by the rotor is lower than TSRs below 1.0. Furthermore, at TSR 1.2, the free stream velocity dominates the turbine's rotational speed, causing a much lower drag formation on the turbine blades, leading to a lower torque generation. Moreover, the distributed flow in the V_{Ins} may have created a higher negative torque due to the equal air attack on both the advancing and returning blade, which may have contributed to the lower torque generation at TSR 1.0 and 1.2 than the H_{Ins}.

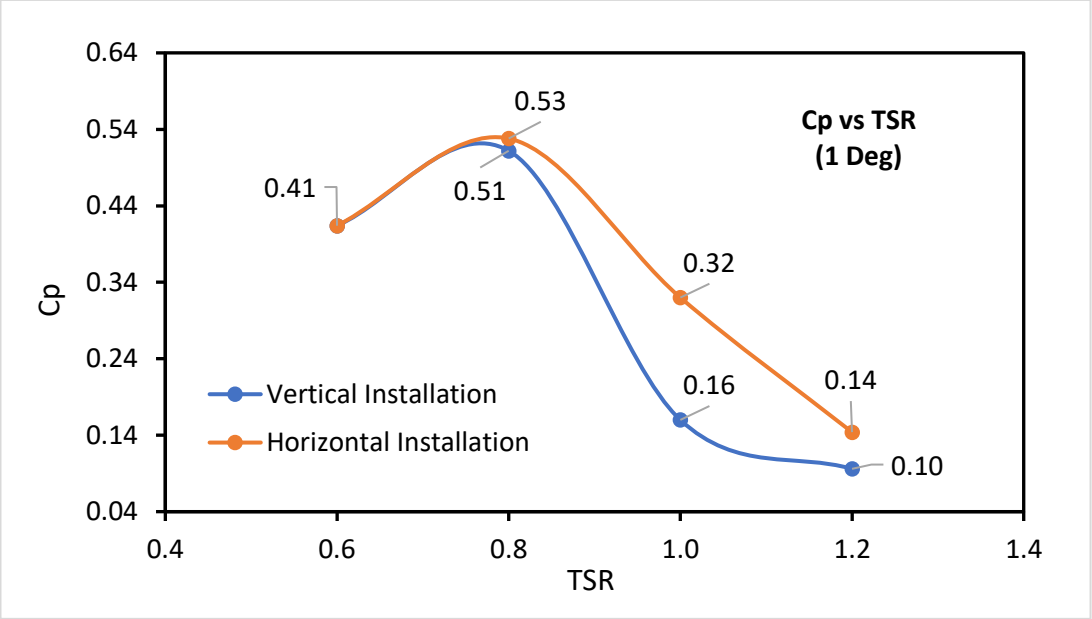

Figure 4.26: Coefficient of Performance for the Vertical and Horizontal Installation at 1° Chimney Divergence

Figure 4.26 presents the performance coefficient of the V_{Ins} and H_{Ins} for the 1° chimney divergence. The maximum performance is observed at TSR 0.8 under the H_{Ins} with a value of 0.53, 3.92% higher than V_{Ins}. The minimum performance is observed at TSR 1.2 under the V_{Ins} with a value of 0.10, 40% lesser than the H_{Ins}. In

general, the H_{Ins} performs better than the V_{Ins}, which may have been the contribution of the higher non-distributed flow that attacks the advancing blade under the H_{Ins} than the V_{Ins}.

The optimal performance occurring at TSR 0.8 is in line with previous literature as discussed in Section 4.4.1. Furthermore, the dominance of the fluid flow over the rotational rate of the turbine aids the performance of the rotor through the optimal production of the lift and drag at TSR 0.8. The lower torque generation in the V_{Ins} than the H_{Ins} may have been due to the distributed fluid flow in the configuration, which adversely impacts the returning blade. This may have reduced the performance of the V_{Ins} than the H_{Ins}, especially at TSR 1.0 and 1.2.

Figure 4.27 presents the power generation for the V_{Ins} and H_{Ins} at 1° chimney divergence. The peak power was generated at TSR 0.8 under the H_{Ins} with a value of 200.87 W, 3.13% higher than V_{Ins}. In contrast, the lowest generated power was produced at TSR 1.2 under the V_{Ins} with a value of 36.52W, 50% lesser than H_{Ins}. The lowest power production by both configurations is still higher than that of the highest power generated in Section 4.4, where the H_{Ins} 1° and V_{Ins} 1° are higher than H_{Ins} 0° and V_{Ins} 0° by 102.07% and 37.71%, respectively.

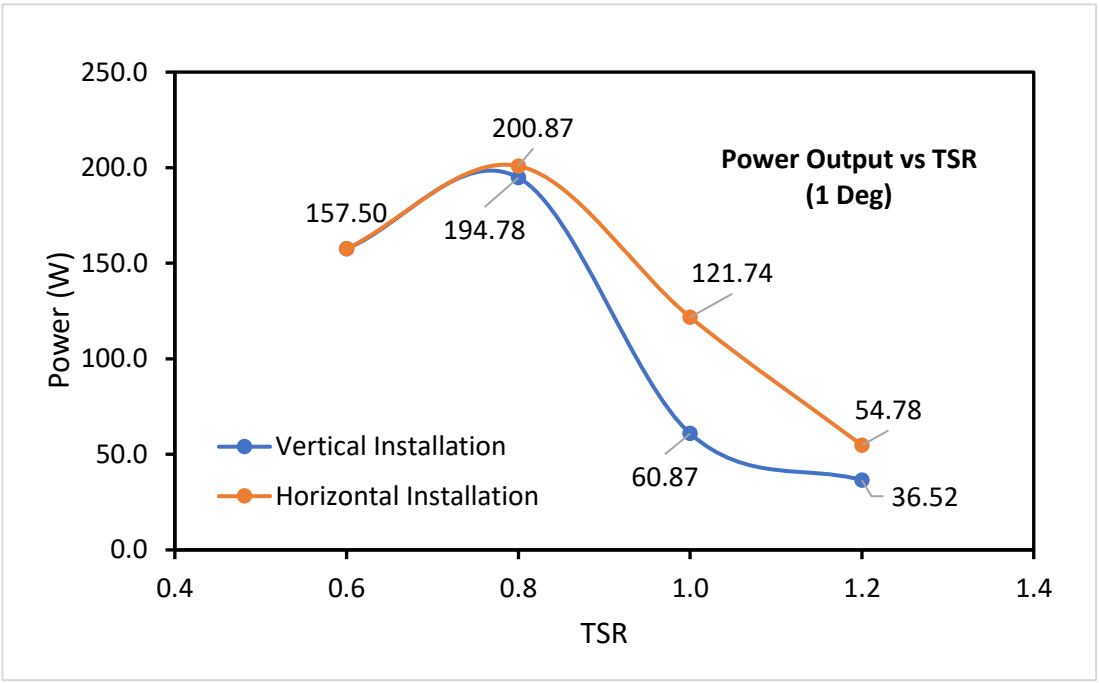

Figure 4.27: Power Output for the Vertical and Horizontal Installation at 1° Chimney Divergence

According to Equation 2.47, the available wind power is influenced by the velocity function, V^3, that has a substantial impact on overall power output. Consequently, the higher magnitude of incoming fluid velocity contributes to a larger power augmentation by both configurations under the influence of the 1° chimney divergence. Although the performance highly varies from TSR 0.6 to TSR 1.2, the power production by both the configurations, H_{Ins} and V_{Ins}, show sound potential in the SCPP.

4.5.2 Instantaneous C_m and C_p for V_{Ins} and H_{Ins} at 1° Divergence

Figure 4.28 presents the instantaneous moment coefficient of the V_{Ins} and H_{Ins} at 1° chimney divergence. The H_{Ins} shows a larger amplitude which suggests a higher moment generation at azimuth angles 0 degrees to 30 degrees, 150 degrees to 240 degrees and 280 degrees to 360 degrees compared to the V_{Ins}. The higher velocity attacking the advancing blade due to the non-uniform velocity profile may have improved the lift and drag contribution in the H_{Ins}, thus creating a higher torque than the V_{Ins}. Similarly, the uniform velocity profile attacking the advancing and returning blade at these azimuth angles may have caused a higher negative torque formation in the returning blade of the V_{Ins}, thus reducing the overall torque generation compared to the H_{Ins}.

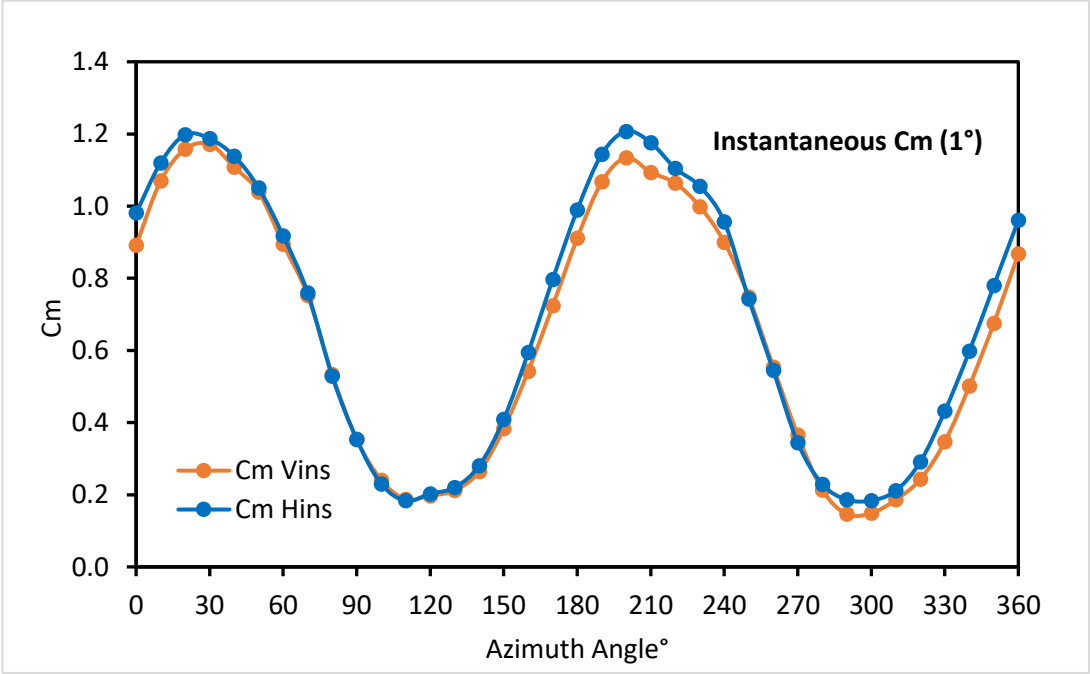

Figure 4.28: Instantaneous C_m at 1° Chimney Divergence

Figure 4.29 presents the instantaneous performance coefficient of the V_{Ins} and H_{Ins} at 1° chimney divergence. The H_{Ins} shows a higher performance with a larger amplitude compared to the V_{Ins} at 0 degrees to 30 degrees, 150 degrees to 240 degrees and 280 degrees to 360 degrees. The blade's aerodynamic design contributing to a higher lift in the advancing blade may have been advantageous for the H_{Ins} as the configuration has a higher velocity impacting the advancing blade compared to the V_{Ins} due to the non-uniform velocity profile. As a result, the H_{Ins} may have been attributed to greater torque production than the V_{Ins}, leading to an enhanced performance at the aforementioned azimuth angles.

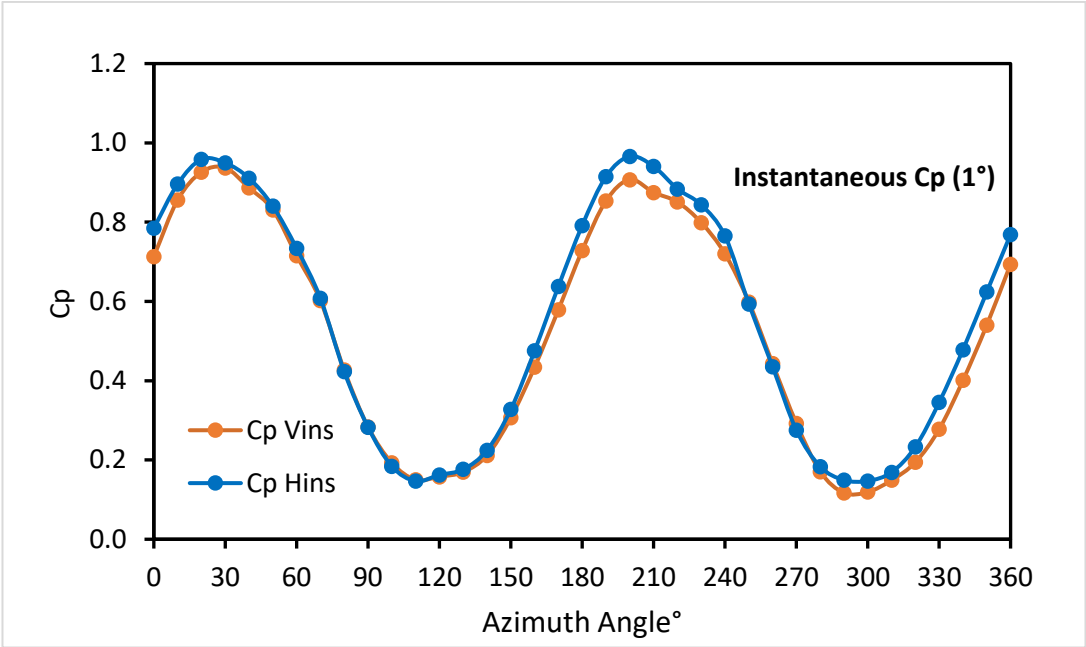

Figure 4.29: Instantaneous C_p at 1° Chimney Divergence

4.5.3 Velocity-Pressure Profiles at TSR 0.8 for Azimuth Angle, $\emptyset = 0°$

Figure 4.30 presents the velocity and pressure profiles of the SSWT under the V_{Ins} and H_{Ins} at an azimuth angle of 0°. From the velocity profile, a higher lift generation is observed at the rear side of the advancing blade in the H_{Ins} than the V_{Ins}, which may have been the influence of the higher velocity profile (from the non-uniform flow) attacking the advancing blade. At the rear end of the returning blade, larger vortices are formed in the H_{Ins} than the V_{Ins}. This may have been due to the large tip vortices that leave the blade tip after a 180° rotation. Consequently, the lower pressure region observed on the rear side of the advancing blade of the H_{Ins} than the V_{Ins} may have contributed to a higher lift generation. Moreover, the lower-pressure wake region at

the rear side of the returning blade of the H_{Ins} may have caused a slightly larger pressure difference between the convex and concave of the returning blade, which may have contributed to a lower negative torque generation in the H_{Ins} than the V_{Ins}. This may have improved the total torque produced in the H_{Ins} than the V_{Ins}.

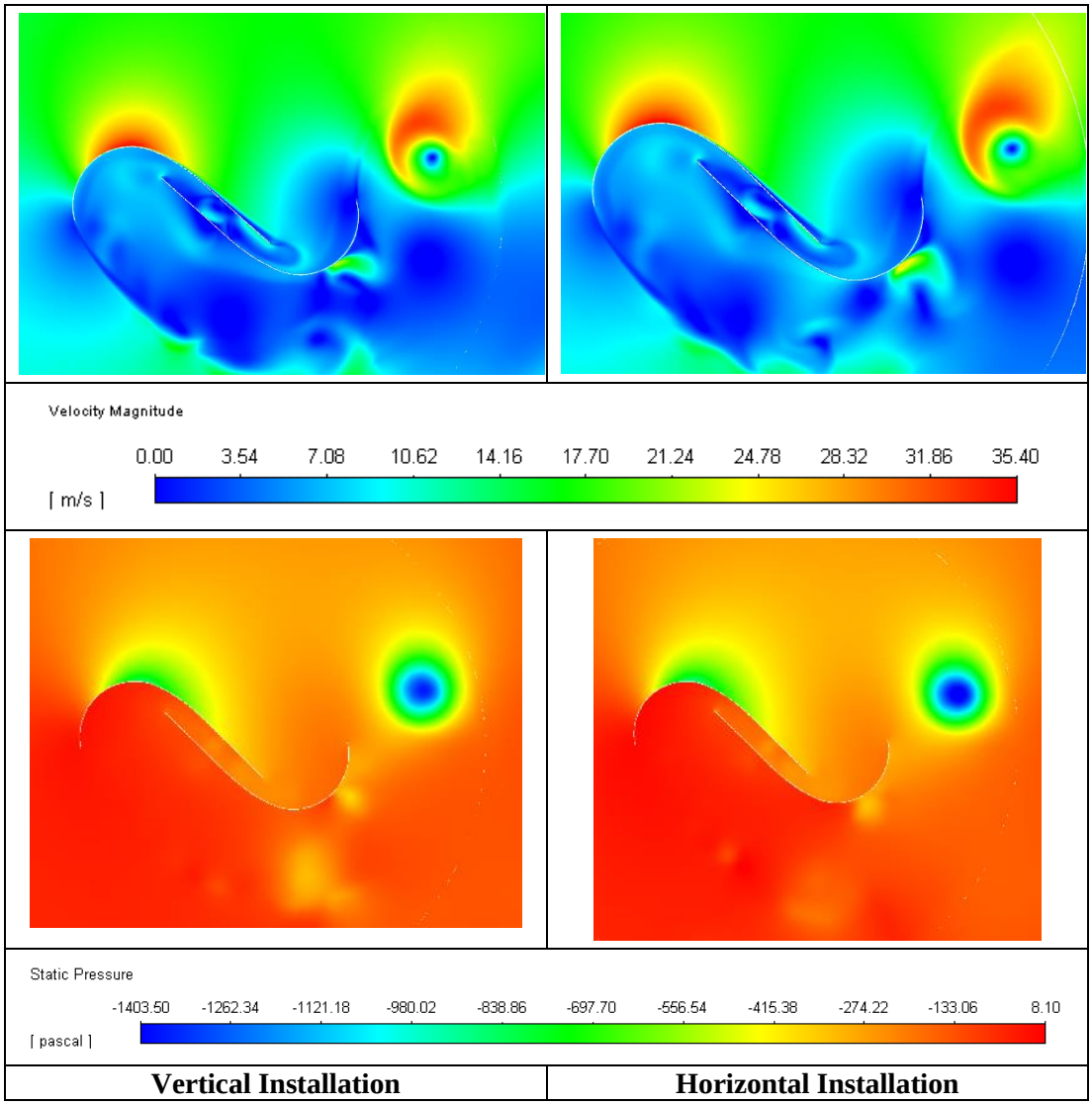

Figure 4.30: 1° Divergence-Velocity and Pressure Profiles for the Vertical and Horizontal Installation at $\emptyset = 0°$

4.5.4 Velocity-Pressure Profiles at TSR 0.8 for Azimuth Angle, $\emptyset = 45°$

Figure 4.31 presents the velocity and pressure profiles of the SSWT under the V_{Ins} and H_{Ins} at an azimuth angle of 45°. From the velocity profiles, the H_{Ins} is observed to generate a stronger lift region than the V_{Ins}. The pressure profiles show that a lower pressure region is formed on the rear top of the advancing blade (Coanda effect flow) of the H_{Ins} compared to the V_{Ins}. Furthermore, a significantly larger pressure

difference between the concave and convex sides of the advancing blade suggests that a larger lift and drag force are experienced by the H_{Ins} than the V_{Ins}.

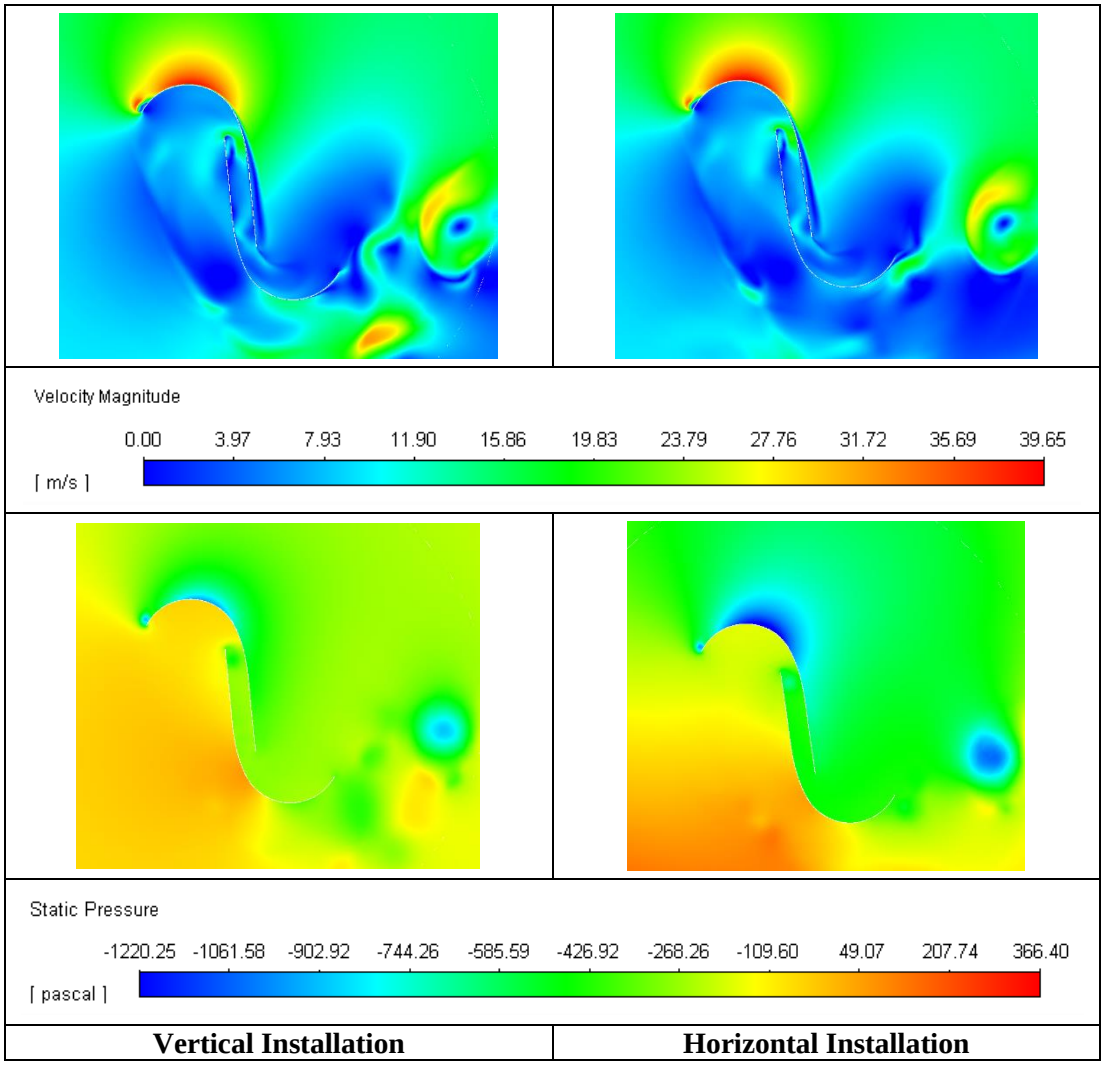

Figure 4.31: 1 Degree Divergence-Velocity and Pressure Profiles for the Vertical and Horizontal Installation at $\emptyset = 45°$

The drag experienced by the H_{Ins} may also be higher than V_{Ins} due to the lower-pressure wake region formation observed at the posterior side of the returning blade. Although a larger pressure difference between the convex and concave sides of the returning blade is noticed in the H_{Ins} than the V_{Ins} leading to higher negative torque, the lift and drag force experienced by the advancing blade in the H_{Ins} may have been sufficient to overcome the effects of the negative torque at this azimuth angle, thus producing a higher total torque generation. These effects may have been the contribution of the non-uniform velocity profile that aids the torque generation in the H_{Ins}.

4.5.5 Velocity-Pressure Profiles at TSR 0.8 for Azimuth Angle, $\emptyset = 90°$

Figure 4.32 presents the velocity and pressure profiles of the SSWT under the V_{Ins} and H_{Ins} at a blade azimuth angle of 90°. Similar velocity profiles are observed between the H_{Ins} and V_{Ins}, with the H_{Ins} having slightly stronger tip vortices than the V_{Ins}. The low-pressure tip wake region at the H_{Ins} advancing blade contributes to the strong formation of tip vortices seen in the velocity profile compared to the V_{Ins}, which promotes a slightly greater lift production in the H_{Ins}. However, a slightly lower pressure region is observed at the convex of the returning blade in V_{Ins} compared to H_{Ins}, decreasing the negative torque generation. The lower negative torque generation in the V_{Ins}, may have aided in producing a similar overall torque production as the H_{Ins}.

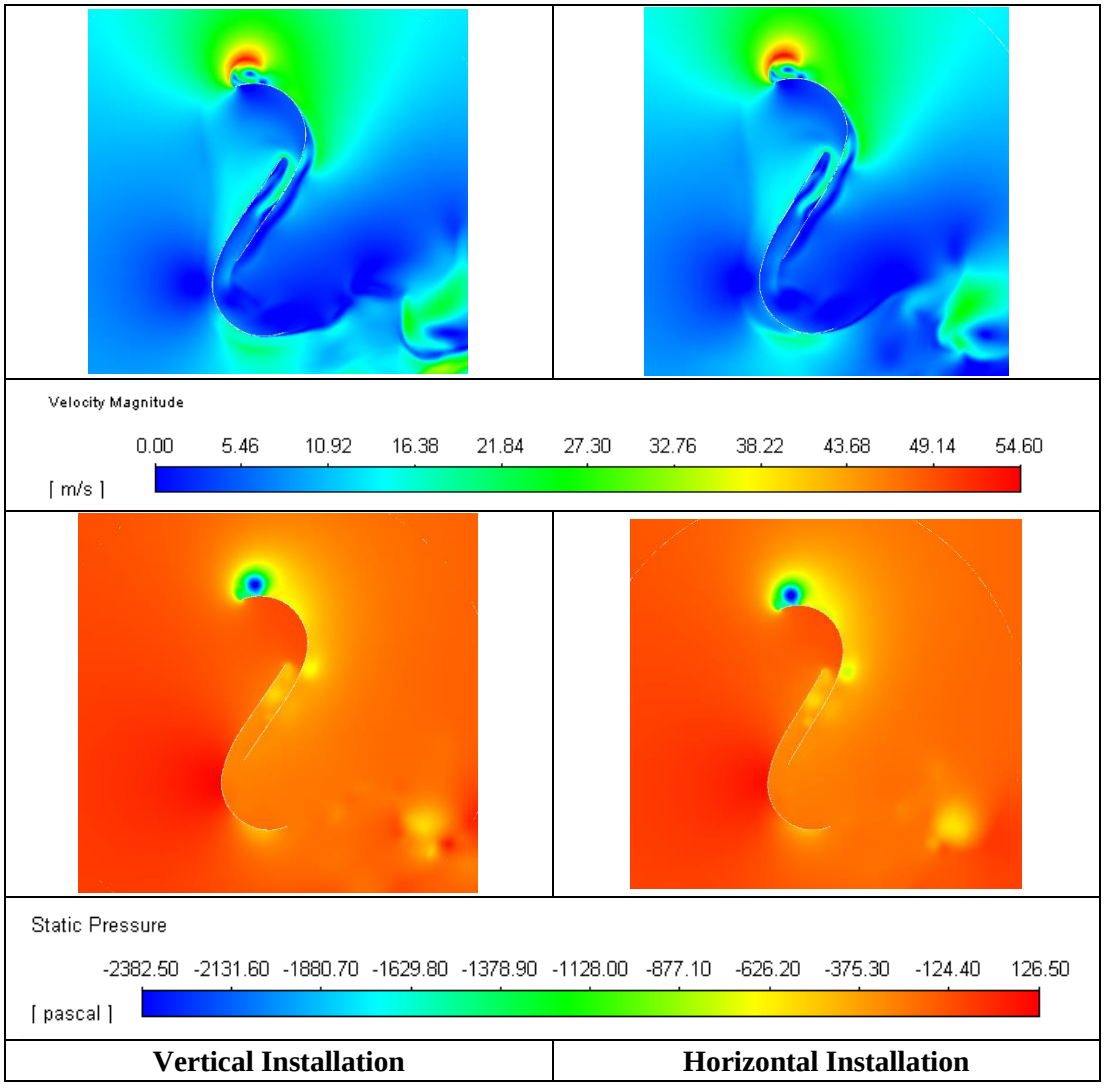

Figure 4.32: 1° Divergence-Velocity and Pressure Profiles for the Vertical and Horizontal Installation at $\emptyset = 90°$

4.5.6 Velocity-Pressure Profiles at TSR 0.8 for Azimuth Angle, $\emptyset = 135°$

Figure 4.33 presents the velocity and pressure profiles of the SSWT under the V_{Ins} and H_{Ins} at a blade azimuth angle of 135°. Both the velocity profiles exhibit similar velocity flow patterns, with the H_{Ins} producing slightly greater tip vortices than the V_{Ins}. The pressure profiles suggest that a larger low-pressure wake region is formed at the tip of the advancing blade of the H_{Ins}, resulting in slightly stronger tip vortices than the V_{Ins}.

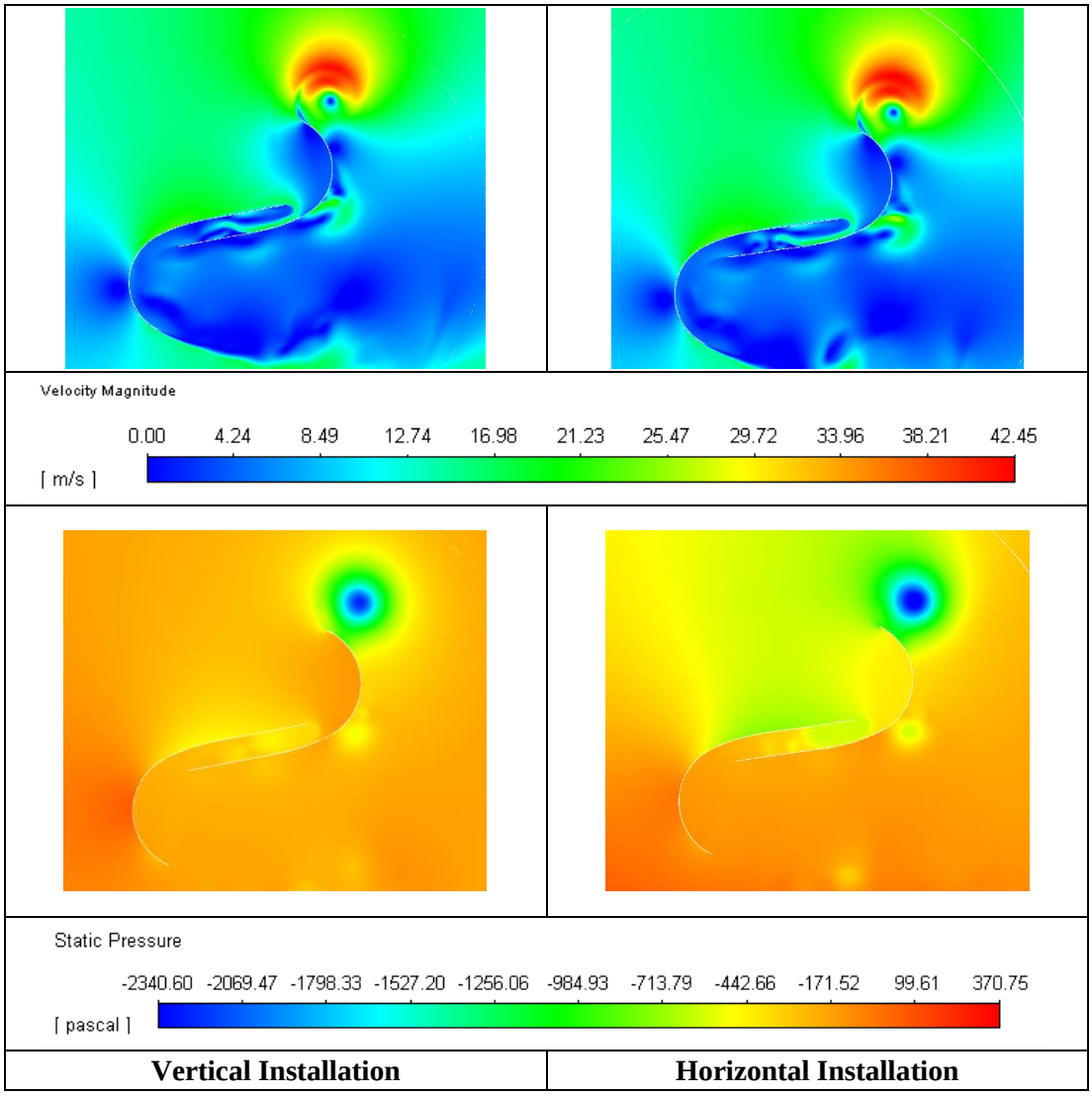

Figure 4.33: 1 Degree Divergence-Velocity and Pressure Profiles for the Vertical and Horizontal Installation at $\emptyset = 135°$

Furthermore, the significantly lower pressure region developed at the rear side (mid-section) of the returning blade in the H_{Ins} suggests a greater lift and drag formation, which contributes to the larger torque generation than the V_{Ins}. Moreover, the H_{Ins}

benefits from the higher magnitude of velocity from the non-uniform velocity profile, as observed at the overlap region of the blade profile, where a pressure region lower than the V_{Ins} is formed.

As a result, a larger pressure difference is developed between the concave and convex sides of the advancing blade, which may have contributed to the slightly larger torque generation in the H_{Ins} than the V_{Ins}. In addition, the returning blade of the V_{Ins} experiences a larger pressure on the rear side, leading to a higher negative torque generation compared to the H_{Ins} due to the larger pressure difference between the convex and the concave sides. This effect could have been the impact of the uniform velocity flow profile experienced by the V_{Ins} blades in the configuration. Consequently, the contribution of the larger negative torque in the V_{Ins} than the H_{Ins} may have affected the V_{Ins} adversely.

4.6 2° Divergence - Performance Analysis of the Turbine under Vertical Installation and Horizontal Installation

This section presents the results obtained from the analysis of the SSWT at TSR 0.6, 0.8, 1.0 and 1.2 under the influence of the 2° chimney divergence for the V_{Ins} and H_{Ins}, respectively. The moment coefficient, performance coefficient, and power output of the turbine are presented and discussed. The instantaneous moment coefficient and performance coefficient for one complete turbine rotation for both configurations are compared and studied at TSR 0.8, respectively. The difference between the turbine configurations is analysed through the velocity and pressure profiles at TSR 0.8.

4.6.1 C_m, C_p and Power Output for V_{Ins} and H_{Ins} at 2° Divergence

Figure 4.34 presents the moment coefficient of the V_{Ins} and H_{Ins} for the 2° chimney divergence. The highest moment coefficient at TSR 0.8 is obtained by the V_{Ins} at 0.49, 59.18% higher than the H_{Ins}, while the lowest moment coefficient at TSR 1.2 obtained by V_{Ins} at 0.06 is 66.67% higher than H_{Ins}. The V_{Ins} is observed to perform better than the H_{Ins} for all TSR values except TSR 1.2. This occurrence opposes the situation in the cylindrical chimney (0°) and 1° chimney divergence, where the H_{Ins} has a higher moment coefficient magnitude than the V_{Ins}. Furthermore, the trend of the moment coefficient decreasing from a lower TSR to a higher TSR is not applicable in the

vertical installation operation. It should be noted that the moment coefficient obtained at all TSR values except TSR 0.8 in the V_{Ins} experienced unstable operations throughout the rotations. The moment coefficient value from one value to another varied severely. Thus, the value obtained for the V_{Ins} at TSR 0.6, 1.0 and 1.2 was an average of the 6^{th} rotation to the 12^{th} rotation.

The strong velocity magnitude at the free-stream leading to a higher Reynolds number may have had a significant effect on the torque generation causing significant fluctuations. This may have been due to the vibrations experienced by the rotors at a comparatively high Reynolds number. For fluid flow with a high Reynolds number, the rotor blades would be subjected to a significant centrifugal force at high turbine rotational speeds, where changes in fluid velocity across the blades would result in the vibration experienced by the blade (Molland 2008). However, these effects may have been minimally experienced at TSR 0.8 for the V_{Ins}. This may have been due to the wind's attack at the optimally designed TSR range value of the turbine. Nevertheless, the magnitude of the moment coefficient experienced at TSR 0.8 for the V_{Ins} is still lower than that achieved under a 1° chimney divergence by 23.43%. The reduced torque generation in V_{Ins} may have been a contribution of the greater force experienced from the higher wind velocity that equally acts on the returning blade, resulting in a larger produced negative torque. Too great of a turbine rotation causes poor spinning stability resulting from large centrifugal forces that act on the rotor's root end, causing high spinning tension (Lawrence 2010). This situation which happens during yarn spinning can be related to the rotation of the turbine rotor at a very high speed, as discussed above.

For the H_{Ins}, it is observed that the magnitude of moment coefficient achieved by all TSR values were more or less similar, with the highest recorded at TSR 0.6 with a value of 0.25, 21.88% lower than V_{Ins}, and the lowest recorded at TSR 1.2 with a value of 0.10, 66.67% higher than V_{Ins}. Although the trendline agrees with previous trends of a reducing moment coefficient over increasing TSRs, unlike the V_{Ins}, a significant variation across the TSRs cannot be noticed. This reflects upon the higher rotational speed of the turbine under the influence of a 2° chimney divergence which causes the incoming free stream velocity to treat the turbine as a wall surface due to highly turbulent air (Ragheb 2014), thus causing it to flow over the rotor rather than attacking

the rotor blades. Increasing a rotor's speed improves the rotor's spinning capabilities up to a certain specific maximum speed that is defined by factors such as the rotor diameter. Thus, at 2° chimney divergence, it can be said the rotor's ability to generate power is close to its maximum potential.

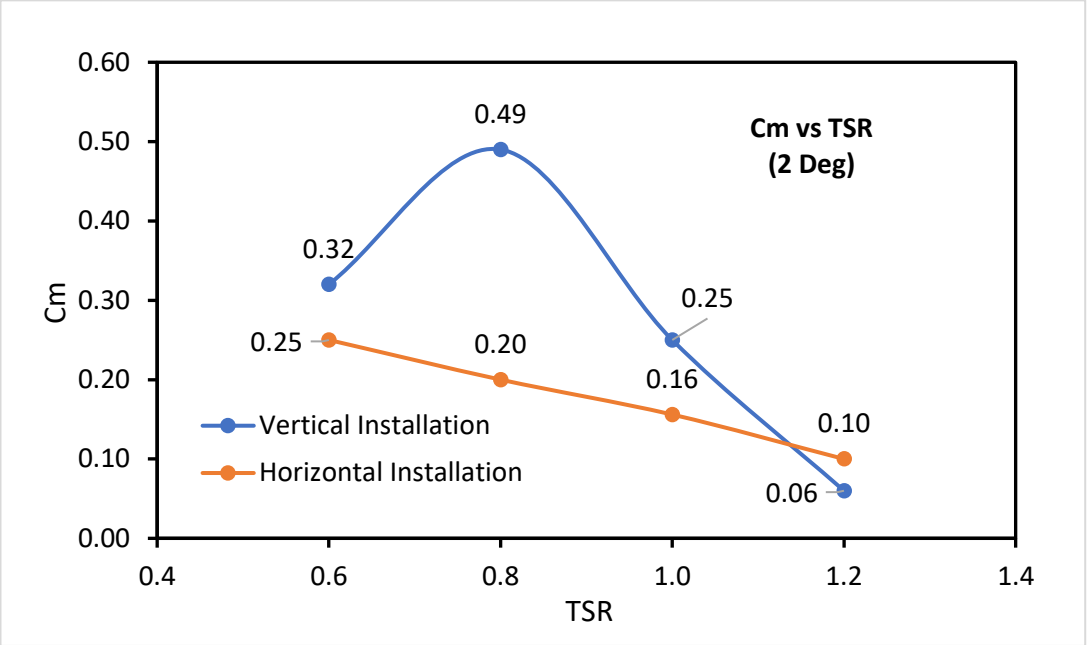

Figure 4.34: Coefficient of Moment for the Vertical and Horizontal Installation at 2° Chimney Divergence

Figure 4.35 presents the performance coefficient comparison between the V_{Ins} and H_{Ins} under the influence of the 2° diverging chimney. The performance of the V_{Ins} is observed to be better than that of the H_{Ins} for every TSR except TSR 1.2, which differs from the performance of the rotor under the cylindrical chimney and the 1° divergent chimney. The highest performance is obtained by the V_{Ins} at TSR 0.8 with a value of 0.39, 58.97% higher than H_{Ins}, while the lowest performance is achieved at TSR 1.2 in the same configuration with the value of 0.07, 71.43% lower than H_{Ins}. The performance of the H_{Ins} is seen to be almost alike, with the highest performance at 0.16 for TSR 0.8 and TSR 1.0.

The findings of Roy and Saha (2015) suggested that the blade profile's performance increases as the Reynolds value increases until an optimal performance peak and reduces thereafter. Thus, the H_{Ins} with the non-uniform velocity profile that channels higher velocity air to the advancing blade does not aid the performance of H_{Ins} 2°, as

the Reynolds number is much higher at 2.82×10^5 than the optimal operating range of the turbine at 1.1×10^5 to 1.3×10^5 (Roy and Saha 2015). Moreover, the high rotating speed of the rotor results in a wall-like structure, in which the fluid flows over the rotor rather than striking the blades, as discussed in the section above. However, the V_{Ins} shows better performance which may be due to the support of the equal fluid flow force on both the advancing and returning blade, thus increasing the negative torque of the configuration, which reduces the overall effect of a high incoming velocity. Although the V_{Ins} 2° achieves reasonably high performance at TSR 0.8, it is still 30.77% lower than that obtained under the 1° chimney divergence. However, it is still noteworthy because the performance of V_{Ins} 2° is 8.89% greater than V_{Ins} 0°.

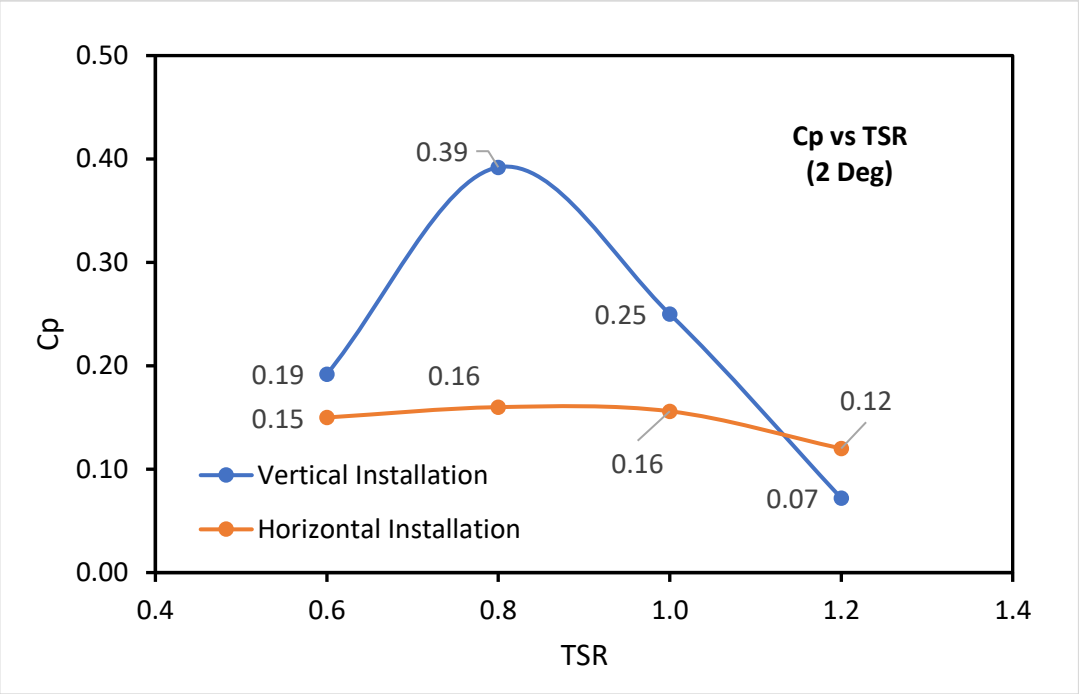

Figure 4.35: Coefficient of Performance for Vertical and Horizontal Installation at 2° Chimney Divergence

Figure 4.36 presents the power output obtained by the V_{Ins} and the H_{Ins} under the influence of the 2° chimney divergence for TSR 0.6, 0.8, 1.0 and 1.2. The V_{Ins} 2° obtained the highest power at TSR 0.8 with an output of 283.89 W, which is 45.75% higher than V_{Ins} 1°. This is the influence of the velocity on the power extracted by the turbine, based on Equation 2.47, where the power increases with the cube of wind speed. The lowest power output generated by the V_{Ins} is at TSR 1.2 with a value of 52.14W, 99.61% higher than the maximum power produced under the cylindrical

chimney, V_{Ins} 0°. Although the potential for power production is present in the V_{Ins} 2°, the significant difference in power output across TSRs and lower stability should be considered when choosing this setup.

The H_{Ins} 2° obtained the highest power output at TSR 0.8 with a value of 115.88 W, 59.18% lower than that achieved by the V_{Ins} 2°. The maximum power obtained by the H_{Ins} 2° is 327.44% higher than H_{Ins} 0° but 73.34% lower than H_{Ins} 1°. Although the rotor generates a significant amount of power, the main problem is the extremely high rotating speed in the H_{Ins} 2°, which leads to fluctuations in torque generation and low air attacks on the rotor blades, thus lowering the turbine's efficiency and power augmentation.

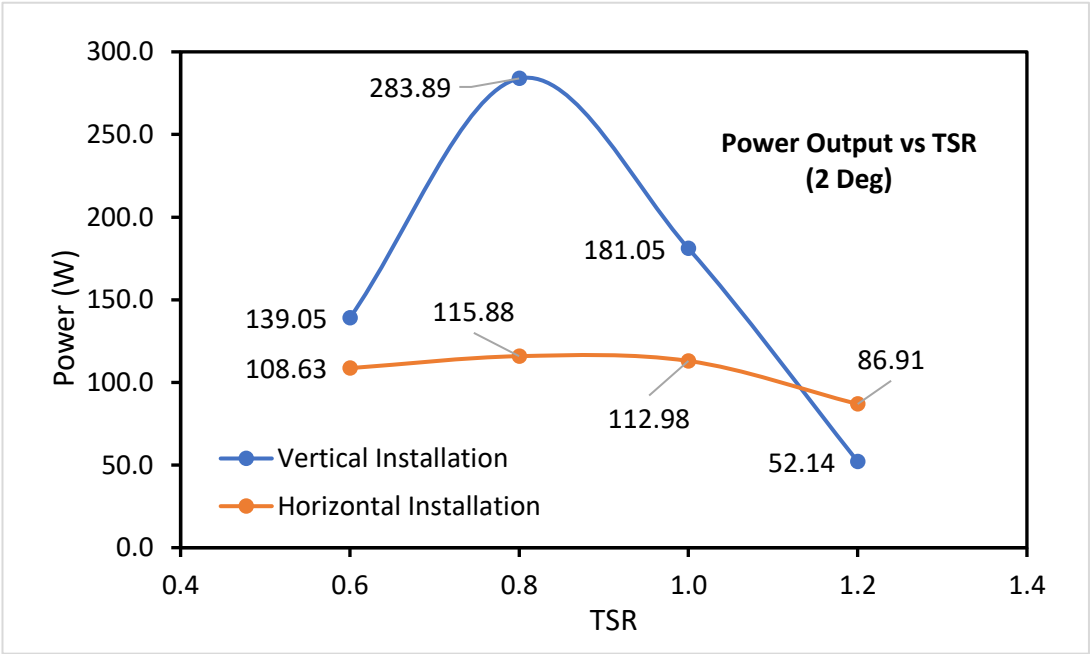

Figure 4.36: Power Output for the Vertical and Horizontal Installation at 2° Chimney Divergence

4.6.2 Instantaneous C_m and C_p for V_{Ins} and H_{Ins} at 2° Divergence

Figure 4.37 presents the instantaneous moment coefficient of the V_{Ins} and H_{Ins} at 2° chimney divergence. The V_{Ins} shows higher amplitude at all azimuth angles, which suggests a higher moment generation compared to the H_{Ins}. The high incoming free stream velocity results in a Reynolds number beyond the suggested optimal operating range of the rotor. Furthermore, the H_{Ins} shows negative torque generation at azimuth angles 110 degrees to 140 degrees and 290 degrees to 330 degrees, suggesting that the

returning blade generates higher negative torque than positive torque. The negative torque generation may be due to the high incoming free stream velocity that flows over the turbine's rotating region rather than attacking the advancing blade for torque production. The same effects are not observed with V_{Ins} which suggests that the uniform velocity profile attacking for the advancing and returning blade acts as an aid for overall positive torque production. Hence, the total torque generation in V_{Ins} is shown to be greater than H_{Ins}.

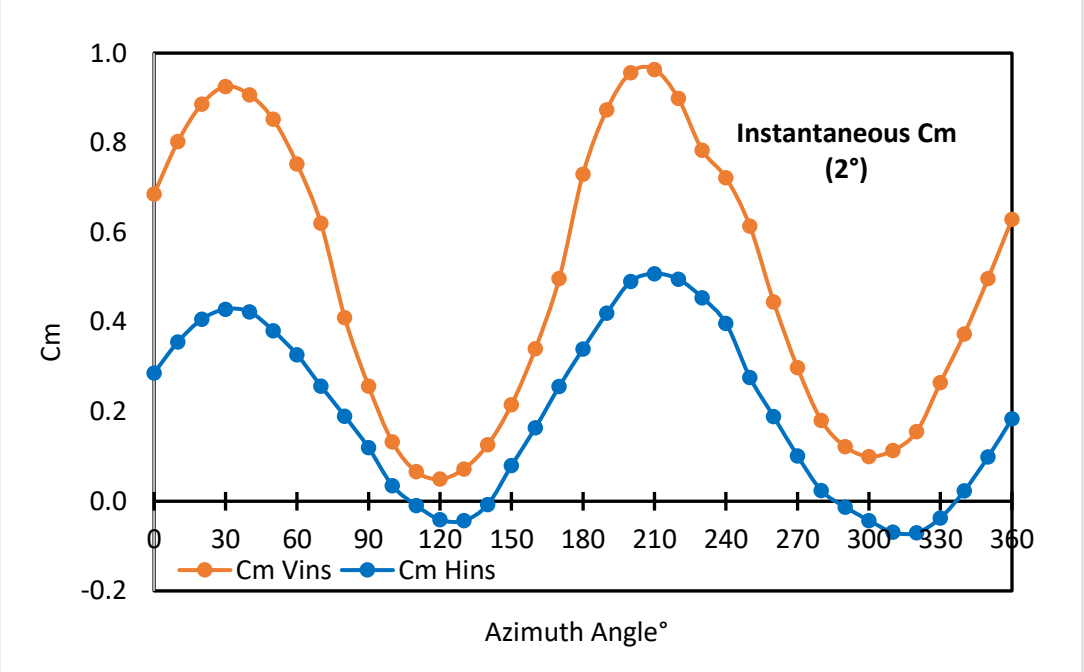

Figure 4.37: Instantaneous C_m at 2° Chimney Divergence

Figure 4.38 presents the instantaneous performance coefficient of the V_{Ins} and H_{Ins} at 2° chimney divergence. The V_{Ins} exhibits a higher performance with a greater amplitude compared to the H_{Ins}. Moreover, the H_{Ins} generates negative performance at azimuth angles 110 degrees to 140 degrees and 290 degrees to 330 degrees, unlike the V_{Ins}. Based on Figure 4.37, the negative torque generation at these angles may have resulted in negative performance in the blade's configuration, H_{Ins}. Moreover, the positive performance at every angle of blade rotation in the V_{Ins} suggests that the uniform flow attack on both the blades aid the rotor performance at 2° chimney divergence. Hence, these effects may have caused the V_{Ins} to perform better compared to the H_{Ins} with a higher incoming free stream velocity.

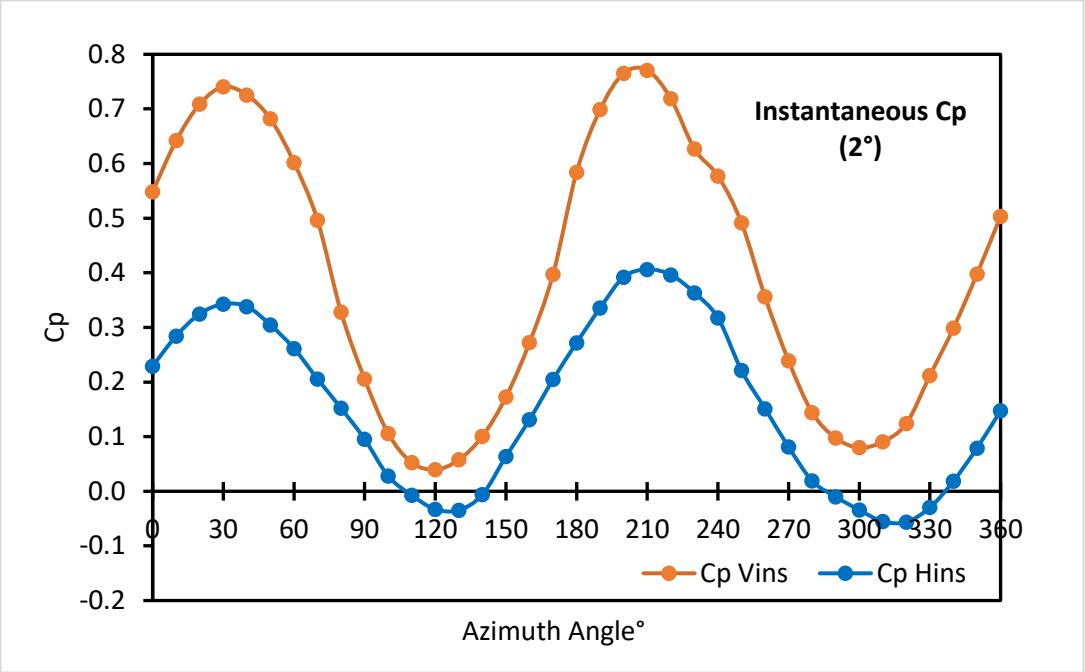

Figure 4.38: Instantaneous C_p at 2° Chimney Divergence

4.6.3 Velocity-Pressure Profiles at TSR 0.8 for Azimuth Angle, $\emptyset = 0°$

Figure 4.39 presents the velocity and pressure profiles of the SSWT under the V_{Ins} and H_{Ins} at blade azimuth angle 0°. The velocity profiles show a strong lift generation in the V_{Ins} than the H_{Ins}. On the other hand, a higher velocity region is observed flowing over the rotation area in H_{Ins}. This effect may have been due to the non-uniform velocity flow experienced by this configuration, where the higher velocity magnitude may have channelled towards the advancing blade. However, due to the very high rotational speed of the blades (resulting from the enhanced flow from the 2° divergent chimney), the rotor exhibits a wall-like characteristic that limits the incoming free stream velocity from fully attacking the turbine blades to generate torque.

In the pressure profiles, a low-pressure region is developed at the rear side of the advancing blade of the V_{Ins}. In the H_{Ins}, a low-pressure region is experienced by the convex of the advancing blade and the concave of the returning blade, respectively. This effect may be due to the fluid flow that channels over the rotating region. Consequently, the returning blade generates a large negative torque due to the large pressure difference between the concave and convex sides. Moreover, the absence of the Coanda effect on the advancing blade suggests that minimal positive torque is generated, hence reducing the total torque production and performance of the H_{Ins}.

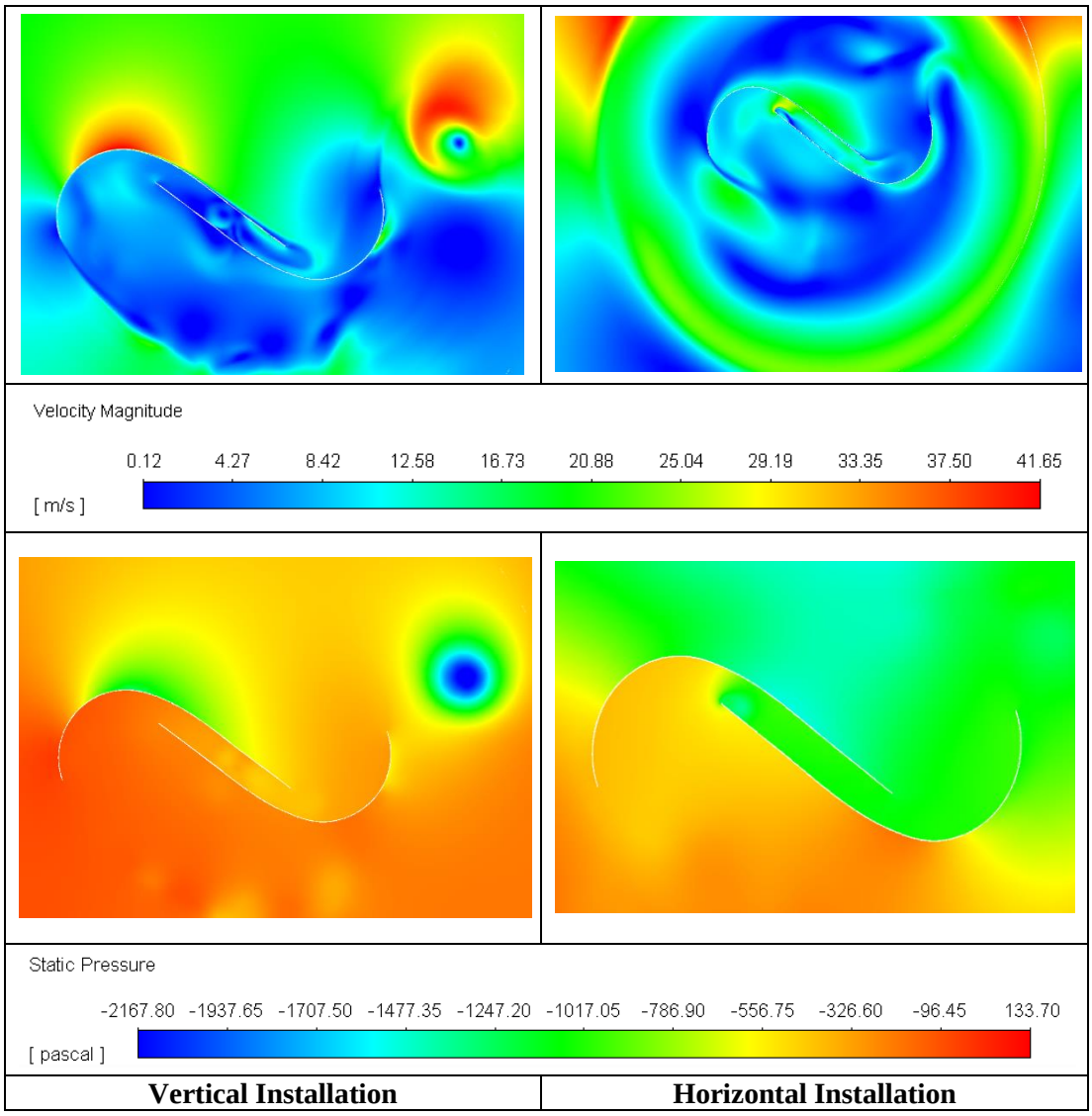

Figure 4.39: 2° Divergence-Velocity and Pressure Profiles for the Vertical and Horizontal Installation at $\emptyset = 0°$

4.6.4 Velocity-Pressure Profiles at TSR 0.8 for Azimuth Angle, $\emptyset = 45°$

Figure 4.40 presents the velocity and pressure profiles of the SSWT under the V_{Ins} and H_{Ins} at a blade azimuth angle of 45°. Similar to azimuth angle 0°, the V_{Ins} experiences a large lift generation at the rear side of the advancing blade. From the pressure profiles, the V_{Ins} shows a low-pressure region on the rear side of the advancing blade, which generates the lift effect observed in the velocity profile. Furthermore, the low-pressure development in the overlap region of the blades and rear of the advancing blade increases the lift and drag in the V_{Ins} configuration.

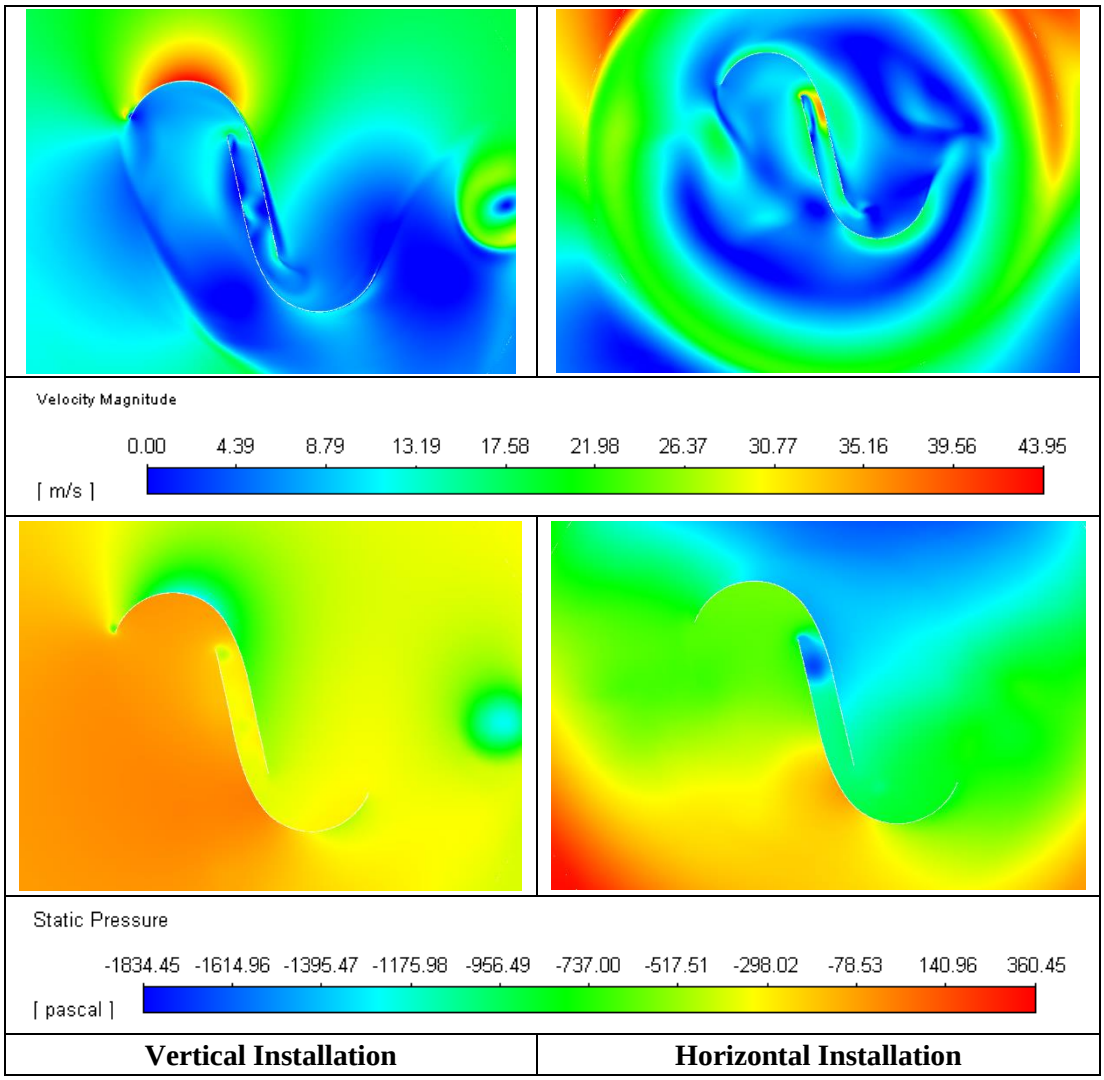

Figure 4.40: 2 Degree Divergence-Velocity and Pressure Profiles for the Vertical and Horizontal Installation at $\emptyset = 45°$

In contrast, the H_{Ins} experiences a high-velocity formation over the rotational area of the rotor with limited air attack on the blade itself. In the H_{Ins}, a low-pressure region is developed on the rear of the advancing blade, which causes a lift and drag effect on the blade. Since the pressure difference between the convex and the concave of the advancing blade in the H_{Ins} is lower than the V_{Ins}, a lower positive torque may have been generated. Moreover, the higher pressure on the convex and lower pressure at the concave of the returning blade in the H_{Ins} result in a larger pressure difference that produces higher negative torque than the V_{Ins}. These effects may have resulted in the V_{Ins} generating a higher total torque than the H_{Ins}.

4.6.5 Velocity-Pressure Profiles at TSR 0.8 for Azimuth Angle, $\emptyset = 90°$

Figure 4.41 presents the velocity and pressure profiles of the SSWT under the V_{Ins} and H_{Ins} at a blade azimuth angle of 90°. The velocity profile illustrates a high vortices region at the tip of the advancing blade in the V_{Ins}, which aids the lift generation in the configuration. However, in the H_{Ins}, a small magnitude of velocity is formed on the convex of the advancing blade, which generates limited lift. Similar to blade angles at 0° and 45°, a higher velocity region is formed over the rotating area of the rotor, resulting from a very high rotational speed.

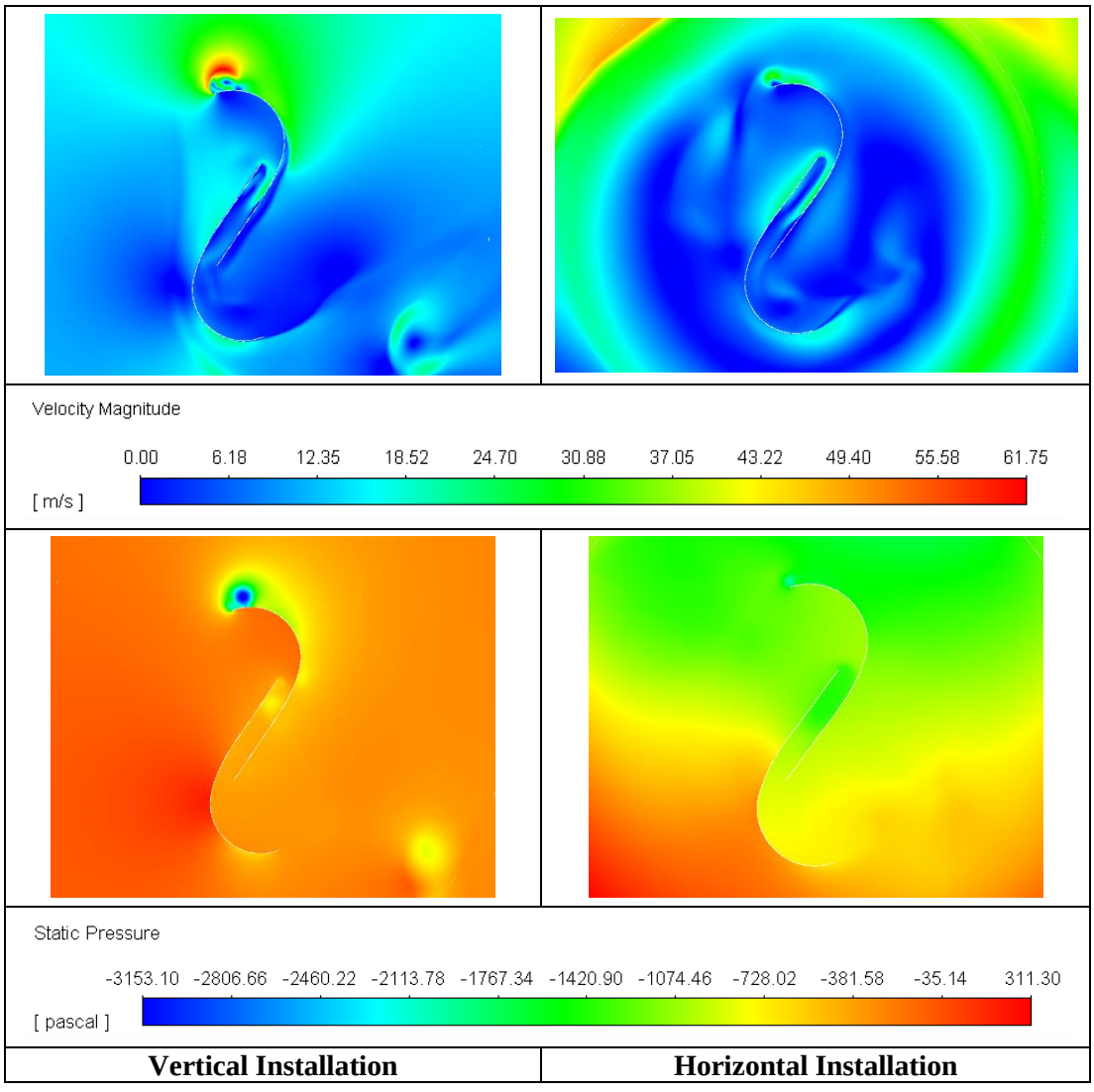

Figure 4.41: 2 Degree Divergence-Velocity and Pressure Profiles for the Vertical and Horizontal Installation at $\emptyset = 90°$

In the pressure profile of the V_{Ins}, a low-pressure wake region is formed on the tip of the advancing blade contributing to the lift generation. Furthermore, a low-pressure region is observed at the rear of the advancing blade, causing the blade to experience a drag force. The higher lift and drag experienced by the advancing blade in the V_{Ins} promote a greater positive torque generation.

In the H_{Ins}, similar pressure is encountered on both sides of the advancing blade resulting in a poor positive torque generation. In addition, the returning blade in the H_{Ins} experiences a larger pressure on the convex side and a lower pressure on the concave side, causing a high negative torque generation. The higher negative torque may have resulted in an overall poor torque generation in the H_{Ins}. On the contrary, the significant lift and drag force experienced by the advancing blade in the V_{Ins}, unlike the H_{Ins}, may have contributed to a greater overall torque generation.

4.6.6 Velocity-Pressure Profiles at TSR 0.8 for Azimuth Angle, $\emptyset = 135°$

Figure 4.42 presents the velocity and pressure profiles of the SSWT under the V_{Ins} and H_{Ins} at a blade azimuth angle of $135°$. The velocity profile of the V_{Ins} exhibits high-velocity vortices formation at the tip of the advancing blade, which contributes to the lift and drag force experienced by the blade. The pressure profile of the V_{Ins} shows a low-pressure wake region generated at the tip of the advancing blade. The pressure difference between the concave and the convex sides may have contributed to the positive torque generation.

The convex side of the returning blade in the V_{Ins} experiences a higher pressure, with a lower pressure on the concave side. This difference may have increased the negative torque experienced at this azimuth angle. However, a lower pressure region on the convex midsection of the returning blade promotes a lift generation, which may have reduced the adversity of the negative torque in the V_{Ins}.

Similar to the azimuth angles discussed above, a high-velocity region is observed flowing over the rotation area of the rotor in H_{Ins} due to the high rotational speeds that result in a wall-like characteristic towards incoming fluid flow. A poor vortices region is observed at the tip of the advancing blade, suggesting minimal lift and drag forces aiding the positive torque generation. Correspondingly, the pressure profile of the H_{Ins} suggests minimal pressure difference between the concave and convex of the

advancing blade, thus leading to a poor lift and drag experience of the blade. Moreover, the greater pressure on the convex and the lower pressure on the concave of the returning blade adversely contributes to the overall torque generation in the H_{Ins}.

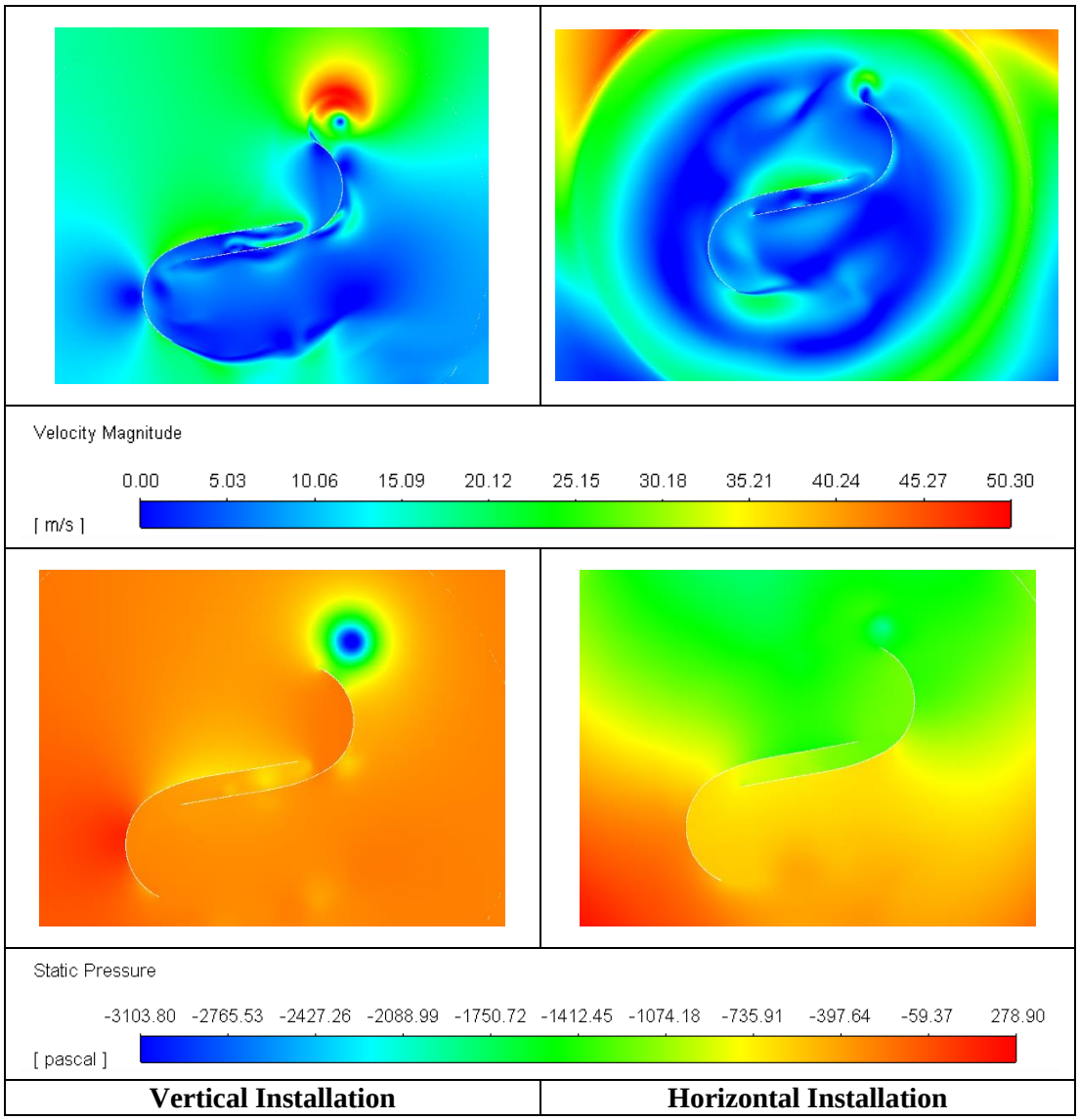

Figure 4.42: 2° Divergence-Velocity and Pressure Profiles for the Vertical and Horizontal Installation at $\emptyset = 135°$

Table 4.2: Summary of the Moment Coefficient, Performance Coefficient and Power Output Values for 0°, 1° and 2° Chimney Divergence

Div°	TSR	Cm			Cp			Power		
		V	H	% Diff	V	H	% Diff	V	H	% Diff
0	0.6	0.51	0.53	3.92	0.31	0.32	3.23	22.55	23.43	3.90
	0.8	**0.45**	**0.46**	**2.22**	**0.36**	**0.37**	**2.78**	**26.52**	**27.11**	**2.22**
	1.0	0.35	0.36	2.86	0.35	0.36	2.86	25.79	26.52	2.83
	1.2	0.24	0.25	4.17	0.29	0.30	3.45	21.22	22.10	4.15
1	0.6	0.69	0.69	0.00	0.41	0.41	0.00	157.50	157.50	0.00
	0.8	**0.64**	**0.66**	**3.13**	**0.51**	**0.53**	**3.92**	**194.78**	**200.87**	**3.13**
	1.0	0.16	0.32	100.00	0.16	0.32	100.00	60.87	121.74	100.00
	1.2	0.08	0.12	50.00	0.10	0.14	40.00	36.52	54.78	50.00
2	0.6	0.32	0.25	-21.88	0.19	0.15	-21.05	139.05	108.63	-21.88
	0.8	**0.49**	**0.20**	**-59.18**	**0.39**	**0.16**	**-58.97**	**283.89**	**115.88**	**-59.18**
	1.0	0.25	0.16	-36.00	0.25	0.16	-36.00	181.05	112.98	-37.60
	1.2	0.06	0.10	66.67	0.07	0.12	71.43	52.14	86.91	66.69

Where $\%\ \text{Diff} = \frac{(H-V)}{V} \times 100$

The C_m, C_p and power output values from the figures discussed in Section 4.4.1, Section 4.5.1 and Section 4.6.1 have been summarised in Table 4.2. The highest performance is achieved by the H_{Ins} 1° while the lowest performance is obtained by H_{Ins} 2°. The H_{Ins} performs better than the V_{Ins} except at 2° chimney divergence where the performance of the H_{Ins} is 58.97% lower than V_{Ins} for TSR 0.8. The H_{Ins} 2° generates lower torque than the V_{Ins} 2° for TSR 0.6, 0.8 and 1.2. However, the V_{Ins} 2° produces a lower torque compared to the H_{Ins} 2° at TSR 1.2, which may have been the influence of the wall-like structure in the V_{Ins} 2° at this TSR. In general, the V_{Ins} 1° and H_{Ins} 1° show a more consistent higher torque generation and performance compared to V_{Ins} 2° and H_{Ins} 2°. Although the V_{Ins} 1° and H_{Ins} 1° demonstrate a better rotor performance, the higher velocity in the V_{Ins} 2° and H_{Ins} 2° contributes to a higher power output since the generated power is directly proportional to the cube of the wind speed for a given wind turbine.

Table 4.3: Performance Analysis of the SSWT at Increasing Chimney Divergence

		0°	1°	2°
Cm	$\mathbf{V_{Ins}}$	0.45	0.64	0.49
	$\mathbf{H_{Ins}}$	0.46	0.66	0.20
Cp	$\mathbf{V_{Ins}}$	0.36	0.51	0.39
	$\mathbf{H_{Ins}}$	0.37	0.53	0.16
Power (W)	$\mathbf{V_{Ins}}$	26.52	194.78	283.89
	$\mathbf{H_{Ins}}$	27.11	200.87	115.88

Table 4.3 presents the performance analysis of the diverging chimneys in comparison to the cylindrical chimney. The torque generation, performance and power output for the cylindrical chimney demonstrates a slightly better outcome for the H_{Ins} 0° than the V_{Ins} 0°. The increase in chimney divergence by 1° improves the SSWT performance for both V_{Ins} 1° and H_{Ins} 1°. However, at 2° chimney divergence, the performance coefficient achieved is lower for the H_{Ins} 2°. The maximum power output is obtained from the V_{Ins} 2°, where the power is enhanced by 10.7 times compared to V_{Ins} 0° mainly due to the increased velocity. However, the H_{Ins} 2° performs adversely compared to H_{Ins} 0° and H_{Ins} 1°, respectively.

Since the power production is the cube of the wind speed, the H_{Ins} 2° manages to produce a power output 4.27 times higher than the H_{Ins} 0°, but the degraded power coefficient compared to the H_{Ins} 1° (e.g., 0.30 times lower) results in the H_{Ins} 1° to be 1.73 times higher than the H_{Ins} 2°. Meanwhile, at 1° divergence, both V_{Ins} 1° and H_{Ins} 1° show higher stability in performance where the power augmentations improved by 7.34 times and 7.41 times (e.g., 634.46% and 640.94%) compared to V_{Ins} 0° and H_{Ins} 0°, respectively. Table 4.2 and Table 4.3 suggest that the 1° chimney divergence provides a more consistent higher power augmentation for both V_{Ins} and H_{Ins} across all the TSRs compared to the 2° chimney divergence.

4.7 Performance Analysis of the SSWT Under the Influence of Guide Vanes and Shield (GVS) at 0° Divergence

This section presents the results obtained from the analysis of the SSWT under the influence of the guide vanes and shield (GVS) in a cylindrical chimney. The operation

of the SSWT with the GVS is investigated at TSR 0.8 for its performance characteristics under the conventional vertical axis of operation. The moment coefficient, performance coefficient, and power output of the turbine are presented and discussed. The instantaneous moment coefficient and performance coefficient for one complete turbine rotation for all configurations are compared and studied at TSR 0.8, respectively. The velocity and pressure profiles of each GVS angle are compared and analysed. The performance enhancement of the SSWT is determined by comparing the SSWT with GVS, and SSWT without GVS, where values are obtained from Section 4.4.1.

4.7.1 C_m, C_p and Power Output for Guide Vanes and Shield (GVS) at TSR 0.8

Figure 4.43 presents the coefficient of moment for the SSWT under the influence of the GVS in a cylindrical chimney at TSR 0.8. The SSWT was investigated with GVS at angles 0°, 22.5° and 45°. The lowest moment coefficient is obtained by GVS at 0° with 0.32, while the highest moment coefficient is attained at GVS 45° with 0.55. From Table 4.2, the moment coefficient obtained for V_{Ins} 0° is 28.89% higher than GVS 0° and 13.33% greater than GVS 22.5°. However, the moment coefficient in GVS 45° is 22.22% higher than that obtained by the V_{Ins} 0°. The enhancement may be due to the angle of the guide vane, 45°, which increases the air attack on the advancing blade of the SSWT, causing an increase in positive torque generation.

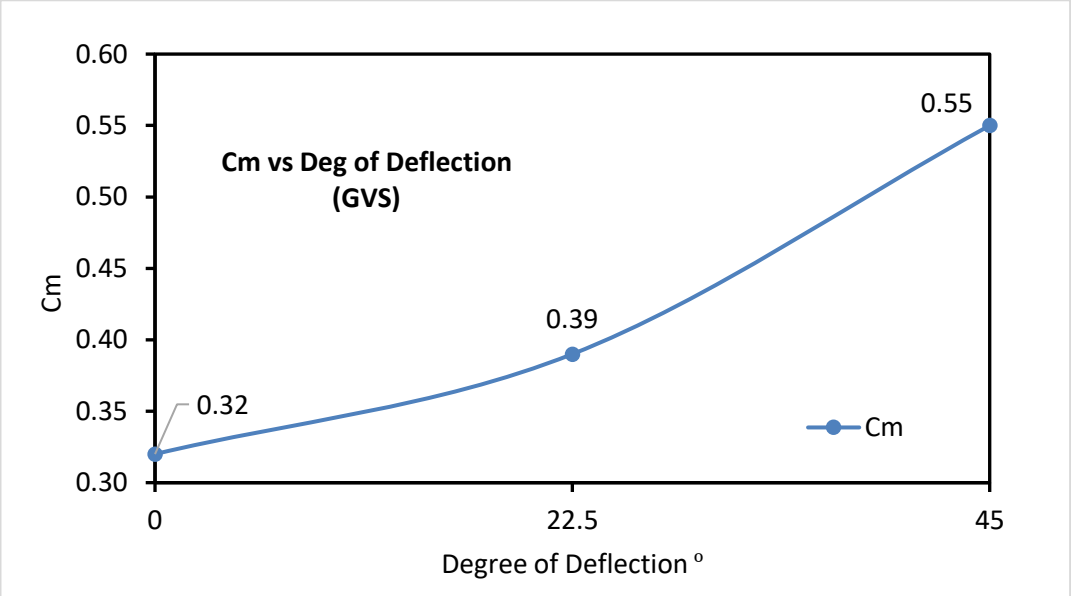

Figure 4.43: Coefficient of Moment of the Guide Vane and Shield for the Vertical Installation in a 0° Chimney Divergence at TSR 0.8

Figure 4.44 presents the coefficient of performance for the SSWT under the influence of the GVS in a cylindrical chimney at TSR 0.8. The performance obtained by GVS 0° and GVS 22.5° is 28.89% and 13.33% poorer than the V_{Ins} 0°. Nevertheless, GVS 45° improves the performance of the SSWT by 22.22% compared to the V_{Ins} 0°. The performance enhancement may have been the influence of higher positive torque generation that increases the overall torque production in the SSWT.

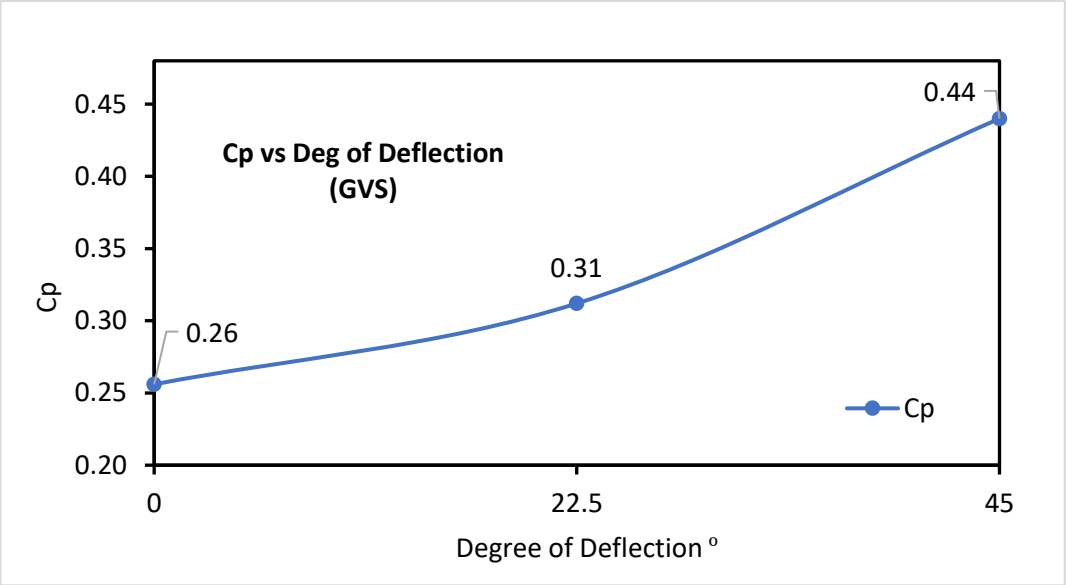

Figure 4.44: Coefficient of Performance of the Guide Vane and Shield for the Vertical Installation in a 0° Chimney Divergence at TSR 0.8

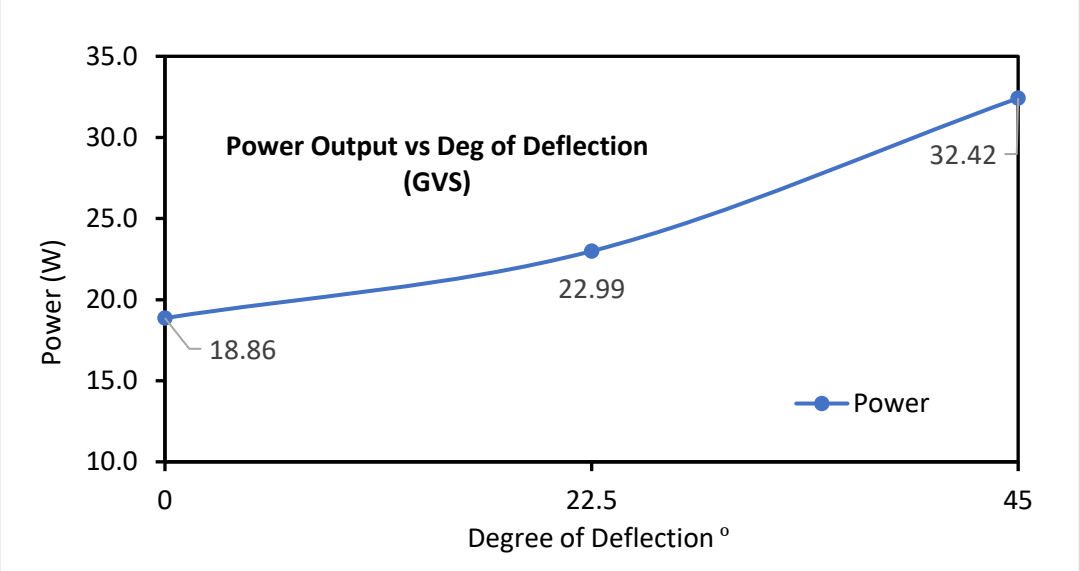

Figure 4.45: Power Output of the Guide Vane and Shield for the Vertical Installation in a 0° Chimney Divergence at TSR 0.8

Figure 4.45 presents the power output for the SSWT under the influence of the GVS in a cylindrical chimney at TSR 0.8. The power generated by the SSWT in GVS 0° and GVS 22.5° is 28.88% and 13.31% lesser than the V_{Ins} 0°. Nevertheless, with GVS 45°, the performance of the SSWT was enhanced by 18.2% compared to V_{Ins} 0°. GVS 45° outperformed GVS 0° and GVS 22.5° by 71.9% and 41.02%, respectively. Sections 4.7.3, 4.7.4, 4.7.5 and 4.7.6 discuss the velocity and pressure characteristics of the GVS at four different blade azimuth angles.

4.7.2 Instantaneous C_m and C_p for Guide Vanes and Shield (GVS) at TSR 0.8

Figure 4.46 presents the instantaneous moment coefficient of the SSWT with guide vane and shield at TSR 0.8. The SSWT with GVS 45° shows a larger amplitude, followed V_{Ins} 0°, GVS 22.5° and GVS 0°, respectively. The larger amplitude suggests that the torque generation in GVS 45° is the highest while GVS 0° is the lowest. GVS 45° may have increased the air attack on the advancing blade, hence creating a higher torque compared to the V_{Ins} 0°. However, at GVS 22.5° and GVS 0°, the lower amplitude suggests that the angle of the guide vanes may have promoted blocking characteristics that reduced the air attack on the advancing blade, thus reducing the torque production. However, all three GVS configurations show lower negative torque generation at azimuth angles 110 degrees to 160 degrees and 300 degrees to 350 degrees compared to V_{Ins} 0°. The reduction in negative torque may have been the influence of the shield, which suppresses the pressure in the rotating region. The pressure suppression may have reduced the pressure on the convex of the advancing blade, hence improving the torque production.

Figure 4.47 presents the instantaneous performance coefficient of the SSWT with guide vane and shield at TSR 0.8. The highest performance is achieved by GVS 45° with larger amplitude, followed by V_{Ins} 0°, GVS 22.5° and GVS 0°. The performance achieved by the four different configurations results from the torque production shown in Figure 4.46. The performance of V_{Ins} 0° at azimuth angles 110 degrees to 160 degrees and 300 degrees to 350 degrees is lower than GVS 45°, GVS 22.5° and GVS 0°, which suggests that the presence of the guide vanes and shield improves the performance of the rotor. However, at azimuth angles 0 degrees to 80 degrees and 180 degrees to 270 degrees, the performance of the V_{Ins} 0° is better than GVS 22.5° and GVS 0°, which suggests that the angle of the guide vane may have demoted the air

attack on the advancing blade and reduced the torque generation. Consequently, GVS 45° may have improved the performance of the rotor compared to V_{Ins} 0° due to the guide vane angle that increased air attack on the advancing blade, and the shield, which suppressed the pressure on the rotor in the rotating region, hence enhancing the total torque generation.

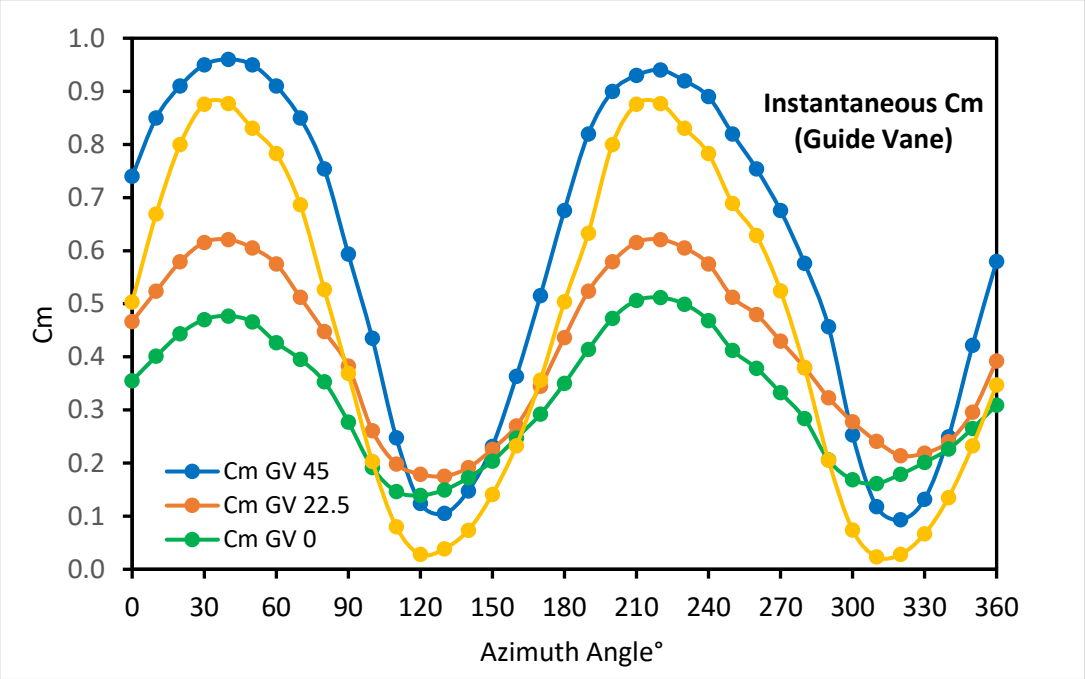

Figure 4.46: Instantaneous C_m for SSWT with Guide Vanes and Shield

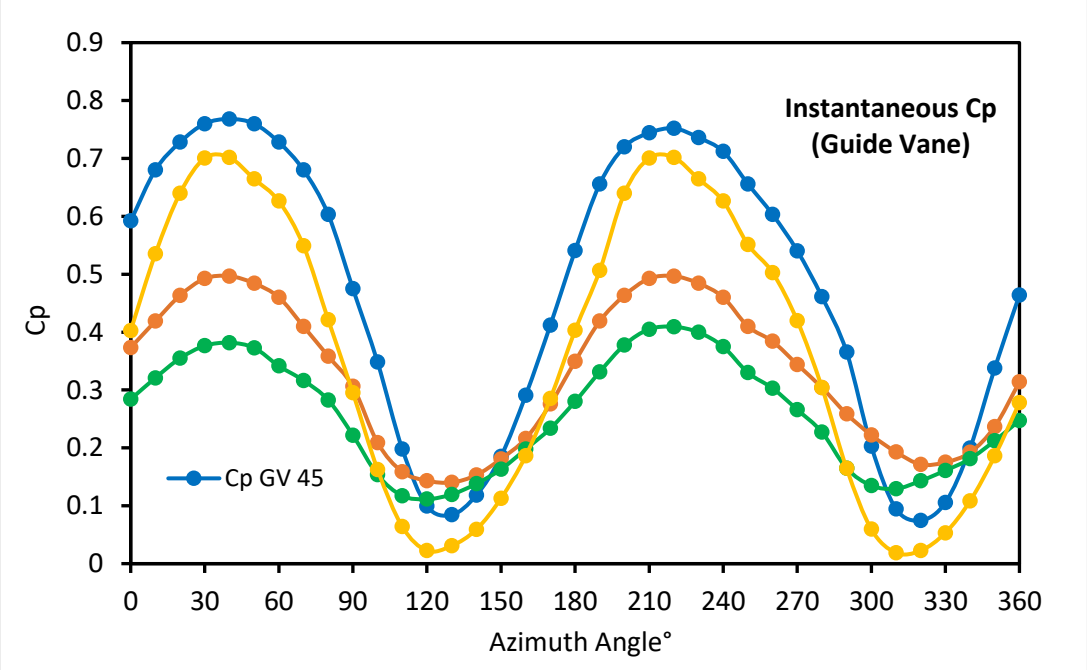

Figure 4.47: Instantaneous C_p for SSWT with Guide Vanes and Shield

4.7.3 Velocity-Pressure Profiles at TSR 0.8 for Azimuth Angle, $\emptyset = 0°$

Figure 4.48 presents the velocity and vector profiles of the SSWT under the influence of the GVS at an azimuth angle of 0°. The highest velocity formation on the advancing blade in the GVS 45° compared to GVS 0° and GVS 22.5° may have resulted in a stronger lift generation. The vector plots suggest that a greater GVS angle led to a more concentrated airflow towards the advancing blade.

At GVS 0° and GVS 22.5°, the guide vane angle channels the airflow away from the turbine blade, thus reducing the air attack on the blade. However, the larger angle of GVS 45° diverts a larger volume of airflow towards the advancing blade, thus increasing the torque generation by the blade. Moreover, the shield attached with the GV retained the flow within the rotating region, promoting the lift generation of the advancing blade. Increasing the length of the guide vane may improve the airflow diversion towards the turbine blades, which will be kept as future work.

Figure 4.49 presents the pressure profiles of the SSWT under the influence of the GVS at an azimuth angle of 0°. At GVS 22.5° and GVS 45°, a more prominent low-pressure region is observed at the rear of the advancing blade compared to GVS 0°, contributing to the lift generation. At GVS 22.5°, the rotational region experiences a very high pressure (suppressed pressure due to shield effect) with slightly low pressure at the rear of the advancing blade, which may have caused a higher pressure difference between the concave and convex of the advancing blade leading to a better performance than GVS 0°. The same shield effect is present in GVS 45°, promoting the returning blade to experience a larger pressure difference between the convex and concave sides, leading to lower negative torque generation compared to GVS 0° and GVS 22.5°.

At the tip of the returning blade, a low wake pressure point is formed for all three GVS angles. The strongest low-pressure wake point is observed at GVS 45°, which may have created a stronger drag and lift force on the returning blade. The weakest low-pressure wake point is observed at GVS 0° since the pressure difference between the convex and concave of the returning blade is not as significant as that of GVS 22.5° and GVS 45°, thus leading to a lower drag experience in comparison to the other two GVS angles. The larger pressure differential between the concave and convex of the

advancing and returning blade of GVS 45° may have promoted a higher lift and drag generation than GVS 0° and GVS 22.5°, thus having a higher total torque generation and better performance.

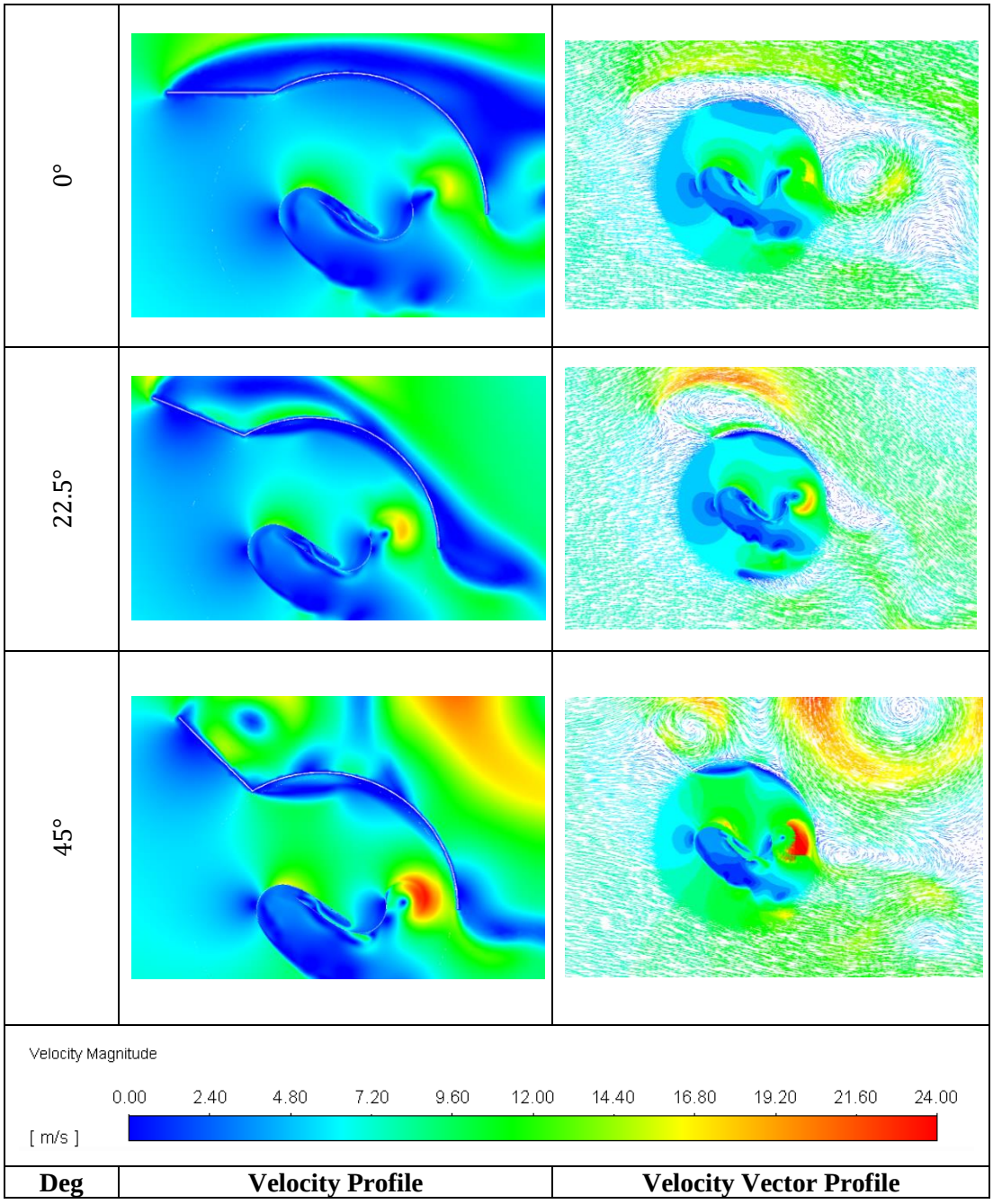

Figure 4.48: Comparison of the Velocity and Vector Profiles of the Guide Vane and Shield at $\emptyset = 0°$

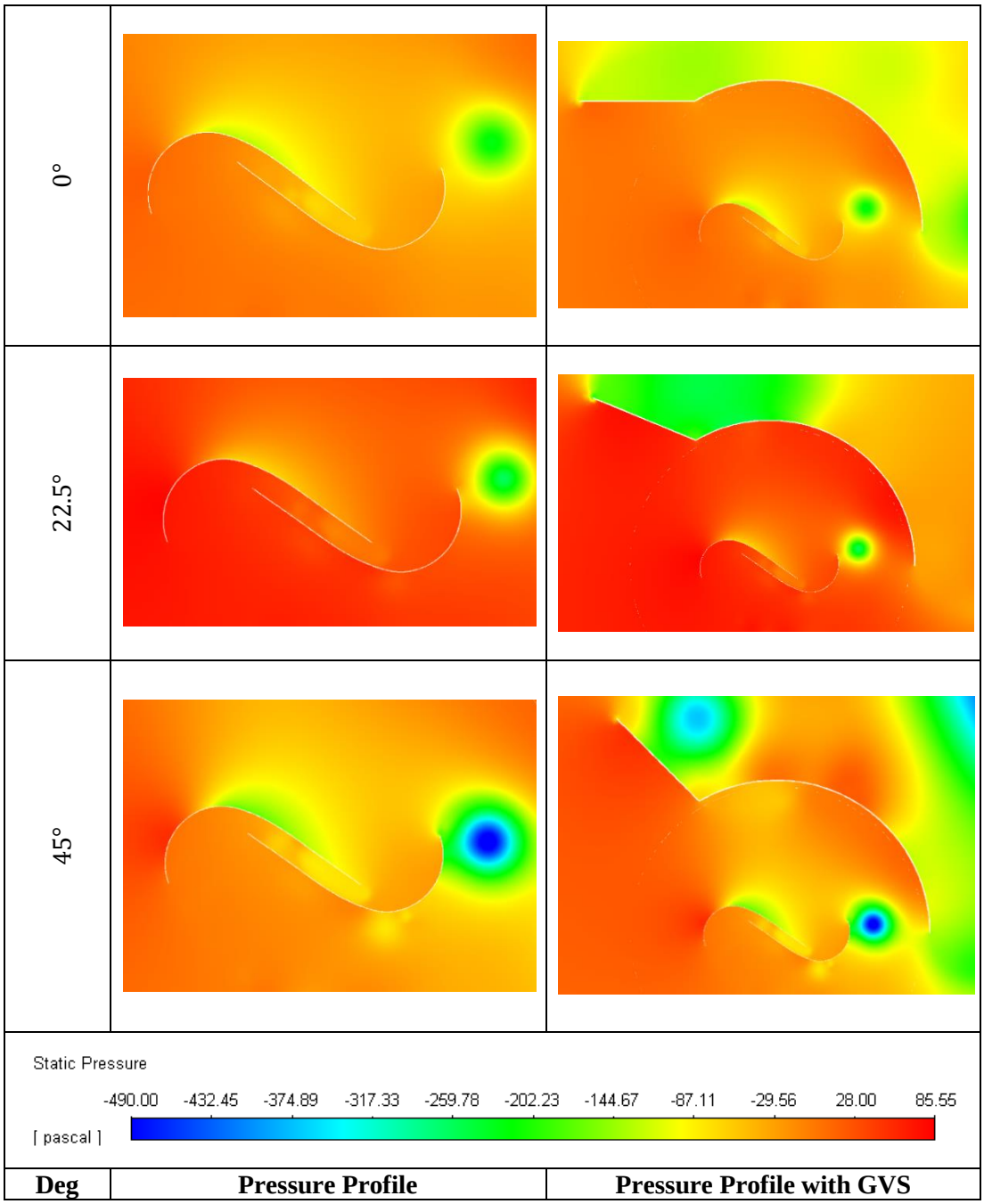

Figure 4.49: Comparison of the Pressure Profiles of the Guide Vanes at $\emptyset = 0°$

4.7.4 Velocity-Pressure Profiles at TSR 0.8 for Azimuth Angle, $\emptyset = 45°$

Figure 4.50 presents the velocity and vector profiles of the SSWT under the influence of the GVS at a blade azimuth angle of 45°. The highest lift generation is observed at GVS 45° while the lowest at GVS 0°. A strong velocity vortices is observed leaving the tip of the returning blade at GVS 45° compared to GVS 0° and GVS 22.5°, which suggests that the blade experienced the strongest drag force.

The shield encompassing the fluid flow within the rotating region benefits the returning blade by increasing the air attack on the blade. The trapped fluid in the shield exerts a force on the concave of returning blade when it flows downwards and outwards from the rotating region. Since the entrapped fluid is the highest in GVS 45° due to the larger fluid diversion by the 45° guide vane into the rotating region, this configuration may have experienced a higher air attack, followed by GVS 22.5° and GVS 0°, respectively. The influence of the GVS 45° on the diversion of fluid into the rotating region can be observed better in the vector plots, which further suggests a higher fluid flow velocity surrounding the advancing blade compared to GVS 22.5° and GVS 0°. The angle of GVS 22.5° is demonstrated to be insufficient to divert the fluid at an angle that beneficially attacks the advancing blade. Moreover, the velocity and vector plots portray that angle GVS 0° not only limits the channelling of the fluid towards the advancing blade but, in fact, it inhibits more fluid from accessing the rotating region of the blade. Consequently, the higher lift generation and lower negative torque production in GVS 45° may have resulted in a higher total positive torque generation, thus improving the performance compared to the V_{Ins} 0°, GVS 22.5° and GVS 0°.

Figure 4.51 presents the pressure profiles of the SSWT under the influence of the GVS at a blade azimuth angle of 45°. From the pressure profiles, a low-pressure region is observed on the advancing blades in all GVSs, where GVS 45° is at the lowest. The largest pressure difference between the concave and convex of the advancing blade is experienced with GVS 45°, where the highest lift formation is noticed, followed by GVS 22.5° and GVS 0°. Furthermore, the lowest wake pressure point and the highest pressure difference between the convex and concave of the returning blade is observed with GVS 45°, thus increasing the drag and lift force experienced compared to GVS 22.5° and GVS 0°. Although a lower pressure region is observed at the rear of the advancing blade in GVS 0°, the pressure plot illustrates that a larger pressure is present in the rotating region of the blades in GVS 22.5° due to the effect of the shield and guide vane.

The greater pressure difference between the convex and the concave of the advancing blade in GVS 22.5° may have influenced a higher torque generation in GVS 22.5° compared to GVS 0°. The lower pressure region at the back (above the GVS) of the

GV 22.5° suggests that the fluid may have been diverted away from the rotating region, thus reducing the blade's performance in GVS 22.5° compared to GVS 45°.

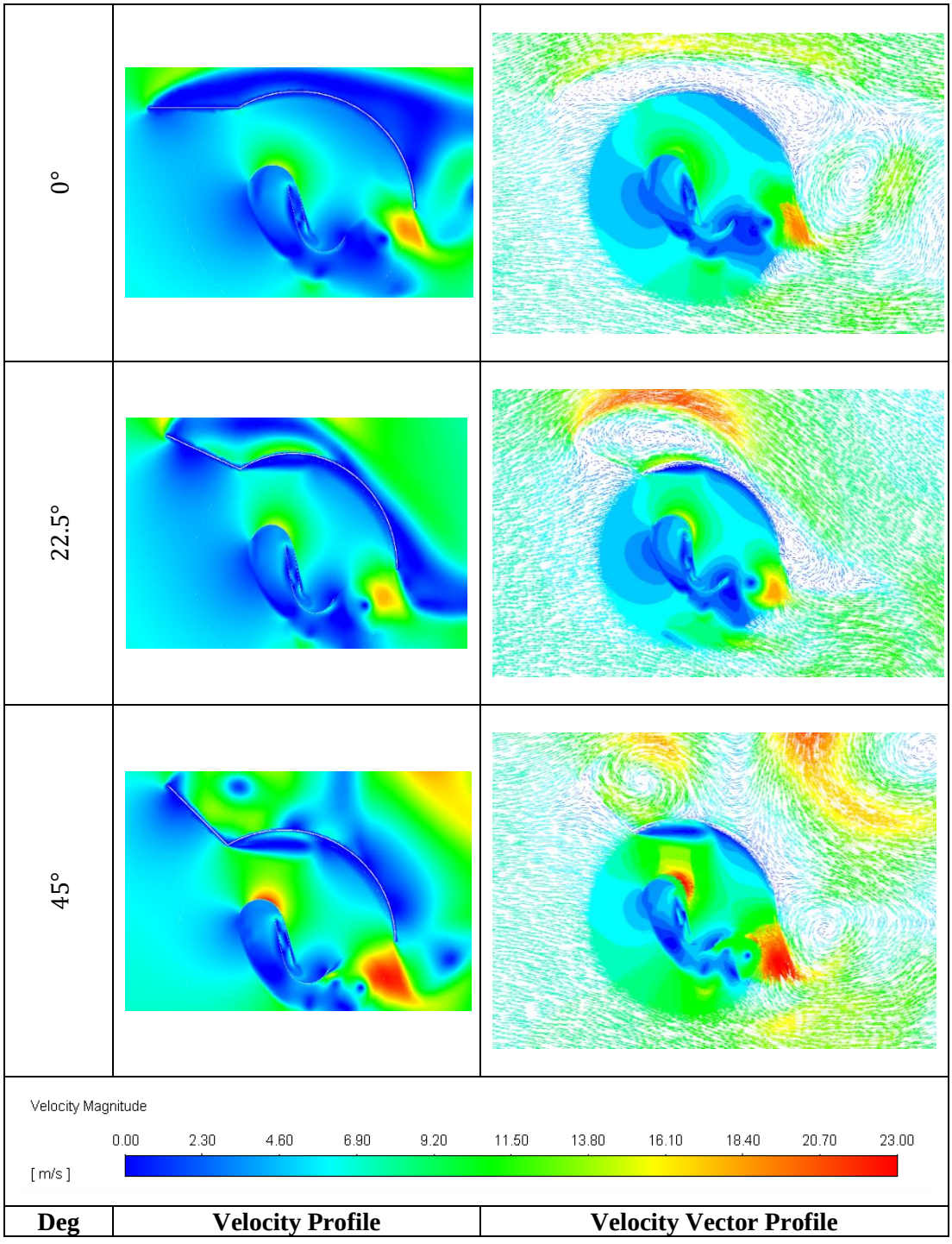

Figure 4.50: Comparison of the Velocity and Vector Profiles of the Guide Vanes at $\emptyset = 45°$

At GVS 45°, the guide vane allows a higher fluid flow into the rotating region that is suppressed by the shield. The fluid flow suppression results in a lower pressure region

at the convex side of the advancing blade, increasing the pressure difference between the concave and convex, thus promoting a higher positive torque generation than GVS 22.5° and GVS 0°.

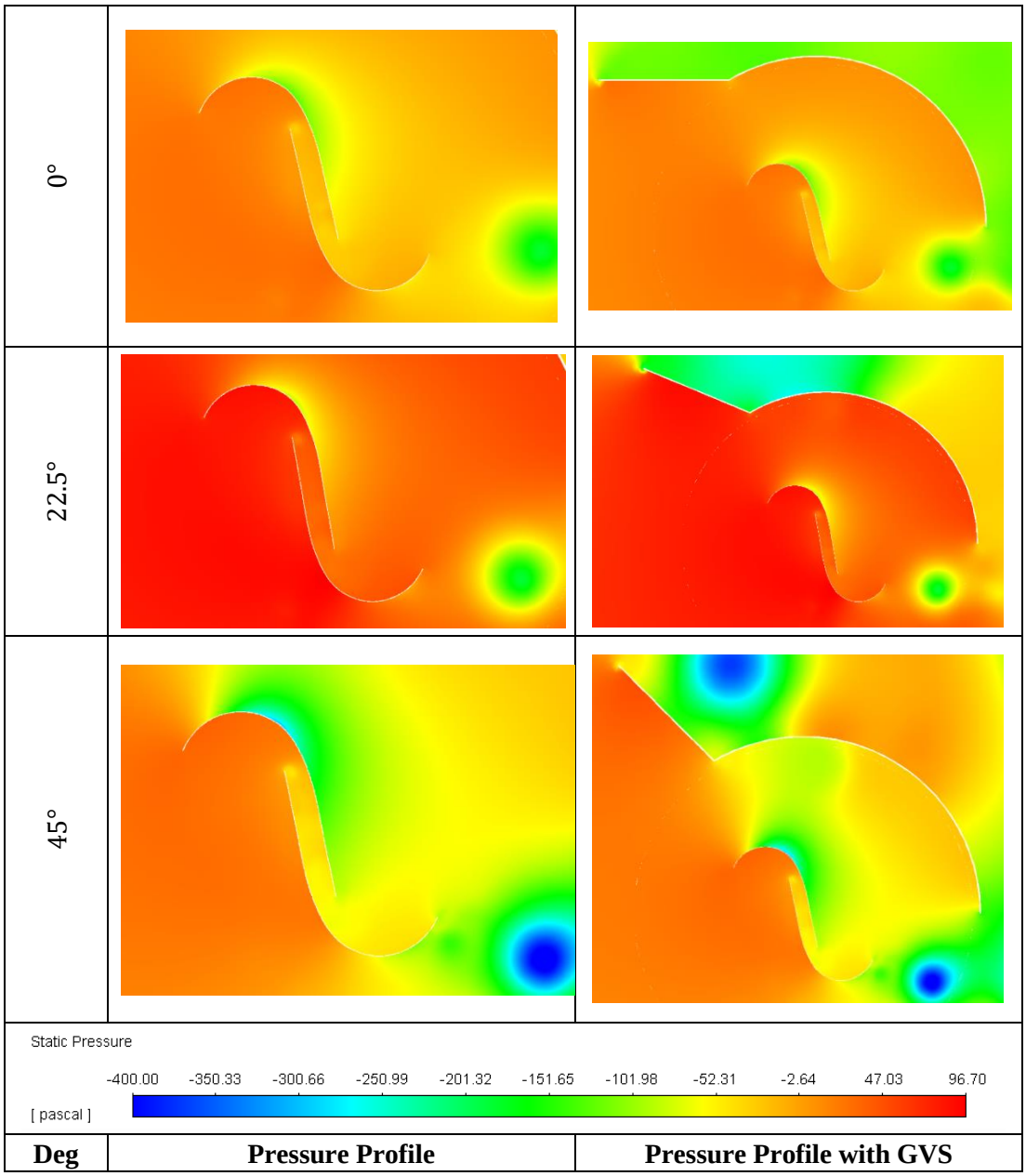

Figure 4.51: Comparison of the Pressure Profiles of the Guide Vanes at $\emptyset = 45°$

In addition, the suppressed pressure region (due to the shield) also caused a low-pressure region experienced by the convex tip area of the returning blade, generating lift and drag, which may have reduced the negative torque produced in GVS 45°. The highest overall drag and lift force experienced due to the higher difference in pressure between the convex and concave in GVS 45° may have contributed to better performance compared to the V_{Ins} 0°, GVS 22.5° and GVS 0°.

4.7.5 Velocity-Pressure Profiles at TSR 0.8 for Azimuth Angle, $\emptyset = 90°$

Figure 4.52 presents the velocity and vector profiles of the SSWT under the influence of the GVS at a blade azimuth angle of 90°. The highest tip vortices are observed to be experienced by the advancing blade in GVS 45° followed by GVS 22.5° and GVS 0°, thus aiding the lift formation of the blade. Moreover, the velocity formation at the rear of the advancing blade is the largest in GVS 45° followed by GVS 22.5° and GVS 0°, which may have improved the drag and lift formation of GVS 45° compared to GVS 22.5° and GVS 0°.

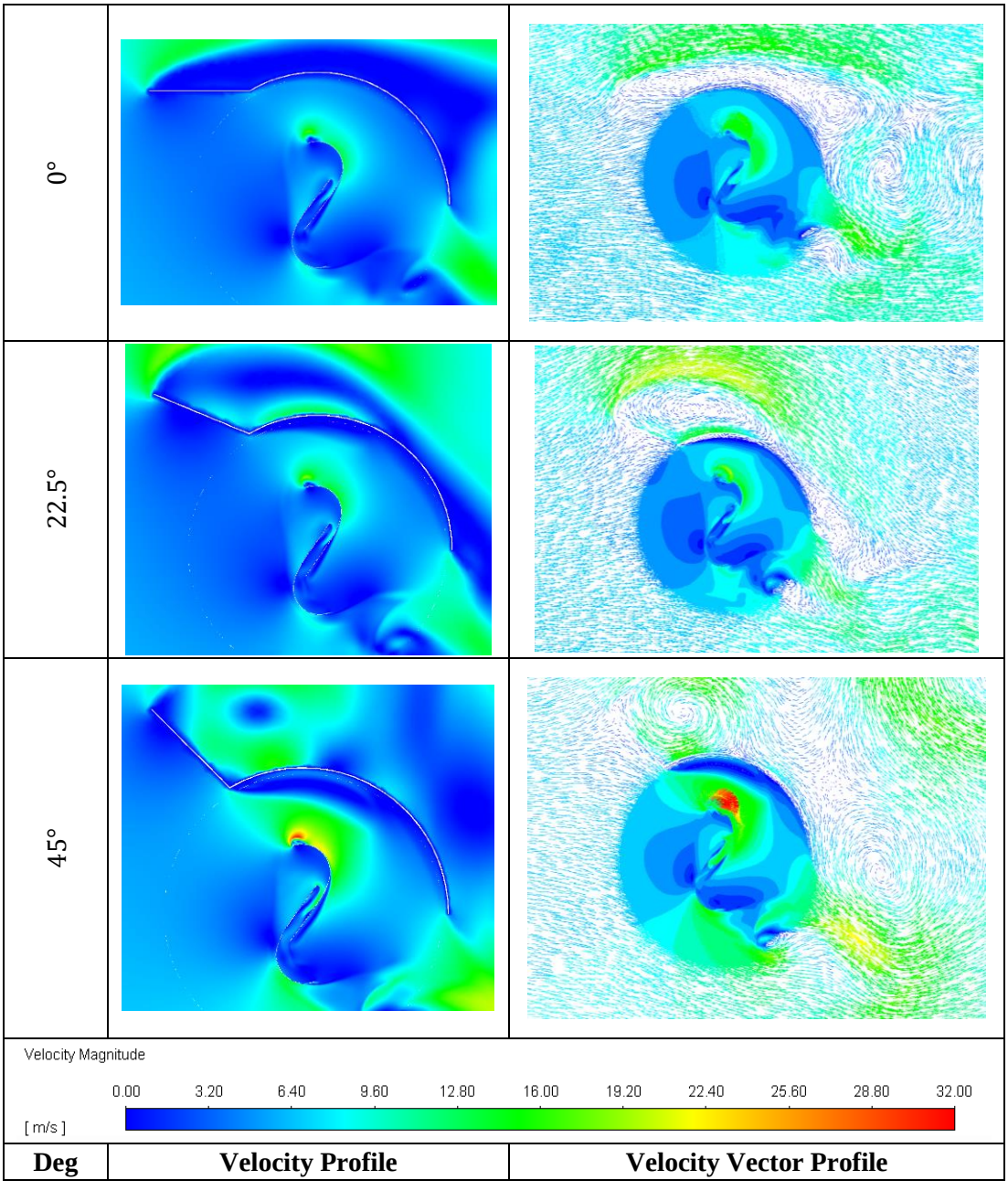

Figure 4.52: Comparison of the Velocity and Vector Profiles of the Guide Vanes at $\emptyset = 90°$

The GVS 0° and GVS 22.5° angles adversely affect the drag and lift formation, as the angle of the GV inhibits fluid flow into the rotating region for GVS 0°, and reduces fluid flow attack on the blade in GVS 22.5°. The fluid recirculation behind the GV (above GVS) in GVS 22.5° promotes the incoming fluid to flow over the guide vane and away from the rotating region in GVS 22.5°. Thus, this possibly cause a lower fluid volume attack on the advancing blade in GVS 22.5°, leading to a lower positive torque generation. In the GVS 0°, recirculation of the fluid is absent. However, the angle of the GV blocks a higher fluid flow into the turbine region, which may have caused a lower torque generation due to lower air attacks on the turbine blades.

The angle of the GV in GVS 45° benefits the positive torque generation as a greater fluid volume is channelled towards the advancing blade. As such, the adverse recirculation effect behind the GV in GVS 45° on the turbine blade's performance is less prominent than that in GVS 22.5°. The formation of higher lift and drag on the advancing blade in GVS 45° may have improved the overall torque generation compared to V_{Ins} 0°, GVS 22.5° and GVS 0°.

Figure 4.53 presents the pressure profiles of the SSWT under the influence of the GVS at an azimuth angle of 90°. The lowest wake pressure point is observed with GVS 45°, followed by GVS 22.5° and GVS 0°, which contributes to the lift generation of the advancing blade. Moreover, the lower pressure region formation at the rear of the advancing blade with GVS 45° being the lowest improves the drag experienced by the advancing blade. The high-pressure difference between the convex and concave sides experienced by the advancing blade in GVS 45° may have resulted from a higher fluid concentration towards the blade than GVS 22.5° and GVS 0°, which may have improved the positive torque generation in the configuration.

The shield's effect on the blades in GVS 0° is minimal as limited fluid flow is diverted into the rotating region. As a result, the pressure difference between the concave and the convex of the advancing blade is lower than GVS 22.5° and GVS 45°. In GVS 22.5°, a higher pressure difference is observed between the concave and convex of the advancing blade that may have improved the performance of the blades compared to GVS 0°. However, the lower pressure region above the shield suggests that more fluid flows to the outer region away from the turbine blades, which may have resulted in a lower positive torque generation in GVS 22.5° compared to GVS 45°.

The increased fluid flow into the rotating region in GVS 45° promotes a better air attack on the advancing blade than GVS 22.5° and GVS 0°, which is observed through the lower pressure region on the convex of the advancing blade. The suppressed pressure within the shield in GVS 45° enhances the drag and lift effect experienced by the advancing blade, unlike the blades in GVS 22.5° and GVS 0°. Also, the fluid flow channelled out of the shield at a higher velocity (refer to vector plot in Figure 4.52) results in a low-pressure region at the rear of the returning blade. The low-pressure region improves the drag formation at the convex of the returning blade, which reduces the negative torque generated.

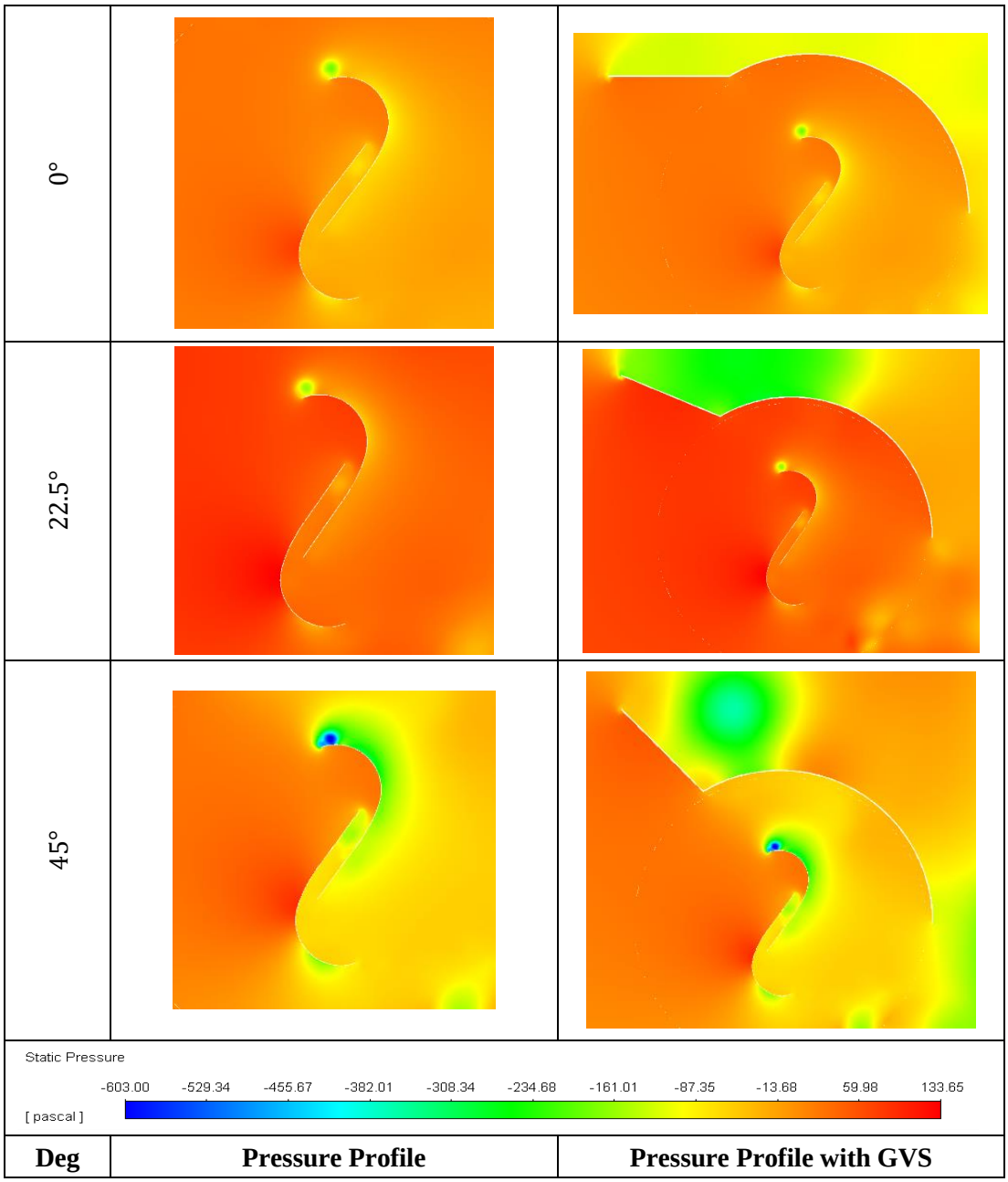

Figure 4.53: Comparison of the Pressure Profiles of the Guide Vanes at $\emptyset = 90°$

In addition, the higher fluid flow attacking the concave of the advancing blade creates a lower pressure region on the concave of the returning blade (due to fluid flow through the overlap gap). This effect, specifically in the overlap gap of the SSWT with GVS 45°, is not prominently seen with GVS 22.5° and GVS 0°. The higher pressure difference between the concave and convex of the returning blade creates a higher drag experienced by the SSWT with GVS 45°, thus reducing the impact of the negative torque generated, contributing to the improved performance of the turbine compared to V_{Ins} 0°, GVS 22.5° and GVS 0°.

4.7.6 Velocity-Pressure Profiles at TSR 0.8 for Azimuth Angle, $\emptyset = 135°$

Figure 4.54 presents the velocity and vector profiles of the SSWT under the influence of the GVS at a blade azimuth angle of 135°. At GVS 45°, the angle of the GV promotes the fluid to flow concentratedly towards the advancing blade compared to GVS 22.5° and GVS 0°, thus causing higher positive torque generation, followed by GVS 22.5° and GVS 0°. The trapped fluid flow in the GVS is forced to exit at the shield end, which causes a higher air attack on the concaves of the advancing blade. Since the fluid volume directed towards the advancing blade is the highest in GVS 45° compared to GVS 22.5° and GVS 0°, the highest tip vortices is formed in this configuration.

On the contrary, the channelled fluid flow in GVS 45° also increases the air attack on the convex of the returning blade. The fluid flow attacking the convex of the blade increases the negative torque experienced by the GVS 45° compared to that in GVS 22.5° and GVS 0°. This effect observed in GVS 22.5° and GVS 0° is less prominent than that in GVS 45°, which may have caused the GVS 45° to produce a lower overall torque. Nevertheless, the implementation of GVS 45° still performs better than V_{Ins} 0°, which may be the contribution of the higher positive torque generation by the advancing blade.

In GVS 0°, the GVS characteristic causes a blockage effect that inhibits the fluid from flowing freely into the turbine region. Due to the zero degree angle, the fluid flow does not accelerate towards the advancing blade, thus reducing the positive torque generation. However, in the presence of the shield, the flow is retained within the

rotating region in GVS 0°, causing a lift and drag formation on the advancing blade. This effect may have aided GVS 0° in a higher positive torque generation than V_{Ins} 0°.

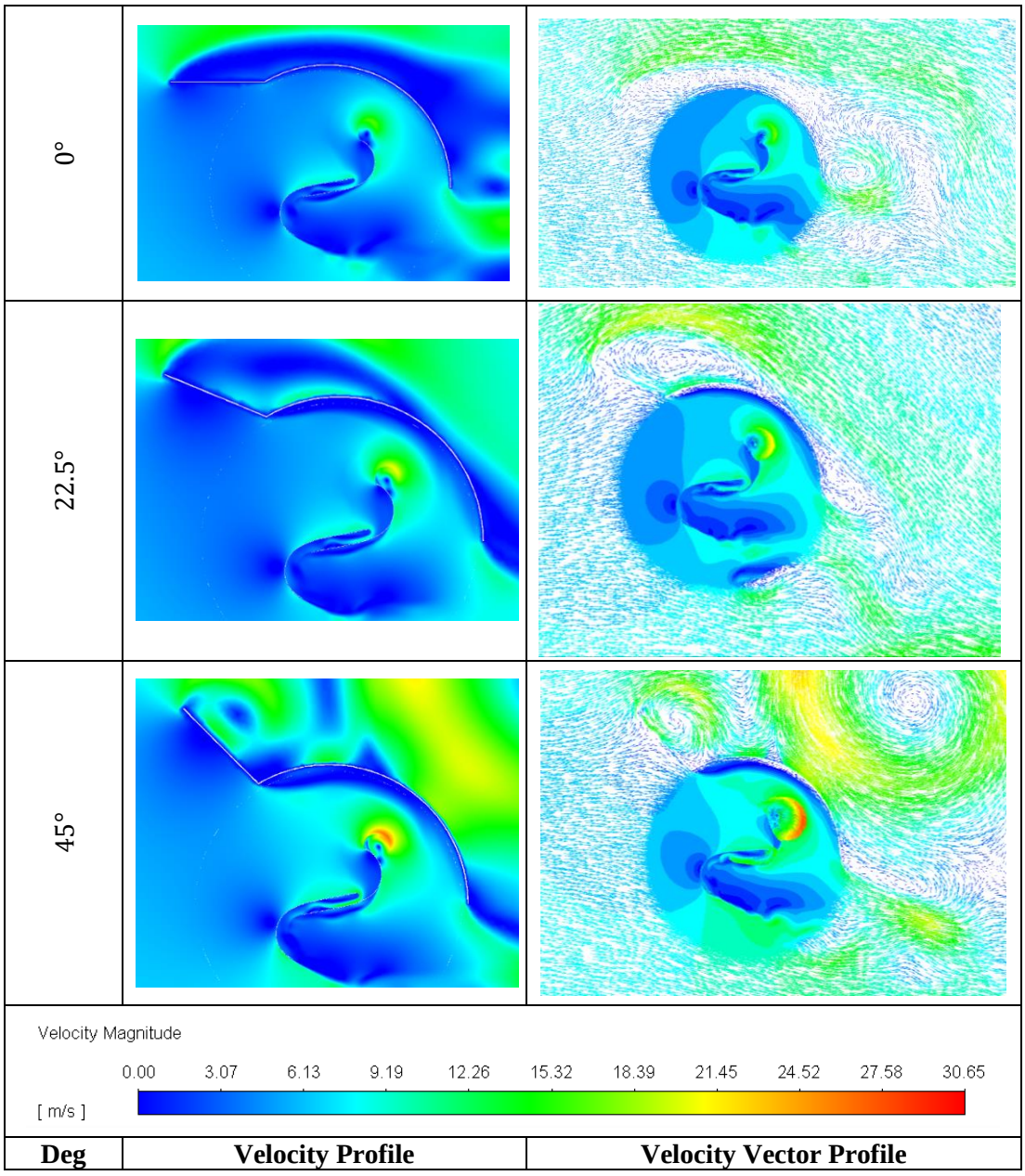

Figure 4.54: Comparison of the Velocity and Vector Profiles of the Guide Vanes at $\emptyset = 135°$

In GVS 22.5°, the angle of the GV channels the fluid towards the advancing blade, with which lift and drag are experienced. However, fluid is diverted upwards and away from the advancing blade, which may have inhibited a higher positive torque generation. Nevertheless, since the angle of GVS 22.5° reduces the fluid's impact on the returning blade, lesser negative torque may have been generated compared to GVS 45°and V_{Ins} 0°. Moreover, the higher positive torque production and lower negative

torque generation compared to V_{Ins} 0°, GVS 0° and GVS 45° may have caused it to have the highest overall torque generation and performance at this azimuth angle.

Figure 4.55 presents the pressure profiles of the SSWT under the influence of the GVS at a blade azimuth angle of 135°. The lowest wake pressure point is identified at GVS 45°, where the highest lift is generated, followed by GVS 22.5° and GVS 0°. Moreover, the advancing blade with GVS 45° experiences the highest pressure difference between the concave and convex of the blade, which may have resulted in increased drag and lift force compared to GVS 22.5° and GVS 0°.

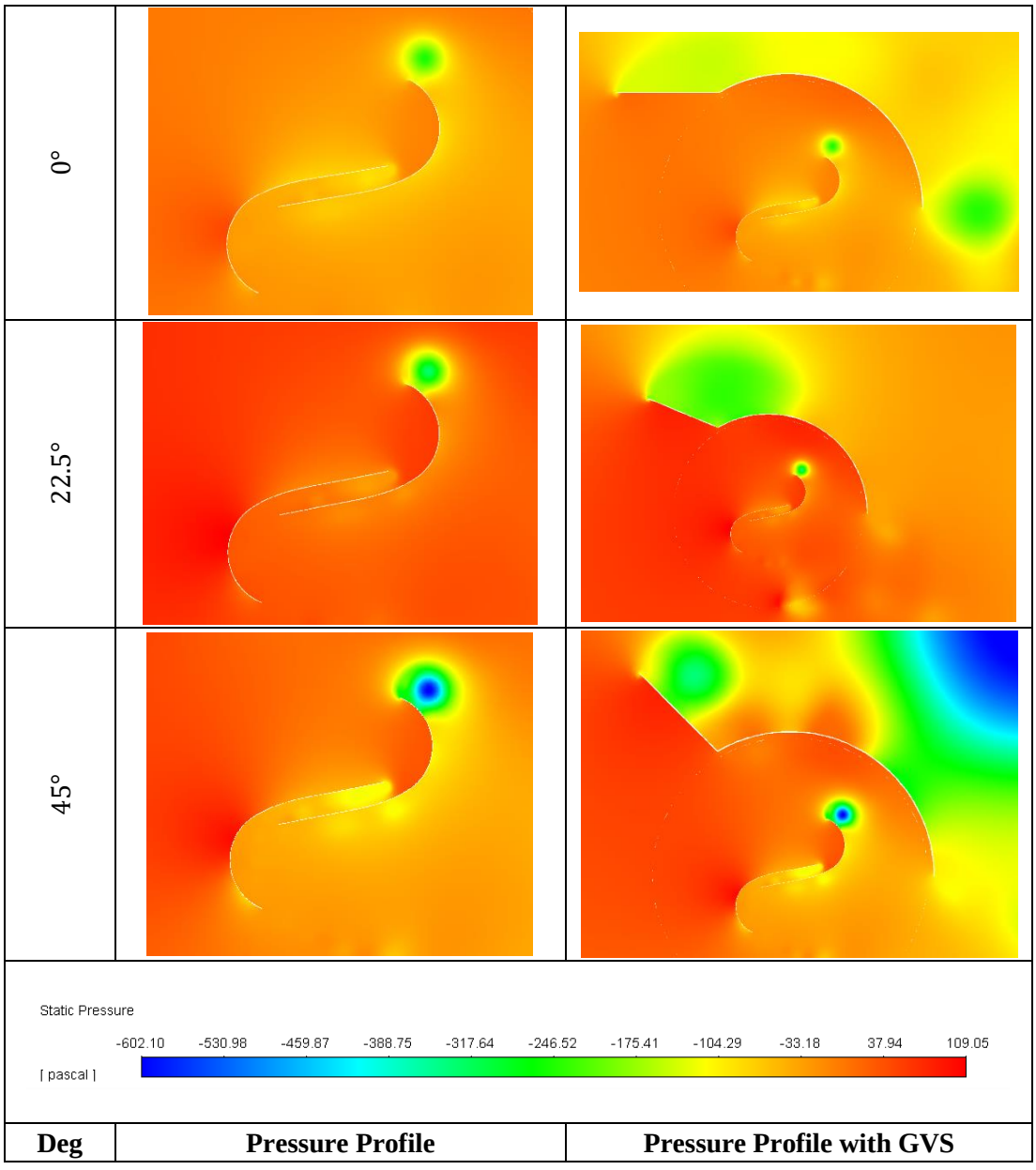

Figure 4.55: Comparison of the Pressure Profiles of the Guide Vanes at $\emptyset = 135°$

However, the accelerated fluid flow towards the convex of the returning blade (due to the GV angle) creates a high-pressure region that adversely affects the returning blade in GVS 45° compared to GVS 22.5° and GVS 0°. This effect is not as prominent in GVS 22.5° and GVS 0°, thus resulting in a lower negative torque generation by the returning blade compared to GVS 45°. Nevertheless, due to the pressure suppression by the shield on the advancing blade in GVS 45°, a higher positive torque may have been generated by the advancing blade, thus allowing a higher total torque generation than V_{Ins} 0°.

The low-pressure region above the shield in GVS 22.5°, as discussed in previous sections, may have caused more fluid to be diverted upwards and away from the rotating region of the blade. The lower fluid volume in the rotating region in GVS 22.5° may have reduced the pressure difference between the concave and convex of the advancing blade compared to GVS 45°. However, the low-pressure wake point suggests that adequate lift and drag are generated to overcome the adverse effects of the negative torque in GVS 22.5°, causing it to perform better than GVS 0° and V_{Ins} 0°. Moreover, the angle of the GV in GVS 22.5° causes a lower adverse fluid attack on the convex of the returning blade that may have resulted in a lower pressure region compared to GVS 45°. This effect may have reduced the generated negative torque compared to GVS 45°, thus allowing it to generate a higher total torque production than GVS 45°, GVS 0° and V_{Ins} 0°.

Table 4.4: Summary of the Moment Coefficient, Performance Coefficient and Power Output Values for Guide Vanes

Vertical Installation with Guide Vanes and Shield (GVS)					
Div °	Angle °	Cm	Cp	Power	% Difference (V_{Ins})
0	0	0.32	0.26	18.86	-28.89
0	22.5	0.39	0.31	22.99	-13.33%
0	**45**	**0.55**	**0.44**	**32.42**	**22.22%**

Table 4.4 summarises the moment coefficient, performance coefficient and power output obtained from the GVS investigation. GVS 0° and GVS 22.5° suggest that the

performance of the SSWT reduces with these configurations compared to V_{Ins} 0° by 13.33% and 22.22%, respectively. The comparison with the V_{Ins} 0° suggests that the best performing GVS is the GVS 45°, where the performance of the SSWT is enhanced by 22.22%. This study's findings portray a similar outcome as previous studies, where the addition of guide vanes upstream of the advancing blade is suggested to increase the positive torque generation (Kailash, Eldho and Prabhu 2012; El-Askary et al. 2015). The addition of the shield, which suppresses the pressure on the convex of the advancing blade, leading to the improvement of the blade performance, has also been highlighted in previous literature (Emmanuel and Jun 2011).

4.8 Performance Analysis of the SSWT Under the Influence of a Deflector at 0° Divergence

This section presents the results obtained from the analysis of the SSWT under the influence of a deflector in a cylindrical chimney. The operation of the SSWT with the deflector was investigated at TSR 0.8 for its performance characteristics under the conventional vertical axis of operation. The moment coefficient, performance coefficient, and power output of the turbine are presented and discussed. The instantaneous moment coefficient and performance coefficient for one complete turbine rotation for all configurations are compared and studied at TSR 0.8, respectively. The velocity and pressure profiles of each deflector angle are compared and analysed. The performance enhancement of the SSWT is determined by comparing the SSWT with deflector and SSWT without deflector, obtained from Section 4.4.1.

4.8.1 C_m, C_p and Power Output for the SSWT with Deflector at TSR 0.8

Figure 4.56 presents the moment coefficient for the SSWT under the influence of a deflector in a cylindrical chimney at TSR 0.8. At Def 140° and Def 145°, the moment coefficient is observed to be similar. However, at Def 150°, the moment coefficient significantly increases by 33.33% and 29.72% compared to Def 140° and Def 145°, respectively. In comparison to V_{Ins} 0°, Def 140° and Def 145° reduce the moment coefficient of the SSWT by 20% and 17.78%, respectively. However, Def 150° improves the moment coefficient of the SSWT by 6.67% compared to V_{Ins} 0°.

Figure 4.57 presents the coefficient of performance for the SSWT under the influence of a deflector in a cylindrical chimney at TSR 0.8. The performance of the SSWT is degraded under the influence of Def 140° and Def 145° compared to V_{Ins} 0° by 20% and 17.78%, respectively. Def 145° may have had a lower performance due to a fluid swirl flow that impacts the advancing blade due to the angle and the distance of the deflector from the rotating region. It is suggested that reducing the distance between the deflector and the rotating region may significantly aid the SSWT in minimising the negative torque experienced. In the current configuration, the performance of the SSWT with Def 140° and Def 145° reflects a similar performance under TSR 1.2 for the V_{Ins} 0°.

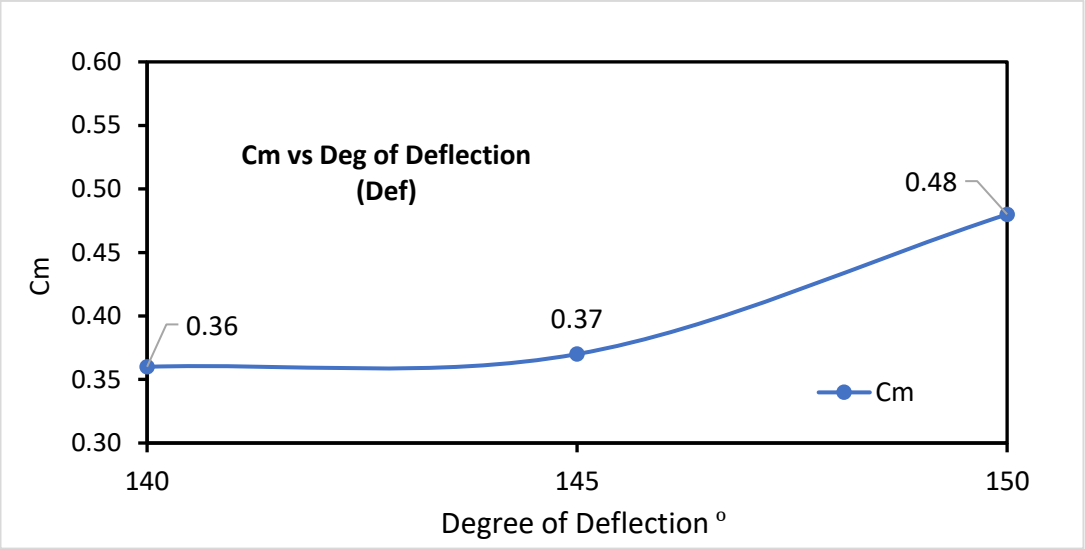

Figure 4.56: Coefficient of Moment of the Deflectors for the Vertical Installation in a 0° Chimney Divergence at TSR 0.8

Nevertheless, at Def 150°, the performance of the SSWT improves by 6.67% compared to the V_{Ins} 0°. The results obtained from this work agrees with previous studies where the usage of deflectors improves the performance coefficient of the SSWT, which will be discussed further at the end of this subsection.

Figure 4.58 presents the power output of the SSWT under the influence of a deflector in a cylindrical chimney at TSR 0.8. The power output obtained by the SSWT under Def 140° and Def 145° were similar at 21.22W and 21.81W, which is 20% and 17.78% lower than V_{Ins} 0°, respectively. The power augmentation of the SSWT boosted to 28.29W, which is 6.67% higher than the V_{Ins} 0°. Section 4.8.3, 4.8.4, 4.8.5

and 4.8.6 discuss the velocity and pressure characteristics of the deflector at four different blade angles.

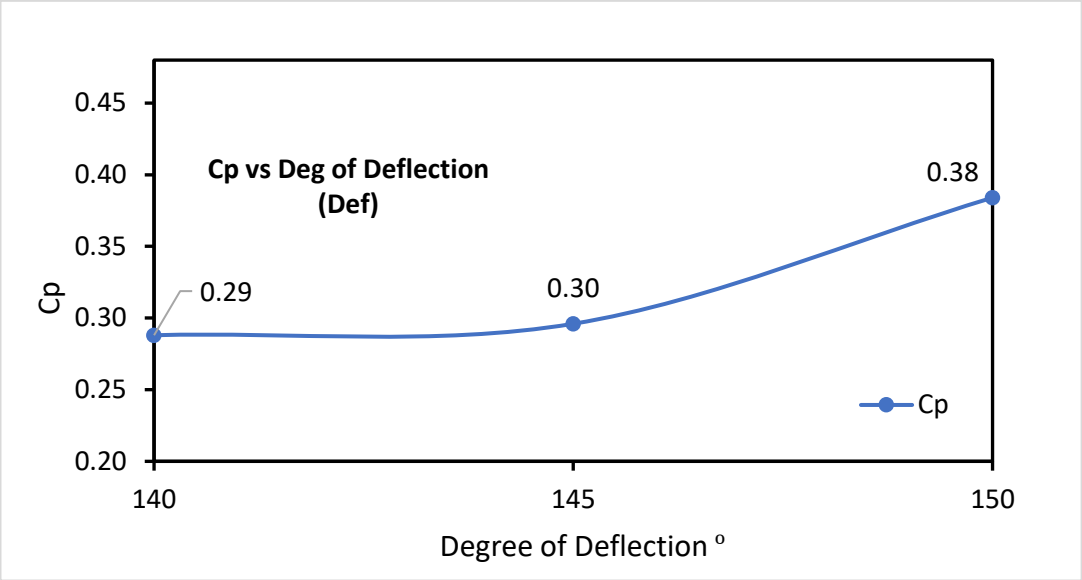

Figure 4.57: Coefficient of Performance of the Deflectors for the Vertical Installation in a 0° Chimney Divergence at TSR 0.8

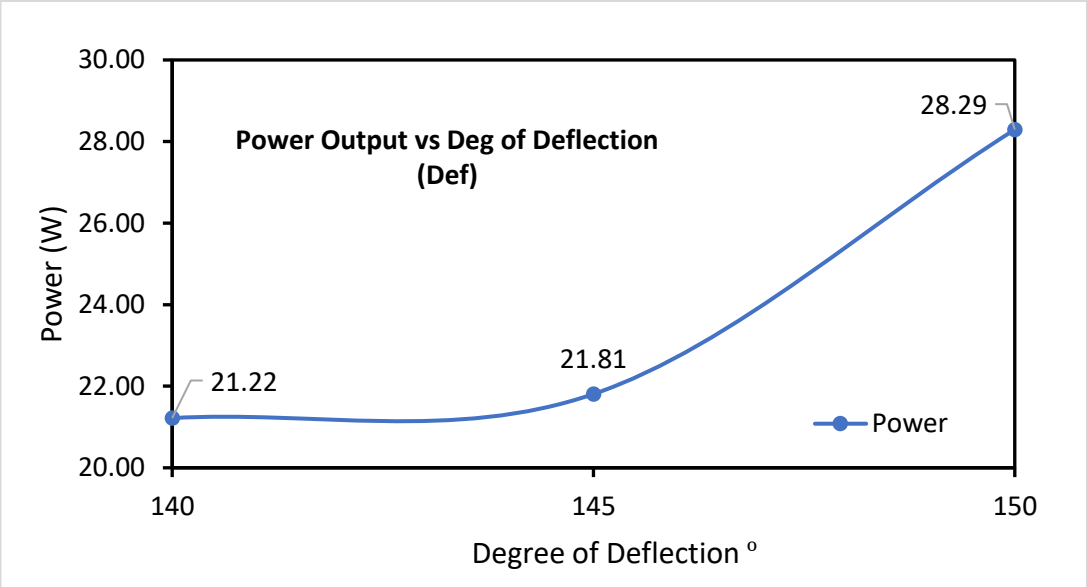

Figure 4.58: Power Output of the Deflectors for the Vertical Installation in a 0° Chimney Divergence at TSR 0.8

4.8.2 Instantaneous C_m and C_p for SSWT with Deflector at TSR 0.8

Figure 4.59 presents the instantaneous moment coefficient of the SSWT with deflector at TSR 0.8. The SSWT with the highest amplitude is with Def 150°, which suggests

having produced the largest torque generation, followed by V_{Ins} 0°, Def 145° and Def 140°. Def 145° and Def 140° show similar torque generations, with Def 145° producing a slightly higher positive torque. This result may be due to the angle of Def 145°, which redirects the flow towards the advancing blade better than Def 140°. The highest peak in Def 150° suggests that the redirection of flow towards the advancing blade is at a better angle of attack for the blade, hence resulting in a larger torque generation than V_{Ins} 0°, Def 145° and Def 140°. However, the negative torque generation by all deflectors suggests that the fluid's attack is not optimally close to the blade, thus causing a swirl flow which may have negatively impacted the returning blade at certain azimuth angles. Nevertheless, the highest torque generation in Def 150°, suggests that the positive torque produced in this configuration is sufficient to overcome the negative torque produced compared to V_{Ins} 0°, Def 145° and Def 140°.

Figure 4.60 presents the instantaneous performance coefficient of the SSWT with deflector at TSR 0.8. The highest performance is achieved with Def 150°, with the largest amplitude, while the lowest performance is achieved with Def 140°, with the smallest amplitude. The highest and lowest performance reflects the highest and lowest torque generation experienced by the SSWT with Def 150° and Def 140°, respectively, as observed from Figure 4.59. The angle of Def 150° may have positively impacted the advancing rotor with increased air attack, hence improving the torque generation compared to V_{Ins} 0°, Def 145° and Def 140°. However, unlike V_{Ins} 0°, Def 145° and Def 140° experience negative performance at azimuth angles 110 degrees to 150 degrees and 300 degrees to 340 degrees, while Def 150° at azimuth angles 130 degrees to 150 degrees and 330 degrees to 350 degrees, respectively. The deflector installed at the returning blade functions to reduce the impact of the negative torque generation. However, the negative torque generation (as shown in Figure 4.60) suggests that the positioning of the deflector may not have been close enough to the returning blade, thus resulting in a swirl fluid flow that negatively impacted the returning blade at certain azimuth angles. However, since the Def 150° has an improved redirection of fluid to the advancing blade, it may have promoted a higher positive torque generation that counters the impact of the negative torque (lesser than Def 145° and Def 140°), hence resulting in an overall higher positive torque compared to V_{Ins} 0°, Def 145° and Def 140°.

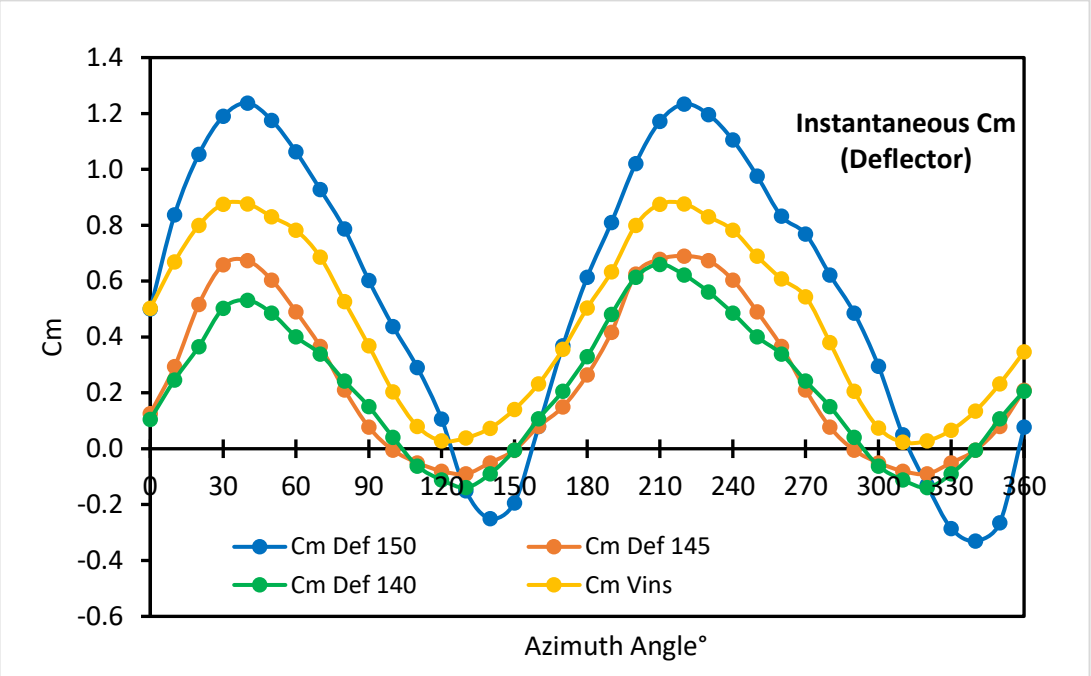

Figure 4.59: Instantaneous C_m for SSWT with Deflector

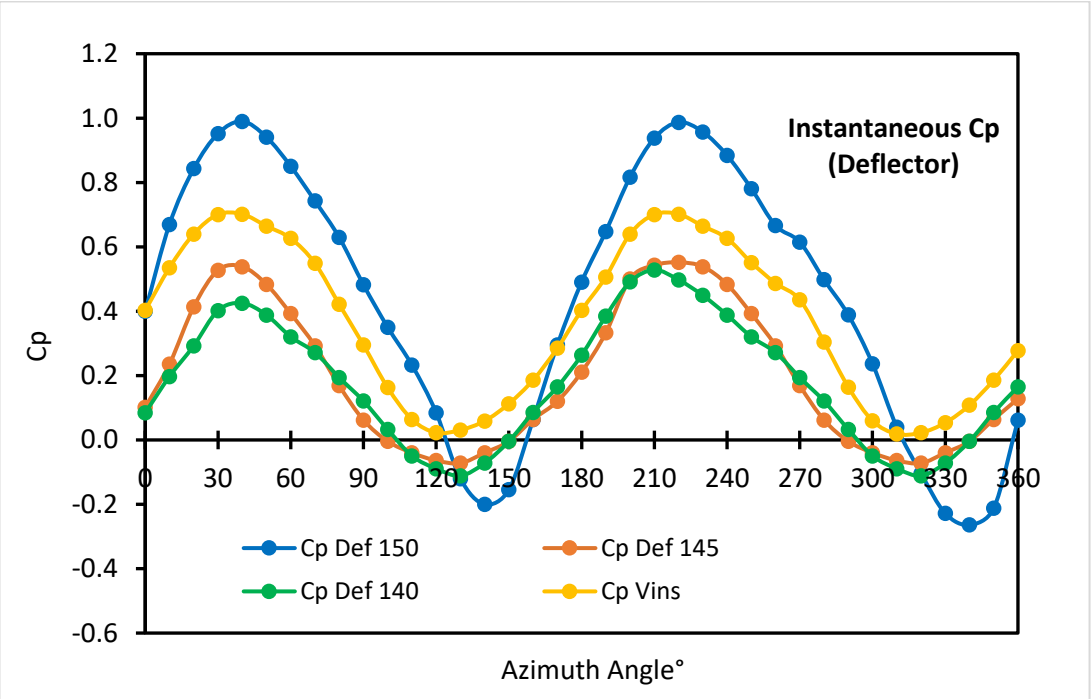

Figure 4.60: Instantaneous C_p for SSWT with Deflector

4.8.3 Velocity-Pressure Profiles at TSR 0.8 for Azimuth Angle, $\emptyset = 0°$

Figure 4.61 presents the velocity profiles of the SSWT under the influence of the deflectors at an azimuth angle of 0°. The lift generation is more prominently seen with

Def 145° and Def 150° compared to Def 140°. The Def 140° angle accelerates the fluid to a region above the advancing blade, thus reducing the lift generation.

At Def 145°, the deflector accelerates the fluid to a region that attacks the curvature (convex) side of the advancing blade, redirecting the fluid flow downwards (since it hits the edge of the advancing blade) but still enabling the blade to generate lift (due to the Coanda effect). At Def 150°, the deflector channels the fluid towards the tip of the advancing blade. Hence, lesser fluid is redirected downwards by the blade tip with Def 150°. The generated lift by Def 150° is observed to be minutely lesser than Def 145°, which may have been due to the angle of fluid flow redirection.

Figure 4.62 presents the pressure profiles of the SSWT under the influence of the deflectors at an azimuth angle of 0°. A lower pressure region formation is observed at the rear of the advancing blade for all deflector angles. At Def 140°, a very poor low-pressure region is observed at the convex of the advancing blade compared to Def 145° and Def 150°. Although Def 145° is seen to create a lower pressure region, upon closer analysis, a much lower pressure region is observed on the rear of the advancing blade with Def 150°, which may have improved the lift generation compared to that of Def 145°.

Moreover, the swirl velocity flow in Def 145° may have caused a higher pressure region at the edge of the advancing blade. The impact of the higher pressure may have reduced the positive torque generated, hence resulting in an overall lower torque generated in Def 145° compared to Def 150°.

With the accelerated fluid directed towards the curvature (convex) of the advancing blade in Def 140° and Def 145°, a higher pressure region formation is observed at the tip area of the advancing blade of Def 140°, followed by Def 145° compared to Def 150°. This may have reduced the positive effect of the lift force on the advancing blade, especially in Def 145°, thus causing the Def 150° blade to have a better torque generation.

In addition, the low-pressure wake point present at the Def 150° returning blade may have increased the pressure difference between the convex and the concave sides of the returning blade compared to Def 140° and Def 145°, which may have reduced the

impact of the negative torque generation in Def 150°. These effects may have caused the blade profile in Def 150° to perform better than the Def 145° and Def 140°.

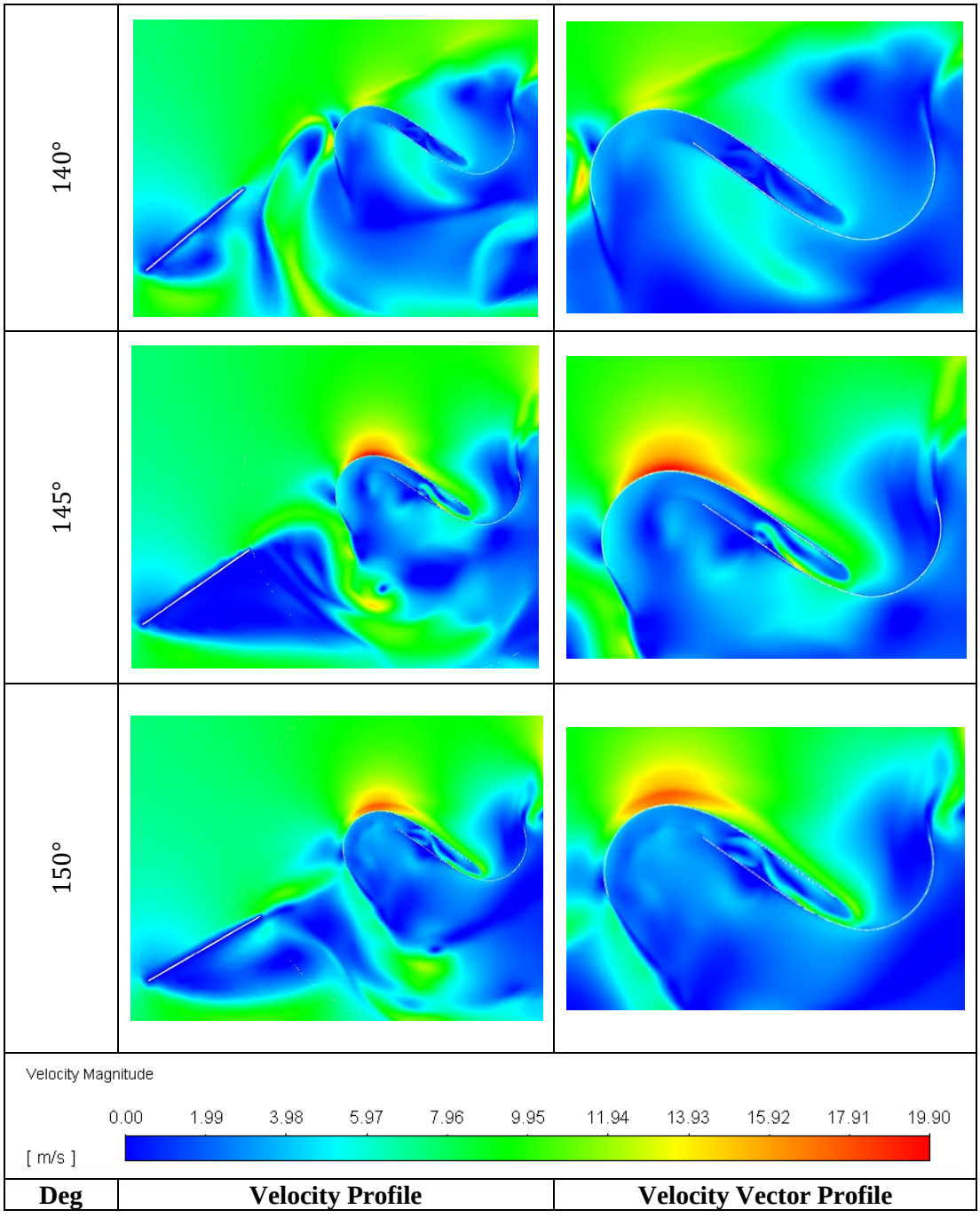

Figure 4.61: Comparison of the Velocity and Vector Profiles of the SSWT with Deflectors at $\emptyset = 0°$

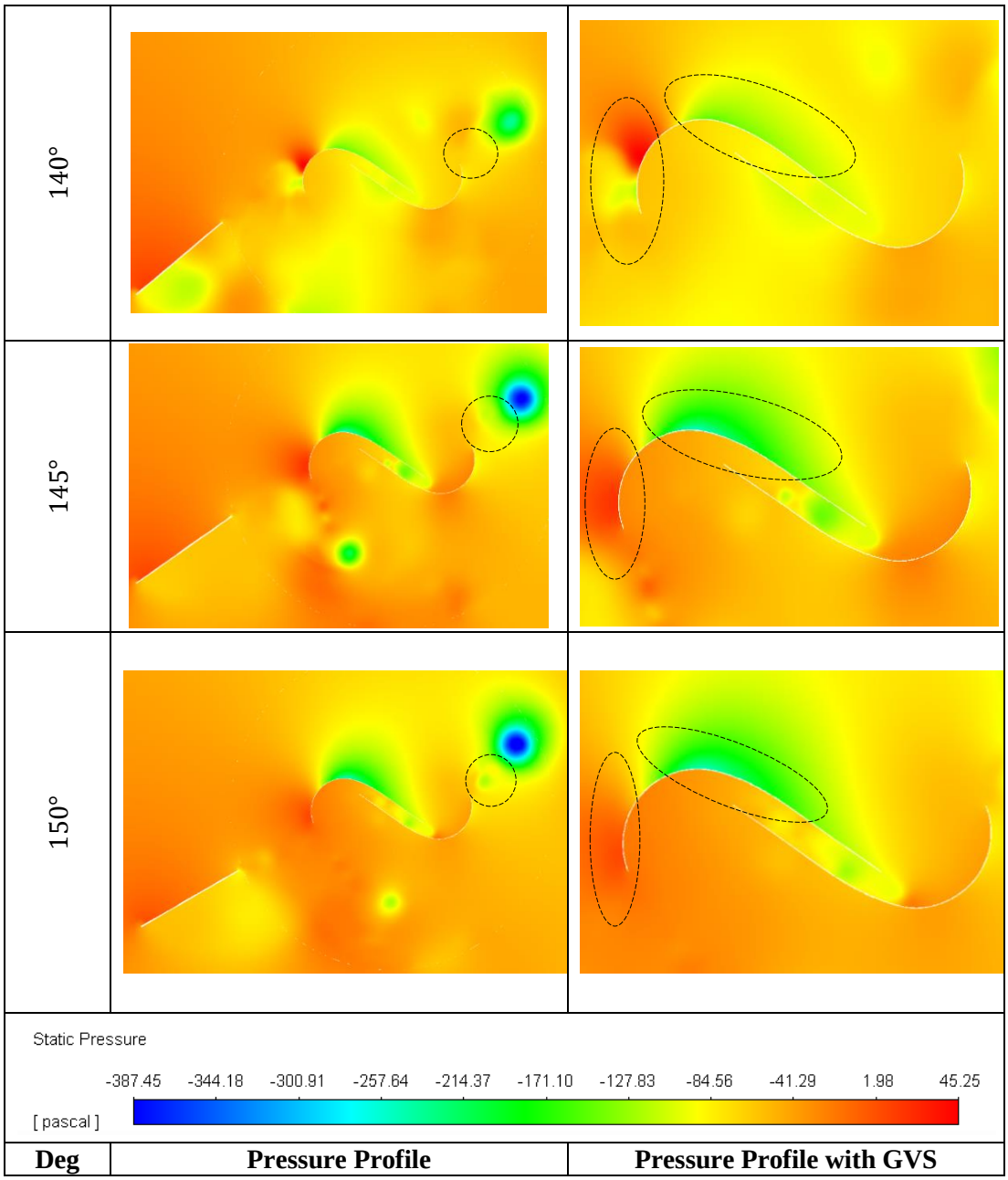

Figure 4.62: Comparison of the Pressure Profiles of the SSWT with Deflectors at $\emptyset = 0°$

4.8.4 Velocity-Pressure Profiles at TSR 0.8 for Azimuth Angle, $\emptyset = 45°$

Figure 4.63 presents the velocity profiles of the SSWT under the influence of the deflectors at an azimuth angle of 45°. At all deflector angles, a prominent lift generation on the advancing blade is observed. However, at Def 140°, a medium-ranged velocity region is observed attacking the returning blade, which may have contributed to the negative torque generation in the profile.

At Def 145°, a medium-ranged velocity region is observed at the concave of the returning blade, which reduces the negative torque generation. However, the medium-ranged velocity attacking the returning blade on the convex side of Def 145° may have reduced the positive effect of the concave side, thus performing poorer than Def 150° but better than Def 140°. At Def 150°, the medium ranged velocity region formed on the concave of the returning blade reduces the negative torque produced, which may have caused it to perform better than the Def 145° and Def 140°.

Figure 4.64 presents the pressure profiles of the SSWT under the influence of the deflectors at an azimuth angle of 45°. A low-pressure region formation is observed on the rear side of the advancing blade for all deflector angles, with Def 145° being the highest, followed by Def 150° and Def 140°. This effect may be the 145° angle effect that accelerates the fluid towards the concave side of the advancing blade, thus generating a higher pressure region compared to Def 150° and Def 140°.

The highest pressure difference between the concave and convex sides of the advancing blade is observed with Def 145°, followed by Def 150° and Def 140°. However, with regards to the returning blade, the highest pressure generated at the convex of the blade is observed at Def 145°, followed by Def 150° and Def 140°. This effect may be due to the deflector angle that directs the flow to the midsection of the returning blade in Def 145°.

As a result, the higher pressure on the rear of the returning blade may have generated a larger negative torque with Def 145° than Def 150°, thus resulting in a better performance in Def 150°. Although the pressure difference at the returning blade of the Def 140° may be higher than Def 145°, the lower positive torque generation of the advancing blade may not have been enough to improve the overall blade performance in Def 140°.

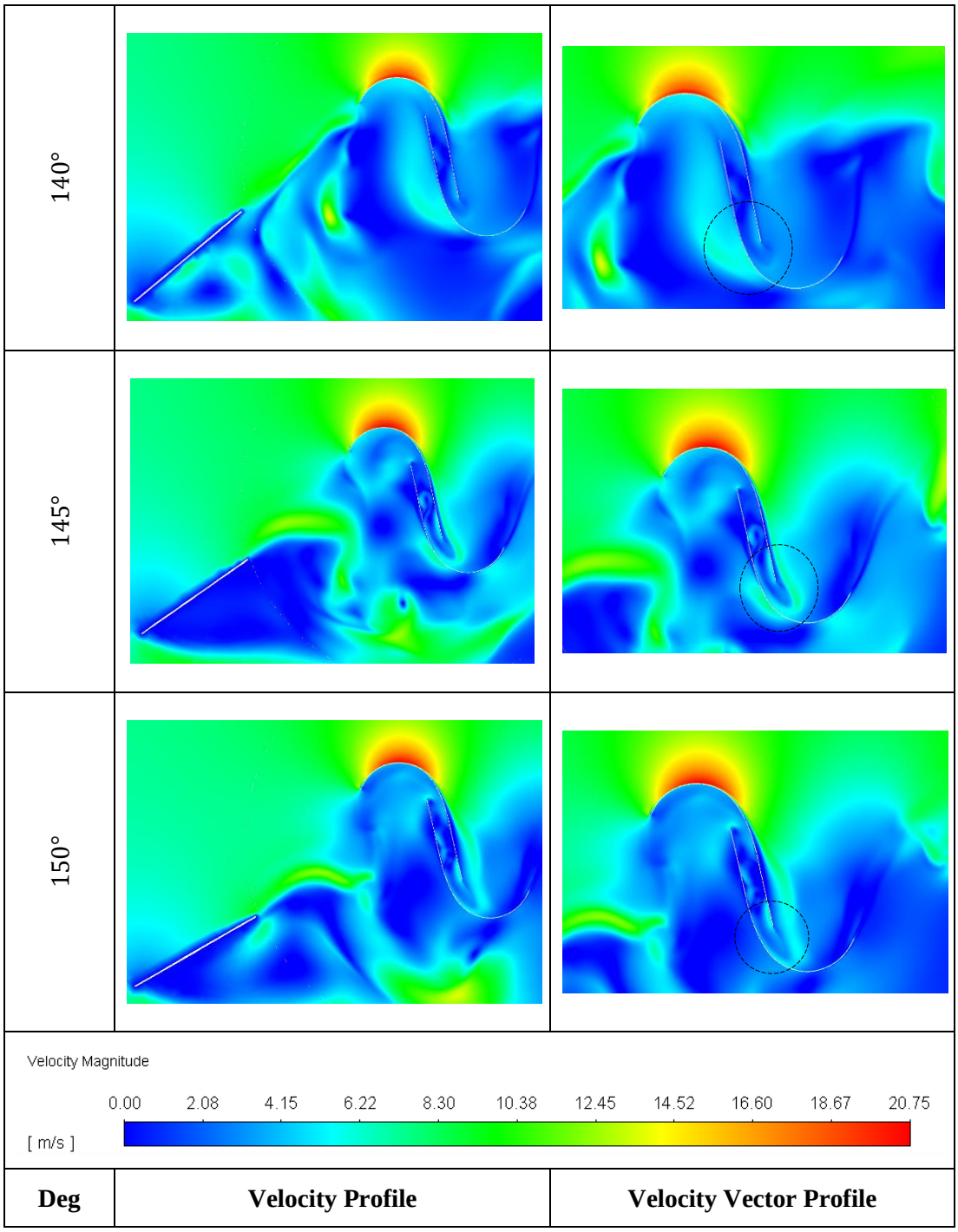

Figure 4.63: Comparison of the Velocity and Vector Profiles of the SSWT with Deflectors at $\emptyset = 45°$

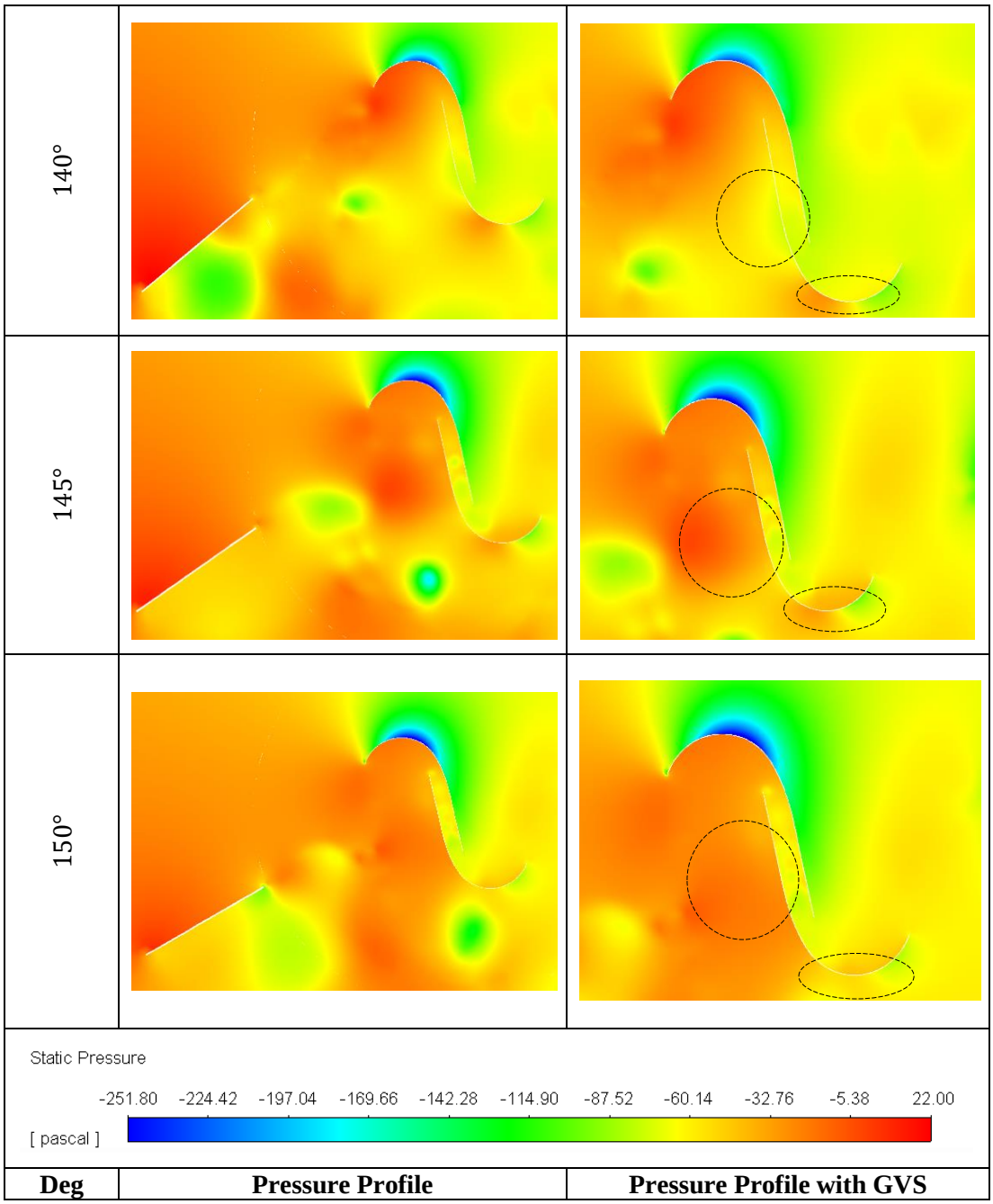

Figure 4.64: Comparison of the Pressure Profiles of the SSWT with Deflectors at $\emptyset = 45°$

4.8.5 Velocity-Pressure Profiles at TSR 0.8 for Azimuth Angle, $\emptyset = 90°$

Figure 4.65 presents the velocity profiles of the SSWT under the influence of the deflectors at an azimuth angle of 90°. For all deflector angles, tip vortices are generated at the tip of the advancing blades, with Def 150° being the highest, followed by Def 145° and Def 140°. This effect may be due to a higher acceleration of fluid directed towards the advancing blade with Def 150°. The higher fluid flow redirected

to the concave of the advancing blade then flows through the blade's overlap region, contributing to the positive torque generation, especially in Def 150°.

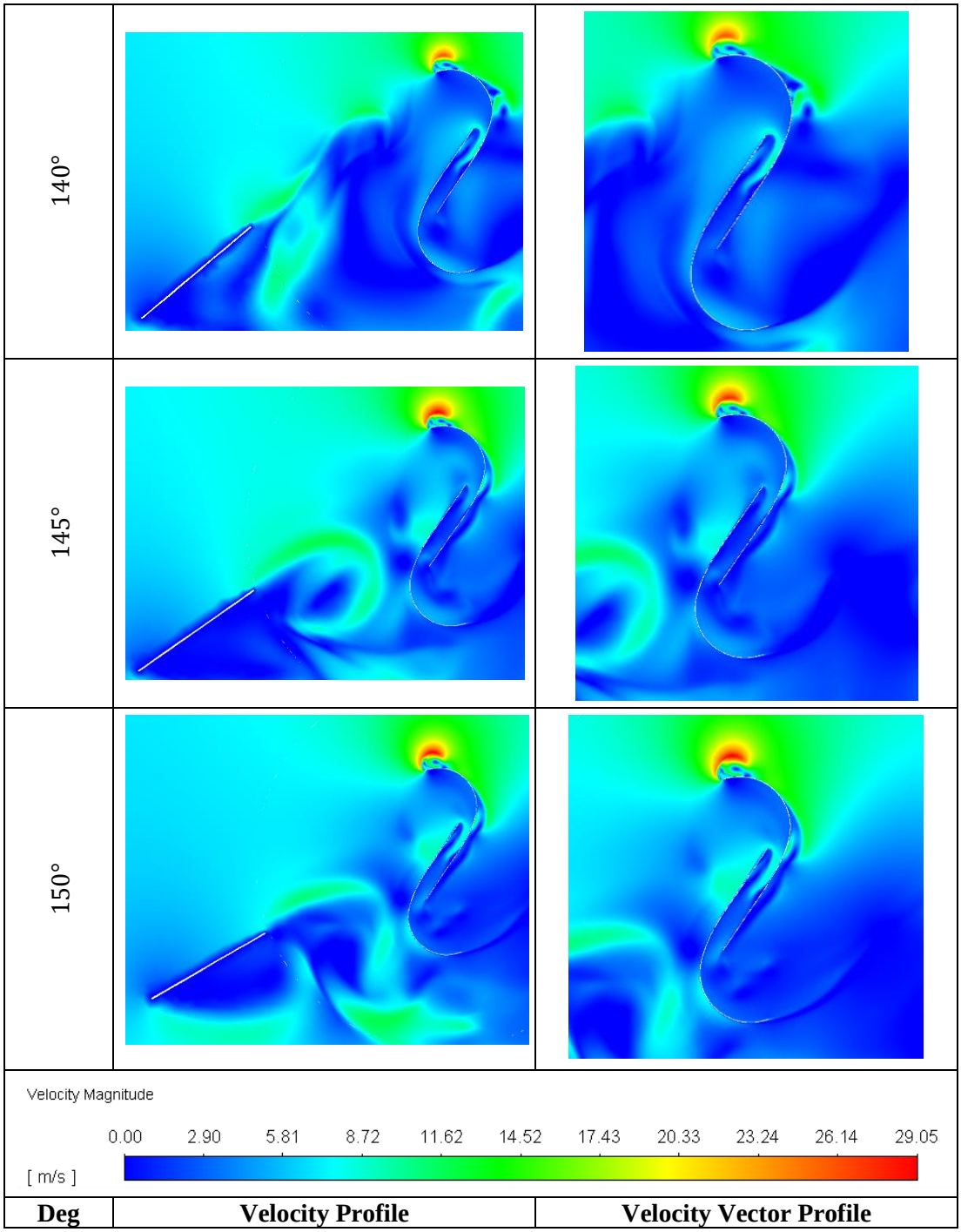

Figure 4.65: Comparison of the Velocity and Vector Profiles of the SSWT with Deflectors at $\emptyset = 90°$

Although a similar flow between the overlap gap of the blades in Def 140° can be observed, the higher tip vortices generated in Def 150° compared to Def 140° may have increased the positive torque production by the blade profile. The swirl-like

velocity flow in Def 145° may have adversely impacted the returning blade, hence resulting in a higher negative torque production compared to Def 140° and Def 150°. The adverse impact experienced by Def 145° may have lowered the overall torque production compared to Def 140° and Def 150°.

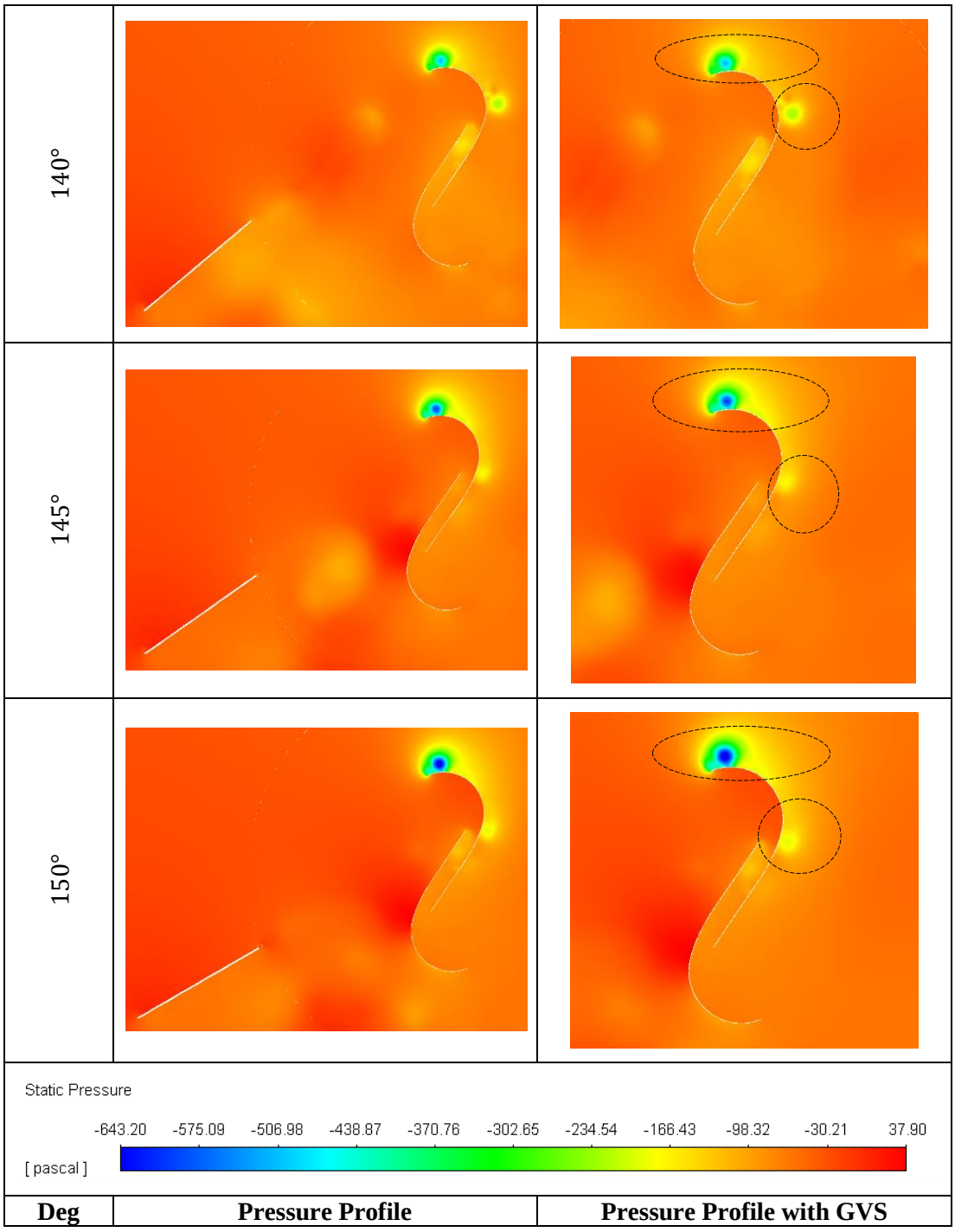

Figure 4.66: Comparison of the Pressure Profiles of the SSWT with Deflectors at $\emptyset = 90°$

Figure 4.66 presents the pressure profiles of the SSWT under the influence of the deflectors at an azimuth angle of 90°. The lowest wake pressure point at the tip of the advancing blade is observed at Def 150°, followed by Def 145° and Def 140°. The rear side of the advancing blade with Def 150° shows the lowest pressure region compared to Def 145° and Def 140°. In turn, the pressure difference between the concave and the convex of the advancing blade in Def 150° is the highest, followed by Def 145° and Def 140°. This effect may have caused a higher lift and drag experienced by the advancing blade of Def 150° compared to Def 145° and Def 140°, consequently producing a greater positive torque generation and improving the overall performance of the configuration. On the other hand, a higher pressure region is observed on the returning blade of Def 145°, which may have been the negative impact of the swirl-like fluid flow. The higher pressure on the convex suggests that the negative torque generated by the returning blade of Def 145° is higher than Def 140° and Def 150°, which may have resulted in the lowest torque generation at this azimuth angle.

4.8.6 Velocity-Pressure Profiles at TSR 0.8 for Azimuth Angle, $\emptyset = 135°$

Figure 4.67 presents the velocity profiles of the SSWT under the influence of the deflectors at an azimuth angle of 135°. The SSWT with Def 145° benefits from this angle, where strong tip vortices at the tip of the advancing blade and commendable drag generation at the convex of the returning blade contributes to higher positive torque and lower negative torque generation compared to Def 140° and Def 150°. This effect may be due to the reduced impact of the fluid on the returning blade, due to the deflector's function, while redirecting the fluid flow to the advancing blade in Def 145°.

At Def 150°, lift formation can be observed at the rear midsection of the returning blade and drag at the rear tip (due to the deflector). However, since the angle of fluid deflection is lower in Def 150°, more fluid is directed to the midsection of the returning blade, thus creating a lower drag and lift formation compared to Def 145°. In Def 140°, the fluid is deflected higher away from the advancing blade area, thus resulting in lower tip vortices, even at the tip of the advancing blade. Nevertheless, a lower fluid impact is observed on the convex of the returning blade in Def 140°, which

may have reduced the negative torque generation and resulted in a better overall torque generation compared to Def 150°.

Figure 4.68 presents the pressure profiles of the SSWT under the influence of the deflectors at an azimuth angle of 135°. The lowest wake pressure region is observed at the tip of the advancing blade at Def 150°, followed by Def 145° and Def 140°.

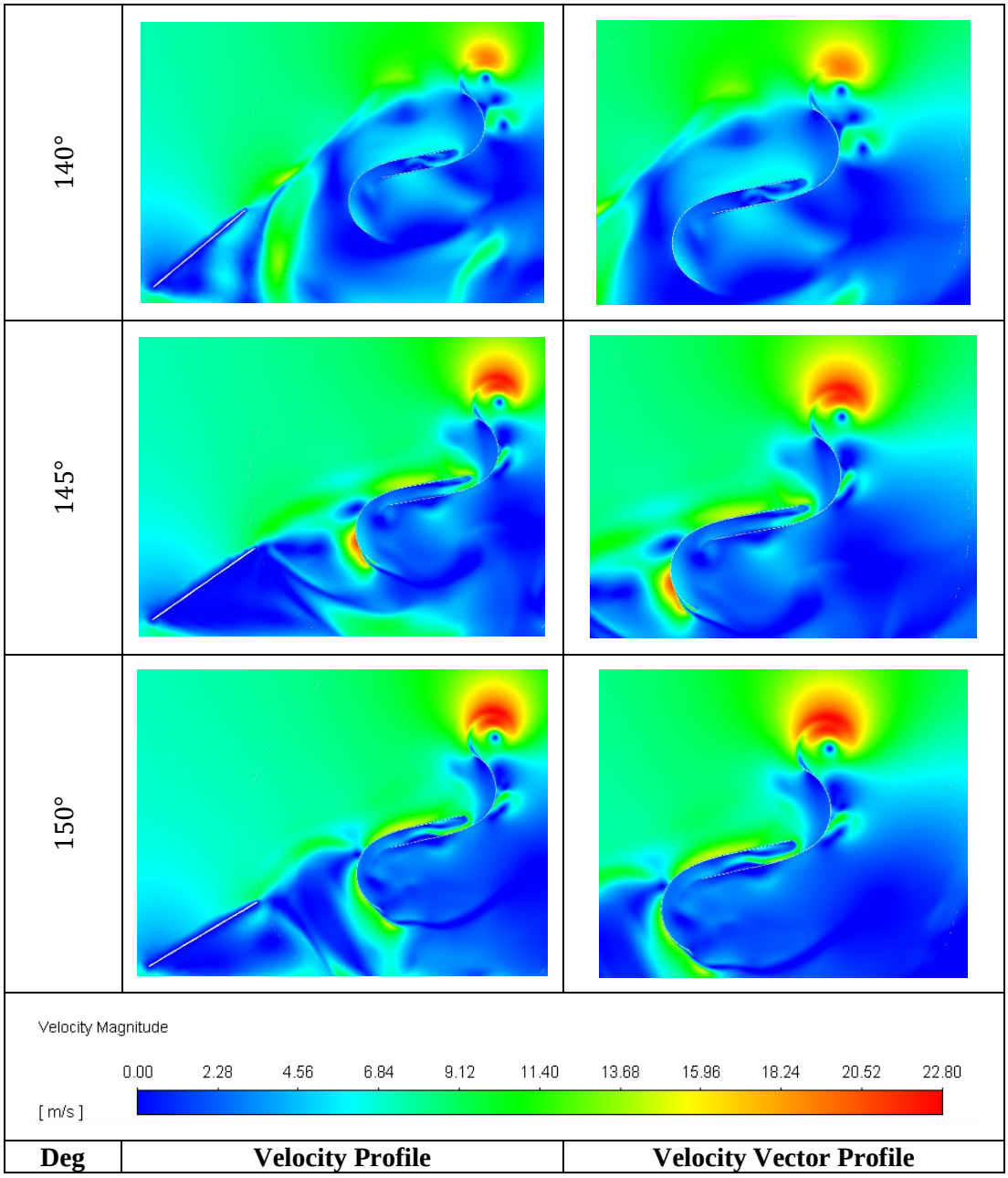

Figure 4.67: Comparison of the Velocity and Vector Profiles of the Deflectors at $\emptyset = 135°$

The pressure difference between the concave and convex of the advancing blade in Def 150° is higher than Def 145° and Def 140°, thus creating a greater drag and lift force experience. However, the rear tip of the returning blade with Def 145° generated a lower pressure region than that of Def 150° and Def 140°, thus significantly reducing the negative torque generation experienced by the blade with an increased drag operation.

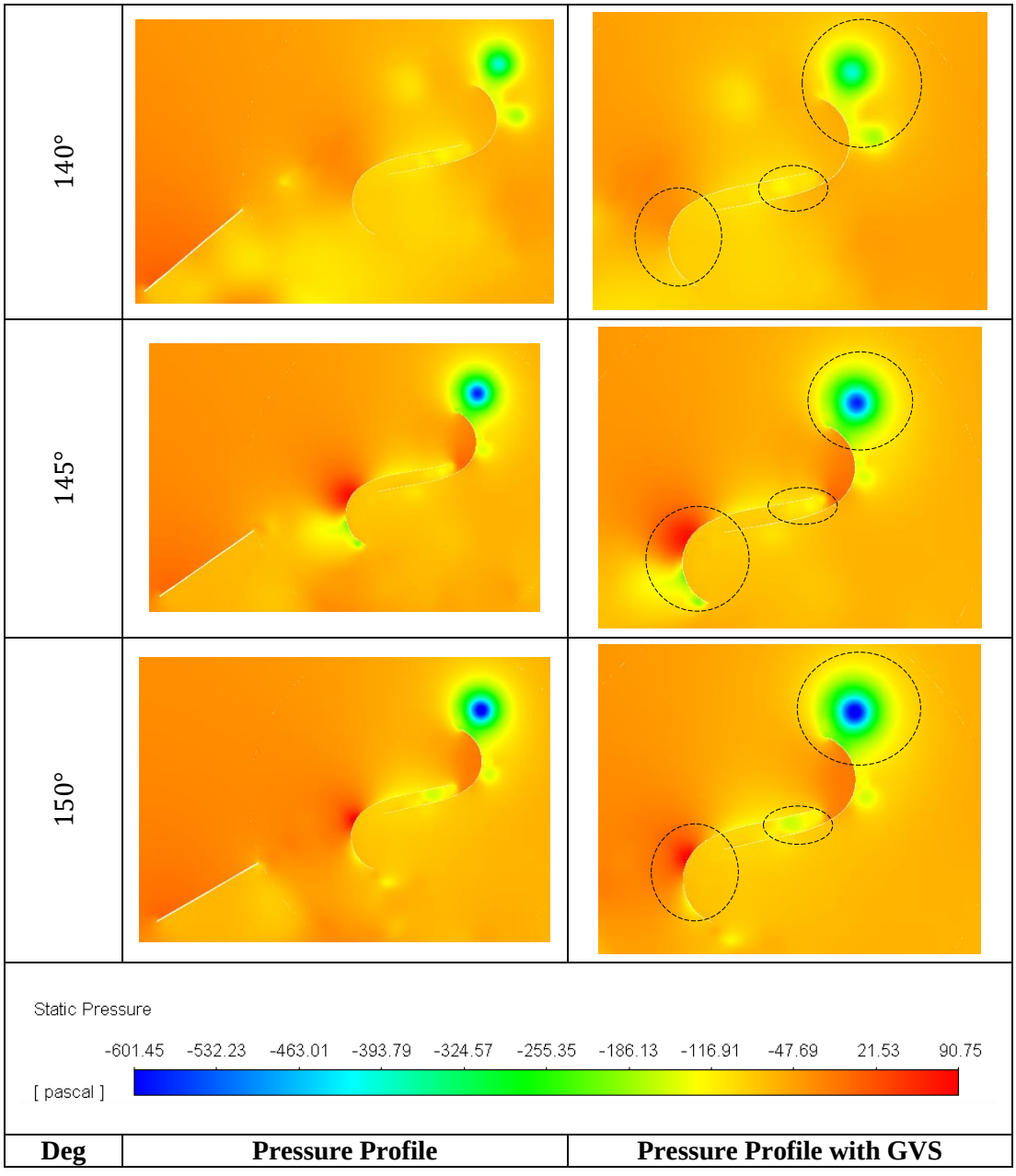

Figure 4.68: Comparison of the Pressure Profiles of the Deflectors at $\emptyset = 135°$

At Def 150°, the overlap region between the blades experiences low pressure, which may have contributed to a better positive torque formation compared to Def 145°.

However, a commendable amount of negative torque reduction is observed in Def 145° through the low-pressure region on the convex of the returning blade compared to Def 140° and Def 150°. Consequently, Def 145° may have experienced a higher overall torque generation, thus contributing to a better performance than Def 140° and Def 150°.

As for Def 140°, the angle deflects the fluid away from the advancing blade, which may have reduced the overall lift and drag experienced by the blade, thus resulting in poor performance compared to Def 145° and Def 150°. However, the fluid impacting the convex of the returning blade may have created a higher pressure region with Def 150° compared to Def 140° and Def 145°. The adverse effect of the fluid's impact on the returning blade in Def 150° may have significantly increased the negative torque generation, thus resulting in the lowest total torque production compared to Def 140° and Def 145° at this azimuth angle.

Table 4.5: Summary of the Moment Coefficient, Performance Coefficient and Power Output Values for Deflectors

Vertical Installation with Deflectors					
Div °	Angle °	Cm	Cp	Power	% Difference (V_{Ins} 0°)
0	140	0.36	0.29	21.22	-20.00
0	145	0.37	0.30	21.81	-17.78%
0	**150**	**0.48**	**0.38**	**28.29**	**6.67%**

Table 4.5 summarises the moment coefficient, performance coefficient and power output of the SSWT under the influence of a deflector. From the tabulated values, Def 140° and Def 145° reduce the performance of the SSWT. The best performing deflector is Def 150°, where the performance of the SSWT is enhanced by 6.67% compared to V_{Ins} 0°. The deflector, which functioned both as a guide vane and a deflector, may have contributed to the enhancement of the SSWT with Def 150°. The results from this work agree with previous studies, which suggests the positive influence of the deflector in reducing the negative torque in the SSWT, thus increasing the performance of the SSWT (Mohamed et al. 2010; Kailash, Eldho and Prabhu 2012; Golecha, Eldho and Prabhu 2011; OGAWA and YOSHIDA 1986; Huda et al. 1992).

4.9 Summary of Chapter 4

In this chapter, the results for the SSWT performance in the SCPP's collector region were presented, where the H_{Ins} 0° has shown better torque generation, performance and power output than V_{Ins} 0°. The effects of chimney divergence on the fluid flow characteristics were analysed. The fluid velocity was enhanced with increasing chimney divergence up to 2°. The SSWT's performance improved with H_{Ins} 1° compared to V_{Ins} 1°. However, at 2° chimney divergence, the V_{Ins} 2° outperformed H_{Ins} 2°. With the addition of guide vane and shield to the SSWT, the GVS 45° performed better than V_{Ins} 0°, GVS 22.5° and GVS 0°. Under the influence of the deflector, the Def 150° performed better than V_{Ins} 0°, Def 145° and Def 140°.

CHAPTER 5
CONCLUSION

5.0 Main Conclusion

In conclusion, there is good potential for the operation of the Savonius in the collector region of the SCPP. The Savonius being advantageous through its low cut-in wind speeds and multidirectional operation benefits the power generation in the SCPP. The objectives proposed in this work were achieved. Listed below are the summarised findings in accordance with each objective studied.

(Objective 1)

1. The SSWT in the V_{Ins} was able to achieve a performance of 0.36 with a power output of 26.52 W at a tip speed ratio of 0.8.
2. The SSWT in the H_{Ins} presented an improved performance by 2.78% compared to the V_{Ins} which may have been the influence of the non-distributed buoyant fluid flow.

(Objective 2)

3. The chimney with 1° divergence enhanced the fluid flow velocity by 72.84% but reduced the temperature rise in the collector region by 21.95%. The increase in fluid flow velocity resulting from the increased pressure differential in the SCPP was due to a larger outlet than the cylindrical chimney.
4. The chimney with 2° divergence enhanced the fluid flow velocity by 114.21% but reduced the temperature rise in the collector region by 24%. The pressure differential increased further with a larger outlet, leading to an increased fluid flow velocity compared to 1° chimney divergence.
5. The performance of the V_{Ins} in a 1° divergent chimney improved by 41.67%, while the power output enhanced by 634.46% compared to the V_{Ins} 0° due to the increased velocity in the diverging chimney. The significant increment in the power output compared to the power coefficient is the influence of the cubed fluid flow velocity in the power output formula.

6. The performance of the H_{Ins} in a 1° divergent chimney improved by 43.24%, while the power output enhanced by 640.94% compared to the H_{Ins} at 0° due to the increased velocity in the diverging chimney.
7. The performance of the H_{Ins} in a 1° divergent chimney improved by 3.92% with 0.51, while the power output enhanced by 3.13% with 200.87W compared to the V_{Ins} at 1°.
8. The performance of the V_{Ins} in the 2° divergent chimney improved by 8.33% with 0.39 against V_{Ins} 0° but reduced by 23.53% with 0.51 against V_{Ins} 1°. The power output enhanced by 970.48% compared to V_{Ins} 0° and 45.75% compared to V_{Ins} 1° due to the increased fluid flow velocity in the diverging chimney.
9. The performance of the H_{Ins} in a 2° divergent chimney at 0.16 was reduced by 55.56% against H_{Ins} 0° and 69.81% against H_{Ins} 1°, which may be due to the wall-like characteristic of the turbine at high rotational speeds. The power output was increased by 327.44% at 115.88W compared to H_{Ins} 0° but was reduced by 42.31% compared to H_{Ins} 1°.
10. The performance of the V_{Ins} in the 2° divergent chimney has improved by 58.97% while the power output was enhanced by 59.18% against the H_{Ins} 2°.

(Objective 3)

11. The guide vane and shield with the best performance was at GVS 45°, with an increased performance of 22.22% at 0.44 and an improved power output by 22.25% at 32.42W against V_{Ins} 0°, which could be attributed to the increased air attack and suppressed pressure on the advancing blade.
12. The deflector with the best performance was Def 150° with improved performance and power output of 5.56% at 0.38 and 6.67% at 28.29W against V_{Ins} 0°, respectively. The deflection of the fluid flow away from the returning blade may have reduced the impact of the negative torque.

5.1 Future Studies

Several aspects can be focused on as future research studies which can be performed in stages.

1. The current study reports on the performance enhancement of the SSWT in various setups with a restricted parametric range. The optimal parametric values of the setups, however, have not yet been established. Hence, a focused investigation on the performance of the SSWT with GVS between angle 22.5° and 50°, GVS and deflectors combined, different deflector distances from the turbine, and larger diameters will be undertaken to identify the parametric values of the SSWT, deflector, and GVS for optimal power generation.
2. The single turbine configuration in the current work may not have fully harnessed the fluid flow's energy since minimal wake regions were identified. Thus, the performance of multi-turbine configurations will be investigated to analyse the power production capabilities compared to a single turbine configuration.
3. The current work is limited to a 2-dimensional analysis, where the volumetric fluid flow impact is not taken into account. Hence, a 3-dimensional performance analysis of the SSWT under vertical and horizontal installations will be explored.
4. The usage of CFD in the current work to identify the optimal parametric values for maximum power augmentation proposes to be time-consuming and costly with increasing parameter studies. Therefore, the Artificial Neural Network (ANN) and Genetic Algorithms (GA) will be adopted to analyse the optimal design parameters of the SSWT for the SCPP.

REFERENCES

Al-Kayeim, Hussain H., Mohammed A. Aurybi, and Syed I. U. Gilani. 2019. "Influence of Canopy Condensate Film on the Performance of Solar Chimney Power Plant." *Renewable Energy* 136: 1012-1021. https://doi.org/https://doi.org/10.1016/j.renene.2019.01.067.

Al-Kayiem, Hussain H, Mohammed A Aurybi, Syed IU Gilani, Ali A Ismaeel, and Sanan T Mohammad. 2019a. "Performance Evaluation of Hybrid Solar Chimney for Uninterrupted Power Generation." *Energy* 166: 490-505.

Al-Kayiem, Hussain H, KV Sreejaya, and Syed Ihtsham Ul-Haq Gilani. 2014. "Mathematical Analysis of the Influence of the Chimney Height and Collector Area on the Performance of a Roof Top Solar Chimney." *Energy and Buildings* 68: 305-311.

Al-Kayiem, Hussain H., and Ogboo Chikere Aja. 2016. "Historic and Recent Progress in Solar Chimney Power Plant Enhancing Technologies." *Renewable and Sustainable Energy Reviews* 58: 1269-1292. https://doi.org/https://doi.org/10.1016/j.rser.2015.12.331.

Al-Kayiem, Hussain H., Mohammed A. Aurybi, Syed I. U. Gilani, Ali A. Ismaeel, and Sanan T. Mohammad. 2019b. "Performance Evaluation of Hybrid Solar Chimney for Uninterrupted Power Generation." *Energy* 166: 490-505. https://doi.org/https://doi.org/10.1016/j.energy.2018.10.115.

Alom, Nur, and Ujjwal K Saha. 2019. "Evolution and Progress in the Development of Savonius Wind Turbine Rotor Blade Profiles and Shapes." *Journal of Solar Energy Engineering* 141 (3): 030801.

Amudam, Yaswanthkumar, and VP Chandramohan. 2019. "Influence of Thermal Energy Storage System on Flow and Performance Parameters of Solar Updraft Tower Power Plant: A Three Dimensional Numerical Analysis." *Journal of cleaner production* 207: 136-152.

Aurybi, Mohammed A, SI Gilani, Hussain H Al-Kayiem, and Ali A Ismaeel. 2018. "Mathematical Evaluation of Solar Chimney Power Plant Collector, Integrated with External Heat Source for Non-Interrupted Power Generation." *Sustainable Energy Technologies and Assessments* 30: 59-67.

Ayadi, Ahmed, Abdallah Bouabidi, Zied Driss, Haithem Nasraoui, Moubarek Bsisa, and Mohamed Salah Abid. 2018. "Study of the Turbulence Model Effect on the Airflow Characteristics inside a Solar Chimney Power Plant." In *Cfd Techniques and Energy Applications*, edited 29-47. Springer.

Ayadi, Ahmed, Zied Driss, Abdallah Bouabidi, and Mohamed S Abid. 2018a. "Effect of the Turbine Diameter on the Generated Power of a Solar Chimney Power Plant." *Energy & Environment* 29 (5): 822-836.

Ayadi, Ahmed, Zied Driss, Abdallah Bouabidi, and Mohamed Salah Abid. 2018b. "Effect of the Number of Turbine Blades on the Air Flow within a Solar Chimney Power Plant." *Proceedings of the Institution of Mechanical Engineers, Part A: Journal of Power and Energy* 232 (4): 425-436.

Ayadi, Ahmed, Haythem Nasraoui, Zied Driss, Abdallah Bouabidi, and Mohamed Salah Abid. 2018. "Unsteady State of a Solar Chimney Power Plant Accoupled with a Turbine: Case Study." *Journal of Engineering, Design and Technology*.

Balijepalli, Ramakrishna, VP Chandramohan, and K Kirankumar. 2020. "Development of a Small Scale Plant for a Solar Chimney Power Plant (Scpp): A Detailed Fabrication Procedure, Experiments and Performance Parameters Evaluation." *Renewable Energy* 148: 247-260.

Beneke, LW, CJS Fourie, and Z Huan. 2016. "Investigation of an Octagon-Shaped Chimney Solar Power Plant." *Journal of Energy in Southern Africa* 27 (4): 38-52.

Bernardes, Marco Aurélio dos Santos. 2011. "Solar Chimney Power Plants–Developments and Advancements." In *Solar Energy*, edited by Aziz Belmiloudi, 171-186. InTech. https://doi.org/10.5772/8068.

Bernardes, Marco Aurélio dos Santos, and Xinping Zhou. 2013. "On the Heat Storage in Solar Updraft Tower Collectors – Water Bags." *Solar Energy* 91 (0): 22-31. https://doi.org/http://dx.doi.org/10.1016/j.solener.2012.11.025.

Bird, R Byron, Warren E Stewart, and Edwin N Lightfoot. 2007. *Transport Phenomena*. John Wiley & Sons.

Cao, Fei, Huashan Li, Qiuming Ma, and Liang Zhao. 2014. "Design and Simulation of a Geothermal–Solar Combined Chimney Power Plant." *Energy conversion and management* 84: 186-195.

Chan, Chun Man, HL Bai, and DQ He. 2018. "Blade Shape Optimization of the Savonius Wind Turbine Using a Genetic Algorithm." *Applied energy* 213: 148-157.

Chen, Jian, HX Yang, CP Liu, CH Lau, and M Lo. 2013. "A Novel Vertical Axis Water Turbine for Power Generation from Water Pipelines." *Energy* 54: 184-193.

Cottam, PJ, P Duffour, P Lindstrand, and P Fromme. 2019. "Solar Chimney Power Plants–Dimension Matching for Optimum Performance." *Energy Conversion and Management* 194: 112-123.

Cuce, Erdem, Abhishek Saxena, Pinar Mert Cuce, Harun Sen, Shaopeng Guo, and K Sudhakar. 2021. "Performance Assessment of Solar Chimney Power Plants with the Impacts of Divergent and Convergent Chimney Geometry." *International Journal of Low-Carbon Technologies*.

Cuce, Erdem, Harun Sen, and Pinar Mert Cuce. 2020. "Numerical Performance Modelling of Solar Chimney Power Plants: Influence of Chimney Height for a Pilot Plant in Manzanares, Spain." *Sustainable Energy Technologies and Assessments* 39: 100704.

Das, Pritam, and VP Chandramohan. 2019. "Computational Study on the Effect of Collector Cover Inclination Angle, Absorber Plate Diameter and Chimney Height on Flow and Performance Parameters of Solar Updraft Tower (Sut) Plant." *Energy* 172: 366-379.

Demirdžić, Ismet, and Samir Muzaferija. 1995. "Numerical Method for Coupled Fluid Flow, Heat Transfer and Stress Analysis Using Unstructured Moving Meshes with Cells of Arbitrary Topology." *Computer methods in applied mechanics and engineering* 125 (1-4): 235-255.

Denantes, F, and E Bilgen. 2006. "Counter-Rotating Turbines for Solar Chimney Power Plants." *Renewable energy* 31 (12): 1873-1891.

El-Askary, WA, MH Nasef, AA Abdel-Hamid, and HE Gad. 2015. "Harvesting Wind Energy for Improving Performance of Savonius Rotor." *Journal of Wind Engineering and Industrial Aerodynamics* 139: 8-15.

El-Wakil, Mohamed Mohamed. 1985. *Powerplant Technology*. Tata McGraw-Hill Education.

Emmanuel, Binyet, and Wang Jun. 2011. "Numerical Study of a Six-Bladed Savonius Wind Turbine." *Journal of Solar Energy Engineering* 133 (4).

Fathi, Nima, Patrick McDaniel, Seyed Sobhan Aleyasin, Matthew Robinson, Peter Vorobieff, Sal Rodriguez, and Cassiano de Oliveira. 2018. "Efficiency Enhancement of Solar Chimney Power Plant by Use of Waste Heat from Nuclear Power Plant." *Journal of cleaner production* 180: 407-416.

Ferziger, Joel H, and Milovan Perić. 2002. *Computational Methods for Fluid Dynamics*. Vol. 3. Berlin: Springer.

Fluent, Ansys. 2009. "12.0 Theory Guide." *Ansys Inc* 5 (5): 15.

Fluri, Thomas Peter. 2008. "Turbine Layout for and Optimization of Solar Chimney Power Conversion Units." Stellenbosch: Stellenbosch University.

Francke, Wolfgang , Renaud de Richter, Oswald Petersen, and Janning Petersen. 2013. "A Realistic Growth Path for Solar Wind Power." *Applied Mechanics and Materials* 283: 57-64. https://doi.org/10.4028/www.scientific.net/AMM.283.57.

Fujisawa, Nobuyuki, and Futoshi Gotoh. 1994. "Experimental Study on the Aerodynamic Performance of a Savonius Rotor."

Gannon, Anthony J, and Theodor W von Backstro¨ m. 2003. "Solar Chimney Turbine Performance." *J. Sol. Energy Eng.* 125 (1): 101-106.

Gholamalizadeh, Ehsan, and Jae Dong Chung. 2017a. "Analysis of Fluid Flow and Heat Transfer on a Solar Updraft Tower Power Plant Coupled with a Wind Turbine Using Computational Fluid Dynamics." *Applied Thermal Engineering* 126: 548-558.

Gholamalizadeh, Ehsan, and Jae Dong Chung. 2017b. "A Comparative Study of Cfd Models of a Real Wind Turbine in Solar Chimney Power Plants." *Energies* 10 (10): 1674.

Golecha, Kailash, TI Eldho, and SV Prabhu. 2011. "Influence of the Deflector Plate on the Performance of Modified Savonius Water Turbine." *Applied Energy* 88 (9): 3207-3217.

Guo, Penghua, Jingyin Li, Yunfeng Wang, and Yuan Wang. 2015. "Numerical Study on the Performance of a Solar Chimney Power Plant." *Energy Conversion and Management* 105: 197-205.

Guo, Penghua, Jingyin Li, Yunfeng Wang, and Yuan Wang. 2016. "Evaluation of the Optimal Turbine Pressure Drop Ratio for a Solar Chimney Power Plant." *Energy Conversion and Management* 108: 14-22.

Guo, Penghua, Tiantian Li, Ben Xu, Xinhai Xu, and Jingyin Li. 2019. "Questions and Current Understanding About Solar Chimney Power Plant: A Review." *Energy Conversion and Management* 182: 21-33. https://doi.org/https://doi.org/10.1016/j.enconman.2018.12.063.

Haaf, W. 1984a. "Solar Chimneys: Part Ii: Preliminary Test Results from the Manzanares Pilot Plant." *International Journal of Sustainable Energy* 2 (2): 141-161.

Haaf, W, K Friedrich, G Mayr, and Jorg Schlaich. 1983. "Solar Chimneys Part I: Principle and Construction of the Pilot Plant in Manzanares." *International Journal of Solar Energy* 2 (1): 3-20.

Haaf, W. 1984b. "Solar Chimneys, Part Ii: Preliminary Test Results from the Manzanares Pilot Plant." *International Journal of Solar Energy* 2 (2): 141-161.

Hanna, Magdy Bassily, Tarek Abdel-Malak Mekhail, Omar Mohamed Dahab, Mohamed Fathy Cidek Esmail, and Ahmed Rekaby Abdel-Rahman. 2016. "Experimental and Numerical Investigation of the Solar Chimney Power Plant's Turbine." *Open Journal of Fluid Dynamics* 6 (04): 332.

Hassan, Aakash, Majid Ali, and Adeel Waqas. 2018. "Numerical Investigation on Performance of Solar Chimney Power Plant by Varying Collector Slope and Chimney Diverging Angle." *Energy* 142: 411-425.

Hassanzadeh, Rahim, Milad Mohammadnejad, and Sajad Mostafavi. 2021. "Comparison of Various Blade Profiles in a Two-Blade Conventional Savonius Wind Turbine." *Journal of Energy Resources Technology* 143 (2).

Hedderwick, Richard Anthony. 2000. "Performance Evaluation of a Solar Chimney Power Plant." Stellenbosch: University of Stellenbosch.

Hooi, Lim Beng, and Saravana Kannan Thangavelu. 2018. "A Parametric Simulation of Solar Chimney Power Plant." Paper presented at the *IOP Conference Series: Materials Science and Engineering, 2018*. IOP Publishing.

Hu, Siyang, Dennis YC Leung, and John CY Chan. 2017. "Impact of the Geometry of Divergent Chimneys on the Power Output of a Solar Chimney Power Plant." *Energy* 120: 1-11.

Hu, Siyang, Dennis YC Leung, and Michael ZQ Chen. 2017. "Effect of Divergent Chimneys on the Performance of a Solar Chimney Power Plant." *Energy Procedia* 105: 7-13.

Hu, Siyang, Dennis YC Leung, Michael ZQ Chen, and John CY Chan. 2016. "Effect of Guide Wall on the Potential of a Solar Chimney Power Plant." *Renewable energy* 96: 209-219.

Huda, MD, MA Selim, AKMS Islam, and MQ Islam. 1992. "The Performance of an S-Shaped Savonius Rotor with a Deflecting Plate." *RERIC International Energy Journal* 14 (1): 25-32.

Hussain, Faisal M, and Fahad A Al-Sulaiman. 2018. "Performance Analysis of a Solar Chimney Power Plant Design Aided with Reflectors." *Energy conversion and management* 177: 30-42.

Jafarifar, Naeimeh, Mohammad Matin Behzadi, and Mohammad Yaghini. 2019. "The Effect of Strong Ambient Winds on the Efficiency of Solar Updraft Power Towers: A Numerical Case Study for Orkney." *Renewable energy* 136: 937-944.

John, A, and WAB Duffie. 2013. "Wiley: Solar Engineering of Thermal Processes." *John and Wailey and Sons: Hoboken, NJ, USA*.

Kailash, Golecha, TI Eldho, and SV Prabhu. 2012. "Performance Study of Modified Savonius Water Turbine with Two Deflector Plates." *International Journal of Rotating Machinery* 2012.

Kalash, Shadi, Wajih Naimeh, and Salman Ajib. 2013. "Experimental Investigation of the Solar Collector Temperature Field of a Sloped Solar Updraft Power Plant Prototype." *Solar Energy* 98: 70-77.

Kasaeian, Alibakhsh, Amir Reza Mahmoudi, Fatemeh Razi Astaraei, and Afshin Hejab. 2017. "3d Simulation of Solar Chimney Power Plant Considering Turbine Blades." *Energy Conversion and Management* 147: 55-65.

Koonsrisuk, Atit, and Tawit Chitsomboon. 2013. "Effects of Flow Area Changes on the Potential of Solar Chimney Power Plants." *Energy* 51: 400-406.

Lautenschlager, H., W. Haaf, and J. Schlaich. 1985. "New Results from the Solar Chimney Prototype and Conclusion for Large Power Plants." Paper presented at the *European Wind Energy Conference, Hamburg, F.R. Germany, 1985*. H.S. Stephens and Associates. http://www.scopus.com/inward/record.url?eid=2-s2.0-0021829841&partnerID=40&md5=0432ec4c82301740f0c958e6a9923504.

Lawrence, Carl A. 2010. *Advances in Yarn Spinning Technology*. Elsevier.

Li, Jianlan, Hongjing Guo, Qiang Cheng, and Shuhong Huang. 2017. "Optimal Turbine Pressure Drop for Solar Chimney-Aided Dry Cooling System in Coal-Fired Power Plants." *Energy conversion and management* 133: 87-96.

Liu, Jia, Rui Tian, and Jing Nie. 2018. "Design of Wind Turbine Blade for Solar Chimney Power Plant." *Journal of Shanghai Jiaotong University (Science)* 23 (6): 820-826.

Menter, Florian R. 1994. "Two-Equation Eddy-Viscosity Turbulence Models for Engineering Applications." *AIAA journal* 32 (8): 1598-1605.

Ming, Tingzhen, Wei Liu, Yuan Pan, and Guoliang Xu. 2008. "Numerical Analysis of Flow and Heat Transfer Characteristics in Solar Chimney Power Plants with Energy Storage Layer." *Energy Conversion and Management* 49 (10): 2872-2879.

Ming, Tingzhen, Xinjiang Wang, Renaud Kiesgen de Richter, Wei Liu, Tianhua Wu, and Yuan Pan. 2012. "Numerical Analysis on the Influence of Ambient Crosswind on the Performance of Solar Updraft Power Plant System." *Renewable and Sustainable Energy Reviews* 16 (8): 5567-5583. https://doi.org/https://doi.org/10.1016/j.rser.2012.04.055.

Mohamed, MH, G Janiga, E Pap, and D Thévenin. 2010. "Optimization of Savonius Turbines Using an Obstacle Shielding the Returning Blade." *Renewable Energy* 35 (11): 2618-2626.

Molland, AF. 2008. "Marine Engines and Auxiliary Machinery." *The maritime engineering reference book: a guide to ship design, construction and operation. New York: Elsevier*: 346-482.

Muhammed, Hardi A, and Soorkeu A Atrooshi. 2019. "Modeling Solar Chimney for Geometry Optimization." *Renewable energy* 138: 212-223.

Nasraoui, Haythem, Zied Driss, and Hedi Kchaou. 2020. "Novel Collector Design for Enhancing the Performance of Solar Chimney Power Plant." *Renewable Energy* 145: 1658-1671.

Negrou, Belkhir, Soumia Rahmouni, Noureddine Settou, and Nasreddine Chennouf. 2018. "Inverse Design Method of Wind Turbine in Solar Chimney Power Plants Coupled with Geothermal Energy." In *Exergy for a Better Environment and Improved Sustainability 1*, edited 159-170. Springer.

OGAWA, Takenori, and Haruo YOSHIDA. 1986. "The Effects of a Deflecting Plate and Rotor End Plates on Performances of Savonius-Type Wind Turbine." *Bulletin of JSME* 29 (253): 2115-2121.

Pasumarthi, N., and SA Sherif. 1998. "Experimental and Theoretical Performance of a Demonstration Solar Chimney Model—Part Ii: Experimental and Theoretical Results and Economic Analysis." *International Journal of Energy Research* 22 (5): 443-461.

Patel, Sandeep K, Deepak Prasad, and M Rafiuddin Ahmed. 2014. "Computational Studies on the Effect of Geometric Parameters on the Performance of a Solar Chimney Power Plant." *Energy conversion and Management* 77: 424-431.

Perić, M, R Kessler, and G Scheuerer. 1988. "Comparison of Finite-Volume Numerical Methods with Staggered and Colocated Grids." *Computers & Fluids* 16 (4): 389-403.

Phillips, Derek Grant. 2003. "An Investigation on Diffuser Augmented Wind Turbine Design." ResearchSpace@ Auckland.

Pretorius, Johannes P, and Detlev G Kröger. 2006. "Solar Chimney Power Plant Performance." *Journal of Solar Energy Engineering* 128 (3): 302-311.

Pretorius, Johannes Petrus. 2004. "Solar Tower Power Plant Performance Characteristics." Stellenbosch: University of Stellenbosch.

Pretorius, JP, and DG Kröger. 2009. "The Influence of Environment on Solar Chimney Power Plant Performance." *R & D Journal, of the South African Institution of Mechanical Engineering* 25.

Rabehi, Rayan, Abla Chaker, Tingzhen Ming, and Tingrui Gong. 2018. "Numerical Simulation of Solar Chimney Power Plant Adopting the Fan Model." *Renewable Energy* 126: 1093-1101.

Ragheb, M. 2014. "Optimal Rotor Tip Speed Ratio." *Lecture notes of Course no. NPRE* 475.

Raithby, GD, and KGT Hollands. 1998. "Natural Convection." *Handbook of heat transfer* 3.

Roy, Sukanta. 2014. "Aerodynamic Performance Evaluation of a Novel Savonius0style Wind Turbine through Unsteady Simulations and Wind Tunnel Experiments."

Roy, Sukanta, and Antoine Ducoin. 2016. "Unsteady Analysis on the Instantaneous Forces and Moment Arms Acting on a Novel Savonius-Style Wind Turbine." *Energy Conversion and Management* 121: 281-296.

Roy, Sukanta, and Ujjwal K Saha. 2015. "Wind Tunnel Experiments of a Newly Developed Two-Bladed Savonius-Style Wind Turbine." *Applied Energy* 137: 117-125.

Satrio, Dendy, IKAP Utama, Ketut Aria Pria, and Mukhtasor. 2018. "The Influence of Time Step Setting on the Cfd Simulation Result of Vertical Axis Tidal Current Turbine." *Journal of Mechanical Engineering and Sciences* 12 (1): 3399-3409.

Schaffarczyk, Alois Peter. 2020. *Introduction to Wind Turbine Aerodynamics.* Springer Nature.

Schlaich, J. 1995. *The Solar Chimney: Electricity from the Sun.* Edition Axel Menges.

Schlaich, J., R. Bergermann, W. Schiel, and G. Weinrebe. 2005. "Design of Commercial Solar Updraft Tower Systems - Utilization of Solar Induced Convective Flows for Power Generation." *Journal of Solar Energy Engineering, Transactions of the ASME* 127 (1): 117-124. http://www.scopus.com/inward/record.url?eid=2-s2.0-14844307147&partnerID=40&md5=c0726ce3094640bff219ad93a63175ce.

Shariatzadeh, O Joneydi, AH Refahi, SS Abolhassani, and M Rahmani. 2015. "Modeling and Optimization of a Novel Solar Chimney Cogeneration Power Plant Combined with Solid Oxide Electrolysis/Fuel Cell." *Energy conversion and management* 105: 423-432.

Shen, Wenqing, Tingzhen Ming, Yan Ding, Yongjia Wu, and Renaud K. de_Richter. 2014. "Numerical Analysis on an Industrial-Scaled Solar Updraft Power Plant System with Ambient Crosswind." *Renewable Energy* 68: 662-676. https://doi.org/https://doi.org/10.1016/j.renene.2014.03.011.

Siavash, Nemat Keramat, G Najafi, Teymour Tavakkoli Hashjin, Barat Ghobadian, and Esmail Mahmoodi. 2020. "Mathematical Modeling of a Horizontal Axis Shrouded Wind Turbine." *Renewable Energy* 146: 856-866.

Tavares Dias do Rio Vaz, Déborah Aline, André Luiz Amarante Mesquita, Jerson Rogério Pinheiro Vaz, Claudio José Cavalcante Blanco, and João Tavares Pinho. 2014. "An Extension of the Blade Element Momentum Method Applied to Diffuser Augmented

Wind Turbines." *Energy Conversion and Management* 87: 1116-1123. https://doi.org/https://doi.org/10.1016/j.enconman.2014.03.064.

Tingzhen, Ming, Liu Wei, Xu Guoling, Xiong Yanbin, Guan Xuhu, and Pan Yuan. 2008. "Numerical Simulation of the Solar Chimney Power Plant Systems Coupled with Turbine." *Renewable energy* 33 (5): 897-905.

Vakilabadi, M Akbari, Mokhtar Bidi, AF Najafi, and Mohammad H Ahmadi. 2019. "Exergy Analysis of a Hybrid Solar-Fossil Fuel Power Plant." *Energy Science & Engineering* 7 (1): 146-161.

Wenehenubun, Frederikus, Andy Saputra, and Hadi Sutanto. 2015. "An Experimental Study on the Performance of Savonius Wind Turbines Related with the Number of Blades." *Energy procedia* 68: 297-304.

Yunus, A Cengel. 2010. *Fluid Mechanics: Fundamentals and Applications (Si Units).* Tata McGraw Hill Education Private Limited.

Zandian, Arash, and Mehdi Ashjaee. 2013. "The Thermal Efficiency Improvement of a Steam Rankine Cycle by Innovative Design of a Hybrid Cooling Tower and a Solar Chimney Concept." *Renewable energy* 51: 465-473.

Zhou, Xinping, and Yangyang Xu. 2014. "Solar Updraft Tower Power Generation." *Solar Energy*. https://doi.org/http://dx.doi.org/10.1016/j.solener.2014.06.029.

Zhou, Xinping, Shuo Yuan, and Marco Aurélio dos Santos Bernardes. 2013. "Sloped-Collector Solar Updraft Tower Power Plant Performance." *International Journal of Heat and Mass Transfer* 66 (0): 798-807. https://doi.org/http://dx.doi.org/10.1016/j.ijheatmasstransfer.2013.07.060.

Zhou, XP, JK Yang, B Xiao, and F Long. 2008. "Numerical Study of Solar Chimney Thermal Power System Using Turbulence Model." *Journal of the Energy Institute* 81 (2): 86-91.

Zou, Zheng, Zhiqiang Guan, and Hal Gurgenci. 2014. "Numerical Simulation of Solar Enhanced Natural Draft Dry Cooling Tower." *Solar Energy* 101: 8-18.

Zou, Zheng, and Suoying He. 2015. "Modeling and Characteristics Analysis of Hybrid Cooling-Tower-Solar-Chimney System." *Energy conversion and management* 95: 59-68.

Zuo, Lu, Pengzhan Dai, Zihan Liu, Ning Qu, Ling Ding, Bo Qu, and Yue Yuan. 2020. "Numerical Analysis of Wind Supercharging Solar Chimney Power Plant Combined with Seawater Desalination and Gas Waste Heat." *Energy Conversion and Management* 223: 113250.

Zuo, Lu, Pengzhan Dai, Ziyang Yan, Chuang Li, Yuan Zheng, and Yunting Ge. 2021. "Design and Optimization of Turbine for Solar Chimney Power Plant Based on Lifting Design Method of Axial-Flow Hydraulic Turbine Impeller." *Renewable Energy*.

Zuo, Lu, Ling Ding, Jiajun Chen, Zihan Liu, Ning Qu, Xiaotian Zhou, and Yue Yuan. 2018. "The Effect of Different Structural Parameters on Wind Supercharged Solar Chimney Power Plant Combined with Seawater Desalination." *Energy conversion and management* 176: 372-383.

Zuo, Lu, Zihan Liu, Ling Ding, Ning Qu, Pengzhan Dai, Bofeng Xu, and Yue Yuan. 2020. "Performance Analysis of a Wind Supercharging Solar Chimney Power Plant Combined with Thermal Plant for Power and Freshwater Generation." *Energy Conversion and Management* 204: 112282.